A theoretical and experimental investigation of non-normal nature of thermoacoustic interaction

A THESIS

submitted by

SATHESH MARIAPPAN

for the award of the degree

of

DOCTOR OF PHILOSOPHY

DEPARTMENT OF AEROSPACE ENGINEERING
INDIAN INSTITUTE OF TECHNOLOGY MADRAS.

August 2011

THESIS CERTIFICATE

This is to certify that the thesis titled **A theoretical and experimental investigation of non-normal nature of thermoacoustic interaction**, submitted by **Sathesh Mariappan**, to the Indian Institute of Technology, Madras, for the award of the degree of **Doctor of Philosophy**, is a bona fide record of the research work done by him under my supervision. The contents of this thesis, in full or in parts, have not been submitted to any other Institute or University for the award of any degree or diploma.

Dr. R. I. Sujith
Research Guide
Professor
Deptartment of Aerospace Engineering
IIT-Madras, 600 036

Place: Chennai

Date: 19th January 2009

ACKNOWLEDGEMENTS

I would like to thank and acknowledge the help rendered by all the people during my past four years of research. It was a wonderful experience for me to perform my PhD in this pleasant ambience. During the years, several people have influenced my academic career at various point of time.

First and foremost, I would like to express my gratitude to my supervisor, Prof. R. I. Sujith for his exceptional guidance and support. I am always amazed by his enthusiasm and extraordinary efforts, that he puts in learning new things, which is a source of motivation. In fact, without his motivation and effort, I would not have joined for PhD. He has shaped my career and taught me lot of things, both academic and non-academic, which helped and will help me to continue my career in the future. Further, I owe him for the enormous freedom that he has given me and the faith he had in me.

I would like to express my gratitude to the members of my Doctoral Committee, Prof. S. Narayanan, Prof. K. Balasubramaniam, Prof. S. R. Chakravarthy, Dr. S. Sarkar and Dr. N. K. Sinha for their valuable comments and suggestions during the meetings. I would like to thank our HODs, Prof. J. Kurian, Prof. P. Sriram and Prof. V. Bhaskar for their support and encouragement during the stay. My sincere gratitude to my teachers, Prof. S. Santhakumar, Prof. M. Ramakrishna, Dr. Velmurugan, Dr. N. R. Panchapakesan, Dr. Amit Kumar, Dr. T. Muruganandam (Aerospace), Prof. N. Gupte, Prof. S. Govindarajan and Prof. V. Balakrishnan (Physics) for their exceptional lectures, which helped to understand the concepts clearer and better. I would like to acknowledge the excellent suggestions from Prof. V. Jayashankar (Electrical) in designing the high current heater that I use in my experimental setup.

Throughout my stay, I have been supported constantly by the administrative staffs, Mrs. Mekala, Mr. Sundar, Mr. Dhanapal, Mr. Stephen, Mr. Siva, Ms. Rajalakshmi and Mrs. Saraswathi (institute administration) during all my paper work. I would like to acknowledge the great help provided by the staffs in the work shop, Mr. Shankaraku-

marasamy, Mr. Kennedy, Mrs. Yamuna and Mr. Dayalan. Special thanks to Mr. John George (Central workshop incharge) for his suggestions regarding safety in my experimental setup. Many thanks to Mr. Ranganathan and Mr. Chandru for making most of the components in my experimental setup.

I am indebted to Prof. P. J. Schmid for answering patiently to my never ending questions regarding non-normality and adjoint optimisation technique. I wish to thank Prof. W. Polifke for his generous support and critical comments during his visits, which made me to think further and understand the problem better. I am indebted to Dr. P. Wahi, Prof. M. K. Verma and Mr. S. Saha for introducing me to the technique of continuation to analyse nonlinear dynamical systems. Special thanks to Prof. Rama Govindarajan for her enthusiastic support and interest in my work. I would like to acknowledge Dr. M. Juniper for organising the AIM meetings, which gave me a good exposure to the tools for analysing the stability of hydrodynamic flows.

I would like to acknowledge the financial assistance from the institute and alumni to present some of my papers in the international conferences, which gave me a good exposure of the outside research world. Further, I am grateful to DST and MHRD, India for funding my research and stay.

This acknowledgement would never be complete, if I do not mention my lab and hostel friends. I am very lucky to got some of best friends of my life over the years in the lab. Everybody in the lab have helped in some way or other during my stay. I am greatly indebted to all of them, particularly, Priya for her endless hospitality especially during my initial period in the lab, Lipika for her kind involvement in the initial fabrication of the experimental setup and subsequent instrumentation, Rahul for his soft and friendly company. My sincere thanks to Balaji for teaching me SIMPLE algorithm and I am always amazed by his patience, which was a motivation during my hard times. I enjoyed the company of Ramgopal & Vivek, with whom I have spent a lot of time in the later part of my stay and will cherish the moments in the future. I thank my senior friends Kushal, Sharath, Bharath, Koushik, Guru, O. J. Sreenivasan, Jayaraman, Jayasurya and Sreerekha for their support and suggestions in handling numerical codes and hardware instruments. My understanding have greatly improved during my discussions with Rajini, Devendra, Irfan, Joseph, Thomas, D(∂)avid, Ramesh, Ganesh, Avishek,

Vikrant, Vineeth, Vinu, Tharun, Girish sir, Rana sir, Ralf, Santhosh (my junior), Trinath, Rajesh, Vishnu, Rupa, and Pushkarini.

In the hostel, I am happy to have got the company of Rajasekar and I use to stay in his room whenever I get bored. I have shared lots of happy and memorable moments with my friends, Somasundaram (taught me to play tennis), Raju, Mahendran, Shyam, Shankar (tennis mate and helped me with his electrical knowledge in my experimental instrumentations), Ravikumar, Gnanasekhar, Mayil, Venkatesh, Mahesh, Joseph. Further thanks for the help rendered by the hostel administrative staffs, Mr. Rajamani, Mr. Balaji (Swamy).

Finally, I should acknowledge that all my successes that I had and will have in my life are due to my parents. I always thank them for their careful attention towards me and dedicate the present thesis to them. I thank God for blessing me with good health and giving me everything that I enjoy in my life.

ABSTRACT

KEYWORDS: LaTeX; Thesis; Style files; Format.

A LaTeX class along with a simple template thesis are provided here. These can be used to easily write a thesis suitable for submission at IIT-Madras. The class provides options to format PhD, MS, M.Tech. and B.Tech. thesis. It also allows one to write a synopsis using the same class file. Also provided is a BIBTeX style file that formats all bibliography entries as per the IITM format.

The formatting is as (as far as the author is aware) per the current institute guidelines.

TABLE OF CONTENTS

LIST OF TABLES

LIST OF FIGURES

ABBREVIATIONS

BC	Boundary Condition
BTCS	Backward Time Central Space
CFD	Computational Fluid Dynamics
FFT	Fast Fourier Transform
IC	Initial Condition
ODE	Ordinary Differential Equation
PDE	Partial Differential Equation
RK4	Runge-Kutta Fourth Order
SIMPLE	Semi-Implicit Method for Pressure Linked Equations
SRM	Solid Rocket Motor
SVD	Singular Value Decomposition

NOTATION

Chapter 1, Introduction

C_n	Constants defining the initial condition
L	Linear operator matrix
p	Acoustic pressure
u	Acoustic velocity
V_n	n^{th} eigenmode of the system
χ	State space vector
$\dagger$	Adjoint operation
ω_n	n^{th} complex eigenvalue
α_n	Growth rate of n^{th} eigenvalue
β_n	Angular frequency of n^{th} eigenvalue
$\Re_n$	Real part of the eigenvalue
$\Im_n$	Imaginary part of the eigenvalue
ϕ_n	Projection along the direction of n^{th} eigenmode
$\|\| \bullet \|\|$	L2 norm of the state space vector

Chapter 2, Solid Rocket Motor

F	ratio of timescales of chamber acoustics and transient heat conduction in the propellant
H	ratio of the heat release at the propellant surface to the thermal capacity of the propellant
l	Length of the propellant grain, m
M	Mach number of steady state flow
m	Mass influx rate from the propellant per unit volume at any axial location, kg/m^3s
m_p	Pyrolysis coefficient of the propellant
n	Burn rate index of the propellant
Q_s	Overall heat release per unit mass at the propellant surface, J/kg
R	Propellant regression rate, m/s
S_c	Port area, m^2
S_l	Port circumference, m
S_p	Specific heat capacity of the propellant, J/kgK
T	Temperature, K
x	Non-dimensional co-ordinate in the axial direction of the motor from the head end
y	Non-dimensional distance from the propellant surface
α	Thermal diffusivity of the propellant, m^2/s
ρ	Density, kg/m^3

Symbols

$\widehat{\ }$	Total dimensional variables
$\bar{\ }$	Reference variables for non-dimensionalisation
$\tilde{\ }$	Dimensional variables

Chapter 3, Rijke tube

ρ	Density of the fluid flow
u	Velocity of the fluid flow
p	Static pressure of the fluid flow
T	Temperature of the fluid flow
l_a	Length of the Rijke tube
l_c	Radius of the electrical heater wire
l_w	Effective length of the heater wire participating in heat trasnfer
S_c	Cross section area of the Rijke tube
t_{ac}	Time scale in the acoustic zone
t_{cc}	Time scale in the hydrodynamic zone
δ	Length scale ratios (l_c/l_a)
ϵ	Time scale ratios ($t_{ac} = t_{cc}$)
γ	Ratio of specific heat capacities
$\hat{e}_r$	Unit vector along the radial direction in the hydrodynamic zone
ω_n	Frequency of the n^{th} Galerkin mode
$\Re$	Specific gas constant
a	Average speed of sound
C_1	Damping coefficient in the acoustic zone
C_2	Damping coefficient in the acoustic zone
Ec	Eckert number
K	Non-dimensional heater power
K_c	Keulegan-Carpenter number
M	Mach number of the steady state flow
N	Number of Galerkin modes used for the simulation
Pe	Peclet number
q	Non-dimensional unsteady heat release rate from the heater
x_a	Co-ordinates in the acoustic zone
x_f	Non-dimensional axial location of the heater
$r,\ \theta$	Co-ordinates in the hydrodynamic zone
Re	Reynolds number
u_f	Non-dimensional acoustic velocity at the heater location x_f

Subscript

0	Steady state variables
a	Variables corresponding to acoustic zone
c	Variables corresponding to hydrodynamic zone
p	Transformed variables in the hydrodynamic zone
s	Steady state variables in non-dimensional form
$p-p$	Peak to peak value of the variable in the asymptotic time

Superscript

d	Downstream variables
u	Upstream variables

Symbols

$\bar{}$	Reference variables for non-dimensionalisation
$\tilde{}$	Dimensional variables

CHAPTER 1

Introduction

Thermoacoustic instability is a challenging problem in solid and liquid rockets, ramjets, aircraft and industrial gas turbines etc. (Mcmanus *et al.*, 1993). A typical combustion chamber, showing a premixed flame as the heat source is indicated in Fig. 1.1. Thermoacoustic instability occurs when the acoustic oscillations in a duct (combustion chamber) are amplified by the positive feed from the unsteady heat release rate from the heat source (Fig. 1.2). The mechanism of instability is as follows.

In combustion chambers, disturbances are always present due to turbulence of the incoming flow, change in the operating conditions etc. The velocity fluctuations generated due to the above phenomenon perturb the heat release rate from the heat source. For example in a premixed flame, an upstream velocity fluctuations causes wrinkles on the flame surface and causes fluctuations in flame surface area, which eventually leads to heat release rate fluctuations (Schuller *et al.*, 2003). In turn, the heat release rate fluctuations cause the surrounding fluid to expand and contract. This motion near the heat source is like a monopole source of sound and creates acoustic oscillations in the duct. The acoustic velocity thus generated again perturbs the heat source and the feed back loop is completed. If the driving from the acoustic - heat source coupling overcomes the

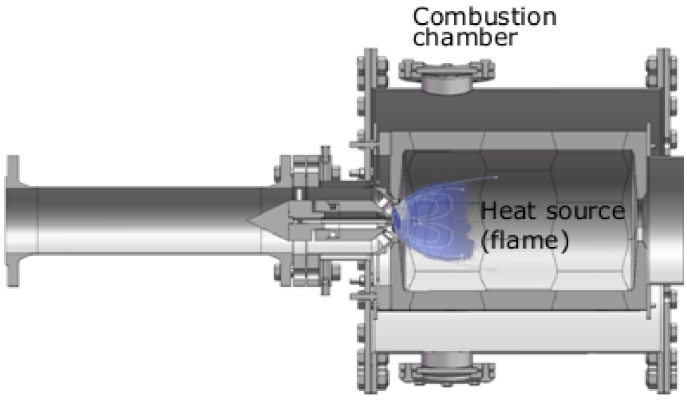

Figure 1.1: A typical combustion chamber, showing a premixed flame as the heat source. The figure is adapted from `http://www.zarm.uni-bremen.de/`

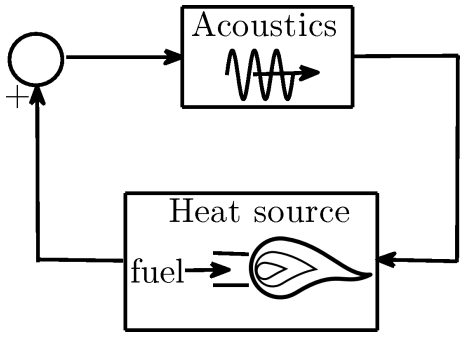

Figure 1.2: Schematic representation of the coupling between acoustic field and unsteady heat release rate in the combustion chamber.

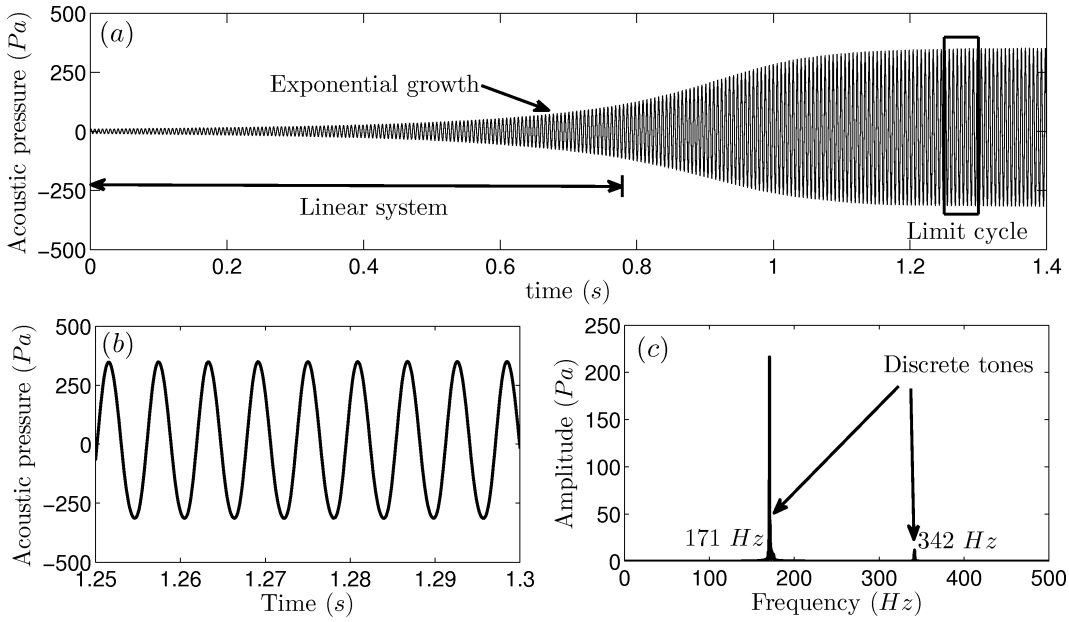

Figure 1.3: A typical experimental data obtained in the thermoacoustic instability of an electrically heated horizontal Rijke tube. (a) Evolution of acoustic pressure during instability. (b) 'Zoomed in' view of the oscillations during limit cycle. The region represented by the rectangle in (a) is shown. (c) Spectral content in the oscillations of the limit cycle. Two discrete tones of frequencies 171 and 342 Hz are observed. Power supplied to the heater is 800 W, mass flow rate through the system is 2.19 g/s, the heater is located at a distance of $1/8^{\text{th}}$ from the upstream end of the tube and the acoustic pressure is measured at a location of 0.525 m from the upstream end.

acoustic damping (viscous and end losses) in the duct, the amplitude of the oscillations increases and eventually saturates to a limit cycle due to the nonlinearity present in the system. The limit cycle thus obtained has well defined frequencies associated with it.

Fig. 1.3(a) represents the evolution of acoustic pressure measured experimentally during thermoacoustic instability in an electrically heated horizontal Rijke tube. Initially, the amplitude of the oscillations are small and can be described by linear theory. The oscillations grow exponentially and as the amplitude increases, the nonlinearity saturates the amplitude of the oscillations to reach a limit cycle. The region represented by the rectangle is zoomed up and is shown in Fig. 1.3(b). The wave form during limit cycle shows well defined sinusoidal oscillation. Further, the spectral content of the acoustic pressure oscillations during limit cycle indicates two well defined peaks as shown in Fig. 1.3(c). The above peaks are associated with the first and second modes of the system.

The above self sustained acoustic oscillations cause excessive turbine blade vibration in gas turbines and damage them eventually. Further, in industrial gas turbines, stringent emission norms require the combustor to operate in lean equivalence ratios where thermoacoustic instabilities are more prone to occur (Annaswamy *et al.*, 1997). The problems arising due to thermoacoustic instability are identified only in the later stages of the development programme. The complex interaction between the chamber acoustic field, the unsteady fluid flow and the combustion makes the problem challenging. Thus, identifying instabilities in the early phase of the design stage is a formidable task. Thermoacoustic instability occurs, when the acoustic pressure oscillations in the combustion chamber are amplified by the positive feedback of the unsteady heat release rate from the heat source in the chamber. Hence, understanding the coupling between the chamber acoustic field and the heat source is vital for the prediction and control of these instabilities.

1.1 Classical linear stability analysis

In the analysis of thermoacoustic instability, the system is initially modelled using mathematical equations. These are in general nonlinear partial differention equations (PDEs) (Poinsot and Veynante, 2005). As the first step in the investigation of the stability of the system, the governing equations are linearised around the steady state. Further, the linearised equations are valid, when the amplitude of the perturbations are small. Even for a system which is unstable, like the one shown in Fig. 1.3(*a*), the amplitude during the initial growth phase of the disturbance is small. Hence the above initial evolution can be described by linear theory. The obtained linearised equations, which are in general PDEs, can be converted to ordinary differential equations (ODEs) in time by suitable discretisation in space (Schmid and Henningson, 2001). The ODEs thus obtained can be cast in the following form (Strogatz, 2000):

$$\frac{d\chi}{dt} = L\chi \tag{1.1}$$

where, χ represents the column vector, where the elements are the state space variables defining the system. For example, χ can contain the evolution of acoustic velocity (u) and pressure (p) at various discretised locations of the system. L is a matrix, which determines the linear evolution of the system.

In classical stability analysis, the eigenvalues of L determines the linear stability of the system (Strogatz, 2000). The spectrum and the corresponding linear evolution of the disturbance are shown in Fig. 1.4. If all the eigenvalues are in the left half of the imaginary axis, as shown in Fig. 1.4(*a*), the system is stable. On the other hand, even if one of the eigenvalue is to the right of the imaginary axis (Fig. 1.4*c*), the system is unstable (Strogatz, 2000). A typical evolution of the acoustic pressure oscillation for a linearly stable and unstable system are shown in Fig. 1.4(*b* & *d*) respectively.

The stability predicted by the above theory is valid only at asymptotic time limit ($t \rightarrow \infty$) and is often termed as 'Lyapunov stability' (Strogatz, 2000). No predictions are made about the evolution of the system, in the initial period (just after the initial perturbation). The non-normal nature of the system plays an important role in this regime.

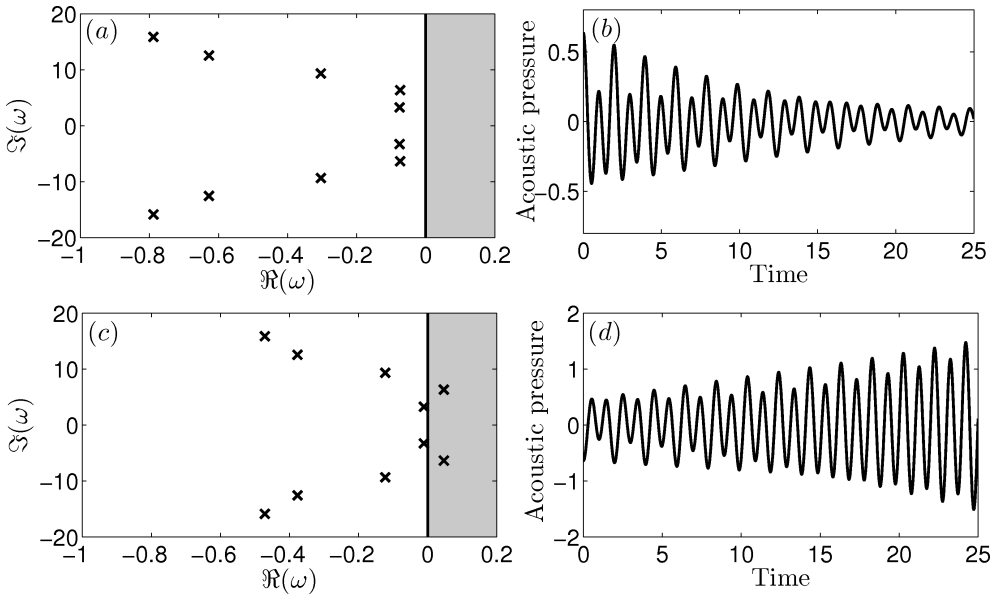

Figure 1.4: *a & c*) Spectrum for a linearly stable and unstable system. *b & d*) Evolution of acoustic pressure for the same system.

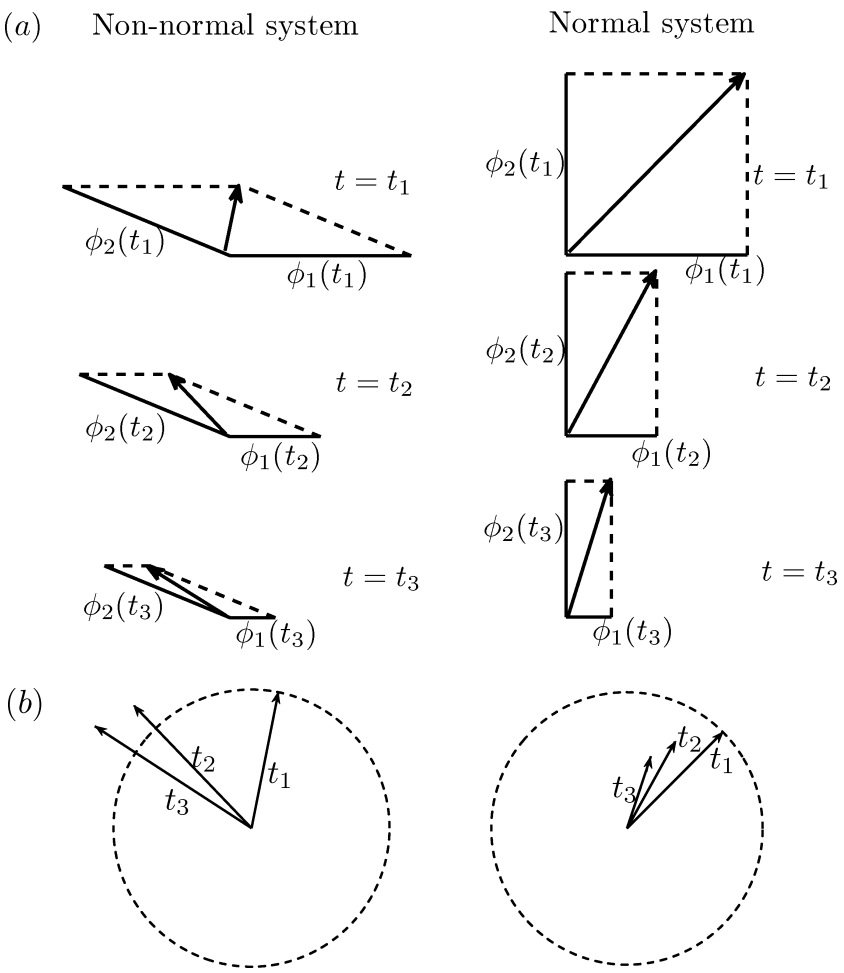

Figure 1.5: *a*) Evolution of an initial condition at various time instants $t_1 < t_2 < t_3$ for non-normal and normal systems. *b*) Evolution of energy in the disturbance ($||\chi(t)||^2$) for the above initial conditions.

1.2 Non-normality and transient growth

A system is said to be non-normal if the linear operator L governing the system evolution does not commute with its adjoint $L^\dagger$ $\left(LL^\dagger \neq L^\dagger L, \quad \dagger \text{ indicates adjoint operator}\right)$ (Golub and Loan, 1989). For such systems, the eigenmodes (eigenvectors) are non-orthogonal. The solution of (1.1) can be written in terms of eigenmodes as follows:

$$\chi(t) = \sum_{n=1}^{N} C_n e^{(\alpha_n + i\beta_n)t} V_n \tag{1.2}$$

where, $\omega_n = \alpha_n + i\beta_n$ is the n^{th} eigenvalue, V_n is the corresponding eigenmode and C_n are the constants, which are determined by the initial condition. The evolution of the system is represented by the linear combination of the projection along the eigenmodes. In order to visualise transient growth, a system with two degrees of freedom is considered and is shown in Fig. 4.2. Then only two eigenmodes are present and can be represented easily in a figure. Let $\phi_n = e^{(\alpha_n + i\beta_n)} V_n$ represent the projection of the disturbance along the direction of eigenmodes. An initial condition ($t = t_1$), which is represented by an arrow is chosen such that, it has projections on both the eigenmodes. For a linearly stable system, ϕ_n decays (as $\alpha_n < 0$) according to their decay rate monotonically to zero. Two cases are considered: Non-normal and normal system. Non-normal system is first analysed and is represented by ϕ_1 & ϕ_2 drawn non-orthogonally. As time evolves, the amplitude of the disturbance grows for a short time, which can be seen from the left hand side of Fig. 4.2(*a*). The disturbance amplitude decays eventually to zero, as the individual ϕ_n also decays to zero, thus confirming the predictions of linear stability. On the other hand, in a normal system (ϕ_1 & ϕ_2 are orthogonal), the same initial condition decays monotonically.

The evolution of the amplitude of the disturbance ($||\chi(t)||^2$) are shown in Fig. 4.2(*b*). The amplitude of the disturbance is defined as the L2 norm of the state space vector χ. For non-normal system, ($||\chi(t)||^2$) increases transiently and eventually decays, whereas the same decreases monotonically for a normal system. One more important point to be noted is the following. If an initial condition has components along only one eigenmode (along ϕ_n), then there is no transient growth as all ϕ_n decays monotonically. Hence the amount of transient growth depends on the initial condition given to the sys-

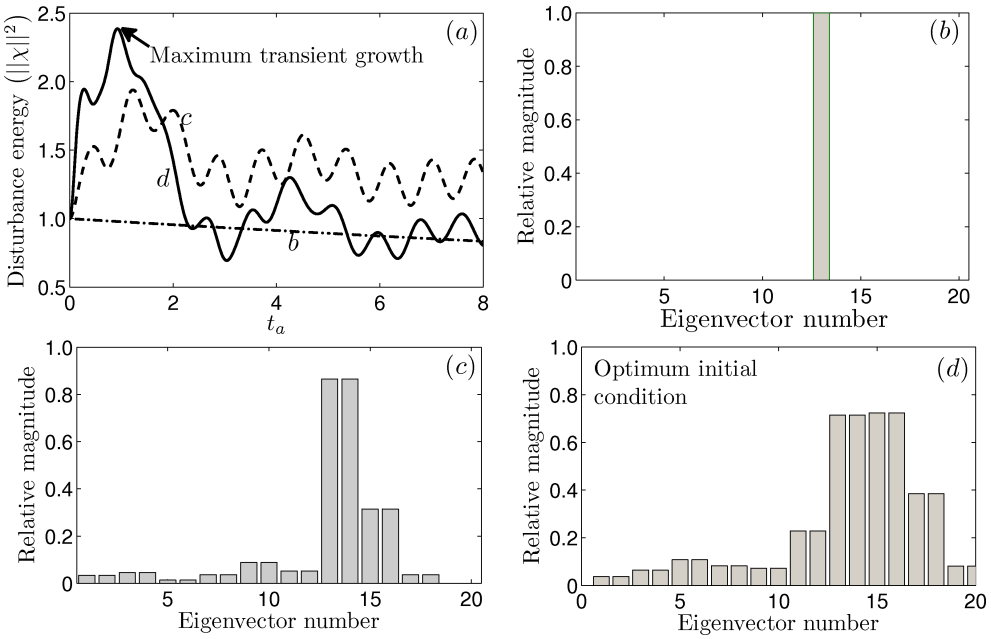

Figure 1.6: *a*) Evolution of the energy in the disturbance for various initial conditions. The initial conditions are marked. *b*) Initial condition along only one eigenmode. *c*) Initial condition along more than one eigenmode. *d*) Distribution of optimum initial condition along various eigenmodes.

tem. The same is illustrated in Fig. 1.6, where the analysis have been performed in a non-normal system (Balasubramanian and Sujith, 2008*b*) with 20 degrees of freedom. Figure 1.6(*a*) shows the evolution of energy in the disturbance for various initial conditions. The evolutions are marked according to the subfigure labels in Fig. 1.6(*b*-*d*), where the initial conditions are shown. When an initial condition, which has projection along only one eigenmode (Fig. 1.6*b*) is given, the disturbance energy decays monotonically. Disturbance energy in the present case is proportional to $(||\chi(t)||^2)$. However, when the initial condition, which has projections on more than one eigenmodes (Fig. 1.6*c*) is chosen, transient growth in the disturbance energy is observed. Moreover, the optimum initial condition which gives the maximum transient growth can also be obtained and is shown in Fig. 1.6(*d*). The detailed technique of obtaining the same is given in Section 2.4. To summarise, for a linearised system, stable under the classical linear stability (no nonlinearities included), all eigenmodes are decaying monotonically in time. However, in the case of the non-normal system, the vectorial sum of the eigenmodes which gives the state of the system at any time *t* can increase (for a suitable initial condition) for a short time and eventually decays after a long time. The transient growth occurring might be of several orders of magnitude and the system might reach a

different dynamical behaviour, e.g. limit cycles, if the nonlinearities become significant as the amplitude increases during this growth (Balasubramanian and Sujith, 2008*a*).

1.3 Non-Normality in thermoacoustic system

Recently, thermoacoustic systems are shown to be non-normal, which leads to the non-orthogonality of the eigenmodes (Balasubramanian and Sujith, 2008*b*). Consider the following acoustic momentum and energy equation for low Mach number flow in non-dimensional form:

$$\frac{\partial u}{\partial t} + \frac{\partial p}{\partial x} = 0 \tag{1.3a}$$

$$\frac{\partial p}{\partial t} + \frac{\partial u}{\partial x} = Q(x) \tag{1.3b}$$

where, 'u' and 'p' represent the non-dimensional acoustic velocity and pressure in the duct respectively, Q represents the non-dimensional unsteady heat release rate from the heat source. In general, the above heat release rate can be written as $Q(x) = R(x)u(x,t) + S(x)p(x,t)$ (Balasubramanian and Sujith, 2008*b*). $R(x)$ & $S(x)$ represent the strength of the coupling between the acoustic variables and the heat source. Equation (1.3) can be cast in the standard form (1.1) as follows:

$$\frac{\partial}{\partial t}\begin{pmatrix} u \\ p \end{pmatrix} = \underbrace{\begin{pmatrix} 0 & -\frac{\partial}{\partial x} \\ -\frac{\partial}{\partial x} + R & S \end{pmatrix}}_{L} \begin{pmatrix} u \\ p \end{pmatrix} \tag{1.4}$$

When $R = 0$, the linear operator 'L' in the above equation is self-adjoint. As the value of R increases due to the presence of heat source, L becomes non-normal. In most of the combustion system, fluctuations in heat release rate from the heat source by acoustic velocity fluctuations is prominent (Candel, 2002) and hence $R(x)$ is non-zero in most of the combustion chamber. Hence thermoacoustic interaction is always non-normal. The transient growth occurs in the evolution of $\int\limits_{\text{domain}} (u^2 + p^2)\, dv$ and is identified as non-dimensional acoustic energy of the system (Nagaraja *et al.*, 2009).

A typical stability map for a thermoacoustic system is shown in Fig. 1.7 for the

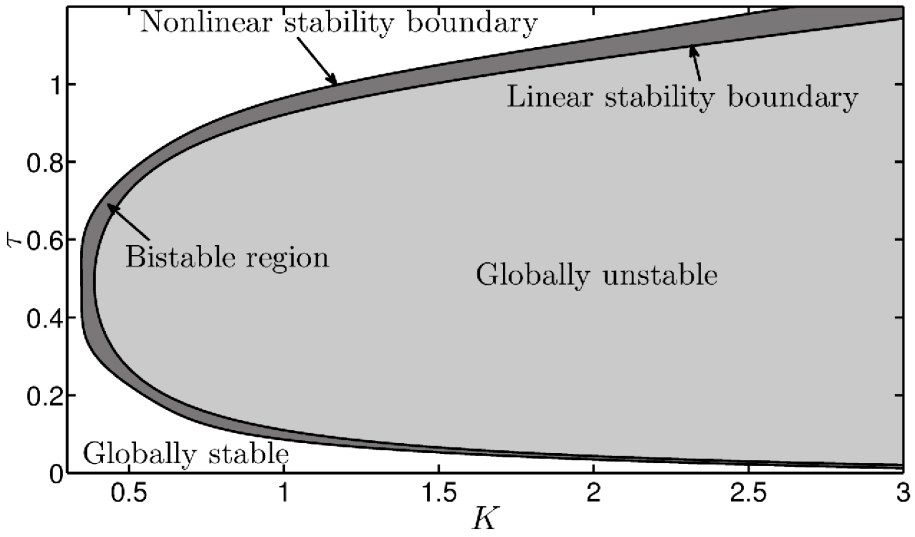

Figure 1.7: Region of bistability obtained for the bifurcation between non-dimensional heater power (K) and time lag (τ) between the response of the heater to acoustic velocity fluctuations. This figure is adapted from Subramanian *et al.* (2010*a*)

variation of two parameters, namely non-dimensional heater power (K) and time lag (τ) between the response of the heater to acoustic velocity fluctuations Subramanian *et al.* (2010*a*). White region indicates the globally stable region i.e., the system is stable for all amplitude perturbations. Globally unstable region, where the system is unstable to any amplitude perturbations is marked in light grey colour. The transition from globally stable to unstable behaviour happens via a bistable region (marked in dark grey colour), where the system is stable for small amplitude perturbations, while the same is unstable for large amplitude perturbations. Transient growth arising due to the non-normal nature of the thermoacoustic interaction plays an important role in the bistable regime (Balasubramanian and Sujith, 2008*a*,*b*).

1.4 Literature review

Thermoacoustic oscillations were first observed by Rijke (1859). They used a vertical tube with a coiled electrical heating filament as the heat source. Self-sustained thermoacoustic oscillations were observed when the heater was positioned at some axial location of the tube and beyond some threshold power level. For example, the acoustic oscillations were observed only, when the heater is positioned at the lower half of the

duct. The tube was name after him: Rijke tube. Rijke gave an explanation based on the pressure pulse generated due to volumetric expansion of the fluid near the heater zone. However, this argument did not explain the fact that instabilities were observed only for some selected range of heater locations. The condition for the occurrence of thermoacoustic instability was given by Rayleigh (1878). Thermoacoustic oscillations are amplified, when the acoustic pressure oscillations are in phase with the unsteady heater release rate from the heat source. Carvalho *et al.* (1989) employed a linear model for the unsteady heat release rate and then applied Rayleigh criteria (Rayleigh, 1878) to predict the axial locations of the heater for which the thermoacoustic oscillations are unstable. The predictions were in good qualitative agreement to the observation made in Rijke (1859). In aero engines, thermoacoustic oscillations were first observed in solid rocket motors (SRM).

1.4.1 Thermoacoustic instabilities in solid rocket motors

Thermoacoustic instabilities in SRMs are known to exist since 1930 (Culick, 2006). Since then, many investigations were conducted to understand the mechanisms behind them and to arrive at measures to control the same. Furthermore, combustion instability alone is not the only source of instability in an SRM. Although other instabilities, such as chuffing or L^* instability (Sutton and Biblarz, 2001), acoustic instability due to vortex shedding in segmented motors (Vuillot, 1995; Kourta, 1997; Anthoine *et al.*, 2002) and instability of shear waves at the propellant surface (Flandro and Majdalani, 1996) are important, acoustic oscillations due to thermoacoustic instabilities play a dominant role. In the SRM, the driving mechanism for combustion instability to happen is the response of the unsteady burn rate of the propellant to chamber acoustics. This leads to unsteady mass addition to the combustion chamber and ultimately causes an unsteady heat release rate.

Initial attempts to analyse thermoacoustic instabilities theoretically were by Culick (1963) and Friedly and Petersen (1966), where the linearised equations were investigated. They obtained an explicit expression for the complex frequency (eigenvalue) of the system. The real part of the frequency gave the growth or decay of the oscillations.

When the real part is positive, the system becomes linearly unstable (Section 1.1) and the amplitude of the oscillations grow exponentially, eventually reaching a limit cycle. Culick (1976*a*) was the first to derive an analytical condition for the existence of stable and unique limit cycle behaviour using a two mode Galerkin approximation with second order acoustics as the only nonlinear process. Nonlinearity in the combustion response was also included in the analysis and the dynamical behaviour was analysed (Levine and Baum, 1983; Flandro *et al.*, 2007).

Another interesting dynamical behaviour observed experimentally was that SRMs stable for small amplitude disturbances were seen to become unstable for larger ones (Blomshield *et al.*, 1997*a*). This was called 'pulsed instability' or 'triggering'. Many mechanisms were proposed for explaining triggering in the past. Second order gas dynamics alone were proved to be insufficient to cause triggering because of the absence of 'self coupling' terms (Culick, 1994). Higher order gas dynamics (third order acoustics) also proved the same (Yang *et al.*, 1990). Hence, a nonlinear combustion response was thought of as an alternate candidate for triggering. Culick *et al.* (1995) used an *ad hoc* nonlinear velocity coupling model for burn rate response to show triggering numerically. Wicker *et al.* (1996) analysed various forms of nonlinear coupling between unsteady burn rate and acoustic variables. By suitably adjusting the parameters and the form of the coupling terms, triggering was demonstrated. Anathakrishnan *et al.* (2005) further explained that velocity coupled models are the only possible candidates for causing triggering in realistic operating regimes of SRMs.

The stability analysis described above concentrated on the behaviour of individual eigenvalues and the associated eigenmodes. Hence, the analysis were termed as modal stability analysis. During the early 90s (Schmid, 2007), a new stability analysis gained popularity in the investigation for stability of fluid flow problems. In this case, the stability of the system is defined based on the dynamics of the energy associated with the perturbations. A mechanism for triggering instabilities (as introduced in the previous paragraph) is described by the above stability analysis. This analysis is termed as non-modal stability analysis, as it involves the dynamics associated with more than one eigenvalue and the corresponding eigenmode.

1.4.2 Non-modal stability theory

Non-modal stability theory was first applied in the analysis of stability of fluid flow problems. Transient growth was first observed by Gustavsson (1991) from the numerical simulations of a plane channel flow. The paper concentrated on the evolution of a three dimensional disturbance. Orr-Sommerfeld equations (Orr, 1907) are used to describe the evolution of wall normal components of velocity and vorticity. In Gustavsson (1991), non-zero initial conditions are prescribed only in the wall normal velocity component and a transient growth in the kinetic energy is observed even for a damped mode.

Butler and Farrell (1992) then performed non-modal stability analysis in the same plane channel flow. The operator governing the linear evolution of the system was shown to be non-normal. As described in Section 1.2, the amount of transient growth in the energy of the perturbations depends on the initial condition. Optimum initial condition for maximum transient growth was obtained using a variational approach. They observed that three-dimensional perturbations are optimal in transiently increasing the amplitude of the perturbations. Streamwise vortices are obtained as the optimal perturbations, which further evolve to streamwise streaks. The ratio of the energy in the streamwise streaks to the streamwise vortices were of the order 10^3 for a Reynolds number of 1000. The higher transient growth thus obtained might trigger the system to become nonlinearly unstable, eventually reach turbulence. Further, the formation of three-dimensional structures during the onset of turbulence were observed much earlier experimentally in boundary layer flows (Klebanoff *et al.*, 1962).

A framework for the non-modal stability analysis was developed by Farrell and Ioannou (1996*a*,*b*) to analyse autonomous and non-autonomous systems respectively. They applied the theory to analyse the stability of atmospheric flows. The idea of obtaining the maximum transient growth and the associated optimum initial condition by singular value decomposition was also introduced. Later numerical simulations in several fluid mechanic problems like, evolution of a pair of oblique waves in a plane channel flow (Schmid and Henningson, 1992), stability analysis of a falling liquid curtain (Schmid and Henningson, 2002), transient growth in a swept Hiemenz flow (Guegan

et al., 2008), etc. were performed and the importance of non-normal nature of the system is identified. Since the nonlinear terms in the Navier-Stokes equation for incompressible flow conserve kinetic energy (Henningson *et al.*, 1993), non-normality was shown to be a necessary condition for the subcritical transition to turbulence (Henningson and Reddy, 1994).

There are a few experimental evidence of transient growth in fluid flow problems. The earliest experimental results were reported by Mayer and Reshotko (1997), who have observed transient growth of the disturbance amplitude in a pipe flow experiment. The formation of streaky structures (regions of high and low velocity field), which appear due to non-normal nature of the system was observed in experiments in boundary layer (Matsubara and Alfredsson, 2001). In the same experiment, stable laminar streaks were generated experimentally and a transient growth in the amplitude of disturbance was observed in the stream wise direction (Fransson *et al.*, 2004). Further, a passive control of transition to turbulence in boundary layer was performed by exploiting the non-normal nature of the system (Fransson *et al.*, 2006).

To summarize, in fluid flows, the interplay between non-normality and nonlinearity is shown to be one of the routes for the sub-critical transition to turbulence (Gebhardt and Grossmann, 1994; Baggett *et al.*, 1995; Barkley and Tuckerman, 1999; Criminale and Drazin, 1999). Non-normality and transient growth are observed in many areas of research including magnetohydrodynamics (Krasnov *et al.*, 2004), astrophysics (Mukhopadhyay *et al.*, 2006) and atmospheric flows (Farrell and Ioannou, 1996*a*). Motivated by the role of non-normality in the stability of fluid flow problems, similar phenomenon were explored in thermoacoustic instability.

1.4.3 Non-normality of thermoacoustic systems

Recently, it was shown that thermoacoustic systems are non-normal (Balasubramanian and Sujith, 2008*b*). They performed stability analysis on electrically heated horizontal Rijke tube. The acoustic field in the duct was described by the acoustic momentum and energy equations. The response of the heat source (electrical heater) to acoustic velocity fluctuations is modeled using a quasi-steady correlation given by Heckl (1990).

A transient growth of $4 - 5$ times in acoustic energy was observed, even for a linearly stable system.

A similar analysis was performed to analyse the stability of ducted diffusion flame by Balasubramanian and Sujith (2008*a*). Burke-Schumann equations, along with the infinite rate chemistry assumption is used to model the dynamics of the heat release rate. Transient growth in the energy of the order of 10^5 is observed, which is much higher than that obtained in the earlier analysis (Balasubramanian and Sujith, 2008*b*). The consequences of non-normality in the subcritical transition regime were discussed in both the papers.

The effects of internal flame dynamics on the non-normal nature of a ducted premixed flame interaction was analysed by Subramanian and Sujith (2011). The dynamics of the premixed flame is modeled using 'G' equation, where the flame front is tracked in a kinematic approach. Further, it was observed that the contribution from the degrees of freedom associated with the internal flame dynamics is more compared to that of the acoustic variables in the optimum initial condition.

Tulsyan *et al.* (2009) have analysed combustion instability involving vortex shedding in the light of non-normal nature of thermoacoustic interaction. The effect of dynamics of the vortex shedding on the acoustic field is modelled as a kicked oscillator. Transient growth is observed from period to period defined by the kicks. The above problem was considered as discrete time system and non-modal stability analysis developed for the same (Schmid, 2007) is employed.

Wieczorek *et al.* (2010) have performed non-modal stability analysis for flame modelled as one-dimensional, which is located in a tube fitted with a nozzle. Apart from the acoustic oscillations, entropy fluctuations were present and are convected by the non-zero base flow. Eigenmodes associated with acoustic and entropy fluctuations were obtained and were shown to be non-orthogonal to each other. Further, transient growth based on acoustic energy led to spurious values. It was concluded that energy associated with the entropy fluctuations should be included in the definition of disturbance energy of the system.

Linear system identification (SI) technique is developed to perform non-modal sta-

bility analysis by Selimefendigil *et al.* (2011). They performed the investigation on a Rijke tube system. The response of the electrical heater to acoustic velocity fluctuations are determined numerically using computational fluid dynamic techniques. Then a reduced order model from SI is obtained for the response of the heat source, which is then coupled with the acoustic field. The SI technique described in the paper captures the transient dynamics of the heater to acoustic velocity fluctuations, making it suitable to analyse the no-normal nature of the thermoacoustic system.

Optimum initial conditions obtained in the earlier analysis were from the linearised equations. Juniper (2011) used a technique of nonlinear adjoint optimisation, in order obtain both the linear and nonlinear optimal initial conditions for maximum transient growth in a Rijke tube system described in Balasubramanian and Sujith (2008*b*). Further, the role of the above optimal initial conditions in the asymptotic stability of the system is also investigated.

The role of non-normality in active control of thermoacoustic instability is investigated by Kulkarni *et al.* (2011). They showed that traditional controllers, which are designed based on the eigenvalue analysis of the system will fail when the system is non-normal. The above conclusion was made in the stability analysis of an electrically heated Rijke tube described in Balasubramanian and Sujith (2008*b*). They observed secondary peaks in the linearised system and the nonlinearity in the system sustains the secondary peaks leading to nonlinear instability. A controller was designed so that the amount of transient growth is minimum, ensuring a monotonic decay in the evolution of the acoustic energy.

In the non-modal stability analysis of thermoacoustic systems described earlier, the coupling between the acoustic field and the heat source was phenomenological. Furthermore, there were two systems of equations involved in the problem; one for the acoustic length scale and the other for the length scale of the heat source. In most of the problems of thermoacoustics, the above two length scales are desperate (Poinsot and Veynante, 2005). In a rigorous analysis, the above two systems of equations have to be derived from the conservation equations of fluid flow by performing asymptotic analysis. Moreover, the governing equations for this fluid flow become stiff and are difficult to solve by computational fluid dynamics (CFD) technique, as the Mach num-

ber of the steady flow and the thickness of the heat source (compared to the acoustic wavelength) are small. Therefore asymptotic analysis is performed in the limit of small Mach number and compact heat source to eliminate the above stiffness problem.

1.4.4 Mathematical modelling of thermoacoustic systems

Wu *et al.* (2003) have pioneered the application of asymptotic expansions to analyse combustion instabilities. They analysed the amplification of sound waves, when a flame propagates in a gravity field. Separate systems of equations for acoustic field and flame zones were derived, by performing asymptotic analysis on the conservation equations. They have performed linear stability analysis for the acoustic-flame coupling, followed by a weakly nonlinear theory for Darrieus-Landau mode of instability of the flame and the acoustic field. The paper explained the experimental observation of the transition from curved to flat flame during instability.

Moeck *et al.* (2007) have also performed asymptotic analysis to investigate thermoacoustic instability in a Rijke tube with flame as the heat source. They obtained with mathematical rigor, the correct systems of equations and the coupling between the acoustic field and the heat source. The presence of an additional global-acceleration term in the momentum equation of the hydrodynamic zone was also observed. Further, they concluded that since one dimensional equations are used in the hydrodynamic zone for their analysis, the above term vanishes leaving the conventional momentum equation intact in the hydrodynamic zone. The unsteady heat release rate from the flame may be due to the equivalence ratio fluctuations at the inlet of the hydrodynamic zone, which in turn may be caused by the acoustic velocity at the location of the flame (Moeck *et al.*, 2007). Recently, Wu and Moin (2010) investigated the generation of acoustic waves from premixed flame due to freestream enthalphy fluctuations, using asymptotic analysis. A vigorous subharmonic parametric instability was observed at moderate levels of enthalpy fluctuations.

1.5 Existing understanding and outstanding issues

A summary of the literature review and some of the outstanding issues that haven been identified is shown in Fig. 1.8. The existing investigations are ordered in a way explained as follows. The horizontal axis represents the mathematical rigor with which the model for a particular thermoacoustic system is developed. The vertical axis represents the sophistication in the stability analysis for the above developed model. The axis out of the plane of the paper represents the experimental investigations performed in the same thermoacoustic system. The scales are qualitative only. Planes A and B represent the numerical and experimental investigations respectively. In plane A, the various levels indicates the following, I - classical stability analysis, II - basic non-modal stability analysis and III - advanced stability analysis. Similarly, in plane B, I & II represent the experiments associated with classical stability and non-modal stability analysis respectively. The papers indicated in the figure are only representatives of the kind of analysis or experimental investigations. Area shaded in grey represents the investigations performed in the present thesis, which is discussed in the following section. Since the present thesis is focussed on the stability analysis in SRM and Rijke tube, only references are made that are associated with the above thermoacoustic systems.

Numerical analysis (plane A) is considered first. In level I, Culick and his coworkers pioneered and developed a framework to perform classical stability analysis in SRMs. Their mathematical modelling is based on asymptotic expansion in terms of the steady state Mach number. In this manner, the governing equations for the acoustic field is obtained. However, the response of the propellant to acoustic fluctuations are modelled using response functions. Further, those response functions are *ad hoc* and lack physical interpretations. On the other hand, Wu *et al.* (2003) pioneered the application of asymptotic analysis to investigate the stability of flames to various inlet fluctuations. Moeck *et al.* (2007) performed similar analysis in a Rijke tube with flame as the heat source. The governing equations at low Mach numbers ($\sim 10^{-3}$) of the steady state flow and compact size of the heat source compared to the acoustic field become stiff (Anderson, 2001). Solving the same by CFD directly is difficult. Hence the other approach of asymptotic analysis is preferred in multiscale problems (Ting *et al.*, 2007). In performing asymptotic analysis, Moeck *et al.* (2007) observed an additional global-acceleration

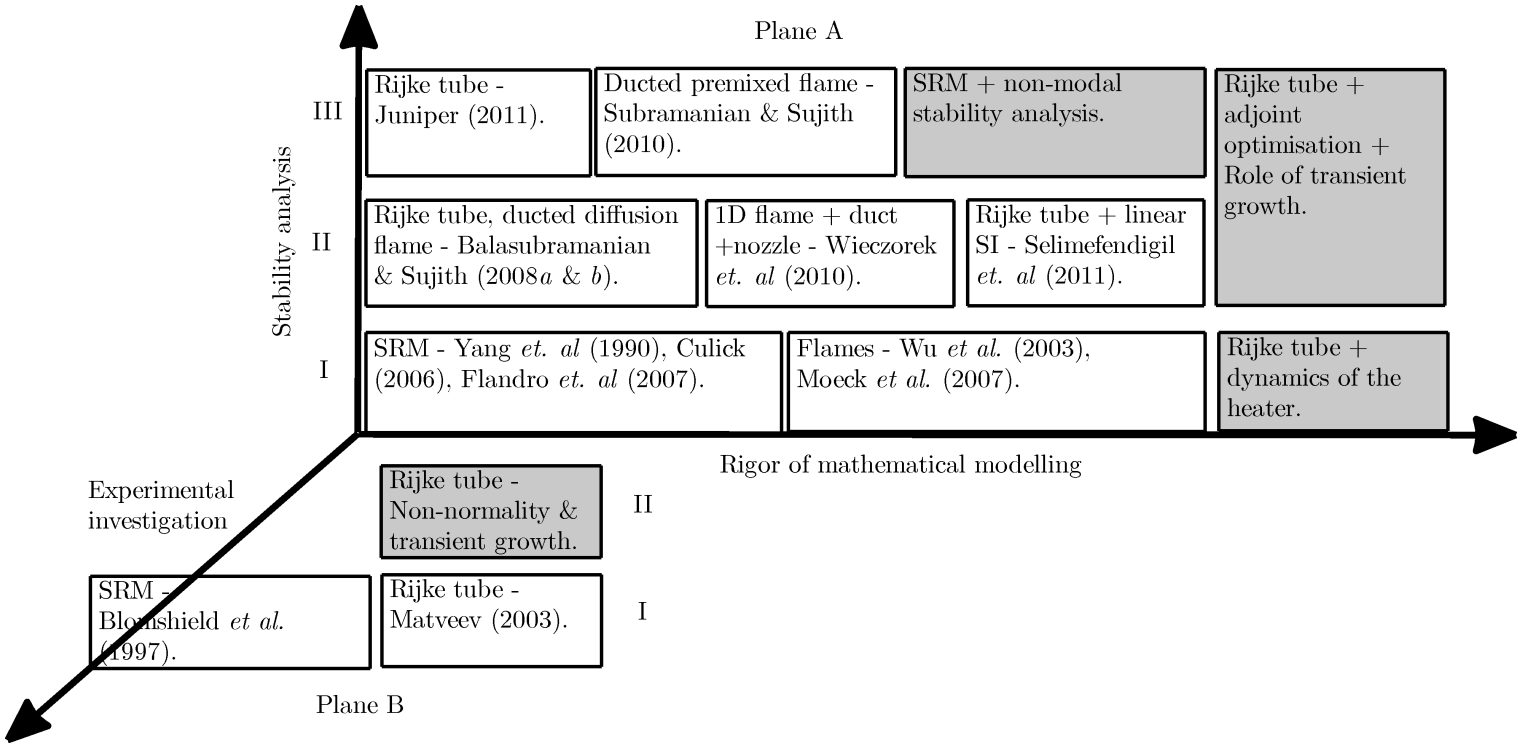

Figure 1.8: Outstanding issues and the current objective of the present thesis. Representative existing literature on the stability analysis of thermoacoustic systems are shown in a qualitative manner. The horizontal axis represents the mathematical rigor with which the coupling between the acoustic field and heat source is performed. The vertical axis represents the sophistications in the stability analysis. The axis out of the paper represents the increasing experimental investigations. Planes A and B represent the numerical and experimental investigations respectively. In plane A, the various levels indicates the following, I - classical stability analysis, II - basic non-modal stability analysis and III - advanced stability analysis. Similarly, in plane B, I & II represent the experiments associated with classical stability and non-modal stability analysis respectively. Area shaded in grey represents the investigations performed in the present thesis.

term in the momentum equation governing the dynamics of the heat source. However, they did not consider the above term, as perform one dimensional calculations for the dynamics of the heat source. Hence it is important to include the effects of global-acceleration term and understand the effect of the same in thermoacoustic system.

As one move on to the next level of stability analysis, Balasubramanian and Sujith (2008*a*,*b*) showed that thermoacoustic interactions are non-normal and non-modal stability analysis have to be performed in order to gain a more complete understanding. Similar analysis was performed by Wieczorek *et al.* (2010), which included entropy fluctuations along with acoustic fluctuations. Further, system identification technique that can be used to perform non-modal stability analysis was developed by Selimefendigil *et al.* (2011). In plane III, investigations using advanced non-modal analysis is shown. Juniper (2011) applied the technique of adjoint optimisation to obtain the optimum initial condition for maximum transient growth for both linear and nonlinear systems. The contributions of the degrees of freedom associated with the flame dynamics on the optimum initial condition is examined in Subramanian and Sujith (2011). By including the dynamics of the heat source, the total number of degrees of freedom of the system is increased. Hence, it is important to include the contribution from the state variables associated with the dynamics of the heat source to the disturbance energy. By performing the above, the relative strength of the contributions from the variables associated with the acoustic field and the dynamics of the heat source have to be obtained. A rational method to identify the same is to be developed.

From the experimental perspective (plane B), Blomshield *et al.* (1997*a*,*b*) performed experiments in SRM. The experiments were focussed to obtain the linear and nonlinear stability behaviour. The growth rates during nonlinear instability were also obtained. The instrumentation in the experiments with SRMs were performed in harsh environments and hence only a fewer quantities can be measured. In order to gain a fundamental understanding of thermoacoustic instability, experiments in a simpler thermoacoustic device; Rijke tube is performed. Matveev (2003) performed a controlled experiment in an electrically heated Rijke tube. He obtained the bifurcation diagram and stability regimes for the system. The above two experiments were focussed from the point of view of classical stability analysis and are designated in level I. As a nat-

ural extension from Matveev (2003), experimental investigation in order to capture the effects of non-normality and its consequence have to be performed.

1.6 Objective of the present thesis

The last section dealt with the existing understanding and some of the outstanding issues in the modeling and analysis of stability in thermoacoustic systems. On the basis of the above conclusions, the following objectives are identified and are described as follows.

1. The first objective deals with the investigation of non-normal nature of thermoacoustic interaction in a solid rocket motor. The reason for choosing the above configuration is the following. Earlier analysis (Culick, 2006), assumed the orthogonality of the eigenmodes in the investigation of the same. The consequence of relaxing the above assumption will indicate the effects and role of non-normality in the stability of the system.
2. The experiments associated with investigation of non-normality and transient growth are difficult to perform in a solid rocket motor. Moreover, the coupling between the acoustic field and the heat source was performed in a phenomenological way (Poinsot and Veynante, 2005) and was not obtained from rigorous mathematical derivations. To address the above two issues, analysis is performed on a simpler thermoacoustic system: Rijke tube. A mathematical framework will be developed to derive the coupling between the acoustic field and a heat source.
3. The modeling of the Rijke tube system will now include the dynamics of the heat source. The issues described in Section 1.5 related to the non-modal stability analysis will be discussed. Further, the effect of non-acoustic initial conditions on the stability of the system will be explored.
4. In order to obtain a more complete view, experimental investigation of non-normal nature of Rijke tube system will be performed. From the experimental data, the thermoacoustic interaction will be shown to be non-normal. Further, a

search will be performed to obtain an evidence of transient growth. Ultimately, the role of transient growth on the asymptotic stability of the system will be explored.

1.7 Tools to be used

In order to achieve the objectives described in the previous section, the following tools will be used. A brief description of the same is itemized as follows. The numbering of the tools is same that in the previous section.

1. Basic tools on non-modal stability analysis will be used (Schmid, 2007). The optimum initial condition for maximum transient growth will be obtained by singular value decomposition (SVD, Golub and Loan 1989).
2. The coupling between the acoustic field and the dynamics of the heat source will be obtained by performing asymptotic analysis (Ting *et al.*, 2007) on the governing equations of fluid flow. Separate systems of equations governing the dynamics of the acoustic field and the heat source are obtained. The obtained equations are later solved numerically.
3. The degrees of freedom encountered in the previous case will be large ($\sim 10^4$), as the dynamics of the heat source will also be taken into account. Hence, an advanced tool, adjoint optimisation (Juniper, 2011) will be preferred to SVD to obtain the optimum initial condition and the associated maximum transient growth.
4. In the experiments perform in Rijke tube, a simultaneous measurement acoustic pressure along the length of the duct will be performed. Later, dynamic mode decomposition (DMD, Schmid 2010) will be used to extract the eigenmodes of the system. The non-orthogonality of the obtained eigenmodes in the presence of the heater will be determined. Further, two microphone technique (Bellows, 2006) will be used to obtain the acoustic velocity data and ultimately the acoustic energy of the system. An evidence of transient growth will be identified from the

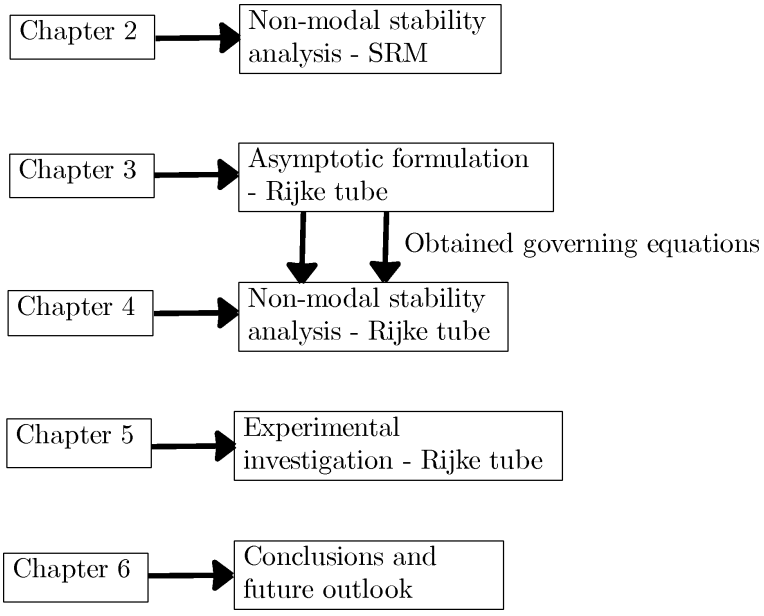

Figure 1.9: Schematic representation of the structure of the thesis.

evolution of the obtained acoustic energy

The details of the individual tools and their techniques of application will be discussed in the places, where it is be applied.

1.8 Structure of the thesis

The present investigation is focussed on four main objectives. Each objective is presented in individual chapters. A schematic representation of the structure of the thesis is shown in Fig. 1.9. The first objective of the investigation of non-normal nature of thermoacoustic interaction in a solid rocket motor is discussed in Chapter 2. In particular, the role of transient growth in the regard to the pulsed instability is focussed.

The third chapter deals with the formulation of the framework to obtain the coupling between the dynamics of the acoustic field and the heat source. The effect of global acceleration on stability of the thermoacoustic oscillations is focussed as the main issue.

The non-normal nature of the governing equations obtained in Chapter 3 are examined. The optimum initial condition for maximum transient growth and the effect of non-acoustic initial conditions on the stability of the system are analysed in Chapter 4.

Experimental investigations related to the identification of the non-normal nature of Rijke tube system are performed in Chapter 5. The non-orthogonality of the eigenmodes and its consequence of transient growth are captured in the experiments.

The last chapter deals with the conclusion and future outlook that could be used in order to gain more understanding of the non-normal nature of the thermoacoustic system.

CHAPTER 2

Thermoacoustic instability in Solid Rocket Motor

2.1 Introduction

Solid rocket motors (SRMs) are often prone to combustion instability. The prediction of combustion instability in the early stage of the design is a formidable task due to the complex unsteady flow field existing in the combustion chamber. Combustion instability occurs when the unsteady burn rate from the propellant (in SRMs) is amplified by the positive feed back of the acoustic oscillations in the chamber. Combustion instability causes excessive pressure oscillations, which might resonate with the structural modes of the rocket, leading to excessive vibration and damage of the payload. Furthermore, during the occurrence of the combustion instability, the heat transfer to the combustion chamber walls is increased, eventually melting them (Sutton and Biblarz, 2001). As described in the previous chapter, the driving mechanism for combustion instability to happen in SRM is the response of the unsteady burn rate of the propellant to chamber acoustics. This leads to unsteady mass addition to the combustion chamber and ultimately causes an unsteady heat release rate.

Thermoacoustic instabilities in SRMs are attributed to the time lag between the unsteady burn rate and the chamber acoustics. The phase delay for a particular frequency can be identified in the time domain as a 'time lag'. The physical origin of this time lag can be attributed to various dynamical processes involved in the burn rate dynamics of the propellant. Instability occurs if the time lag is in some suitable range such that fluctuating energy is added to the system. The above idea gave rise to the '$n-\tau$' model (n is the interaction index that gives the coupling strength between the acoustic velocity and the unsteady combustion process and τ is the time lag) developed by Crocco (1956) for liquid rocket engines. The model was simple; n and τ vary with frequency in realistic situations. However, it gave a basic understanding of the physical origin of instability.

Initial attempts to tackle the instabilities theoretically were by Culick (1963) and Friedly and Petersen (1966), where the linearised equations were investigated. They obtained an explicit expression for the complex frequency of the system. The real part of the frequency gave the growth or decay of the oscillations. Because the unsteady heat release rate was the main driving source for the acoustic oscillations, a relation between the two was developed in order to characterize the system dynamics. This coupling between the unsteady burn rate in response to acoustic oscillation was captured by the frequency dependent admittance function ($Y = M_b \left[(m'/\bar{m}) \,/\, (p'/\gamma\bar{p}) - (\rho'/\bar{\rho}) \,/\, (p'/\gamma\bar{p}) \right]$) described by Culick (1968), where M_b denotes the Mach number at the burning surface, m is the mass addition rate, p is the pressure and ρ is the density. The prime ($'$) denotes fluctuating quantities, while the over bar ($\bar{}$) denotes mean quantities. The admittance function calculated was used to determine the growth of the acoustic oscillations. Analytical expressions for the admittance function in the linear regime were derived by Williams (1962) and Deluca *et al.* (1995). The governing equations are nonlinear partial differential equations for the burn rate, which makes the problem difficult to solve for composite propellants. Some semi-empirical theories were proposed to handle these difficulties (Brewster and Son, 1995). The form of the admittance function was derived and its exact parameters were found experimentally (Price, 1984). One of the successful experimental techniques used to calculate the parameter values was the T-burner technique (from the admittance function), which was demonstrated by Lin and Wang (1995). Experimental and theoretical analysis were used in tandem to predict instabilities.

A theoretical analysis starts with linearising the governing equations and analyzing their stability. This leads to finding the eigenvalues (complex frequency) and eigenmodes of the system. In a classical linear stability analysis, a system is said to be linearly stable if the oscillations decay to zero in the asymptotic time limit, reaching finally the steady state (stable fixed point). The system is linearly unstable if the oscillations grow exponentially. Both the definitions are for 'small' disturbances with respect to the corresponding mean quantities. The stability of the system is determined by the real part of the complex frequency as described earlier. A linearly unstable system grows exponentially, and after some time the oscillation amplitudes are not small. The nonlinear effects start playing a major role in the time evolution of the system, causing the

evolution to reach a limit cycle (oscillations with constant amplitude). This nonlinearity is attributed to the nonlinear chamber acoustics and nonlinear combustion response of the propellant (Culick, 2006).

Culick (1976*a*) was the first to derive an analytical condition for the existence of stable and unique limit cycle behaviour using a two mode Galerkin approximation with second order acoustics as the only nonlinear process. Nonlinearity in the combustion response was also included in the analysis and the dynamical behaviour was analysed (Levine and Baum, 1983; Flandro *et al.*, 2007). Apart from these, the effect of particulate damping (Culick, 1976*b*), vorticity (Flandro, 1995*a*) and flow turning (Flandro, 1995*b*) on SRM stability was discussed. A Computational fluid dynamics (CFD) analysis was performed by Shimada *et al.* (2007) using the admittance function for burn rate – acoustic coupling and quasi-steady flame model in the gas phase. Growth rates at low Mach numbers were predicted more accurately by a second order finite volume method than the Galerkin technique usually used for such analysis (Culick, 2006).

Another interesting dynamical behaviour observed experimentally was that SRMs stable for small amplitude disturbances were seen to become unstable for larger ones (Culick, 2006). This was called 'pulsed instability' or 'triggering'. Many mechanisms were proposed for explaining triggering in the past. Second order gas dynamics alone were proved to be insufficient to cause triggering because of the absence of 'self coupling' terms (Culick, 1994). Higher order gas dynamics (third order acoustics) also proved the same (Yang *et al.*, 1990). Hence, a nonlinear combustion response was thought of as an alternate candidate for triggering. Culick *et al.* (1995) used an *ad hoc* nonlinear velocity coupling model for burn rate response to show triggering numerically. (Wicker *et al.*, 1996) analysed various forms of nonlinear coupling between unsteady burn rate and acoustic variables. By suitably adjusting the parameters and the form of the coupling terms, triggering was demonstrated. (Anathakrishnan *et al.*, 2005) further explained that velocity coupled models are the only possible candidates for causing triggering in realistic operating regimes of SRMs.

In the above analyses, there are some common assumptions and procedures that were adopted to solve the thermoacoustic instability problem in the SRM. They are (i) the orthogonality of the eigenmodes, (ii) the use of admittance (response) functions

or *ad hoc* models for burn rate-acoustic coupling and (iii) the use of classical linear stability theory for all time 't'. Culick (1997) showed that the frequency shift due to the non-orthogonality of the eigenmodes is second order in a mean flow Mach number. However, the system dynamics change dramatically during the initial time because of the non-orthogonality of the eigenmodes (Kedia *et al.*, 2008). The use of admittance (response) functions or *ad hoc* coupling models for burn rate – acoustic coupling does not account for the initial transients in the burn rate. These can lead to erroneous prediction of the system dynamics, both qualitatively and quantitatively. If the evolution of the unsteady propellant burn rate is modelled using a differential equation in time, then the degrees of freedom for the system are increased. This implies that the thermoacoustic system variables include not only acoustic pressure and velocity but also other variables related to the unsteady burn rate. Therefore, the initial condition on the problem is restricted not only to acoustic variables but also to unsteady burn rate, which might show an interesting behaviour. Indeed, it is found that the effects of non-orthogonality of the eigenmodes play an important role in the initial conditions related to the unsteady burn rate. The last assumption, i.e. the validity of the classical linear stability theory, is applicable only in the asymptotic time limit (Strogatz, 2000). This assumption is valid during the initial period, only if the eigenmodes are orthogonal to each other. Therefore, a new generalized stability criterion (Farrell and Ioannou, 1996*a*) has to be used to account for the short term dynamics. This chapter relaxes the above three assumptions and offers a more complete analysis of the thermoacoustic instability in the SRM. A homogeneous propellant is considered for the present analysis.

2.2 Role of non-normality

In the past, linear stability analyses of SRMs were performed using the classical linear stability theory (Culick, 2006). Energy in the eigenmodes can be transferred from one eigenmode to another, either due to nonlinear coupling (Culick, 1976*a*) or due to non-orthogonality of the eigenmodes (Balasubramanian and Sujith, 2008*b*). In the former case, the coupling comes from the nonlinear time evolution equation for the eigenmodes. This is a 'direct interaction'. This requires some threshold amplitude (system

dependent) to be reached for it to have significant effects in the dynamical evolution of the system. In the latter case, the energy transfer occurs even with small disturbances. In this limit, the nonlinearity present in the system (will have a mild effect at small amplitudes) transfers a small amount of energy from one eigenmode to another. If the energy transfer leads to a distribution of energy among the modes in such a way that transient growth happens, there is a net energy transfer from the base flow to the eigenmodes. For a linearly stable case, the energy given in one eigenmode is fed to the base flow and from it, the energy is fed back again to other eigenmodes. Thus energy transfer happens through the base flow. It is an 'indirect interaction'.

It is evident that the stability analysis of the SRM has to be modified including taking the non-orthogonality of eigenmodes into consideration. The phenomenon of pulsed instability observed in SRMs has been demonstrated theoretically only with *ad hoc* burn rate-acoustic coupling models. This chapter concentrates on the four main issues. The first issue is the inclusion of the non-orthogonality of eigenmodes, which plays an important role in the short term dynamics of the system. The second is to use a physics based model for the burn rate response of a homogeneous propellant to demonstrate the various observed phenomena, especially pulsed instability. The model also captures the transients (important for non-normal systems), which facilitates the prediction of system dynamics during the initial time. Therefore, a differential equation for the time evolution of the state vector is derived for the unsteady burn rate – acoustic coupling and is solved simultaneously along with the equations for the acoustic field. The dynamical system now considered comprises not only the acoustic variables with a source from the unsteady propellant burn rate, but also an extended one, also comprising the unsteady burn rate variables. The third issue is to include all the nonlinear processes involved, so that the energy transfer and large amplitude oscillations (limit cycles) are accurately predicted. The fourth issue is that experiments performed by Blomshield *et al.* (1997*a*) indicate that the triggering pressure amplitude required for pulsed instability is very small (see Fig. 13 and table 5 of Blomshield *et al.* (1997*a*)) compared to the steady state and mean pressure during the limit cycle (triggering pressure amplitude is $\approx 4\%$ of the steady state pressure). Furthermore, the triggering pressure amplitude in their study is much smaller than the limit cycle amplitude. This chapter investigates if pulsed instability can be obtained from a small amplitude initial pulse (compared with the limit

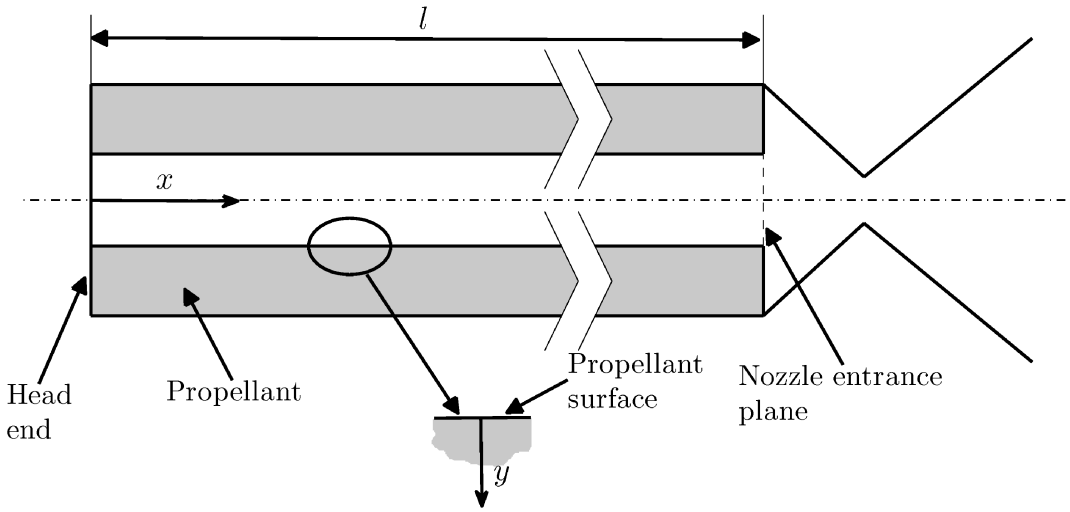

Figure 2.1: Schematic diagram of the combustion chamber geometry of the SRM considered.

cycle amplitude) as observed by Blomshield *et al.* (1997*a*).

2.3 Formulation

The SRM considered here has a prismatic cylindrical propellant grain of length l, port circumference S_l and a constant port area S_c. A schematic of the geometry considered with the coordinate system used is shown in Fig. 2.1. A cylindrical geometry is studied so as to make the analysis simple.

2.3.1 Chamber acoustics

In the SRM, the amplitude of the limit cycle pressure oscillations is often about 20% of the mean chamber pressure (Culick, 1976*a*; Flandro, 1996). In this range of pressure oscillations, nonlinear acoustics plays an important role in the nonlinear dynamical evolution of the system. This is in contrast to gas turbines, where the limit cycle pressure oscillations are 3%-4% of the mean chamber pressure (Lee and Santavicca, 2005) and the nonlinearity in combustion response alone can be assumed to play an important role. Hence the present analysis includes a second order nonlinearity in acoustics (Culick, 1976*a*,*b*; Yang *et al.*, 1990) and a physics based nonlinear model for combustion response (Krier *et al.*, 1968). The acoustic oscillations are assumed to be isentropic,

which is valid up to the inclusion of second order nonlinearities (Culick, 1997). Reddy and Trefethen (1994) have shown that convection differential operator causes non-normality in the system $\Big((d/dx)^{\dagger} = -d/dx,\ \dagger \text{ indicates adjoint operator}\Big)$. Therefore, the stronger the convection the higher is the level of non-normality. In SRM combustion chambers, the mean flow Mach number is around 0.1, which creates strong convective effects. Hence, the distribution of mean axial velocity plays a key role in characterizing the non-normality of the system. The above picture can be looked as an asymmetry in the flow field, which eventually leads to non-normality. A similar kind of asymmetry is present in the earlier analysis with diffusion flame (Balasubramanian and Sujith, 2008*a*) and Rijke tube (Balasubramanian and Sujith, 2008*b*) due to the presence of a localized heat source. In contrast to these, SRM has distributed heat sources; however, the strong convection leaves the system non-normal. In general, non-normality in a convection-diffusion problem occurs from the convection term that creates asymmetry in the distribution of any flow variable because of the directionality of the base flow, whereas diffusion is a gradual process which does not create any asymmetry (Balasubramanian and Sujith, 2008*a*). In order to keep the analysis tractable, we assume a constant mean chamber pressure $\bar{p}$, density $\bar{\rho}$ and temperature $\bar{T}$, which are valid assumptions for SRM (Culick, 1997). The effects of 'flow turning' (stabilizing) and 'pumping' (destabilizing) cancel each other exactly for cylindrical propellant geometry (Flandro, 1995*b*); hence, they do not appear in this analysis. The one-dimensional steady continuity equation is

$$\frac{\partial(\bar{\rho}\bar{u})}{\partial\tilde{x}} = \bar{m} \quad \& \quad \bar{m} = \bar{R}\rho_p\frac{S_l}{S_c} \tag{2.1}$$

where, $\bar{m}$ is the mean mass influx rate from the propellant per unit volume at any axial location, $\bar{u}$ is the base flow velocity, $\bar{R}$ is the mean propellant regression rate and ρ_p is the propellant density. Integrating the equation with head end velocity as zero gives

$$\bar{u} = \frac{\bar{m}}{\bar{\rho}}\tilde{x} \tag{2.2}$$

The above equation gives the axial variation of mean velocity, which is used for further calculations. At low Mach numbers *M*, the isentropic relation for fluctuations in density can be used up to second order acoustics (Culick, 1976*a*). Hence, the continuity equa-

tion is decoupled from momentum and energy equations. The unsteady momentum and energy equations are given by

$$\widehat{\rho}\left(\frac{\partial\widehat{u}}{\partial\tilde{t}}+\widehat{u}\frac{\partial\widehat{u}}{\partial\tilde{x}}\right)=-\frac{\partial\widehat{p}}{\partial\tilde{t}}-\widehat{m}\widehat{u} \tag{2.3a}$$

$$\left(\frac{\partial\widehat{p}}{\partial\tilde{t}}+\widehat{u}\frac{\partial\widehat{p}}{\partial\tilde{x}}+\gamma\widehat{p}\frac{\partial\widehat{u}}{\partial\tilde{x}}\right)=(\gamma-1)\,\widehat{Q} \tag{2.3b}$$

where $\widehat{m}=\widehat{R}\rho_p S_l\Big/S_c, \widehat{Q}=\widehat{m}\Delta h$, Δh is the heat of reaction of the propellant at a constant pressure per unit mass and γ is the ratio of specific heat capacities at constant pressure and volume. The source term $\widehat{m}\widehat{u}$ in Eqn. (2.3) is due to the reduction of the momentum of the fluid in the chamber due to the low velocity inflow of the burning propellant. The source term $\widehat{Q}$ in Eqn. (2.3) is due to the energy released by the propellant to the fluid in the chamber. Decomposing the flow variables as, $\widehat{u}=\bar{u}+\tilde{u}', \widehat{p}=\bar{p}+\tilde{p}', \widehat{m}=\bar{m}+\tilde{m}', \widehat{Q}=\bar{Q}+\tilde{Q}'$ and $\widehat{R}=\bar{R}+\tilde{R}'$, followed by substituting the above in Eqn. (2.3), one obtains the governing equations for the perturbations. The acoustic momentum and energy equations thus obtained are (with nonlinear terms given within curly {})

$$\bar{\rho}\left[\frac{\partial\tilde{u}'}{\partial\tilde{t}}+\bar{u}\frac{\partial\tilde{u}'}{\partial\tilde{x}}+\tilde{u}'\frac{d\bar{u}}{d\tilde{x}}\right]+\left\{\bar{\rho}\tilde{u}'\frac{\partial\tilde{u}'}{\partial\tilde{x}}-\tilde{\rho}'\frac{\partial\tilde{p}'}{\partial\tilde{x}}\right\}=-\frac{\partial\tilde{p}'}{\partial\tilde{x}}-[\tilde{m}'\bar{u}+\bar{m}\tilde{u}'+\{\tilde{m}'\tilde{u}'\}] \tag{2.4}$$

$$\frac{\partial\tilde{p}'}{\partial\tilde{t}}+\bar{u}\frac{\partial\tilde{p}'}{\partial\tilde{x}}+\gamma\left[\bar{p}\frac{\partial\tilde{u}'}{\partial\tilde{x}}+\tilde{p}'\frac{d\bar{u}}{d\tilde{x}}\right]+\left\{\tilde{u}'\frac{\partial\tilde{p}'}{\partial\tilde{x}}+\gamma\tilde{p}'\frac{\partial\tilde{u}'}{\partial\tilde{x}}\right\}=(\gamma-1)\tilde{Q}' \tag{2.5}$$

where $\tilde{Q}'=\tilde{m}'\Delta h=\tilde{R}'\rho_p\Delta h\,(S_l/S_c)$, the tilde $(\tilde{})$ denotes dimensional quantities, $\tilde{u}'$ is the acoustic velocity, $\tilde{p}'$ is the acoustic pressure, $\tilde{m}'$ is the fluctuations in mass influx rate per unit volume, $\tilde{Q}'$ is the fluctuating heat release rate per unit volume by the propellant combustion and $\tilde{R}'$ is the fluctuating burn rate.

Non-dimensionalising the above equations as follows: $p=\tilde{p}'/\bar{p},\ u=\tilde{u}'/u_m, \bar{U}=\bar{u}/u_m,\ R=\tilde{R}'\Big/\bar{R},\ x=\tilde{x}/l,\ M=u_m/a$, where $u_m=(\bar{m}l)\,/\,(2\bar{\rho})$ is the average base flow velocity, $\bar{U}=2x$ is the non-dimensional base flow velocity, *a* is the sonic speed and *M* is the average base flow Mach number. The non-dimensionalised acoustic

momentum and energy equations are

$$\frac{\partial u}{\partial t} + M\left[\bar{U}\frac{\partial u}{\partial x} + \frac{dU}{dx}u\right] + \frac{1}{\gamma M}\frac{\partial p}{\partial x} = k_m[R\bar{U} + u] + \left\{k_m R u - Mu\frac{\partial u}{\partial x} + \frac{p}{\gamma M}\frac{\partial p}{\partial x}\right\} \tag{2.6}$$

$$\frac{\partial p}{\partial t} + \gamma M\left[\frac{\partial u}{\partial x} + \frac{d\bar{U}}{dx}p\right] + M\bar{U}\frac{\partial p}{\partial x} = k_e R - \left\{Mu\frac{\partial p}{\partial x} + \gamma M p\frac{\partial u}{\partial x}\right\} \tag{2.7}$$

where $k_m = -(\bar{m}u_m l)\,/\,(\bar{p}\gamma M),\ k_e = ((\gamma-1)\,l\bar{m}\Delta h)\,/\,(\bar{p}a)$.

2.3.2 Solution procedure

The Galerkin technique (Zinn and Lores, 1971; Padmanabhan, 1975) is used to solve Eqns. (2.6) and (2.7). The dependent variable is expanded as a linear combination of basis functions, which are chosen to satisfy the boundary conditions. The basis functions are chosen for a duct, which is acoustically closed at both ends, in spite of the non-zero admittance at the nozzle entry. The actual eigenmode shape is shown to deviate from the above, which is of the order of average mean flow Mach number ($M \sim 0.1$) (Culick, 1976*a*). Although non trivial boundary conditions lead to the non-normality of the system (Nicoud *et al.*, 2007), our investigation mainly focuses on the non-normal nature of the system, arising purely from the interaction of chamber acoustics and unsteady burn rate. This can be regarded as the first step in analysing the non-normal nature of the thermoacoustic interaction in the SRM. Hereafter, the term 'mode' specifies only the Galerkin mode unless specified. The spatial distribution of the unsteady burn rate is expanded on the above basis. The coefficients R_m^c and R_m^s are obtained from the unsteady burn rate equation discussed in Section 2.3.4. The variables are expanded as follows:

$$\begin{aligned} u(x,t) &= \sum_{m=1}^{N} U_m(t)\sin(\omega_m x), \quad p(x,t) = \gamma M\sum_{m=1}^{N} P_m(t)\cos(\omega_m x) \\ R(x,t) &= \sum_{m=1}^{N}\left[R_m^c(t)\cos(\omega_m x) + R_m^s(t)\sin(\omega_m x)\right], \quad \omega_m = m\pi \end{aligned} \tag{2.8}$$

where *N* is the number of Galerkin modes used in the above expansion, The above expressions are substituted in Eqns. (2.6) and (2.7). Then the evolution of the coefficients ($U_m,\ P_m,\ R_m^c$ and $\mathrm{R_m^s}$) is obtained by projecting the obtained equation onto the basis

function (Galerkin mode) used for expansion, utilizing the orthogonality of the basis function. The following evolution equations are finally obtained:

$$\dot{U}_n + 2\sum_{m=1}^{N}\left(U_m I^1_{n,m} + P_m I^2_{n,m} + R^c_m I^3_{n,m} + R^s_m I^4_{n,m}\right) = 2\left\{k_m N^1_n - M N^2_n - \gamma N^3_n\right\} \tag{2.9}$$

$$\dot{P}_n + \frac{2}{\gamma M}\left(\sum_{m=1}^{N}\left[U_m I^5_{n,m} + P_m I^6_{n,m} + R^c_m I^7_{n,m}\right]\right) = \frac{2}{\gamma M}\left\{\gamma M^2 N^4_n - (\gamma M)^2 N^5_n\right\} \tag{2.10}$$

The coupling terms are given in Appendix A.

The set of *2N* coupled first order ordinary differential equations is solved by using fourth-order Runge-Kutta scheme (Riley *et al.*, 2006). The integrals $I^1_{n,m}$, $I^3_{n,m}$ and $I^4_{n,m}$ are the major contributors for the non-normality of the system. The terms contain the convective terms $\bar{U} = 2x$, which is a linear function of *x* giving a non-vanishing coupling integral. Thus the coupling among the Galerkin modes is formed and termed as 'apparent linear coupling'. These terms lead to the initial transient growth and its relation to eigenmodes is discussed by Kedia *et al.* (2008). Note that the mean flow velocity $\bar{U} = 2x$ creates asymmetry in the flow field as discussed in Section 2.3.1.

2.3.3 Damping

Nozzle damping and viscous dissipation are the sources of damping of acoustic oscillations in SRMs. The former contributes much to the damping of acoustic waves. A part of the incident wave at the choked nozzle is carried away by the mean flow (the remaining is reflected at the choked throat). Thus, some part of the acoustic energy is carried away from the system and hence leads to loss. The loss coefficient α_{NO} evaluated for short nozzles (nozzle length is small compared to acoustic wavelength) is given by (Zinn, 1972)

$$\alpha_{NO} = -\left[M_N\left(\frac{\gamma+1}{2}\right)\left(1 + \frac{\gamma+1}{2}M_N^2\right)\right], \quad M_N = \frac{\bar{m}l}{\bar{\rho}a}, \tag{2.11}$$

where, M_N is the Mach number at the nozzle entrance plane. Even though a closed-closed boundary condition is assumed for the rocket combustion chamber, some part

of the acoustic energy is carried away by the mean flow. The effect of which has to be accounted for in the governing equations. It is a standard practice (Culick, 2006) to use the natural duct modes as the basis for projecting the equations and at the same time include the effect of nozzle as a damping term in the governing equation. An acoustic boundary layer develops because of the viscous effect and no slip boundary condition at the propellant surface. The effect is modelled as a volumetric sink term with the damping coefficient ξ_m given by (Matveev, 2003).

$$\xi_m = -\left(C_1 \frac{\omega_m}{\omega_1} + C_2 \sqrt{\frac{\omega_1}{\omega_m}}\right) \tag{2.12}$$

where ω_m is the frequency of the m^{th} Galerkin mode, C_1 and C_2 are constants that determine ξ_m. For the rocket motor considered in table 2.1, $l = 8$ m (a medium sized motor) and the frequency of oscillations encountered during the limit cycle oscillation is 66.25 Hz (Section 2.7.4), which is close to the fundamental mode of the rocket configuration. Hence, the frequency of oscillation is not very small and viscous damping is expected to play a role. The higher acoustic modes will have higher frequencies and are affected by viscous damping and hence viscous damping has to be included. Moreover the viscous damping coefficients chosen for the present simulations are small $(C_1, C_2 \sim \mathrm{O}\left(10^{-2}\right))$ compared with the nozzle damping $(\alpha_{NO} \sim \mathrm{O}\left(10^{-1}\right))$. The decay of m^{th} Galerkin pressure mode due to damping is given by

$$\frac{\partial P_m}{\partial t} = \left(\xi_m + \alpha_{NO}\right) P_m \tag{2.13}$$

The right hand side of Eqn. (2.13) is added to the right hand side of Eqn. (2.10) to account for the losses. A similar analysis is performed by (Matveev, 2003). The final acoustic momentum and energy equations are as follows:

$$\dot{U}_n + 2\sum_{m=1}^{N}\left(U_m I^1_{n,m} + P_m I^2_{n,m} + R^c_m I^3_{n,m} + R^s_m I^4_{n,m}\right) = 2\left\{k_m N^1_n - M N^2_n - \gamma N^3_n\right\} \tag{2.14}$$

$$\dot{P}_n - \left(\xi_n + \alpha_{NO}\right) P_n + \frac{2}{\gamma M}\left(\sum_{m=1}^{N}\left[U_m I^5_{n,m} + P_m I^6_{n,m} + R^c_m I^7_{n,m}\right]\right) = \frac{2}{\gamma M}\left\{\gamma M^2 N^4_n - (\gamma M)^2 N^5_n\right\} \tag{2.15}$$

2.3.4 Unsteady burn rate

The unsteady burning of the propellant in response to the acoustic oscillations is shown to be the main driving source of acoustic instabilities in SRMs (Williams, 1962; Kuo and Summerfield, 1984). Gusachenko and Zarko (2008) give an excellent review of the unsteady solid propellant burn rate models. The burn rate fluctuates in response to acoustic pressure and velocity (parallel to the propellant surface) oscillations in the chamber (Culick, 1968). Much less is known about the velocity coupling models and only *ad hoc* response functions are used for the SRM stability analysis (Levine and Baum, 1983; Baum and Levine, 1986). The acoustic velocity leads to the convective heat transfer at the propellant surface leading to unsteady burn rates. Sometimes flow reversal takes place which further increases the nonlinearity of the response. In this investigation, acoustic pressure - burn rate coupling alone is investigated, as the acoustic velocity – burn rate coupling needs a more involved treatment. The models available to study acoustic velocity – burn rate coupling are few and are insufficient to represent the dynamics involved in sufficient detail.

On the other hand, a number of models exist for unsteady burn rate - acoustic pressure coupling. When a propellant burns, there exist a condensed phase and a gas phase above the propellant surface. The flame is present in the gas phase and most of the heat release is from that phase. There are three basic time scales involved in the problem: (i) the reaction time scale of the flame, (ii) the flow time scale in the gas and condensed phase, (iii) the conduction timescale in the solid phase. A homogeneous propellant is analysed in the present case, which results in a premixed flame in the gas phase (Williams, 1985). Premixed flame reaction time scales are very small compared with the acoustic time scales of the chamber. Furthermore, assuming a quasi-steady gas phase and a small condensed phase (solid and pyrolysed gaseous propellant) leads to analyzing the dynamic response only in the solid phase (Williams, 1962; Krier *et al.*, 1968). Later, the restriction of small condensed phase was relaxed (Romanov, 1999). Thermal inertia in the gas phase has been studied by Kumar and Lakshmisha (2000). Culick (2000) incorporated the dynamics in the condensed and gas phases. Apart from these, the burn rate response with phase transitions in the condensed phase (Cozzi *et al.*, 1999), propellant heterogeneity (Cohen and Strand, 1985) and some specific class of

propellants (Ward *et al.*, 1998) have been investigated. An asymptotic analysis has also been used to obtain the burn rate response of the propellant (Margolis and Armstrong, 1986*b*,*a*). However, the above analysis is mathematically complex and analytical solutions are very much limited.

The unsteady burn rate model used in this paper is from Krier *et al.* (1968). The model used here is simple but it captures the essential physics of the problem. The time lag between the acoustic pressure and burn rate is due to the finite speed of thermal wave propagation in the solid phase and the time scale $\left(\tau_{th} = \alpha/\bar{R}^2\right)$ associated is comparable with the chamber acoustic time scale $(\tau_a = l/a)$. The ratio $F = \tau_a/\tau_{th}$ for the SRM parameters shown in table 2.1 equals 1.37. A differential equation in time for non-dimensional temperature (T) inside the propellant grain is derived from the energy equation. The propellant burn rate is then related to the surface temperature by a power law (Krier *et al.*, 1968). The dynamical boundary condition is written, relating the acoustic pressure and heat transfer at the propellant surface. The derivation of the equation is given in Krier *et al.* (1968) and the final nonlinear equation is as follows.

At each *'x'* location,

$$\left.\begin{aligned} &\frac{\partial T}{\partial \tau} - (1+R)\frac{\partial T}{\partial y} - \frac{\partial^2 T}{\partial y^2} = 0, \quad 0 \le y < \infty, \;\; 0 \le \tau < \infty \\ &R = T_S^{m_p} - 1, \;\; T_S(\tau) = T(y=0,\tau), \;\; \tau/t = \left(l\bar{R}^2\right) \Big/ (a\alpha) = F \end{aligned}\right\} \tag{2.16}$$

Boundary Condition (BC):

$$\left.\frac{\partial T}{\partial y}\right|_{y=0} = -\frac{(1+p)^{2n}((1+p)^{n/m_p} - H)}{1+R} - H(1+R) \tag{2.17a}$$

$$T(y \to \infty, \tau) = 0 \tag{2.17b}$$

Initial condition (IC):

$$T(y,0) = T_{st}(y) + T_p^0(y) \tag{2.18}$$

where, $y = \tilde{y}/\left(\alpha/\bar{R}\right)$, $\tau = t(l/a)/\left(\alpha/\bar{R}^2\right)$, $H = Q_S \Big/ \left(S_p\left(\tilde{T}_{S,0} - \tilde{T}_\infty\right)\right)$, $T = \left(\tilde{T} - \tilde{T}_\infty\right) \Big/ \left(\tilde{T}_{S,0} - \tilde{T}_\infty\right)$,$T_{st} = e^{-y}$, $\tilde{T}_\infty$ is the temperature of the propellant at $y \to \infty$, $\tilde{T}_{S,0}$ is the surface temperature of the propellant, T_{st} is the non-dimensional steady state temperature, T_p^0 is the non-dimensional temperature fluctuation at *t* = 0, *n* is the

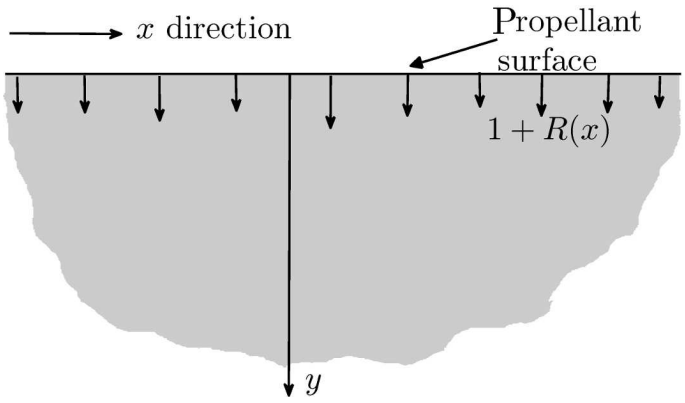

Figure 2.2: Geometry of the pressure coupled propellant response model.

burn rate index, m_p is the pyrolysis coefficient, α is the thermal diffusivity of the propellant, Q_S is the overall heat release per unit mass at the propellant surface, S_p is the specific heat capacity of the propellant, y is the non-dimensional distance from the propellant surface, H is the ratio of the heat release at the propellant surface to its thermal capacity and F is the ratio of timescales of the chamber acoustics (τ_a) and transient heat conduction in the propellant (τ_{th}).

The co-ordinate system is fixed to the propellant surface which regresses according to the burn rate. The geometry is shown in Fig. 2.2. A Dirichlet type boundary condition far from the propellant surface and a Neumann type at the surface Eqn. (2.17a), which comes from the balance between the amount of heat transfer from the flame in the gas phase to the propellant surface, are applied. The steady state temperature profile $(T_{st} = e^{-y})$ obtained as the solution of the corresponding steady state problem $\partial T/\partial y + \partial^2 T/\partial y^2 = 0$, is exponentially decaying in y. The problem is formulated in one dimension as the response function predicted is shown to be accurate by Baum and Levine (1986) and Culick (2000). Note that $(1+R)$ in Eqn. (2.16) appears as a convection term, as the coordinate system is fixed to the propellant surface, which is regressing with the burn rate at that time (see Fig. 2.2). As described in Section 2.3.1, this term contributes to the non-normality in the burn rate response. The other term in Eqn. (2.16), i.e. the diffusion term has no preferred direction associated with it $\left((d^2/dx^2)^\dagger = d^2/dx^2\right)$ and hence does not contribute to the non-normality of the burn rate response. The above advection diffusion equation is shown to produce high transient growth by Reddy and Trefethen (1994). The presence of a non-normal behaviour

in both combustion and acoustics leads to high transient growth when coupled together. Hence, the short-term dynamics obtained from both the unsteady burn rate and acoustic equations will be very different from those predicted by the classical linear stability theory for asymptotic time. It is now important to understand the various physical processes that contribute to the dynamics of the unsteady burn rate.

The mechanism of the burn rate - acoustic pressure coupling is as follows. The reaction rate of a premixed flame is dependent on the pressure and, to a weaker extent, on the temperature. During the compression part of the acoustic cycle, the flame speed increases, and the flame comes closer to the solid thereby causing more heat transfer to the solid. The pyrolysis of the propellant is assumed to obey the Arrhernius law, which under practical values of activation energy leads to a power law dependence on surface temperature (Krier *et al.*, 1968). Higher heat transfer to the solid phase increases the solid phase surface temperature and hence the burn rate. Thus the acoustic forcing comes through the boundary condition stated in Eqn. (2.17a), which is a crucial difference from the earlier analysis of Balasubramanian and Sujith (2008*a*), where the forcing explicitly appears through the convective term in the equation.

From the physics of the problem, the temperature fluctuations are expected to be high near the propellant surface and decrease towards the chamber casing (Dirichlet boundary condition). Thus, it is necessary to cluster more grid points near the surface, which will yield accurate results with fewer grid points and hence lesser computational time (Anderson, 2001). The transformation $\eta = e^{-ky}$ is performed on Eqn. (2.16) and *k* controls the amount of grid clustered near the propellant surface.

Equation (2.16) with boundary (Eqn. 2.17) and initial (Eqn. 2.18) conditions are transformed into

$$\left.\begin{aligned}
&\frac{\partial T}{\partial \tau} + ((1+R)k\eta - k^2\eta)\frac{\partial T}{\partial \eta} - (k\eta)^2\frac{\partial^2 T}{\partial \eta^2} = 0, \quad 0 \le \eta \le 10 \le \tau \le \infty \\
&R = T_S^{m_p} - 1, \;\; T_S(\tau) = T(\eta = 1, \tau) \\
&\text{BC}: \;\; \left.\frac{\partial T}{\partial \eta}\right|_{\eta=1} = \frac{1}{k}\left(\frac{(1+p)^{2n}((1+p)^{n/m_p} - H)}{(1+R)} - H(1+R)\right), \\
&\qquad T(\eta \to 0, \tau) = 0 \\
&\text{IC}: \; T(\eta, 0) = \eta^{1/k} + T_p(\eta)
\end{aligned}\right\} \tag{2.19}$$

Equation (2.19) is solved by a semi-implicit backward time central space (BTCS) scheme similar to that used by Junye (2000). The burn rate $R(x)$ at each axial location is obtained for the corresponding pressure at that location. Now, in order to use the source terms $R(x)$ in Eqns. (2.14) and (2.15), $R(x)$ is projected onto the Galerkin modes andR_m^c, R_m^s are obtained as:

$$R_m^c\,(t) = 2\int_0^1 R(x,t)\cos(\omega_m x)dx, \quad R_m^s\,(t) = 2\int_0^1 R(x,t)\sin(\omega_m x)dx \tag{2.20}$$

To track the evolution of the system, the nonlinear equations (2.14) and (2.15) are integrated using the fourth order Runge–Kutta (RK4) method with Eqn. (2.19) updated at each sub-step of RK4 using the semi-implicit BTCS scheme. General conclusions about non-normality of the system can be made with the linearised equations. To quantify the effect of non-normality, the equations are cast in a standard linearised form, which can be analysed using an existing frame work (Schmid and Henningson, 2001).

2.4 Short term dynamics and transient growth

To analyse the non-normal system, a state space vector formulation is used. Farrell and Ioannou (1996*a*) developed a generalized stability theory for non-normal linear operators, in the context of atmospheric sciences. In the state space vector representations, a general '*N*' dimensional linear dynamical system is given by

$$\frac{d\chi\,(t)}{dt} = L\chi\,(t) \tag{2.21}$$

where L is an *N* dimensional square matrix. Balasubramanian and Sujith (2008*a*,*b*) have shown that *L* is non-normal ($LL^\dagger \neq L^\dagger L$) for a thermoacoustic system. The general solution is given by $\chi(t) = e^{Lt}\chi(0)$, where $\chi(0)$ is the initial condition. An amplification factor is defined as $\sigma^2 = \langle\chi(t) \mid \chi(t)\rangle/\langle\chi(0) \mid \chi(0)\rangle$ ($\langle\bullet \mid \bullet\rangle$ denotes inner product in the linear vector space, $|\chi(t)\rangle = \chi(t)$, $\langle\chi(t)| = \chi^\dagger(t)\big)$ as a measure of growth or decay of fluctuations in the system during its time evolution. Note that σ^2 can be related to some physical quantity such as the disturbance energy of the system (Schmid and Henningson, 2001; Nagaraja *et al.*, 2009). Moreover, σ^2 will depend on

the choice of the initial condition. The maximum value of σ^2 for all possible initial conditions is given by $G(t) = \underset{\chi(0)}{Max} \left(\langle \chi(t) \mid \chi(t) \rangle / \langle \chi(0) \mid \chi(0) \rangle \right) = \left\| e^{Lt} \right\|^2$ (Golub and Loan, 1989). Here, $\|A\|$ denotes the 2-norm of the matrix *A*. The optimum initial condition (V_{opt}) to attain the maximum transient growth is obtained as follows. The formal solution of Eqn. (2.21) is given by:

$$\chi(t) = e^{Lt} \chi(0) \tag{2.22}$$

where, $\chi(0)$ is the initial condition of the state space variables. The matrix e^{Lt} is called as the propagator matrix, which advances the system from $\chi(0)$ to $\chi(t)$. Now a singular value decomposition (Golub and Loan, 1989) of e^{Lt} is performed as below

$$e^{Lt} = UDV^{\dagger} \tag{2.23}$$

where U & V are the left and right singular vectors, D is the matrix, whose diagonal elements form the singular values. Further, U & V are orthogonal matrices $\left(UU^{\dagger} = VV^{\dagger} = I \right)$. Multiplying Eqn. (2.23) throughout by V, the following equation is obtained

$$e^{Lt} V = UD \tag{2.24}$$

The matrix above equation can be interpreted schematically as in Fig. 2.3. Now, comparing the left hand side of Eqn. (2.24) with the right hand side of Eqn. (2.22), one can interpret V containing the initial condition $\chi(0)$. The rows of V, i.e., $v_1,\ v_2, ...$ forms the initial conditions. Since the matrix D is diagonal, the action of e^{Lt} on $v_1,\ v_2, ...$ gives the output $u_1,\ u_2, ...$ amplified by the numerical value of $d_1,\ d_2, ...$ As the singular values are arranged in the descending order, maximum amplification is obtained for v_1 and is termed as the optimum initial condition. u_1 is the corresponding optimum output and the associated amplification is given by d_1. Further, the numerical value of d_1 is the L2 norm of the matrix e^{Lt} as discussed above. Now, from the evolution of *G*(*t*), maximum amplification over all possible initial conditions and time can be obtained. For a system that is unstable according to classical linear stability theory, $G_{\max} = \max(G(t)) \rightarrow \infty$. For a system, that is stable according to the classical linear stability and is highly non-normal, $G_{\max} >> 1$. This shows high initial transient growth. For a linearly stable

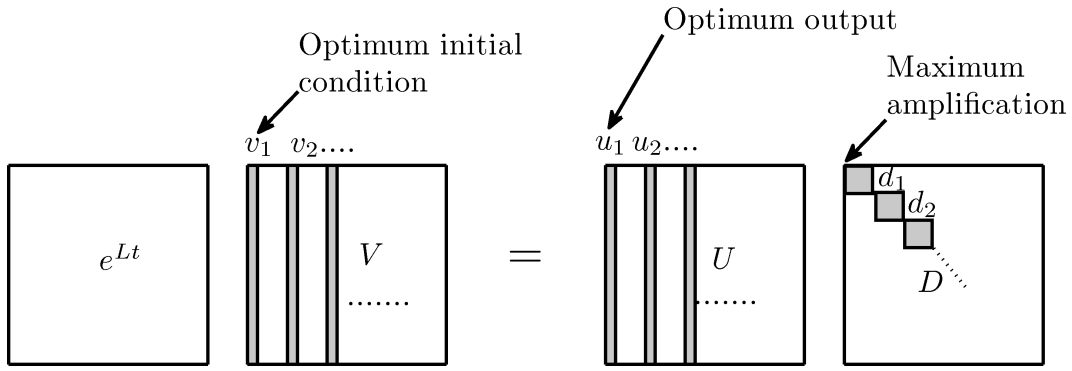

Figure 2.3: Schematic representation of performing SVD.

normal system $G_{\max} = 1$.

2.5 Linear analysis

To analyse the generalized stability of the system as discussed in the previous section, Eqns. (2.14), (2.15) and (2.19) are linearised to give the following:

$$\dot{U}_n + 2\sum_{m=1}^{N}\left(U_m I^1_{n,m} + P_m I^2_{n,m} + R^c_m I^3_{n,m} + R^s_m I^4_{n,m}\right) = 0 \tag{2.25}$$

$$\dot{P}_n - \left(\xi_n + \alpha_{NO}\right) P_n + \frac{2}{\gamma M}\left(\sum_{m=1}^{N}\left[U_m I^5_{n,m} + P_m I^6_{n,m} + R^c_m I^7_{n,m}\right]\right) = 0 \tag{2.26}$$

$$\left.\begin{aligned} &\frac{\partial T_p}{\partial \tau} + (k - k^2\eta)\frac{\partial T_p}{\partial \eta} - (k\eta)^2\frac{\partial^2 T_p}{\partial \eta^2} + m_p \eta^{1/k} T_{ps} = 0 \\ &R = m_p T_{ps},\ \ T_{ps}(t) = T_p(\eta = 1, t),\ \ \tau/t = l\bar{R}^2/a\alpha = F \\ &\text{BC}: \ \left.\frac{\partial T_p}{\partial \eta}\right|_{\eta=1} = \left(\frac{AT_{ps} - Bp}{k}\right),\ \ T_p(\eta \to 0, \tau) = 0 \end{aligned}\right\} \tag{2.27}$$

where $A = (2H - 1)/m_p$, $B = \left(2H - 1/m_p - 2\right)/n$, T_p is the fluctuating temperature in the propellant given by $T_p = T - T_{st} = T - \eta^{1/k}$. Equation (2.27) has to be applied at all axial locations. Because R is a linear function of T_{ps}, T_p can be decomposed as follows:

$$T_p(x,t) = \sum_{k=1}^{N}\left[T^c_k(t)\cos(\omega_k x) + T^s_k(t)\sin(\omega_k x)\right], \quad R^c_k = T^c_k/m_p, \quad R^s_k = T^s_k/m_p \tag{2.28}$$

The above expression, when substituted in Eqn. (2.27) and then projected onto the Galerkin basis as described earlier, leads to the following equations:

$$\left.\begin{aligned} &\frac{\partial T_n^c}{\partial \tau} + (k - k^2\eta)\frac{\partial T_n^c}{\partial \eta} - (k\eta)^2\frac{\partial^2 T_n^c}{\partial \eta^2} + m_p\eta^{1/k}T_{sn}^c = 0 \\ &T_{sn}^c(t) = T_n^c(\eta = 1, t) \\ &\text{BC}: \ \left.\frac{\partial T_n^c}{\partial \eta}\right|_{\eta=1} = \left(\frac{AT_{sn}^c - B\gamma M P_n}{k}\right), \ T_n^c(\eta \to 0, \tau) = 0 \end{aligned}\right\} \tag{2.29}$$

$$\left.\begin{aligned} &\frac{\partial T_n^s}{\partial \tau} + (k - k^2\eta)\frac{\partial T_n^s}{\partial \eta} - (k\eta)^2\frac{\partial^2 T_n^s}{\partial \eta^2} + m_p\eta^{1/k}T_{sn}^s = 0 \\ &T_{sn}^s(t) = T_n^s(\eta = 1, t) \\ &\text{BC}: \ \left.\frac{\partial T_n^s}{\partial \eta}\right|_{\eta=1} = \left(\frac{AT_{sn}^s}{k}\right), \ T_n^s(\eta \to 0, \tau) = 0 \end{aligned}\right\} \tag{2.30}$$

An important observation in the linear regime is that the Galerkin pressure mode is absent in the boundary condition for Eqn. (2.30). Hence, R_n^s is not affected (in the linearised equations) by the acoustic fluctuations, and it evolves depending only on its initial condition. However, it affects the acoustic momentum equation Eqn. (2.25) through the $R_m^s I_{n,m}^4$ term. Equations (2.25), (2.26), (2.29) and (2.30) can be cast in the form of (2.21). Equations (2.29) and (2.30) are discretised using a second-order central difference at M_g equally spaced points in $'\eta'$. The linearised equations are

$$\frac{d\chi}{dt} = L\chi \tag{2.31}$$

$$\chi = \begin{pmatrix} \Omega & \Psi_1^c & \Psi_2^c & . & . & \Psi_N^c & \Psi_1^s & \Psi_2^s & . & . & . & \Psi_N^s \end{pmatrix}_{1\times 2NM_g}$$

$$\Omega = \begin{pmatrix} U_1 & P_1 & . & . & . & U_N & P_N \end{pmatrix}^T_{1\times 2N} \ \textit{T} \text{ represents matrix transpose}$$

$$\Psi_n^c = \begin{pmatrix} \beta_1 T_{n(1)}^c & \beta_2 T_{n(2)}^c & . & . & . & . & \beta_{M_g-1} T_{n(M_g-1)}^c \end{pmatrix}^T_{1\times(M_g-1)}$$

$$\Psi_n^s = \begin{pmatrix} \beta_1 \ T_{n(1)}^s & \beta_2 T_{n(2)}^s & . & . & . & . & \beta_{M_g-1} T_{n(M_g-1)}^s \end{pmatrix}^T_{1\times(M_g-1)}$$

where the subscripts $n(1),\ n(2),\ n(3)....n(M_g-1)$ represents the fluctuating temperature at 1st, 2nd, 3rd .... $(M_g-1)^{\text{th}}$ points from the propellant surface for the n^{th} mode. The homogeneous boundary condition $(T_n^s(\eta \to 0, \tau) = 0)$ at the last point, leave Ψ_n^c

and Ψ_n^s with $(M_g - 1)$ discrete points. The linear operator matrix is expanded in Appendix B. Now, as mentioned in Section 2.2, Eqn. (2.27) indicates the extra degree of freedom for the system apart from acoustics and it appears as extra variables Ψ_n^c, Ψ_n^s in Eqn. (2.31). This implies that not only does the system comprise acoustic variables, but it is also an extended one with variables from the burn rate response. Hence, acoustic energy (Rienstra and Hirschberg, 2008), which defines the growth or decay of acoustic oscillations is inadequate. A new generalized disturbance energy is defined which accounts for the perturbations in burn rate variables (Ψ_n^c, Ψ_n^s). A formal derivation of fluctuating thermal energy in the propellant is performed. The thermal energy obtained is then added to the acoustic energy with appropriate weight factors (arrived at from the consideration of entropy generation at the propellant surface) to get the 'generalized disturbance energy'. The factor β_i in Eqn. (2.31) is present for the reason, that the 2 norm or L2 norm of $\chi(t)$ represents the disturbance energy. The following section deals with the disturbance energy and its relation to $\langle \chi(t) \mid \chi(t) \rangle$.

2.6 Generalised disturbance energy

As mentioned in Section 2.4, σ^2, which is a relative measure of the 2-norm of $\chi(t)$ $\left(\|\chi(t)\| = \left(\langle \chi(t) \mid \chi(t) \rangle \right)^{1/2} \right)$, can be related to the energy in the disturbance calculated from the state space variables in Eqn. (2.31). From our analysis, this energy has two components. The first component is from the chamber acoustic field and the second is from the unsteady thermal energy of the propellant. Energy in the acoustic field can be characterized by the familiar acoustic energy (Rienstra and Hirschberg, 2008) given by

$$\tilde{E}_{ac}(t) = \frac{1}{2} \iiint_{chambervolume} \left[(\bar{\rho}\tilde{u}'(x,t))^2 + \left(\tilde{p}'(x,t)/\bar{\rho}a^2 \right)^2 \right] dV \tag{2.32}$$

Non-dimensionalising the above by $\bar{\rho}u_m^2 S_c l/2$ and assuming 1-D variation, leads to the following:

$$E_{ac}(t) = \frac{\tilde{E}_{ac}(t)}{\frac{1}{2}\bar{\rho}u_m^2 S_c l} = \int_0^1 \left[(u(x,t))^2 + \left(\frac{p(x,t)}{\gamma M} \right)^2 \right] = \frac{1}{2} \sum_{n=1}^{N} \left(U_n^2 + P_n^2 \right) \tag{2.33}$$

Now a similar expression for the fluctuating energy stored in the solid phase of the propellant has to be calculated to get the total disturbance energy. Equation (2.16) is written in its linearised and dimensional form for the fluctuating temperature $\tilde{T}'$ as

$$\rho_p S_p \left(\frac{\partial \tilde{T}'}{\partial \tilde{t}} - \bar{R} \frac{\partial \tilde{T}'}{\partial \tilde{y}} - \tilde{R}' \frac{\partial \tilde{T}_{st}}{\partial \tilde{y}} \right) = \lambda_p \frac{\partial^2 \tilde{T}'}{\partial \tilde{y}^2} \tag{2.34}$$

where λ_p is the thermal conductivity of the solid phase of the propellant. Multiplying the above equation by $\tilde{T}' \Big/ \bar{T}$ and rearranging, we obtain

$$\frac{\rho_p S_p}{2\bar{T}} \frac{\partial \tilde{T}'^2}{\partial \tilde{t}} = \frac{\lambda_p}{\bar{T}} \left(\frac{\partial}{\partial \tilde{y}} \left(\tilde{T}' \frac{\partial \tilde{T}'}{\partial \tilde{y}} \right) - \left(\frac{\partial \tilde{T}'}{\partial \tilde{y}} \right)^2 \right) + \frac{\rho_p S_p \bar{R}}{2\bar{T}} \frac{\partial \tilde{T}'^2}{\partial \tilde{y}} + \frac{\rho_p S_p}{2\bar{T}} \frac{\partial \tilde{T}_{st}}{\partial \tilde{y}} \tilde{R}' \tilde{T}' \tag{2.35}$$

Integrating Eqn. (2.35) over the entire solid phase propellant volume and applying Gauss divergence theorem, we get

$$\begin{aligned} \frac{\rho_p S_p}{2\bar{T}} \frac{\partial \iiint_{V_1} \tilde{T}'^2 dV}{\partial \tilde{t}} =& \frac{1}{\bar{T}} \left(\iint_{S_l} \lambda_p \tilde{T}' \frac{\partial \tilde{T}'}{\partial \tilde{y}} dS + \frac{\rho_p S_p \bar{R}}{2} \left(\tilde{T}'^2 \Big|_{S_u} - \tilde{T}'^2 \Big|_{S_l} \right) \right) \\ &+ \frac{\rho_p S_p}{2\bar{T}} \iiint_{V_1} \frac{\partial \tilde{T}_{st}}{\partial \tilde{y}} \tilde{R}' \tilde{T}' dV - \frac{\lambda_p}{\bar{T}} \iiint_{V_1} \left(\frac{\partial \tilde{T}'}{\partial \tilde{y}} \right)^2 dV \end{aligned} \tag{2.36}$$

where V_1 is the entire propellant volume, S_l is the entire propellant surface, S_u is propellant upper surface and S_l is the propellant lower surface (casing). The left-hand side of Eqn. (2.36) is a positive definite quantity, which is the fluctuating energy due to temperature fluctuations in the propellant. The first term in the right-hand side is the corresponding energy flux term. The second term is due to the contributions from the unsteady burn rate and the last term is from the loss due to thermal conduction (the term is always negative). Now the equation is the conservation equation for the fluctuating energy $\tilde{E}_p$ present in the solid propellant. The fluctuating energy $\tilde{E}_p$ is

$$\tilde{E}_p = \frac{\rho_p S_p}{2\bar{T}} \iiint_{V_1} \tilde{T}'^2 dV = \frac{\rho_p S_p}{2\bar{T}} \left(\tilde{T}_{S,0} - \tilde{T}_\infty \right)^2 l S_l \frac{\alpha}{\bar{R}} \int_{y=o}^{\infty} \int_{x=0}^{1} T_p^2 dx dy \tag{2.37}$$

Non-dimensionalising the above by $\bar{\rho} u_m^2 S_c l/2$, substituting for T_p from Eqn. (2.28) and

substituting $\eta = e^{-ky}$, we obtain

$$E_p = \frac{\tilde{E}_p}{\frac{1}{2}\bar{\rho}u_m^2 S_c l} = \frac{\delta}{2}\int_{\eta=o}^{1}\sum_{n=1}^{N}\left(\left(\frac{T_n^c}{\sqrt{\eta}}\right)^2 + \left(\frac{T_n^s}{\sqrt{\eta}}\right)^2\right)d\eta \tag{2.38}$$

where $\delta = \left(\rho_p S_p \alpha S_l \left(\tilde{T}_{S,0} - \tilde{T}_\infty\right)^2\right) \Big/ \left(\bar{R}\bar{\rho}\bar{T}u_m^2 S_c k\right)$. Discretising in the η domain leaves Eqn. (2.38) as

$$E_p = \frac{\tilde{E}_p}{\frac{1}{2}\bar{\rho}u_m^2 S_c l} = \frac{\delta}{2}\sum_{n=1}^{N}\sum_{i=1}^{M_g-1}\left(\left(\frac{T_n^c}{\sqrt{\eta_i}}\right)^2 + \left(\frac{T_n^s}{\sqrt{\eta}_i}\right)^2\right)\Delta\eta \tag{2.39}$$

Now, the weightage to energies $\tilde{E}_{ac}$ and $\tilde{E}_p$ in forming the total disturbance energy $\tilde{E}_T$ is fixed by considering the energy from entropy fluctuations. Chu (1965) has derived an expression for the disturbance energy $\left(\tilde{E}_{chu}\right)$ and is given as follows:

$$\tilde{E}_{chu}(t) = \frac{1}{2}\iiint_{\text{chamber volume}}\left[(\bar{\rho}\tilde{u}'(x,t))^2 + \frac{\tilde{p}'^2(x,t)}{\bar{\rho}a^2} + \left(\frac{(\gamma-1)\,\bar{P}}{\gamma}\right)\left(\frac{\tilde{s}'}{\Re}\right)^2\right]dV \tag{2.40}$$

where $\tilde{s}'$ is the entropy fluctuation and $\Re$ is the characteristic gas constant of the gas in the combustion chamber. Flame is the source of entropy fluctuations in the motor. The entropy fluctuations are computed from propellant surface temperature and acoustic fluctuations, as derived by Krier *et al.* (1968), as

$$\frac{\tilde{s}'}{\Re} = \frac{\gamma}{\gamma-1}\Theta\left[\left(2nH - 2n - {}^{n}/_{m_p} - 1\right)p + \left(2m_p + 1 - 2m_pH\right)T_{ps}\right] \tag{2.41}$$

where $\Theta = \left(\tilde{T}_{S,0} - \tilde{T}_\infty\right) \Big/ \left(\tilde{T}_f\right)$. Note that $\tilde{T}_f$ is the steady flame temperature. Now the coefficient proportional of T_{ps}^2 in the entropy part of $\tilde{E}_{chu}$ after substituting Eqn. (2.41) in $\tilde{E}_{chu}$ is $\left[\Theta\left(2m_p + 1 - 2m_pH\right)\right]^2 (\gamma P) \,/\, (\gamma - 1)$. This gives the weight factor W_f for $\tilde{E}_p$ which has to be added to $\tilde{E}_{ac}$. Hence, the total disturbance energy is

$$\tilde{E}_T = \tilde{E}_{ac} + W_f\tilde{E}_p, \quad W_f = \frac{2\gamma\bar{P}\bar{T}}{(\gamma-1)\,\rho_p S_p}\left[\frac{\Theta\left(2m_p + 1 - 2m_pH\right)}{\tilde{T}_{S,0} - \tilde{T}_\infty}\right]^2 \tag{2.42}$$

Non-dimensionalising as before, we get the total non-dimensional generalized disturbance energy E_T. This energy incorporates the contributions from the entropy fluctua-

tions released by the flame as well as the temperature fluctuations inside the propellant.

$$E_T = \frac{\tilde{E}_T}{\frac{1}{2}\bar{\rho}u_m^2 S_c l} = E_{ac} + W_f E_p \tag{2.43}$$

Now, using Eqns. (2.33) and (2.39), we get

$$\begin{aligned} E_T(t) = \frac{\tilde{E}_T}{\frac{1}{2}\bar{\rho}u_m^2 S_c l} = E_{ac} + W_f E_p &= \frac{1}{2}\sum_{n=1}^{N}\left[\left(U_n^2 + P_n^2\right) + \sum_{i=1}^{M_g-1}\left(\left(\beta_i T_n^c\right)^2 + \left(\beta_i T_n^s\right)^2\right)\right] \\ &= \frac{1}{2}\left\|\chi(t)\right\|^2 \end{aligned} \tag{2.44}$$

where $\beta_i = \sqrt{\Delta\eta\delta W_f/\eta_i}$. Thus, the 2-norm of $\chi(t)$ is related to the physical generalized disturbance energy and σ^2 gives the amplification of the same during the system evolution. It should be noted that Chu's energy is derived in the limit of zero mean flow Mach number. However, in the present case the mean flow Mach number is not zero $(M \sim 0.1)$. If one includes the energy contribution due to mean flow, the disturbance energy (E_T) can not be represented by the L2 norm. The reason for choosing E_T as the L2 norm is as follows. In a dynamical system, L2 norm can be calculated easily using singular value decomposition (SVD). The optimum initial condition and the maximum transient growth can then be obtained directly from the SVD. The choice of norms other than the L2 norm brings the complication of defining new inner products. The inner products thus defined can be mathematically inconsistent, and some special techniques (such as adjoint optimisation) other than SVD should be used, which is beyond the scope of this paper. Hence in this analysis, Chu's energy is used, so that E_T coincides with the L2 norm. The L2 norm can then be computed using SVD.

2.7 Result and discussion

Simulations are performed for a rocket motor, whose system parameters are given in table 2.1.

The numerical simulations are performed with the simulation parameters *N*, M_g and

Gas properties	Propellant properties	Combustion chamber dimensions
$\bar{p}$=60 *bar*	Δh=7 *MJ/kg*	l=8 *m*
$\bar{T}$=2900 *K*	α=1.6$\times 10^{-6} m^2/s$	S_l=1.59 *m*
$\bar{\rho}$=4.82 *kg/m*^{3}	m_p=6	S_c=0.2 *m*^{2}
γ=1.35	n=0.4	**Numerical parameters**
$\Re$=287 *J/kg k*	$\bar{R}$=0.017 *m/s*	N=5
H=0.76	ρ_p=1800 *kg/m*^{3}	M_g=150
Θ= 0.19	S_p = 3542 *J/KgK*	Time step $\Delta t = 0.005$

Table 2.1: SRM parameter values and operating conditions.

time integration time step Δt as shown in table 2.1. Increasing N, M_g and decreasing Δt beyond the above values leads to a difference of less than 1 %. Hence, the above values are chosen for all simulations shown below. The damping coefficients C_1 and C_2 are varied to get a different dynamical behaviour for the simulation.

2.7.1 Linearly stable and unstable system

The linearised equation (2.21) is analysed for the stability of the system to small amplitude disturbances. Eigenvalues of the discretised linear operator L determine the linear stability of the system in the asymptotic time limit. If all the eigenvalues lie in the left half of the complex plane, the system is asymptotically stable to small disturbances. This above predictions are given by 'classical linear stability'. However, the short term behaviour is different due to the non-normal nature of the linearised operator. Using Farrell and Ioannou (1996*a*) terminology, a system with $G_{\max} = 1$ is called a 'linearly stable' (generalised linear stability) and the finite amplitude small disturbances die down monotonically. The time evolution of unsteady oscillations is shown at one fourth of the motor length (l/4) from the head end as a representative position. Acoustic pressure oscillation is shown in Fig. 2.4 for a system, stable according to classical linear stability. The amplitude decays in the asymptotic time limit, eventually reaching a stable fixed point. The phase space plot between p(x=1/4) and R(x=1/4) (Fig. 2.5) shows a spiral trajectory, eventually collapsing to a single point (0, 0) corresponding to

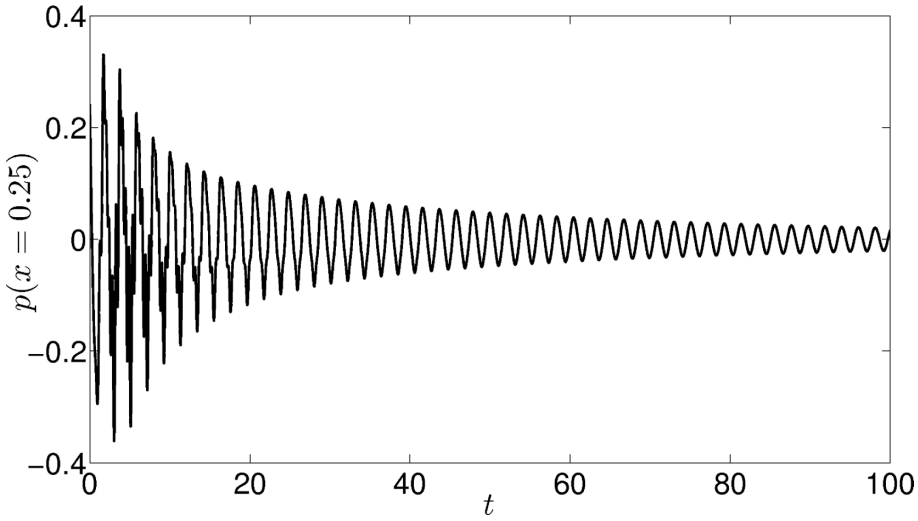

Figure 2.4: The evolution of acoustic pressure at x = 0.25 for a linearly stable system. $U_1(0) = 3,\ P_1(0) = 3,\ P_{m\neq1}(0) = U_{m\neq1}(0) = 0,\ MT_p\,(\eta, 0) = 0,\ C_1 = 0.05,\ C_2 = 0.001.$

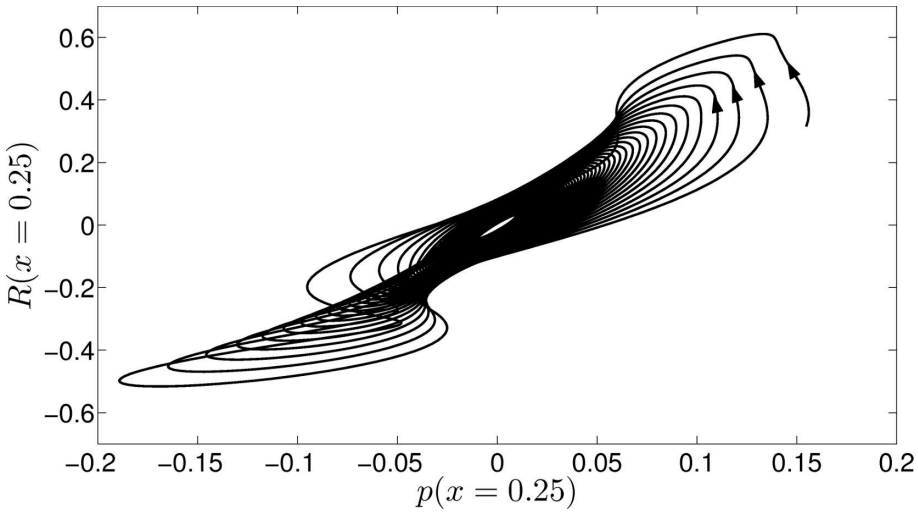

Figure 2.5: The phase portrait of the acoustic pressure and the unsteady burn rate at x = 0.25. $U_1(0) = 3,\ P_1(0) = 3,\ P_{m\neq1}(0) = U_{m\neq1}(0) = 0,\ MT_p\,(\eta, 0) = 0,\ C_1 = 0.05,\ C_2 = 0.001.$

the mean flow (arrows indicate the direction of the time evolution). This type of fixed point is called 'stable focus'. The actual dimensions of the phase space in the modal and discretized form is $2N$ +$2N(M_g$-1)=$2N(M_g)$, which corresponds to the total number of state space variable in Eqn. (2.31). The plot in Fig. 2.5 is just the projection of $2N(M_g)$ space onto a two dimensional space. Hence we observe apparent intersections of the phase trajectories, which are actually evolving without intersection in a higher dimension space. On the other hand, if the real part of one of the eigenvalues is positive, the system is linearly unstable. Fig. 2.6 shows the acoustic pressure evolution from a small initial disturbance for a linearly unstable system. Initially, the oscillations grow exponentially as predicted by linear stability theory, reaching amplitudes where nonlinear terms start dominating. The nonlinear terms in Eqns. (2.14) and (2.15) start dominating, balancing the driving terms resulting in the formation of oscillations of constant amplitude called limit cycle. The corresponding phase plot between $p(x$=1/4) and $R(x$=1/4) after removing the transients leaves a closed curve (Fig. 2.7). This corresponds to limit cycles, where the trajectories close itself as $t \rightarrow \infty$. The presence of apparent multiple intersections in Fig. 2.7 shows the presence of more dominant frequencies, which is a characteristic of limit cycle oscillations in SRMs. The existence of limit cycle was explained by Culick (1976*a*) with second-order nonlinear acoustics. However, another important phenomenon is the occurrence of 'pulsed instabilities' (Blomshield *et al.*, 1997*a*) in SRMs. This is a type of instability leading to unpredicted damage of the motors and was not explained to date with a physics-based acoustic – burn rate coupling model. This issue is addressed in Section 2.7.4. Before examining the nonlinear regime of oscillations, it is important to discuss some more interesting results pertaining to the non-normal nature of the linear operator L in the following section.

2.7.2 Pseudospectra and transient growth

The linear operator Eqn. (2.31) in its discretised form (L matrix) is used for pseudospectra computation. For normal operators, resonance (maximum amplification) happens at the eigenvalues; at other points, the amplification is inversely proportional to the distance of the forcing frequency from the nearest eigenvalue. However, for non-normal operators, resonant amplification of many orders occurs far from the eigenvalues and is

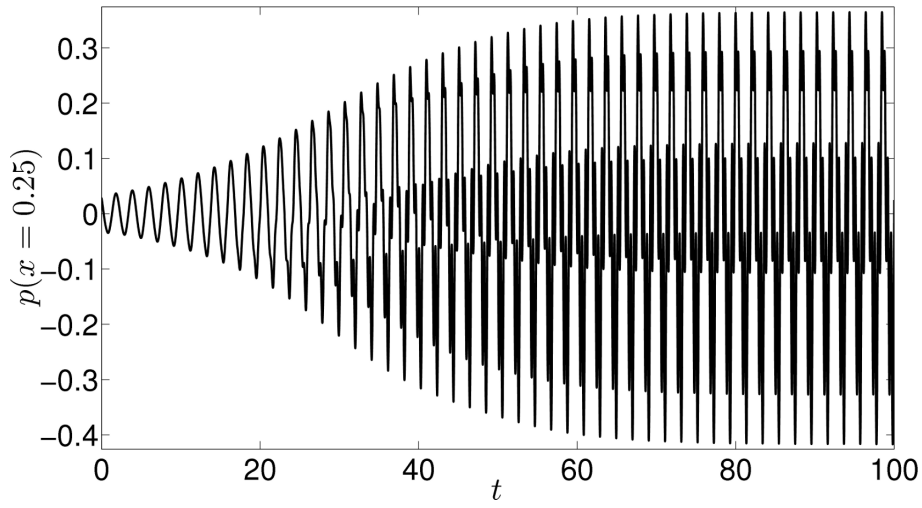

Figure 2.6: The evolution of acoustic pressure at x = 0.25 for a linearly unstable system. $U_1(0) = 0.3,\ P_1(0) = 0.3,\ P_{m\neq1}(0) = U_{m\neq1}(0) = 0,\ MT_p\,(\eta, 0) = 0,\ C_1 = 3 \times 10^{-4},\ C_2 = 1 \times 10^{-4}$.

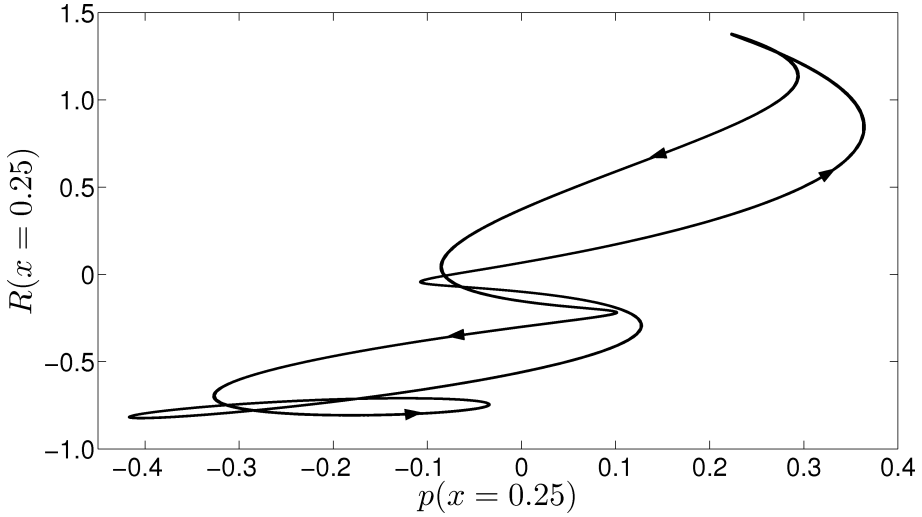

Figure 2.7: The phase portrait of the acoustic pressure and unsteady burn rate at x = 0.25. $U_1(0) = 0.3,\ P_1(0) = 0.3,\ P_{m\neq1}(0) = U_{m\neq1}(0) = 0,\ MT_p\,(\eta, 0) = 0,\ C_1 = 3 \times 10^{-4}, C_2 = 1 \times 10^{-4}$.

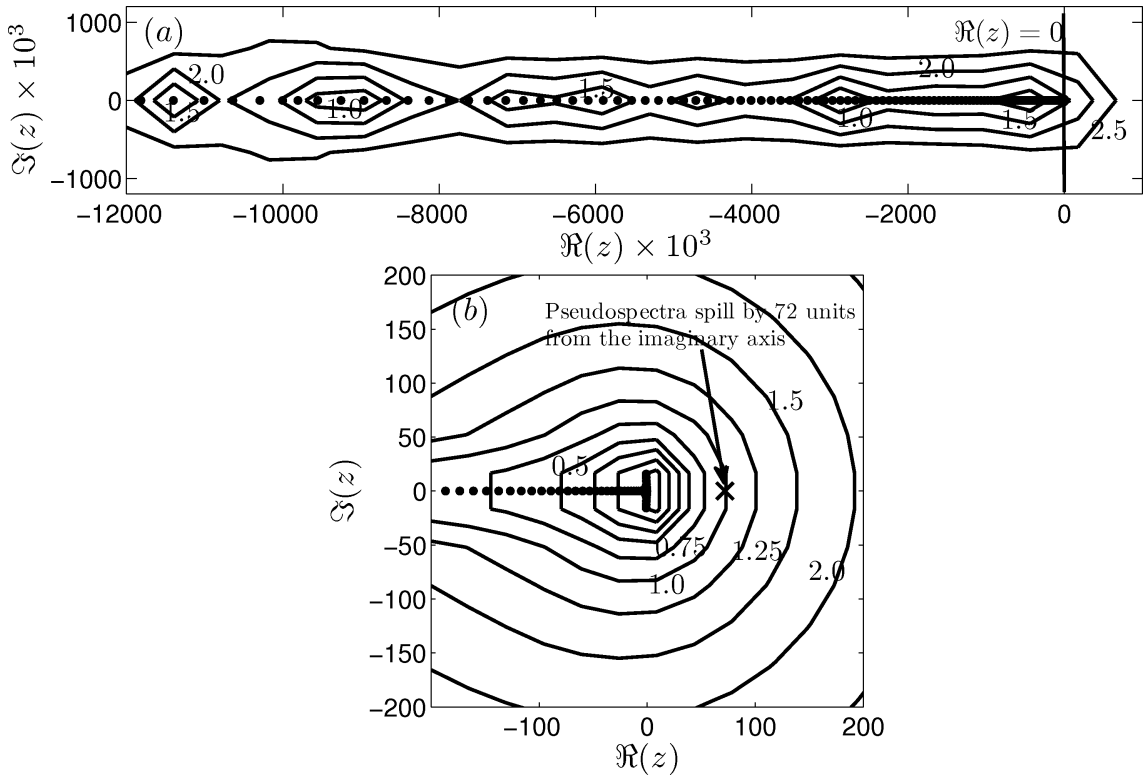

Figure 2.8: *a*) Pseudospectra of the non-normal linear operator *'L'*. *b*) Zoomed in view near the origin and the calculation of the lower bound for the maximum transient growth. The contour value represents $\log_{10}\varepsilon$. $C_1 = 0.03$, $C_2 = 0.02$, $\|L\| = 1.88 \times 10^4$, $\varepsilon_{\max} = 1 \times 10^{2.5}$, $\varepsilon_{max}/||L|| \ll 1$. $\Re(z)$ and $\Im(z)$ indicates the real and imaginary part of z respectively.

called 'pseudoresonance' (Trefethen and Embree, 2005). The ε pseudospectra plot is used to analyse non-normal operators and *z* is called an ε pseudoeigenvalue of the operator *L,* if it satisfies $\left\|(zI - L)^{-1}\right\| \geq \varepsilon^{-1}$ (Trefethen and Embree, 2005). The perturbations ε given are very small compared with the size of the linear operator ($\varepsilon << \|L\|$). For normal operators, ε pseudospectrum consists of concentric circles, confirming the inversely proportional relationship between the amplification and the distance between the excitation frequency and the nearest eigenfrequency of the system. However, for non-normal operators the contours are distorted.

Fig. 2.8(*a*) shows that the pseudospectra of the *L* matrix are highly distorted near the imaginary axis. The system considered is stable according to the classical linear stability theory. All the eigenvalues of the system lie on the left half of the complex plane. The perturbation in the linear operator *L* is depicted in its pseudospectra. The relation between transient growth and the geometry of the pseudospectra is described

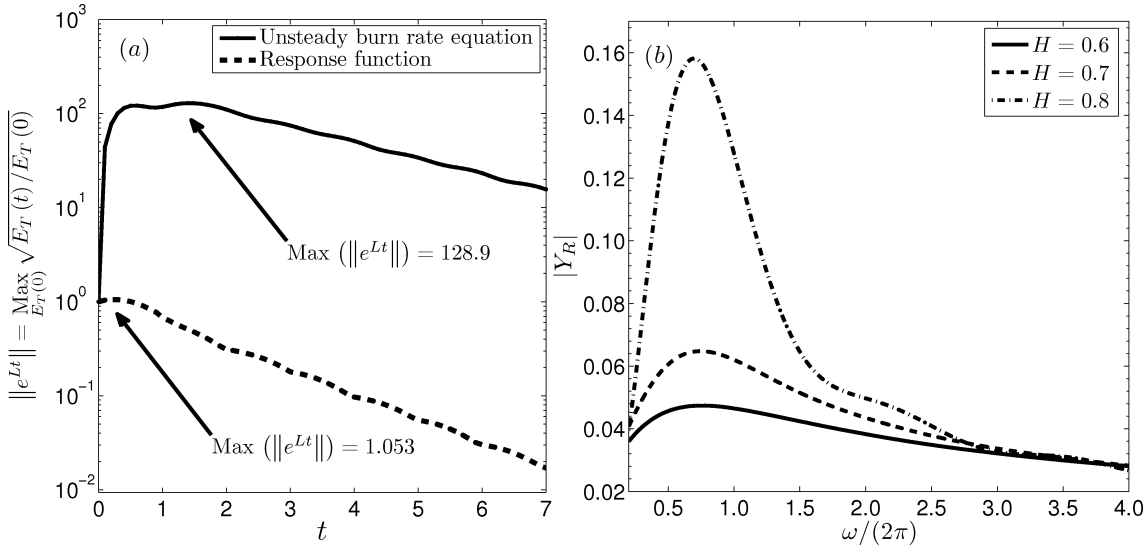

Figure 2.9: *a*) Comparison of the evolution of $\left\|e^{Lt}\right\|$ with differential equation for unsteady burn rate and response function (Y_R) calculations, $C_1 = 0.03$, $C_2 = 0.02$, $\chi(0) = V_{opt}$. *b*) The magnitude of the response functions $(|Y_R|)$of the propellant for various values of *H*.

by Trefethen and Embree (2005). The contours spill over to the right half of the complex plane, which is an indication of transient growth in the system evolution. The zoomed-in contour of Fig. 2.8(*a*) near the origin is shown in Fig. 2.8(*b*). For example, a perturbation of $\varepsilon = 10^1$ $(\varepsilon/\|L\| = 5.33 \times 10^{-4})$ leads to the spilling of the pseudospectra to the right by z = 72 units from the imaginary axis. From this, the transient growth is estimated to be $(z/\varepsilon)^2 = 7.2^2 = 51.84$ (Trefethen and Embree, 2005). This is just one point in the ε contour. Maximizing this over all ε contours results in 'Kreiss constant (κ)', which gives the lower bound for the maximum transient growth (G_{max}). For a normal system, ε contours move proportionally outwards with z and hence $\kappa = 1$ with no transient growth. Thus, qualitative information can be obtained from the contours of the pseudospectra. As is shown in Section 2.6 the square of the 2-norm of the state space vector equals the total disturbance energy in the system. Hence, the transient growth obtained now directly gives the disturbance energy amplification. We also note that a very small perturbation (0.1%) leads to an energy rise of 2 orders of magnitude. All these are obtained from investigating the geometry of the pseudospectra.

2.7.3 Effects of the internal degrees of freedom

The exact calculation of maximum transient growth is to evolve $G(t) = \|\exp(Lt)\|^2$ and find its maximum as discussed in Section 2.4. Fig. 2.9(*a*) shows the evolution of *exp*(*Lt*) and the maximum transient growth is found to be $128.9^2 = 1.66 \times 10^4$, which is higher than the previous estimate based on the lower bound of G_{max} from pseudospectra. Also, the same figure shows that the use of response function for modelling the acoustic - burn rate coupling gives rise to very small transient growth. The response function is calculated as follows. The unsteady burn rate equation (2.19) is solved for a forced pressure oscillation $p = p_0 \sin(\omega t)$ to get the unsteady burn rate in the form $R = R_0 \sin(\omega t + \phi)$. Here R_0 is obtained from the Fourier transform of the signal *R* at the frequency $\omega/2\pi$. The associated phase (ϕ) is determined from $\cos\phi = \int_0^\infty p(t)R(t)dt \Big/ \left(\sqrt{\int_0^\infty p^2(t)dt}\sqrt{\int_0^\infty R^2(t)dt}\right)$. The response function (Y_R) is then calculated as $Y_R = R/p = R_0 e^{i\phi}/p_0$. The magnitude of Y_R for various excitation frequencies is shown in Fig. 2.9(*b*). It is also observed that magnitude of Y_R is maximum around 1, which corresponds to the timescale for unsteady conduction inside the unburnt propellant.

Next for the extended system, the optimum initial condition (V_{opt}) for the maximum transient growth is calculated. The state space vector $\chi(t)$ has *N* pairs of acoustic variables called 'acoustic modes'. The remaining $2N(M_g\text{-}1)$ variables describe the unsteady propellant burn rate response called 'burn rate modes'. Neither the acoustic modes, nor the burn rate modes are the eigenmodes of the system. They are only reference modes (basis functions) satisfying the boundary condition and the variables are just projected along these modes.

The relative amplitude of various modes in the 'initial condition' (V_{opt}) is shown in Fig. 2.10 with the acoustic modes shown in the inset. The important observation is that, for obtaining maximum transient growth, one should also excite in the 'burn rate modes'. Although, the appropriate response function (Y_R) is used instead of solving simultaneously the unsteady burn rate equations along with the acoustic equations, there is a huge difference in the transient growth between the two curves in Fig. 2.9(*a*). By using a response function, the dynamics involved in the unsteady burn rate are implicitly

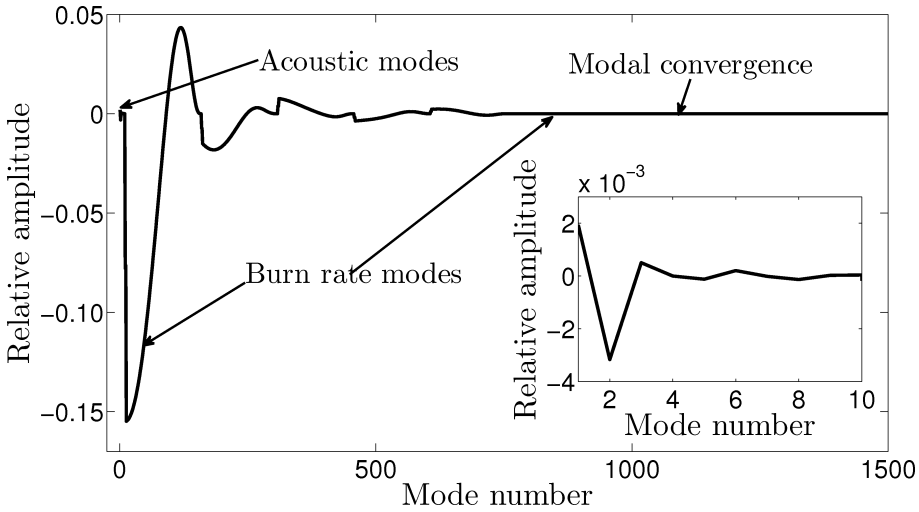

Figure 2.10: Relative amplitude of the optimum initial condition direction. Inset shows the relative amplitude of the acoustic modes, $C_1 = 0.03,\ C_2 = 0.02,\ \chi(0) = V_{opt},\ N = 5,\ M_g = 150$.

not taken into account. Now, if the optimum initial condition for the maximum transient growth is distributed more in the burn rate modes, then it is natural to expect a small transient growth, if the dynamics in the burn rate modes are not taken into account. Fig. 2.10 shows indeed that the optimum initial condition is distributed among the burn rate modes, and hence there is a large difference in transient growth of both curves in Fig. 2.9(a). Therefore, for a stable system, according to classical linear stability, a very small local change in propellant burn rate (might be due to inhomogeneity in the propellant) can give rise to an initial perturbation in the burn rate mode. Also, as the motor is fired initially, the temperature distribution is uniform in the propellant. As the SRM operates, and as the port configuration changes as time evolves, after some time, there might be fluctuations in the temperature at the surface of the propellant. This serves as an initial condition, where non-normality of the system plays a role and transient growth will happen. This can cause transient growth and the amplitude increases, eventually reaching a limit cycle (in the presence of nonlinearities). This important observation cannot be made, if one uses the propellant response for modelling the burn rate, which neglects the transient dynamics of the burn rate response. Higher modes in both acoustics and burn rate do not contribute to the initial condition showing the modal independence of the discretization with increasing number of modes. The role of transient growth is shown to play an important role in pulsed instability, which is discussed below.

2.7.4 Pulsed instability

In SRMs, experiments indicate that rockets which are stable to small-amplitude disturbances become unstable for larger ones (Blomshield *et al.*, 1997*a*). They then exhibit limit cycle oscillations or the rocket motor may be damaged. This phenomenon is known as 'pulsed instability' or 'triggering' (Culick, 2006). From a dynamical systems' point of view, this kind of phenomenon is termed as 'sub-critical transition' to instability. The system is linearly stable, but nonlinearly unstable. In the previous studies, only *ad hoc* models for burn rate – acoustic velocity coupling were used to simulate the experimental results (Wicker *et al.*, 1996; Anathakrishnan *et al.*, 2005; Flandro *et al.*, 2007). Wicker *et al.* (1996) tried different forms of nonlinear propellant response functions Y_R to demonstrate triggering. Flandro *et al.* (2007) have given a comprehensive compilation of his earlier work and new formulations to predict the nonlinear stability of SRMs. However, his model also assumes an *ad hoc* propellant response function, which is not derived from the physics of the problem. Moreover, the coefficients in the forms of the *ad hoc* function are obtained from experiments (i.e. like matching limit cycle waveforms) and there is no rigorous theoretical reasoning behind them. This chapter solves both acoustic and propellant response equations simultaneously, without any ad hoc assumptions on burn rate dependence on the acoustic field being made in the formulation. The present numerical simulations show 'pulsed instability' in some parameter range. Pulsed instability can possibly occur in two ways. The first is when the initial disturbance amplitude is large enough for the nonlinear terms to be dominant compared with the linear terms right from the start of the evolution. The linearised equations (2.25), (2.26) and (2.27) are solved numerically and Fig. 2.11 shows decaying acoustic pressure oscillations. This means that the system is linearly stable. Linearised equations scale with initial conditions and the dynamical evolution will look similar for all scaled amplitudes. Now, for the same parameters and initial condition, the nonlinear terms are included and equations (2.14), (2.15) and (2.19) are solved. Fig. 2.12 shows that the acoustic pressure initially decays, and after sometime it starts growing with the amplitude eventually reaching a limit cycle. The initial high amplitude disturbance leads to the modal energy transfer from one mode to another by 'direct interaction' as explained in Section 2.2. The energy transfer sustains the oscillations by keeping the

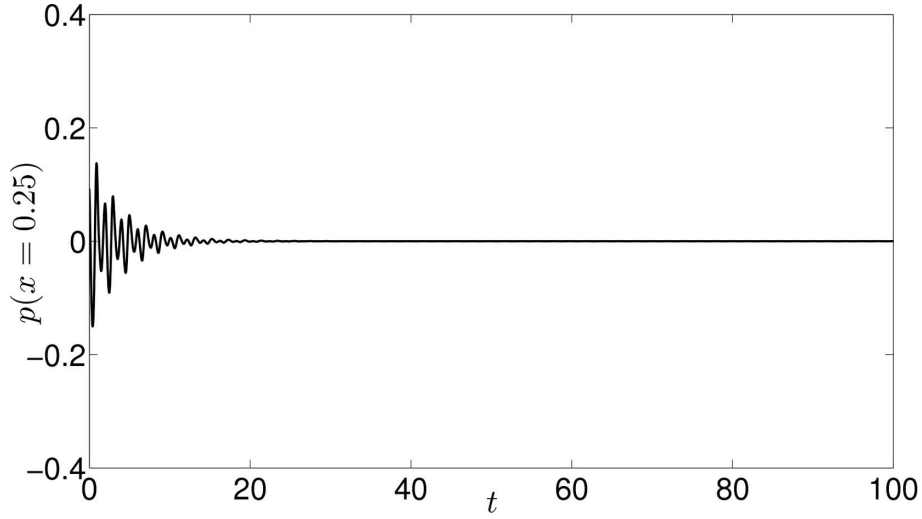

Figure 2.11: Evolution of acoustic pressure at x = 0.25 from the linear simulation. $U_2(0) = 3,\ P_2(0) = 3,\ P_{m\neq 2}(0) = U_{m\neq 2}(0) = 0,\ MT_p\,(\eta = 1, 0) = 0.03$, $MT_p\,(\eta \neq 1, 0) = 0,\ C_1 = 0.02,\ C_2 = 0.02$.

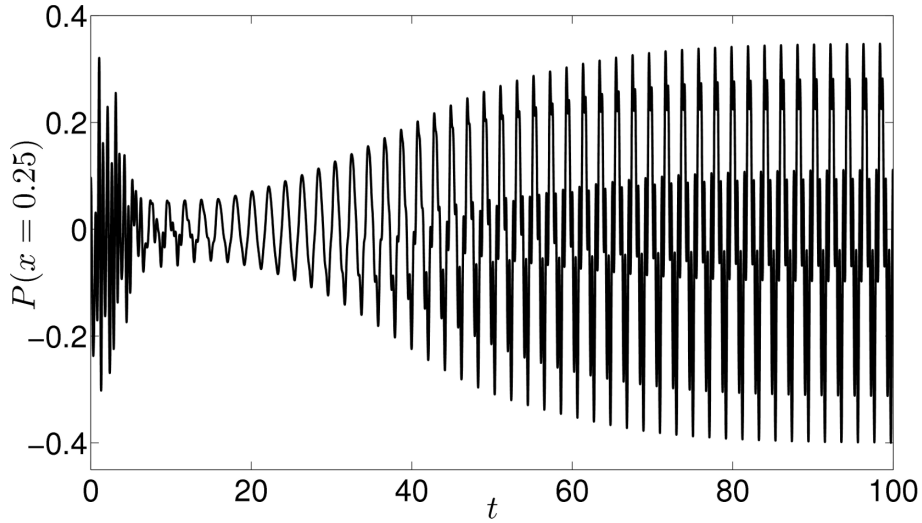

Figure 2.12: Evolution of acoustic pressure at x = 0.25 from the nonlinear simulation. $U_2(0) = 3,\ P_2(0) = 3,\ P_{m\neq 2}(0) = U_{m\neq 2}(0) = 0,\ MT_p\,(\eta = 1, 0) = 0.03,\ MT_p\,(\eta \neq 1, 0) = 0,\ C_1 = 0.02,\ C_2 = 0.02$.

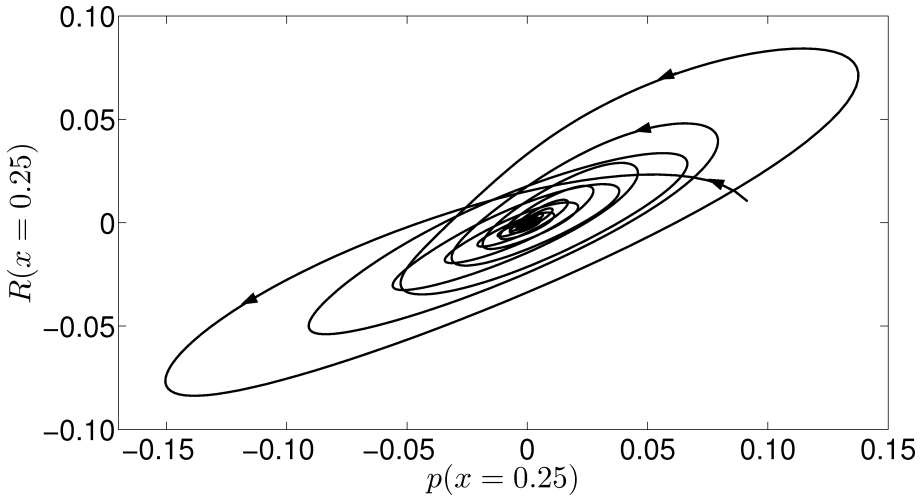

Figure 2.13: The phase portrait of the acoustic pressure and unsteady burn rate at x = 0.25 from the linear simulation. $U_2(0) = 3,\ P_2(0) = 3,\ P_{m\neq 2}(0) = U_{m\neq 2}(0) = 0,\ MT_p\,(\eta = 1, 0) = 0.03,\ MT_p\,(\eta \neq 1, 0) = 0,\ C_1 = 0.02,\ C_2 = 0.02.$

disturbance energy among the modes, while in the linearised case, the energy can only get transferred to the base flow leading to the eventual decay of the acoustic oscillations. The same picture is shown in the phase space plot in Fig. 2.13. The trajectory from the linear evolution ends in a stable focus showing classical linear stability. On the other hand, in Fig. 2.14, which is obtained from nonlinear simulation, the trajectory ends in a limit cycle eventually. A plot of acoustic energy (Fig. 2.15) shows that the linear and nonlinear simulations initially show a similar qualitative behaviour and after some time they both diverge, leading to a qualitatively different dynamical behaviour.

The second route is by non-normal transient growth. Here even if one starts with a finite small amplitude suitable initial condition, transient growth due to the non-normal nature of the system makes the oscillation grow even for a system stable according to linear stability theory. The transient growth leads to large amplitude oscillations, which cause the nonlinear terms to play dominant roles and 'direct interaction' of eigenmodes occur. Fig. 2.16(*a*) shows the comparison of acoustic energy evolution with linear and nonlinear simulations. The transient growth in the linear simulation decays eventually, while the nonlinear simulation leads to a limit cycle. The higher transient growth in the linear simulation than that in the nonlinear one is due to the damping effect from the nonlinear terms. Here, the initial condition is chosen to be the optimum initial condition for the maximum transient growth ($\chi\,(0) = V_{opt}$) to show the importance of this route

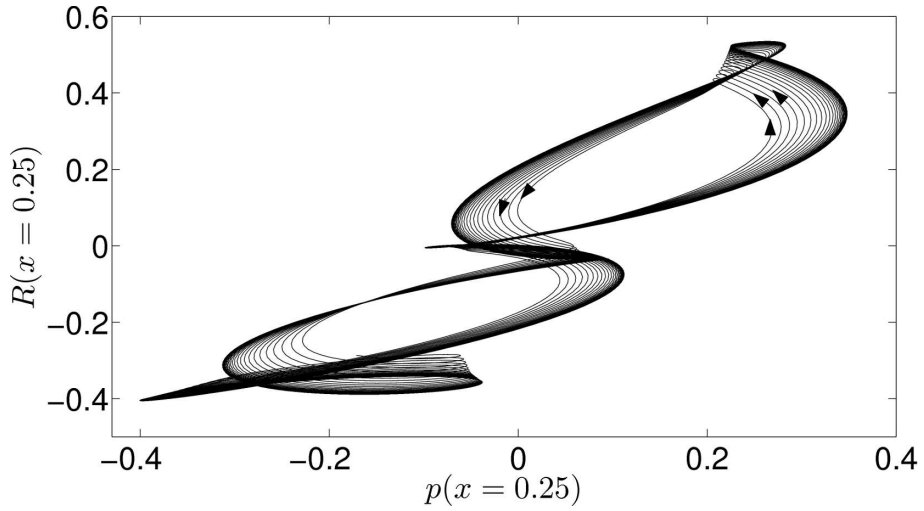

Figure 2.14: The phase portrait of the acoustic pressure and unsteady burn rate at x = 0.25 (near the limit cycle) from the nonlinear simulation $U_2(0) = 3,\ P_2(0) = 3,\ P_{m\neq 2}(0) = 0,\ U_{m\neq 2}(0) = 0,\ MT_p\,(\eta = 1, 0) = 0.03,\ MT_p\,(\eta \neq 1, 0) = 0,\ C_1 = 0.02,\ C_2 = 0.02.$

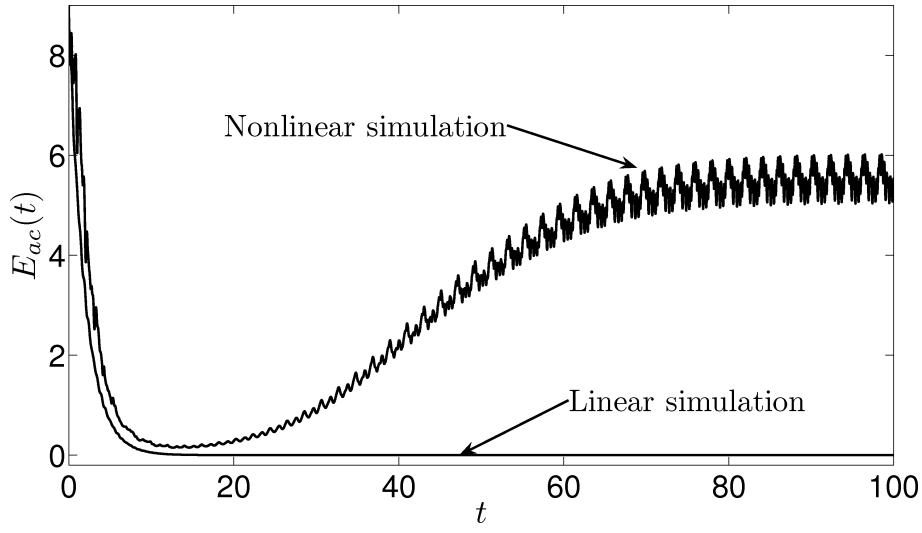

Figure 2.15: The evolution of acoustic energy $\left(E_{ac}\,(t) = \sum_{m=1}^{N}\left(U_m^2 + P_m^2\right)\right)$ from linear and nonlinear simulations. $U_2(0) = 3,\ P_2(0) = 3,\ P_{m\neq 2}(0) = U_{m\neq 2}(0) = 0,\ MT_p\,(\eta = 1, 0) = 0.03,\ MT_p\,(\eta \neq 1, 0) = 0,\ C_1 = 0.02,\ C_2 = 0.02.$

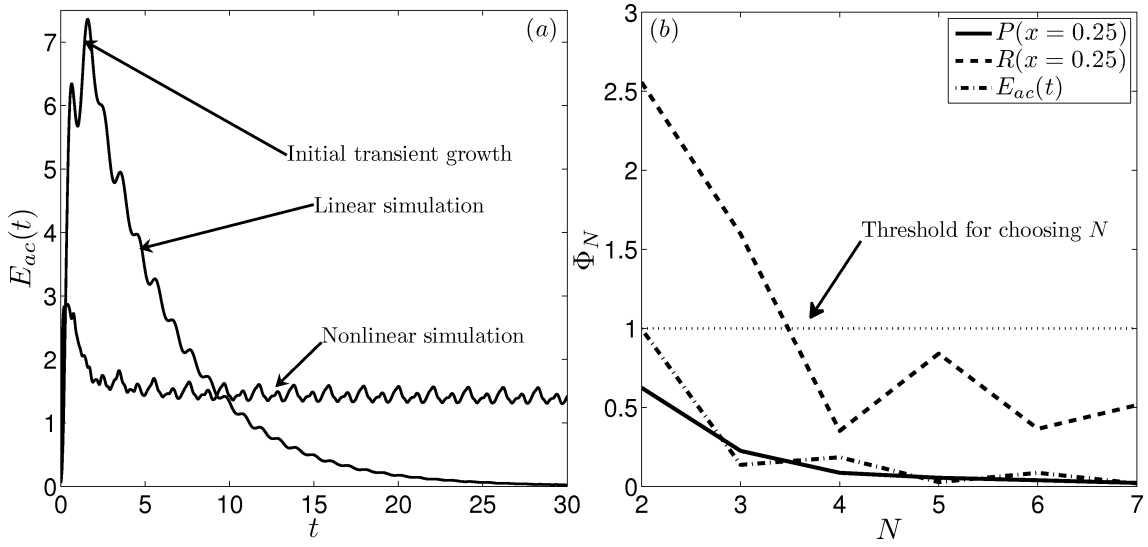

Figure 2.16: *a*) The evolution of acoustic energy $\left(E_{ac}(t) = \sum_{m=1}^{N}(U_m^2 + P_m^2)\right)$ with optimum initial condition $\chi(0) = V_{opt}$, $C_1 = 0.03$, $C_2 = 0.02$. *b*) Convergence study for the previous figure with *N*. Note that, $\Phi_N = \sqrt{\sum_{i=1}^{I}\left(\left(\phi_N(t_i) - \phi_{N-1}(t_i)\right)/\phi_N(t_i)\right)^2} \times 100$ is the measure used for studying the convergence of the simulations. Moreover, Φ_N represents any one of the variables $P(x = 1/4)$, $R(x = 1/4)$ & E. The summation index '*i*' represents the value of the variables at the i^{th} time step in the numerical simulation. The threshold of Φ_N is chosen as 1% for convergence of the solution, which corresponds to *N*=5 in the present case.

to triggering. Also note that the initial acoustic energy $(E_{ac}(t=0) = 6.4 \times 10^{-4})$ is very small compared with that in Fig. 2.15 $(E_{ac}(t=0) = 8.43)$.

A convergence study is performed to evaluate the number of Galerkin modes used for the above simulations. Fig. 2.16(*b*) shows the plot between percentage change (Φ_N) in the results of $P(x = 1/4)$, $R(x = 1/4)$ and E for various values of '*N*'. It is found that for a threshold of 1% change in the solution variables, *N*=5 is sufficient. The non-dimensionalised dominant Fourier frequency of the acoustic pressure during limit cycle corresponding to Fig. 2.16(*a*) is 0.48, which is very close to the fundamental frequency for the corresponding to a pipe, closed at both the ends. The non-dimensional frequency in Fig. 2.16(*a*) corresponds to 66.25 *Hz* for the SRM configuration given in table 2.1.

Transient growth is quantified in a particular measure (Section 2.4). In this chapter, generalized disturbance energy $E_T(t)$ (defined to include the contribution of energy in the disturbance from the degrees of freedom associated with the unsteady burn rate, see

Section 2.6) is used as a measure to quantify non-normality of the system. Transient growth from the present simulation can be observed and compared with the experiments, when $E_T(t)$ is measured. It is very difficult to devise an experiment to measure $E_T(t)$ in an SRM. The existing experiments with SRM (Blomshield *et al.*, 1997*a*,*b*; Harris and Champlain, 1998) measured only the acoustic pressure at the head end of the motor. Therefore, it is difficult to have one-to-one comparison of transient growth of thermoacoustic oscillations in SRM from the available experimental acoustic pressure data with the present simulation.

2.7.5 Bootstrapping

Bootstrapping is a phenomenon, where the dominant frequency of a system changes during the dynamical evolution of the system. This phenomenon is observed in SRMs (Yoon *et al.*, 2001). Yoon *et al.* (2001) attributed this phenomenon to the nonlinearity alone. This is due to the transfer of energy among the modes by either nonlinear coupling or non-orthogonality of eigenmodes. The phenomenon of bootstrapping is discussed in the context of turbulence (Gebhardt and Grossmann, 1994) and thermoacoustic system (Yoon *et al.*, 2001; Balasubramanian and Sujith, 2008*a*,*b*). An *ad hoc* acoustic velocity – combustion coupling model is used to simulate the observed behaviour in Rijke tube (Yoon *et al.*, 2001; Balasubramanian and Sujith, 2008*b*), whereas in Balasubramanian and Sujith (2008*a*), it comes by actually solving the unsteady equations for a ducted diffusion flame.

The initial condition (t=0) is chosen as given in Fig. 2.17. The system, which is stable according to the classical linear stability theory, is excited in the second Galerkin mode and the evolution of the other Galerkin modes is tracked. Fig. 2.17(*a*-*e*) shows the evolution of the individual Galerkin pressure modes. Initially, the projection on the second mode decays and transfers the energy to the first mode (Fig. 2.17*a* & *b*). After some time, the first mode grows to sufficient extent, transferring the energy back to the second mode causing it also to grow.

The time evolution of acoustic pressure at x = 0.25 plotted in Fig. 2.17(*f*) shows that the pressure amplitude decreases initially and then, after some time, it increases by

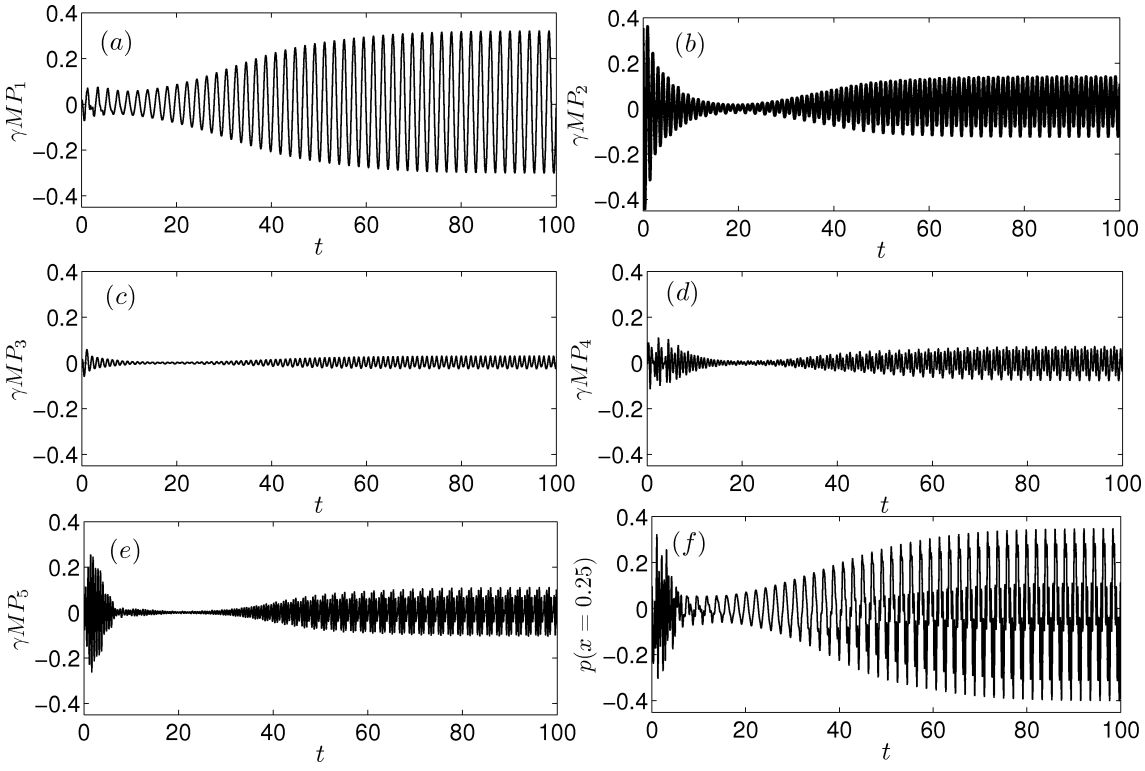

Figure 2.17: The evolution of Galerkin pressure modes *a*) first mode, *b*) second mode, *c*) third mode, *d*) fourth mode, e) fifth mode, *f*) acoustic pressure at $x = 0.25$, $U_2 = 3.0,\ P_2 = 3.0,\ P_{m\neq 2}(0) = U_{m\neq 2}(0) = 0,\ MT_p\,(\eta, 0) = 0,\ C_1 = 0.02,\ C_2 = 0.02$.

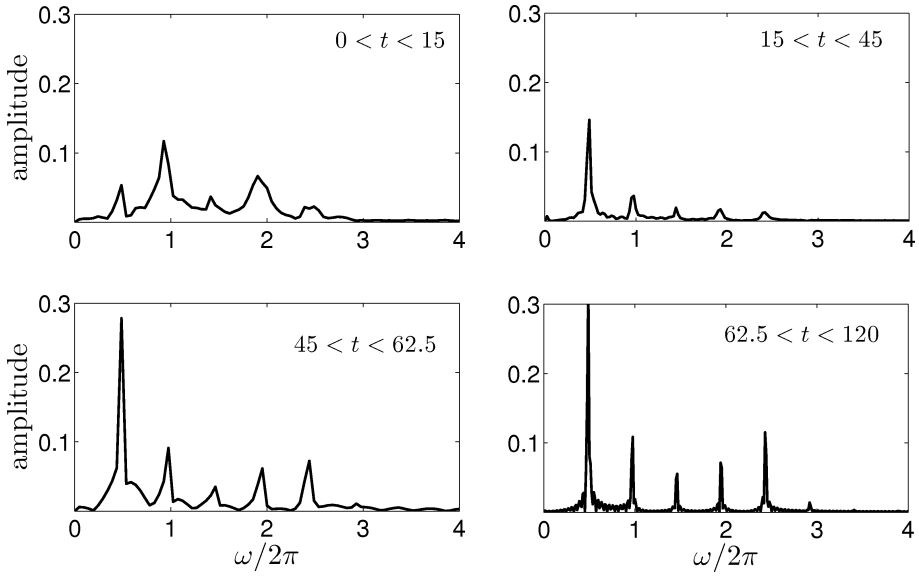

Figure 2.18: The Fourier transform of acoustic pressure at $x = 0.25$ during different time intervals, $U_2 = 3.0,\ P_2 = 3.0,\ P_{m\neq 2}(0) = U_{m\neq 2}(0) = 0,\ MT_p\,(\eta, 0) = 0,\ C_1 = 0.02,\ C_2 = 0.02$.

the modal energy transfer. The plot of the fast Fourier transform (FFT) of the acoustic pressure (Fig. 2.18) illustrates this phenomenon. For $0<t<15$, the second and fourth eigenmodes are the dominant ones, which decay as time evolves. In $15<t<45$, the first eigenmode grows because of the energy transfer from the second and fourth modes. Then, the first eigenmode transfers energy back to the second and fourth eigenmodes ($45<t<62.5$) causing them to grow again. In the end ($62.5<t<120$), there are higher harmonics due to the energy transfer to higher eigenmodes. The dominant frequencies present in the system in the limit cycle are close to the natural acoustic frequency of a closed-closed duct. A crucial difference is that the past analyses have demonstrated bootstrapping in acoustic velocity – combustion coupling systems (Yoon *et al.*, 2001; Balasubramanian and Sujith, 2008*a*,*b*), whereas the present analysis used the acoustic pressure – combustion coupling model.

2.8 Interim summary

A thermoacoustic stability analysis of a solid rocket motor is performed with emphasis on the following. First, the non-orthogonality of the eigenmodes is accounted for incorporating the mean flow (convection) effects in the acoustic equations. The classical linear stability theory predicts stability, which is valid only in the asymptotic time limit. For non-normal systems, the short term behaviour can be completely different from the prediction by the classical linear stability theory for some initial conditions. The transient dynamics of the unsteady propellant burn rate are included instead of the *ad hoc* response models used in the earlier analysis. The acoustic and burn rate equations are solved simultaneously.

In the present case, burn rate equations are solved for a homogeneous propellant. The inclusion of a differential equation in time for the unsteady burn rate leads to an increase in the degrees of freedom of the system. Therefore, the growth or decay of oscillations is quantified by a 'generalized disturbance energy', which includes the acoustic energy and the unsteady energy in the propellant. The same energy is related to the 2-norm of the state space vector that shows a transient growth because of the non-normal nature of the system. The optimum initial condition for maximum transient growth in-

dicates large contribution from the unsteady burn rate modes. The use of a burn rate response function would have not captured this observation, because it neglects transients in burn rate modes. Using this model, exponential and pulsed instabilities are simulated.

In the past, pulsed instability is simulated only by using *ad hoc* response functions, which are not physics based. Moreover, in the present case, pulsed instabilities are simulated with burn rate pressure coupling as against the burn rate velocity coupling used in the earlier analysis. Pulsed instabilities can occur in two ways. First, is by introducing a large pulse into the system where nonlinearities are important, leading to a limit cycle. Second, is through a small initial condition in the appropriate direction that causes transient growth. As the amplitude of the oscillation increases, nonlinear terms can then contribute, leading to limit cycle. Finally, other observed phenomena such as dominant frequency switching during the dynamical evolution of the system and 'bootstrapping' are also demonstrated. In summary it is essential to include all the dynamics in the propellant response and the non-orthogonality of eigenmodes to predict instabilities more accurately in solid rocket motors. The system is no longer purely acoustic, but an extended one that degrees of freedom in the combustion dynamics.

2.9 Outlook

There are three issues that need to be addressed in the above analysis. They are listed as follows. The first and most important is performing experiments in SRM in order verify the above conclusions regarding transient growth. A time resolved measurement for the state space variables (χ) is difficult. Further, the coupling between the acoustic field Eqn. (2.3) and the heat source (burn rate equation, 2.16) is performed phenomenologically without mathematical rigor. This forms the second issue. The third is that the generalised disturbance energy (E_T) derived in Section 2.6 is also phenomenological, as the coupling is not obtained with mathematical rigor. The amount of transient growth obtained depends on the weight factors associated with the acoustic and burn rate variables in the disturbance energy. In order to resolve the above mentioned issues, analysis is performed in a simpler thermoacoustic system: Rijke tube. The next chapter deals

with the description of a theoretical framework to analyse thermoacoustic interaction in the Rijke tube system. The equations governing the acoustic field and the heat source are obtained from the conservation equations of fluid flow with mathematical rigor.

CHAPTER 3

Modeling the thermoacoustic interaction in a Rijke tube

3.1 Introduction

Rijke tube is a simple thermoacoustic device, but has much of the essential physics of thermoacoustic interaction. Rijke tube is an acoustic resonator tube, with a heat source (in the present case, an electrical heater). The heat source is positioned at some axial location as shown by the configuration of a horizontal Rijke tube in Fig. 3.1.

Thermoacoustic instability of the Rijke tube has been studied for a long time. Rijke tube oscillations were first observed by Rijke (1859). He used a vertical tube with a coiled electrical heating filament as the heat source. Self-sustained thermoacoustic oscillations were observed when the heater was positioned at some axial location of the tube and beyond some threshold power level. Rijke gave an explanation based on the pressure pulse generated due to volumetric expansion of the fluid near the heater zone. However, this argument did not explain the fact that instabilities were observed only for some selected range of heater locations. Carvalho *et al.* (1989) employed a linear model for the unsteady heat release rate to calculate the stability of the modes. They applied Rayleigh criteria (Rayleigh, 1878) and predicted the axial locations of the heater for which the thermoacoustic oscillations are unstable. However, the above model (Carvalho *et al.*, 1989) for the heat source is valid only for small acoustic velocity fluctuations. The stability thus predicted is the linear stability of the system.

For a linearly unstable system, the oscillations grow exponentially as predicted by the linear stability theory for small amplitudes of oscillations and eventually reach a limit cycle due to nonlinearities in the heat release rate response of the heater. Nonlinearities in the acoustic field do not contribute to the dynamical evolution of the system as the Mach number $(M \sim 10^{-3})$ of the steady state flow is very low (Culick, 2006). Linear stability theory was further applied to analyse thermoacoustic instability in configurations with multiple heat sources and complex geometries (Bittanti *et al.*, 2002).

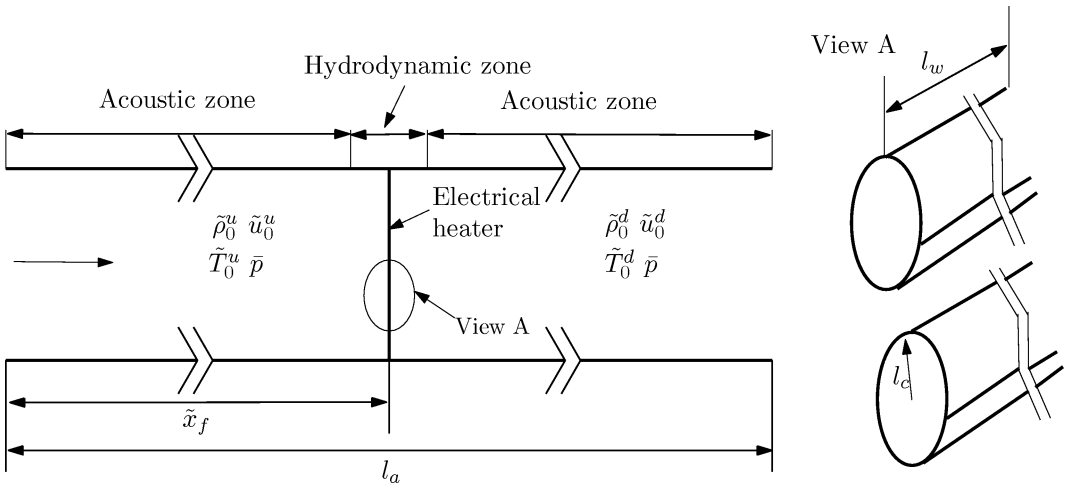

Figure 3.1: Configuration of the Rijke tube showing the acoustic and hydrodynamic zones

Recently, Heckl and Howe (2007) used Green's function technique to determine the occurrence of thermoacoustic oscillations in a ducted premixed flame.

Estimation of the amplitude of acoustic oscillations during limit cycle is important from the design point of view for gas turbines (Zinn and Lieuwen, 2006). In order to achieve this, the nonlinearity in the heat release rate response of the heater has to be accounted for in the model. The nonlinear response of the heater can be determined by solving the governing equations for the fluid flow over the electrical heater, using computational fluid dynamics (CFD) technique. On the other hand for low dimensional modeling, the nonlinear response of the heat source can be obtained from a correlation of the heat transfer between the heater and the local flow velocity (Heckl, 1990). The response of the heat source thus obtained can be considered as a source of acoustic energy, thus coupling the chamber acoustic field with the heat source (Poinsot and Veynante, 2005).

A CFD based analysis was also used to study Rijke tube oscillations. The earliest one was performed by Kwon and Lee (1985). They determined the stability curve for various mean flow rates. Hantschk and Vortmeyer (1999) numerically investigated thermoacoustic oscillations by considering the heat source to be a heated flat plate. They obtained the amplitude and frequency of the thermoacoustic oscillations during limit cycle. Kopitz and Polifke (2008) used Nyquist criterion along with CFD to determine the stability of the system. Nyquist criterion has the advantage of being applicable to

complex geometries and non-compact heat sources. Recently, Moeck *et al.* (2009) have numerically investigated thermoacoustic instabilities with the heating source being a flat flame and compared the numerical results with those of experiments.

This extensive analytical and numerical analysis for thermoacoustic instability of a Rijke tube are supplemented by experiments. Matveev and Culick (2003*b*) and Song *et al.* (2006) performed experiments in a horizontal Rijke tube with a mesh-type electrical heating element. The acoustic pressure oscillations were monitored and limit cycle amplitudes were obtained. For low values of the heater power, the system was stable. As the heater power was increased, the system became linearly unstable and eventually reached a limit cycle.

All the investigations in the analysis of thermoacoustic instability in a Rijke tube described above except Moeck *et al.* (2009) have used either a response function or solved the Navier-Stokes and energy equations for fluid flow by CFD to obtain the dynamics of the heat source. They assumed a compact heat source (the size of the heat source along the length of the tube is small compared to the acoustic wavelength) and coupled the unsteady heat release rate to the acoustic energy equation as a source. In the above method, the coupling between the chamber acoustic field and the unsteady heat release rate was not obtained with mathematical rigor. Furthermore, there were two systems of equations involved in the problem; one for the acoustic length scale and the other for the length scale of the heat source. They were written and used without mathematical justification. In a rigorous analysis, the above two systems of equations have to be derived from the conservation equations of fluid flow by performing the asymptotic analysis.

Wu *et al.* (2003) have pioneered the application of asymptotic expansions to analyse combustion instabilities. They analysed the amplification of sound waves, when a flame propagates in a gravity field. Separate systems of equations for acoustic field and flame zones were derived, by performing the asymptotic analysis on the conservation equations. They have performed linear stability analysis for the acoustic-flame coupling, followed by a weakly nonlinear theory for the Darrieus-Landau mode of instability of the flame and the acoustic field. The paper explained the experimental observation of the transition from curved to flat flame during instability. Moeck *et al.* (2007) have

also performed the asymptotic analysis to investigate thermoacoustic instability in a Rijke tube with flame as the heat source. They obtained with mathematical rigor the correct systems of equations and the coupling between the acoustic field and the heat source. The presence of an additional global-acceleration term in the momentum equation of the hydrodynamic zone was also observed. Furthermore, they concluded that since one dimensional (1D) equations are used in the hydrodynamic zone for their analysis, the above term vanishes, leaving the conventional momentum equation intact in the hydrodynamic zone. The unsteady heat release rate from the flame may be due to the equivalence ratio fluctuations at the inlet of the hydrodynamic zone, which in turn may be caused by the acoustic velocity at the location of the flame (Moeck *et al.*, 2007). Recently, Wu and Moin (2010) investigated the generation of acoustic waves from premixed flame due to freestream enthalpy fluctuations, using asymptotic analysis. A vigorous subharmonic parametric instability was observed at moderate levels of enthalpy fluctuations.

In the present paper, an investigation of the thermoacoustic instability in an electrically heated Rijke tube is performed starting from the governing equations of fluid flow. An asymptotic analysis (Zeytounian, 2002; Ting *et al.*, 2007) is then performed in the limit of a compact heat source and zero Mach number of the steady flow to obtain two systems of equations: one governing the acoustic field and the other governing the unsteady flow and heat transfer near the heat source. The separation of equations for the acoustic field and heater (hydrodynamic zone, see Fig. 3.1) occurs. The coupling between the above two systems of equations is obtained. Also, the additional global-acceleration term, as obtained by Moeck *et al.* (2007, 2009), appears in the momentum equation for the hydrodynamic zone. It is also found in the present investigation that the presence of global-acceleration term has serious consequences for the bifurcation diagram. The nonlinear evolution equations obtained from the asymptotic analysis in both acoustic and hydrodynamic zones are solved simultaneously. The limit cycle amplitudes are obtained, which are required to estimate the tolerance limit of the realistic combustors (Zinn and Lieuwen, 2006) during instability.

3.2 Governing equations

The Rijke tube configuration considered here has a length $_a$ with the heater positioned at an axial location $\tilde{x}_f$ (Fig. 3.1). A mean flow is maintained in the tube at a desired flow rate using a blower. The electrical resistance heater, which acts as a heat source is made up of a thin wire of radius l_c strung around the heater frame. The effective length of the wire filament, which participates in the heat transfer to the fluid flow, is l_w. The typical length of the duct (l_a) is around 1m and the dimension of the heater along the axial direction of the tube (thickness, l_c) is around 1mm. The thickness of the heater is very small compared to the length scale of the acoustic field. Hence, the heater can be assumed to be compact compared to the acoustic field in the tube. The zone around the heat source is termed as the hydrodynamic zone. Acoustic and hydrodynamic zones are schematically shown in Fig. 3.1.

The length of the hydrodynamic zone in the axial direction is of the order of the thickness of the heater. Hence the hydrodynamic zone can also be assumed to be compact compared to the acoustic field. The heater heats the flow and creates a temperature rise across the heater. Since the heater is compact, piecewise constant steady flow properties can be assumed on either side of the heater (Kaufmann *et al.*, 2002). The Mach number of the flow is $O(10^{-3})$, which leads to a negligible steady state pressure loss. Hence the steady state pressure is assumed to be constant along the duct. All upstream steady state variables are known and specifying any one downstream steady state variable, such as density (obtained by solving the steady state version of the equations governing the hydrodynamic zone, which are described in Section 3.4.2), is enough to compute the other steady state variables from the following ideal gas and steady state continuity equations:

$$\tilde{\rho}_0^d = \frac{\tilde{\rho}_0^u \tilde{T}_0^u}{\tilde{T}_0^d},\ \tilde{u}_0^d = \frac{\tilde{\rho}_0^u \tilde{u}_0^u}{\tilde{\rho}_0^d} \tag{3.1}$$

where superscripts 'u' and 'd' represent upstream and downstream variables, subscript '0' represents steady variables and '$\sim$' indicates dimensional variables. The governing equations are

$$\frac{\partial \tilde{\rho}}{\partial \tilde{t}} + \tilde{\nabla} \bullet (\tilde{\rho}\tilde{u}) = 0 \tag{3.2a}$$

$$\tilde{\rho}\left(\frac{\partial}{\partial\tilde{t}}+\tilde{u}\bullet\tilde{\nabla}\right)\tilde{u}+\nabla\tilde{p}=\mu\left(\tilde{\nabla}^2+\frac{1}{3}\tilde{\nabla}\left(\tilde{\nabla}\bullet\right)\right)\tilde{u} \tag{3.2b}$$

$$\frac{1}{\gamma}\left(\frac{\partial}{\partial\tilde{t}}+\tilde{u}\bullet\tilde{\nabla}\right)\tilde{p}+\tilde{p}\nabla\bullet\tilde{u}=\frac{(\gamma-1)}{\gamma}k\tilde{\nabla}^2\tilde{T} \tag{3.2c}$$

Non-dimensionalising the above equations using the following scales $\rho=\tilde{\rho}/\bar{\rho},\ p=\tilde{p}/\bar{p},\ u=\tilde{u}/\bar{u},\ T=\tilde{T}\Big/\bar{T},\ x=\tilde{x}/l_a,\ t_a=\tilde{t}/(l_a/c_0)$, where $\bar{p}=\tilde{p}_0^u=\tilde{p}_0^d,\ \bar{\rho}=\tilde{\rho}_0^u,\ \bar{T}=\bar{p}/(\Re\bar{\rho}),\ \bar{u}=\tilde{u}_0^u,\ c_0=\sqrt{\gamma\Re\bar{T}},\ \Re$ is the specific gas constant and c_0 is the local speed of sound, which leads to

$$\frac{\partial\rho}{\partial t_a}+M\nabla_a\bullet(\rho u)=0 \tag{3.3a}$$

$$\rho\left(\frac{\partial}{\partial t_a}+Mu\bullet\nabla_a\right)u+\frac{1}{\gamma M}\nabla_a p=\frac{M}{Re_a}\left(\nabla_a^2+\frac{1}{3}\nabla_a\left(\nabla_a\bullet\right)\right)u \tag{3.3b}$$

$$\frac{1}{\gamma}\left(\frac{\partial}{\partial t_a}+Mu\bullet\nabla_a\right)p+Mp\nabla_a\bullet u=\frac{M}{Pe_a}\nabla_a^2T \tag{3.3c}$$

where $Re_a=\bar{\rho}\bar{u}l_a/\mu,\ Pe_a=\bar{\rho}\bar{u}l_aC_p/k,\ M=\bar{u}/c_0$ and subscript 'a' indicates that non-dimensionalisation is performed with the acoustic length scale $_a$.

An analysis of thermoacoustic instability in a Rijke tube involves the study of a coupled system which consists of the acoustic field in the tube and the unsteady heat transfer from the heat source (hydrodynamic zone). Therefore, it is important to track variations on the length scale of the tube (acoustic scale, $l_a\sim 1m$) and the length scale of the radius of the heater wire filament ($l_c\sim 1mm$) in the hydrodynamic zone. Furthermore, the acoustic time scale $t_{ac}=l_a/c_0$ and the wire heat transfer time scale $t_{cc}=l_c/\bar{u}$ are of the same order for typical values mentioned above. This leads to an effective coupling of the dynamics of the acoustic field and the unsteady heat release rate.

The length and time scale ratios are defined as $\delta=l_c/l_a,\ \varepsilon=t_{ac}/t_{cc}=M/\delta\sim 1$. The system has two length scales separated by a large factor $(1/\delta\to\infty)$ and a single time scale. Since the flow is at very low Mach number ($M\to 0$), the system of equations (Eqn. 4.3) becomes ill-conditioned (Anderson, 2001). Moreover, a smaller grid size near the heater will restrict the maximum timestep that can be allowed for the numerical scheme. All these make Eqn. (4.3) stiff. As a consequence, solving the

problem using the CFD technique is a difficult task. An alternative technique available to solve such a two length-scale problem is asymptotic analysis (Zeytounian, 2002; Ting *et al.*, 2007), which is used in the present paper and is discussed in the next section.

3.3 Asymptotic analysis

In the present investigation, asymptotic analysis is performed in the limit: $M \to 0,\ \varepsilon \sim 1,\ \delta \to 0$. The flow variables are expanded in powers of Mach number (M). The following ansatz for the flow variables is used:

$$\begin{aligned} &\rho = \rho_s + \rho_c + M\rho_a,\ u = u_s + u_a + u_c, \\ &p = 1 + Mp_a + M^2 p_c,\ T = T_s + T_c + MT_a \end{aligned} \tag{3.4}$$

where subscript 's' stands for steady state variables, 'a' for fluctuations due to the acoustic field and 'c' for fluctuations in the hydrodynamic zone. Here, the acoustic fluctuations exist all along the tube, while the fluctuations due to the heater are confined to a zone around the heater (hydrodynamic zone), which is small compared to the acoustic length scale. Hence the variables with subscript 'a' exist over the length of the tube (acoustic zone, see Fig. 3.1), while the variables with subscript 'c' exists only in the region around the heater (hydrodynamic zone, see Fig. 3.1) and vanishes as one moves away from it. It is important to note that the form of the power series used in ansatz (4.4) are different for various flow variables and the reason is as following.

The acoustic fluctuations in u are zeroth order in M, whereas the fluctuations in $\rho,\ p,\ T$ are first order in M. This is in agreement with the experimental observations and theoretical formulations (Rienstra and Hirschberg, 2004). On the other hand, temperature fluctuations near the heater (hydrodynamic zone) are comparable to the steady state temperature T_s and hence T_c appears as a zeroth order fluctuation (Fu and Tong, 2002). The mode of heat transfer from the heater to the gas is by convection. Hence the zeroth order fluctuation T_c in temperature (T) is caused by a zeroth order fluctuation u_c in velocity (u). Because of zeroth order temperature fluctuations (T_c) and a constant leading order pressure (Eqn. 4.4), a zeroth order fluctuation of density (ρ_c) in

the hydrodynamic zone is present[†]. Furthermore, the fluid properties are assumed to be independent of temperature. Now the ansatz (Eqn. 4.4) is substituted in Eqn. (4.3) to get the following:

$$\frac{\partial}{\partial t_a}\left(\rho_s+\rho_c+M\rho_a\right)+M\nabla_a\bullet\left(\left(\rho_s+\rho_c+M\rho_a\right)\left(u_s+u_a+u_c\right)\right)=0 \tag{3.5a}$$

$$\left(\rho_s+\rho_c+M\rho_a\right)\left(\frac{\partial}{\partial t_a}+M\left(u_s+u_a+u_c\right)\bullet\nabla_a\right)\left(u_s+u_a+u_c\right) +\frac{1}{\gamma M}\nabla_a\left(1+Mp_a+M^2p_c\right)=\frac{M}{Re_a}\left(\nabla_a^2+\frac{1}{3}\nabla_a\left(\nabla_a\bullet\right)\right)\left(u_s+u_a+u_c\right) \tag{3.5b}$$

$$\frac{1}{\gamma}\left(\frac{\partial}{\partial t_a}+M\left(u_s+u_a+u_c\right)\bullet\nabla_a\right)\left(1+Mp_a+M^2p_c\right) +M\left(1+Mp_a+M^2p_c\right)\nabla_a\bullet\left(u_s+u_a+u_c\right)=\frac{M}{Pe_a}\nabla_a^2\left(T_s+T_c+MT_a\right) \tag{3.5c}$$

Initially equations which are of zeroth order in M are obtained. Then, first order equations in M are obtained using the solutions from the zeroth order equations. This process is repeated until governing equations for all the variables in the ansatz (Eqn. 4.4) are obtained. Furthermore, the system of equations for various orders of M is written both for the acoustic and hydrodynamic zones. In the following analysis, equations governing the acoustic zone are first derived and the same exercise is repeated for the hydrodynamic zone.

3.3.1 Continuity equation: acoustic zone $O(M)$

The zeroth order continuity equation in M reduces to the steady state equation, which is already used in the analysis (Eqn. 4.1). Collecting terms of first order in M, the Eqn. (3.6) is obtained. Since the non-dimensionalisation is performed with respect to the acoustic length scale for Eqn. (4.2), Eqn. (3.6) represents continuity equation in the acoustic zone.

$$\frac{\partial\rho_a}{\partial t_a}+\nabla_a\bullet\left(\left(\rho_s+\rho_c\right)\left(u_s+u_a+u_c\right)\right)=0 \tag{3.6}$$

[†]The authors are grateful to an anonymous reviewer for pointed out the errors of the constant density assumption adopted in an earlier version of the analysis. The asymptotic analysis is reformulated with the variable density formulation as per the suggestions of the reviewer.

Furthermore, using the continuity equation for steady state in the acoustic zone, $\nabla_a \bullet (\rho_s u_s) = 0$, $\rho_c = 0$ and $u_c = 0$ as described in the ansatz (Eqn. 4.4), Eqn. (3.6) becomes

$$\frac{\partial \rho_a}{\partial t_a} + \nabla_a \bullet (\rho_s u_a) = 0 \tag{3.7}$$

3.3.2 Momentum equation: acoustic zone $O(M)$

In equation (3.5b), as M is in the denominator of the pressure term, the entire equation is multiplied by M to obtain,

$$\begin{aligned} &\left(M(\rho_s + \rho_c) + M^2 \rho_a\right) \left(\frac{\partial}{\partial t_a} + M\left(u_s + u_a + u_c\right) \bullet \nabla_a\right) \left(u_s + u_a + u_c\right) \\ &+ \frac{1}{\gamma} \nabla_a \left(1 + M p_a + M^2 p_c\right) = \frac{M^2}{Re_a} \left(\nabla_a^2 + \frac{1}{3} \nabla_a \left(\nabla_a \bullet\right)\right) \left(u_s + u_a + u_c\right) \end{aligned} \tag{3.8}$$

The zeroth order equation in M gives a zero spatial gradient for the steady state pressure in the system, i.e. $\nabla_a(1) = 0$, where '1' appears due to non-dimensionalisation of $\tilde{p}$ with $\bar{p}$. The condition for constant $\bar{p}$ along the duct is already included in the analysis (Eqn. 4.1). Gathering $O(M)$ terms from Eqn. (3.8) in the limit $Re_a \to \infty$, leads to the momentum equation in the acoustic zone.

$$\rho_s \frac{\partial u_a}{\partial t_a} + \frac{1}{\gamma} \nabla_a p_a = 0 \tag{3.9}$$

3.3.3 Energy equation: acoustic zone $O(M)$

The zeroth order terms from Eqn. (3.5c) represent the steady state energy equation. Since the upstream ($\tilde{T}_0^u$) steady state temperature is known, steady state equations governing the heat transfer from the heater are used to obtain the corresponding downstream value ($\tilde{T}_0^d$) thus making the collection of $O(1)$ terms from Eqn. (3.5c) redundant. Now the $O(M)$ terms are gathered to obtain the acoustic energy equation:

$$\frac{1}{\gamma} \frac{\partial p_a}{\partial t_a} + \nabla_a \bullet u_a = \frac{1}{Pe_c \delta} \nabla_c^2 T_c \tag{3.10}$$

where $Pe_c = \bar{\rho}\bar{u}l_c C_p/k$. The unsteady heat release rate from the heater is delivered into the acoustic zone by local thermal conduction. Hence, the last term in Eqn. (3.10) represents the coupling term from the hydrodynamic to the acoustic zone. Assuming one dimensional acoustic field in the axial direction 'x_a', equation (3.10) is integrated over the cross-sectional area (S_c) of the tube. In order to convert from 3D to 1D space, the terms with gradients (∇_a) in the acoustic length scale are replaced by $\partial/\partial x_a$ in Eqn. (3.10). The acoustic energy equation takes the following form.

$$S_c\left(\frac{1}{\gamma}\frac{\partial p_a}{\partial t_a}+\frac{\partial u_a}{\partial x_a}\right)=\frac{1}{Pe_c\delta}\left(\iiint_{V_c}\nabla_c^2 T_c d\tilde{V}_c\right)\widehat{\delta}\left(\tilde{x}-\tilde{x}_f\right) \tag{3.11}$$

where V_c is the volume of the hydrodynamic zone and $\widehat{\delta}(x)$ is the Dirac-delta function, which is used to indicate the compactness of the hydrodynamic zone in the equations. The volume integral is converted into surface integral using Gauss's divergence theorem. In order to apply the above theorem, the last term in Eqn. (3.11) is dimensionalised, followed by the application of Gauss divergence theorem and again non-dimensionalised back to get the following acoustic energy equation,

$$\frac{1}{\gamma}\frac{\partial p_a}{\partial t_a}+\frac{\partial u_a}{\partial x_a}=\frac{l_w l_c}{Pe_c S_c}\left(\int_0^{2\pi}\left(-\nabla_c T_c\right)_{\hat{e}_r}d\theta\right)\widehat{\delta}\left(x-x_f\right) \tag{3.12}$$

where l_w is the length of the wire which contributes to the heat transferred to the fluid, $\hat{e}_r$ is the unit vector along the radial direction from the cylinder surface, $(\nabla_c T_c)_{\hat{e}_r}$ represents the component of gradient of T_c along $\hat{e}_r$. The term on the right hand side of Eqn. (3.12) is identified as the coupling term from hydrodynamic zone to the acoustic zone, which drives the acoustic oscillations in a Rijke tube. The unsteady heat release rate from the hydrodynamic zone is given by $q = (l_w l_c/Pe_c S_c)\left(\int_0^{2\pi}\left(-\nabla_c T_c\right)_{\hat{e}_r}d\theta\right)$ with the integral evaluated over surface of the cylinder. The equations governing the acoustic zone are thus obtained and the coupling of the acoustic field with the unsteady heat release rate of the heater appears from the asymptotic analysis. The equations for the hydrodynamic zone are derived in the following subsections.

3.3.4 Continuity equation: hydrodynamic zone $O(1)$

In order to obtain the equations with respect to the hydrodynamic zone, the spatial derivatives in the acoustic length scale (l_a) have to be converted to the length scale (l_c) of the heater, only for variables with subscript 'c'. The transformation $\nabla_a = \nabla_c/\delta$ is applied to Eqn. (3.5). The subscript 'c' in ∇ operator represents the derivatives that are non-dimensionalised with $_c$. During the scale change from l_a to l_c, terms which are second order in M, for e.g. $M^2\nabla_a$, become first order in M, $M\varepsilon\nabla_c$. The inclusion of such terms leads to the continuity equation in the hydrodynamic zone as follows.

$$\frac{\partial}{\partial t_c}(\rho_s + \rho_c) + \nabla_c \bullet \left((\rho_s + \rho_c)\left(u_s + u_c + u_a|_{x_f}\right)\right) = 0 \tag{3.13}$$

where, $u_a|_{x_f}$ represents u_a at the non-dimensionalised heater location x_f ($x_f = \tilde{x}_f/l_a$) and $\partial/\partial t_c = (1/\varepsilon)\partial/\partial t_a$. In equation (3.13), '$\rho_s + \rho_c$' and '$u_s + u_c + u_a|_{x_f}$' appear effectively as one variable. Hence the following change of variables '$\rho_p = \rho_s + \rho_c$' and '$u_p = u_s + u_c + u_a|_{x_f}$' is applied in Eqn. (3.13) to obtain

$$\frac{\partial \rho_p}{\partial t_c} + \nabla_c \bullet (\rho_p u_p) = 0 \tag{3.14}$$

which is the conventional continuity equation for flows of variable density fluid.

3.3.5 Momentum equation: hydrodynamic zone $O(1)$

The zeroth order momentum equation in the hydrodynamic zone is as follows.

$$\begin{aligned}(\rho_s+\rho_c)\left(\frac{\partial}{\partial t_c} + \left(u_a|_{x_f} + u_s + u_c\right) \bullet \nabla_c\right)\left(u_a|_{x_f} + u_s + u_c\right) \\ + \frac{1}{\gamma}\nabla_c p_c = \frac{1}{Re_c}\left(\nabla_c^2 + \frac{1}{3}\nabla_c(\nabla_c \bullet)\right)\left(u_a|_{x_f} + u_s + u_c\right) - \frac{1}{\varepsilon}\nabla_a\left(\frac{p_a}{\gamma}\right)\Big|_{x_f}\end{aligned}$$

$$\text{Boundary condition (BC)} : u_c \to 0, \text{ as } \mathrm{x_c} \to \infty \tag{3.15}$$

where $Re_c = \bar{\rho}\bar{u}l_c/\mu$ and $\nabla_a\left(p_a/\gamma\right)|_{x_f}$ represents $\nabla_a\left(p_a/\gamma\right)$ evaluated at x_f. The equations are then written in terms of ρ_p and u_p and the acoustic momentum equation

(3.9) is used to replace the last term in Eqn. (3.15) to obtain,

$$\rho_p \left(\frac{\partial}{\partial t_c} + u_p \bullet \nabla_c \right) u_p + \frac{1}{\gamma} \nabla_c p_c = \frac{1}{Re_c} \left(\nabla_c^2 + \frac{1}{3} \nabla_c (\nabla_c \bullet) \right) u_p + \rho_s \left. \frac{\partial u_a}{\partial t_c} \right|_{x_f} \quad (3.16)$$

$$\text{BC}: \; u_p \rightarrow u_s + u_a|_{x_f} \, , \; \text{as x}_\text{c} \rightarrow \infty,$$

where $\partial u_a / \partial t_c |_{x_f}$ represents $\partial u_a / \partial t_c$ evaluated at the non-dimensional heater location x_f. The important point to be noted is that, equation (3.16) is the momentum equation for unsteady variable density flow over the heater, with an additional term $\partial u_a / \partial t_c |_{x_f}$. The above additional term is referred to as the global-acceleration term (Moeck *et al.*, 2009), which can be identified as a coupling term for the momentum equation in the hydrodynamic zone from the acoustic zone, apart from that due to the boundary condition associated with Eqn. (3.16).

The global-acceleration term occurs in two length scale problems (Klein, 1995; Klein *et al.*, 2001). This term would not have been identified had the asymptotic analysis not been performed. In most thermoacoustic systems, there are at least two length scales; the length scale of the acoustic field and the length scale of the heat source. Therefore, the above term is expected to be present in the analysis of thermoacoustic systems. The same term can be interpreted as the pressure gradient imposed by the acoustic field on the hydrodynamic zone (Ting *et al.*, 2007). An important point to be emphasized here is the following. If one performs response function calculations numerically (for example Preetham *et al.* 2008) for the unsteady heat release rate from the heater, where no acoustic field is imposed, then $\partial u_a / \partial t_c |_{x_f}$ will not be anticipated and hence will not be included. This leads to solving an incorrect system of equations and prediction of the dynamics of thermoacoustic interaction in a Rijke tube system. Numerical simulations are performed with and without the global-acceleration term in the present paper. It is observed that the error due to neglecting the above term is large and predictions of the dynamical evolution of the system are modified to a large extent. This observation has been emphasized in Section 3.5.2.

3.3.6 Energy equation: hydrodynamic zone $O(1)$

Since the temperature fluctuations due to the heater are zeroth order in M as explained in the ansatz (Eqn. 4.4), $O(1)$ terms are gathered from Eqn. (3.5c) to obtain

$$\nabla_c \bullet \left(u_s + u_a|_{x_f} + u_c \right) = \frac{1}{Pe_c} \nabla_c^2 \left(T_s + T_c \right) \tag{3.17}$$

A change of variable, $T_p = T_s + T_c$ is performed in Eqn. (3.17) leading to,

$$\begin{gathered} \nabla_c \bullet u_p = \frac{1}{Pe_c} \nabla_c^2 T_p \\ \mathrm{BC} : \nabla_c T_p \rightarrow 0, \text{ as } \mathrm{x_c} \rightarrow \infty, \ \& \ \mathrm{T_p} = \tilde{\mathrm{T}}_\mathrm{w}/\bar{\mathrm{T}}, \ \mathrm{x_c} = \text{cylinder surface}, \end{gathered} \tag{3.18}$$

where, $\tilde{T_w}$ represents the surface temperature of the heater wire. The energy equation (3.3c) simplifies to an algebraic constraint (Eqn. 3.18) on the velocity field u_p. The amount of local dilatation of the fluid is governed by the equation (3.18). Integration of the same equation over the hydrodynamic zone gives the net dilatation in the volume of the fluid as it passes through the hydrodynamic zone. The presence of the heat source which leads to the dilatation in the volume of the fluid manifests as the acoustic velocity jump $(u_a|_{x_f})$ across the heat source. This in turn drives the acoustic field in the tube. The above argument is consistent with the derivation of the acoustic energy equation described in Section 3.3.3, where the Dirac-delta function in Eqn. (3.12) causes the acoustic velocity jump across x_f. Thus the acoustic velocity jump is used as the matching condition across the hydrodynamic zone. The above conclusion is independent of the type of the heat source and the interpretation is valid as long as the heat source can be considered as compact with respect to the acoustic field.

In multiple scale asymptotics, averaging the flow variables over the small scale - hydrodynamic zone, is performed to obtain the flow variables in the large scale - acoustic zone (Klein *et al.*, 2001). Accordingly, the term $\partial u_a/\partial t_c|_{x_f}$ in Eqn. (3.16) is evaluated as the average of the values at the upstream and downstream locations of the heat source, due to acoustic velocity jump. Averaging the momentum equation of the hydrodynamic zone (Eqn. 3.16) leads to acoustic momentum equation (Eqn. 3.9) defined at the location of the heat source, with the acoustic velocity obtained as the average of

u_a upstream and downstream of the heat source. The same averaging procedure is performed for the global acceleration term as well, which is used in equation (3.16). The system of equations for the hydrodynamic zone (3.14, 3.16 & 3.18) are not closed. The ideal gas equation is used to obtain the relation between ρ_p & T_p in the hydrodynamic zone as follows.

$$(1 + Mp_a + M^2 p_c) = (\rho_s + \rho_c + M\rho_a)(T_s + T_c + MT_a) \tag{3.19}$$

Equating the zeroth order terms gives the following.

$$\rho_p = \frac{1}{T_p} \tag{3.20}$$

Solving equation (3.18), simultaneously with (Eqns. 3.14, 3.16 & 3.20) gives the temperature field T_p. The unsteady heat release rate from the hydrodynamic zone is then determined as $q = (l_w l_c / Pe_c S_c) \left(\int_0^{2\pi} -\nabla_c (T_p - T_s)_{\hat{e}_r} d\theta \right)$ from T_p. This q serves as the source term for Eqn. (3.12).

3.4 Solution technique

The governing equations in the acoustic and hydrodynamic zones are solved using different solution techniques. First, the solution technique used in the acoustic zone is discussed.

3.4.1 Equations governing the acoustic zone : one-dimensional form

The acoustic continuity (Eqn. 3.7) and momentum (Eqn. 3.9) equations are converted from 3D to 1D space as described earlier in Section 3.3.3. The governing equations thus obtained for the acoustic zone are as follows.

$$\rho_s \frac{\partial u_a}{\partial t_a} + \frac{1}{\gamma} \frac{\partial p_a}{\partial x_a} = 0 \tag{3.21a}$$

$$\frac{1}{\gamma} \frac{\partial p_a}{\partial t_a} + \frac{\partial u_a}{\partial x_a} = q \widehat{\delta} \left(x - x_f \right) \tag{3.21b}$$

The above partial differential equations (Eqn. 4.5) are converted to ordinary differential equations (ODEs) by the Galerkin technique (Zinn and Lores, 1971; Padmanabhan, 1975). In the Galerkin technique, the unknown variables are expanded using basis functions, which satisfy the boundary conditions. In the present paper, the Rijke tube considered is open at both ends. The basis functions are chosen accordingly to satisfy the acoustic boundary conditions. The acoustic variables u_a and p_a are expanded in terms of the basis function as follows:

$$p_a = \gamma \sum_{m=1}^{N} P_m \sin(\omega_m x),\ u_a = \sum_{m=1}^{N} U_m \cos(\omega_m x) \tag{3.22}$$

where $\omega_m = m\pi$, N is the number of modes chosen in the Galerkin expansion. The dynamical evolution equation for P_m and U_m is obtained by projecting Eqn. (4.5) on to the Galerkin basis, after substituting the expansion for p_a and u_a from Eqn. (3.22). The application of the Galerkin technique to the present problem is similar to that performed by Balasubramanian and Sujith (2008*b*). The final ODEs are of the following form:

$$\sum_{m=1}^{N} \left(\rho_s^u I_{m,n}^u - \rho_s^d I_{m,n}^d\right) \dot{U}_m + P_n \omega_n = 0 \tag{3.23a}$$

$$\dot{P}_n - \omega_n U_n + \zeta_n \omega_n P_n = 2q \sin\left(\omega_n x_f\right) \tag{3.23b}$$

where

$$I_{m,n}^u = \rho_s^u \begin{cases} \dfrac{\sin\left(\left(\omega_m + \omega_n\right) x_f\right)}{\omega_m + \omega_n} + \dfrac{\sin\left(\left(\omega_m - \omega_n\right) x_f\right)}{\omega_m - \omega_n}, & \omega_m \neq \omega_n \\ \dfrac{\sin\left(2\omega_n x_f\right)}{2\omega_n} + x_f, & \omega_m = \omega_n \end{cases}$$

$$I_{m,n}^d = \rho_s^d \begin{cases} \dfrac{\sin\left(\left(\omega_m + \omega_n\right)\left(1 - x_f\right)\right)}{\omega_m + \omega_n} + \dfrac{\sin\left(\left(\omega_m - \omega_n\right)\left(1 - x_f\right)\right)}{\omega_m - \omega_n}, & \omega_m \neq \omega_n \\ 1 - \dfrac{\sin\left(2\omega_n x_f\right)}{2\omega_n} - x_f, & \omega_m = \omega_n \end{cases}$$

$\zeta_n = \left(C_1\left(\omega_n/\omega_1\right) + C_2\sqrt{\omega_1/\omega_n}\right)\Big/(2\pi)$, $\omega_n = n\pi$, ζ_n represents damping in the acoustic zone due to viscosity and end losses. Here, C_1, C_2 are the coefficients that determine the amount of damping and whose numerical value is given by Matveev and Culick (2003*a*). The system of equations (Eqn. 3.23) is solved using the fourth order

Runge-Kutta (RK4) method (Riley *et al.*, 2006). The value of the unsteady heat release rate q is obtained at each substep of RK4 by solving the equations corresponding to the hydrodynamic zone (Eqn. 4.6), which is discussed in the following section.

3.4.2 Equations governing the hydrodynamic zone

The governing equations for the hydrodynamic zone are summarised below:

$$\frac{\partial \rho_p}{\partial t_c} + \nabla_c \bullet (\rho_p u_p) = 0 \tag{3.24a}$$

$$\rho_p \left(\frac{\partial}{\partial t_c} + u_p \bullet \nabla_c \right) u_p + \frac{1}{\gamma} \nabla_c p_c = \frac{1}{Re_c} \left(\nabla_c^2 + \frac{1}{3} \nabla_c (\nabla_c \bullet) \right) u_p + \rho_s \left. \frac{\partial u_a}{\partial t_c} \right|_{x_f} \tag{3.24b}$$

$$\nabla_c \bullet u_p = \frac{1}{Pe_c} \nabla_c^2 T_p \tag{3.24c}$$

$$\rho_p = \frac{1}{T_p} \tag{3.24d}$$

As described in Section 4.1, the heater in its primitive form is a thin wire filament. To simulate the dynamics of the heater, Selimefendigil *et al.* (2008) have analysed the unsteady convective heat transfer from a heated circular cylinder. Following this approach, the above system of equations (Eqns. 4.6) is solved for the unsteady convective heat transfer over the circular cylindrical heated wire filament. The flow field over the heater wire filament is assumed to be two dimensional. The governing equations are solved by CFD. The details of the geometry of the heat source and the boundary conditions imposed on the hydrodynamic zone are discussed in Appendix C. The unsteady heat release rate q is obtained from the temperature field T_p. The obtained q is then used as the source term for Eqn. (3.23b) at each substep of RK4, as described in Section Eqn. 3.4.1. Thus the system of equations in acoustic (Eqn. 3.23) and hydrodynamic zone (Eqn. 4.6) is solved simultaneously.

Acoustic zone	Hydrodynamic zone	CFD simulations
$l_a = 1\ m,\ S_c = 0.01\ m^2$	$Re_d = 20$,	Number of grids $(r, \theta) = 100 \times 120$
$\bar{P} = 1\ bar$	$l_c = 2.6\ mm$	Residue for continuity = 10^{-6}
$\tilde{\rho}_0^u = 1.18\ kg\ m^{-3}$	$l_w = 10\ m$	Residue for momentum = 10^{-6}
$\tilde{T}_0^u = 295\ K$	$\tilde{T}_w = 700\ K$	Residue for energy = 10^{-6}
$\tilde{\rho}_0^d = 0.84\ kg\ m^{-3}$	$M = 5 \times 10^{-4}$	$\Delta t_a = 5 \times 10^{-4}$

Table 3.1: Physical parameters in acoustic zone, hydrodynamic zone and numerical parameters used for CFD simulations

3.5 Results and discussions

Numerical simulations are performed with the parameters shown in table 4.1. In the following simulations, the number of the Galerkin modes is chosen as $N = 100$ (to capture the acoustic velocity jump across the heat source), such that a further increase in N leads to less than 5% variation in the results. Unless otherwise specified, the parameter values in table 4.1 are used for the simulations. The numerical values of the damping coefficients used for the present simulations are $C_1 = 0.27$ and $C_2 = 0.03$ (Matveev and Culick, 2003*a*). In the acoustic zone upstream and downstream of the heater, one dimensional governing equations are used. The hydrodynamic zone equations in the present case are solved in a two dimensional domain (see Appendix C). Hence the density ($\tilde{\rho}_d^0$) in the hot side of the acoustic zone is obtained by averaging the steady state density ρ_s at the far downstream end of the hydrodynamic zone. The value of $\tilde{\rho}_d^0$ thus obtained is listed in table 4.1.

3.5.1 Stability regimes

The experimental results of Matveev and Culick (2003*b*) indicate that the system becomes linearly unstable beyond some critical value of the heater power. As the heater power is increased, the present numerical simulations show two stability regimes: linearly stable regime and linearly unstable regime. The non-dimensional heater power (K) is defined as $K = (l_w l_c) \Big/ (Pe_c S_c)$ (see Section 3.3.6 for the expression of q). The

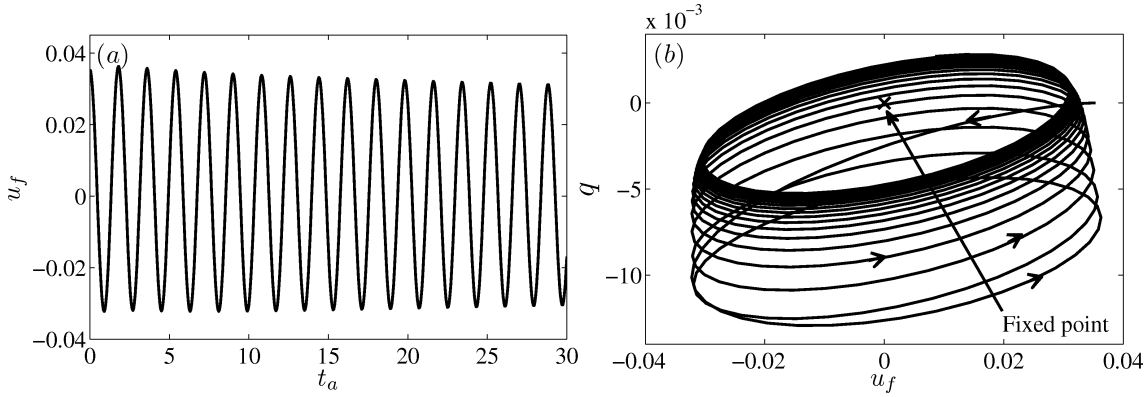

Figure 3.2: Linearly stable system: (*a*) evolution of acoustic velocity (u_f) at the heater location (x_f), (*b*) phase portrait between u_f and unsteady heat release rate q, $x_f = 0.25,\ K = 0.10,\ U_1(t=0) = 0.05,\ U_{m\neq1}(t=0) = 0,\ P_m(t=0) = 0$.

average of the acoustic velocity upstream and downstream of the heat source is taken as the acoustic velocity (u_f) at the heat source. In the subsequent sections, the variables u_f and q are considered as the representative variables to illustrate the dynamical behaviour of the system in the acoustic and hydrodynamic zones, respectively. The subsequent sections discuss the results of the numerical simulation.

Linearly stable regime

For low values of the heater power K, the system is stable to small amplitude initial perturbations. In Fig. 3.2(*a*) the initial perturbation in acoustic velocity ($u_f = u_a|_{x_f}$) at the heater location is around 5% of the mean flow velocity. The perturbation decays to zero in the asymptotic time limit. The phase plot between u_f and the non-dimensional fluctuating heat release rate (q) shows the evolution of the system in Fig. 3.2(*b*) towards a stable focus. The arrows indicate the direction of the evolution of the system in the phase plane.

Linearly unstable regime

In the second stability regime, the system is unstable for small amplitude perturbation, $u_f(t=0) = 0.4$, which is 10% of the limit cycle amplitude, see Fig. 3.3(*a*). The figure shows that u_f grows exponentially, eventually reaching a limit cycle. The limit cycle is

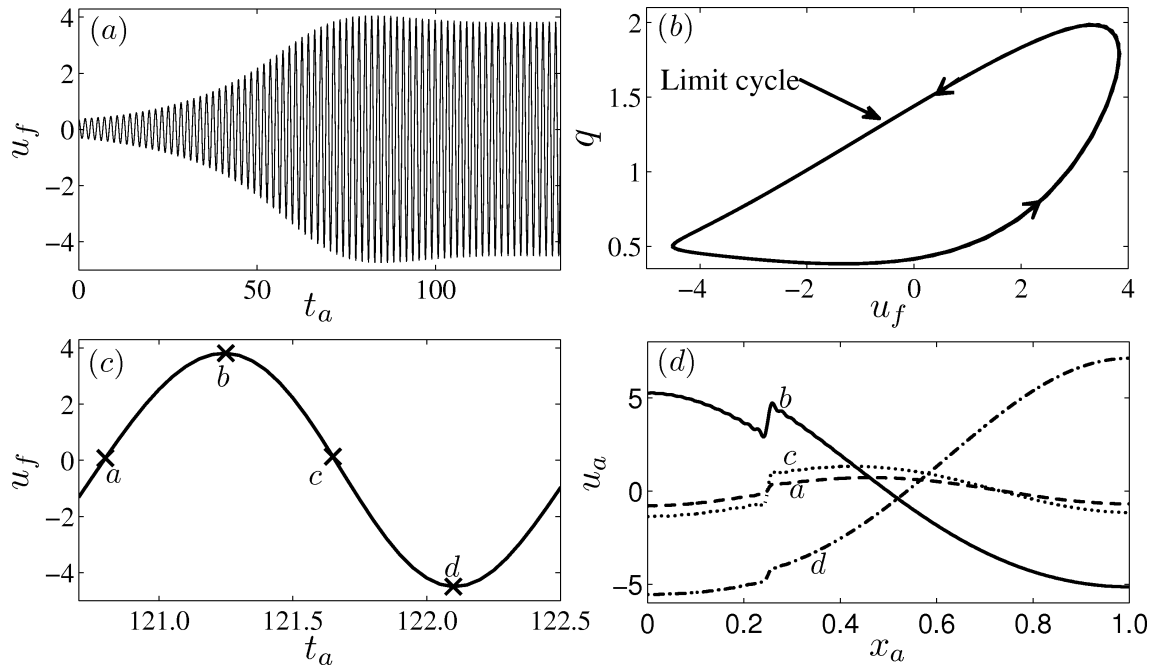

Figure 3.3: Linearly unstable system: (a) evolution of acoustic velocity (u_f) at the heater location (x_f), (b) phase portrait between u_f and unsteady heat release rate q (only limit cycle is shown, transients are not shown for clarity), (c) evolution of u_f during a period of the limit cycle, (d) distribution of the acoustic velocity u_a in the Rijke tube during a period of the limit cycle. $x_f = 0.25, K = 0.1785,\ U_1(t=0) = 0.5,\ U_{m\neq 1}(t=0) = 0,\ P_m(t=0) = 0$.

a closed curve in the phase portrait as shown in Fig. 3.3(b). The acoustic velocity (u_a) distribution along the duct at various instances over a period, as marked in Fig. 3.3(c) is shown in Fig. 3.3(d). It is observed that the acoustic velocity jump is captured by the Galerkin technique. The stability regimes of a system with the variation of a parameter can be represented using a bifurcation diagram.

Bifurcation diagram

Simulations are performed with the heater power as the control parameter and the peak to peak value of acoustic velocity $\left(u_f|_{p-p}\right)$ at the heater location (x_f) in the asymptotic time limit is chosen as the representative variable. The resolution in the control parameter K for Fig. 3.4 is 2×10^{-3}, which is 1.8% of the value of $K = 0.11$ at the Hopf point (B). In the bifurcation diagram shown in Fig. 3.4, solid lines indicate stable solutions, while dashed line indicates unstable solutions. For low values of K (say,

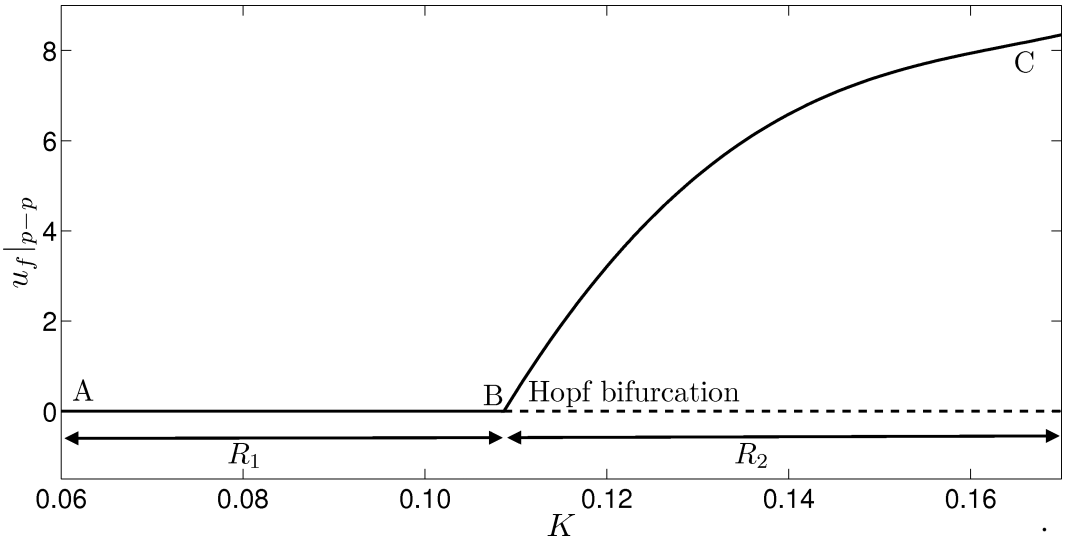

Figure 3.4: Bifurcation diagram with the non-dimensional heater power 'K' as the control parameter. The other parameters are, $x_f = 0.25$. The two regimes are R_1 - linearly stable regime and R_2 - linearly unstable.

$K = 0.06$), the asymptotic state ($u_f = 0$) is the stable fixed point. This corresponds to the first stability regime (Section 3.5.1), where the system is linearly stable. As the heater power is increased, beyond point 'B' ($K = 0.11$), the system becomes linearly unstable and reaches a limit cycle. The above transition happens via Hopf bifurcation. Also the amplitude of the limit cycle increases as the heater power is increased further. This corresponds to the second stability regime.

3.5.2 Effect of global-acceleration on the stability of the system

An asymptotic analysis is performed to obtain separate systems of equations governing the dynamics in the acoustic and hydrodynamic zones. The critical outcome of the above analysis is the presence of the additional term $\partial u_a/\partial t_c|_{x_f}$ in Eqn. (3.16). The importance of the global-acceleration term is shown in Fig. 3.5. In Fig. 3.5(*a*), evolution of u_f is shown with and without this term for identical system parameters and initial conditions. The system parameters are chosen, such that the simulation performed is in the linearly unstable regime ($K = 0.1785$, see Fig. 3.4). With the initial perturbation $U_1(t = 0) = 0.5$, the simulation with the $\partial u_a/\partial t_c|_{x_f}$ term indicates that the system reaches a limit cycle eventually. The evolution of the system to a limit cycle is shown in the inner Fig. 3.5(*b*). However, for the same system parameters and initial conditions,

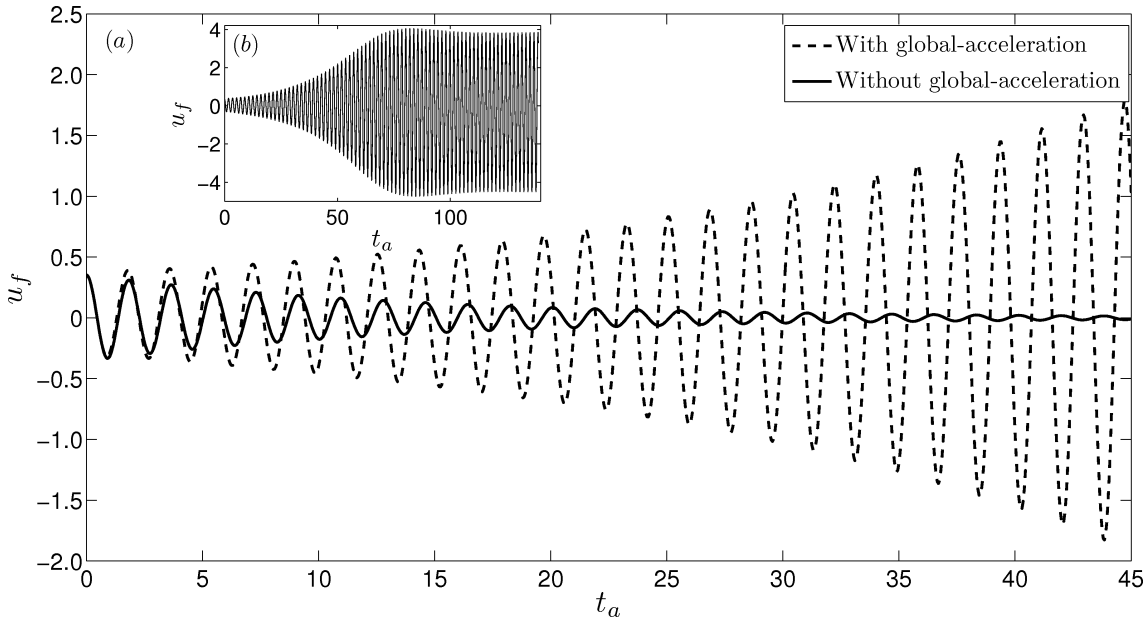

Figure 3.5: (*a*) Comparison of the evolution of acoustic velocity (u_f) at the heater location (x_f) with and without the global-acceleration term in Eqn. (3.15), (*b*) Evolution of u_f for a longer period of time with the global-acceleration term, 'zoomed out' view of (*a*). $x_f = 0.25,\ K = 0.1785,\ U_1(t=0) = 0.5,\ U_{m\neq 1}(t=0) = 0$ and $P_m(t=0) = 0$.

if the above term is dropped from Eqn. (3.16), the simulation indicates that the system reaches a stable focus in the asymptotic time limit.

To analyse the behaviour of the system in the absence of the global-acceleration term, the bifurcation diagram is computed without the term $\partial u_a/\partial t_c|_{x_f}$ in Eqn. (3.16), as shown in Fig. 3.6. A significant difference to be observed between the bifurcation diagram with (Fig. 3.4) and without (Fig. 3.6) the inclusion of the global-acceleration term is that the system becomes linearly unstable at $K = 0.11$ (see Fig. 3.4) for the simulation performed with the global-acceleration term, whereas the same behaviour happens at $K = 2.89$ (see Fig. 3.6) for the simulation performed without the same term. The numerical simulation without the global-acceleration term predicts linear instability at a value of K which is one order of magnitude higher than that obtained from the numerical simulation with the inclusion of the same term. The term $\partial u_a/\partial t_c|_{x_f}$ acts as a forcing term for Eqn. (3.16) from the acoustic zone. Hence, dropping the above term breaks the feedback from the acoustic to the hydrodynamic zone apart from the feedback from the free stream boundary condition for Eqn. (3.16). The strength of the feedback loop between the acoustic and hydrodynamic zones is thus weakened.

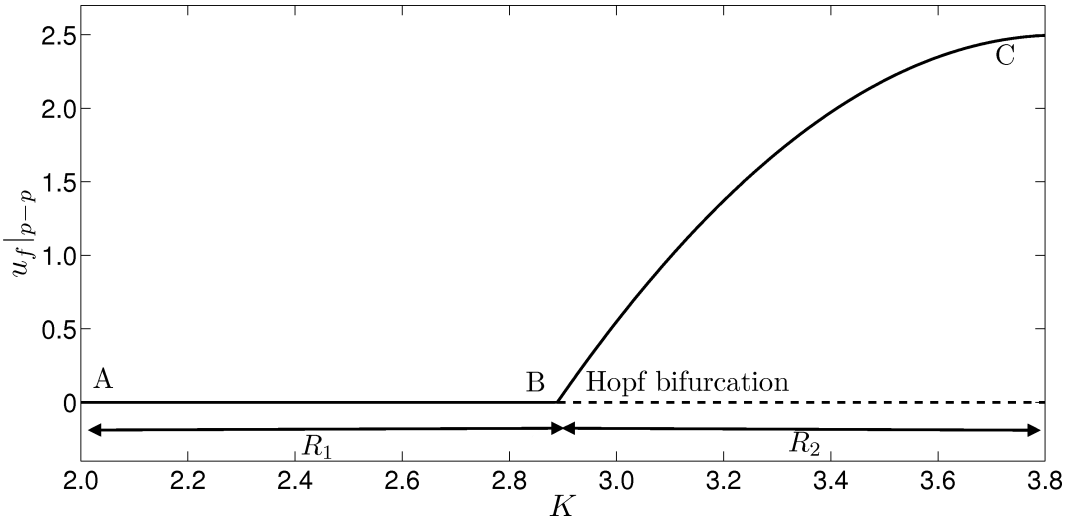

Figure 3.6: Bifurcation diagram with non-dimensional heater power 'K' as the control parameter without the global-acceleration term in Eqn. (3.15). The parameters chosen are the same as for the simulation shown in Fig. 3.4.

Therefore, it is important to perform the asymptotic analysis to obtain the correct system of equations for the two zones in solving the two length scale problems.

An analysis of thermoacoustic instability using the response function (to capture the dynamics of the heat source) is termed as a two-part approach (Candel, 2002). In this approach, the response function of the heat source to velocity fluctuations is first obtained. The response function thus obtained is used in the acoustic energy equation. The acoustic equations are then solved with the appropriate boundary conditions and the stability of the system is determined. When the response function is obtained numerically, for example Preetham *et al.* (2008), the global-acceleration term is not taken into account in the governing equations for the dynamics of the heat source. If the prediction of thermoacoustic instability is performed based on the response function of the heat source, the effect of the above term is absent. As a consequence, the coupling between the acoustic and hydrodynamic zones is weakened, which leads to over prediction of the stability of the thermoacoustic system.

Furthermore, it is important to analyse the dynamics of the system in the asymptotic time limit. As fluid convection is the source of energy transfer from the heated wires to the flow, the flow field during a limit cycle will reveal important insights about them.

3.5.3 Unsteady flow field in the hydrodynamic zone

The flow field in the hydrodynamic zone during a limit cycle is investigated in this section. Fig. 3.7 shows the streamlines of the velocity field u_p for the flow over the heater wire at various instants of a limit cycle. Only one half of the flow field is shown in the figure due to the symmetry condition (see Appendix C). The acoustic velocity $u_a|_{x_f}$ at the heater location ranges from -4 to +4 during one period of the limit cycle (Fig. 3.7*f*). Hence, during the first half of the limit cycle, the flow is from left to right and during the next half, it is from right to left. A complete flow reversal in the freestream happens, as shown in Fig. 3.7(*a–e*). Labels (*a-e*) illustrated in Fig. 3.7(*f*) indicate the flow field at various instants of the acoustic velocity $\left(u_a|_{x_f}\right)$ shown in Fig. 3.7(*a–e*).

When $u_a|_{x_f} = 0$ (Fig. 3.7*a*), the flow field resembles the steady flow over the cylinder. As $u_a|_{x_f}$ increases and reaches a maximum, the recirculation zone is pushed further downstream (Fig. 3.7*b*) and during subsequent time, $u_a|_{x_f}$ decreases, followed by flow reversal in the freestream direction (Fig. 3.7*e*). Thus the fluctuations in the velocity field (u_p) during the limit cycle are comparable to the steady base flow (u_s). Hence nonlinear effects such as steady streaming (Telionis, 1981) will be predominant. In the present case, since the acoustic velocity (u_a) is responsible for flow oscillation in the hydrodynamic zone, the steady streaming thus obtained is termed as acoustic streaming (Andres and Ingard, 1953).

Fig. 3.8(*a–c*) shows the effects of acoustic streaming during the limit cycle. Fig. 3.8(*a*) shows the averaged streamlines of u_p during one period of the limit cycle (Fig. 3.7*f*). The streamlines of the steady state flow u_s are shown in Fig. 3.8(*b*). There are visible differences between the Fig. 3.8(*a* & (*b*) and hence, apart from the steady base flow, a non-zero mean flow arises during the limit cycle due to the nonlinearity. The streamlines obtained from the difference of the above two flow fields (Fig. 3.8*a* & *b*) are shown in Fig. 3.8(*c*). The streamlines are slightly tilted towards the right due to the steady base flow from left to right. Also, note that in Fig. 3.8(*c*) the streaming velocity is towards the cylinder along the direction of the propagation of the sound waves (X direction). In the present case, the Strouhal number (St) and the streaming Reynolds

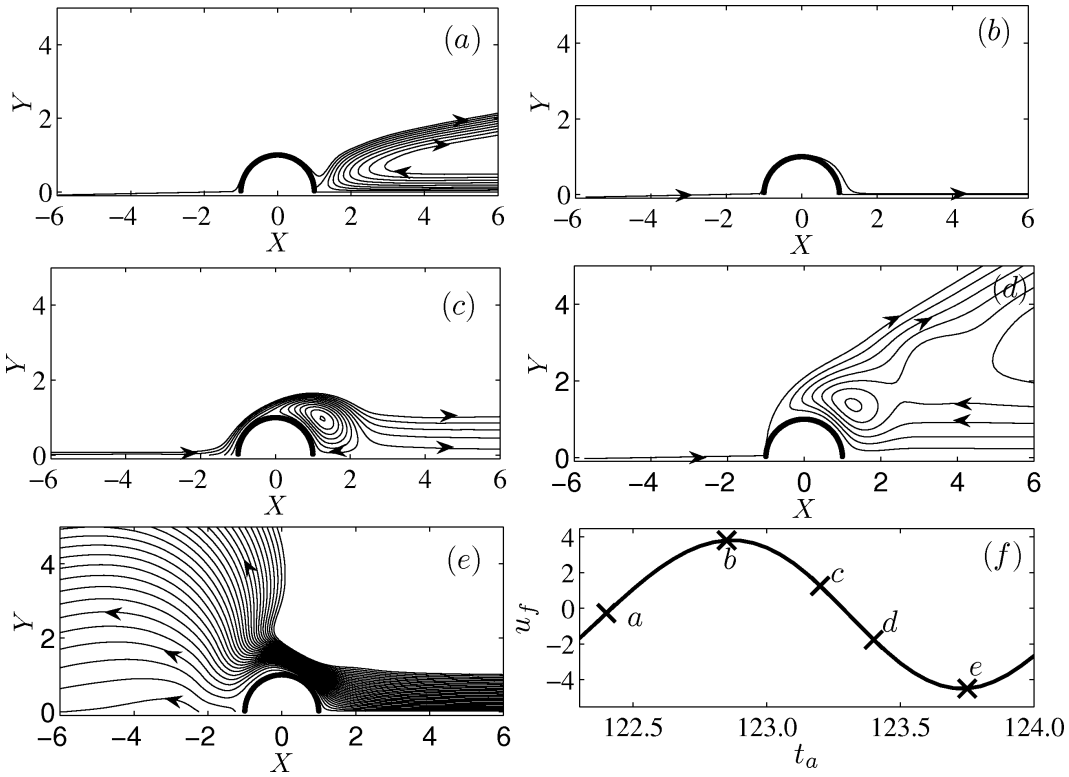

Figure 3.7: Streamlines (*a*-*e*) in the hydrodynamic zone (corresponding to u_p) at various instants during one period of the limit cycle, (*f*) evolution of u_a at x_f during the limit cycle: $K = 0.1785,\ x_f = 0.25,\ l_w = 10\ m$.

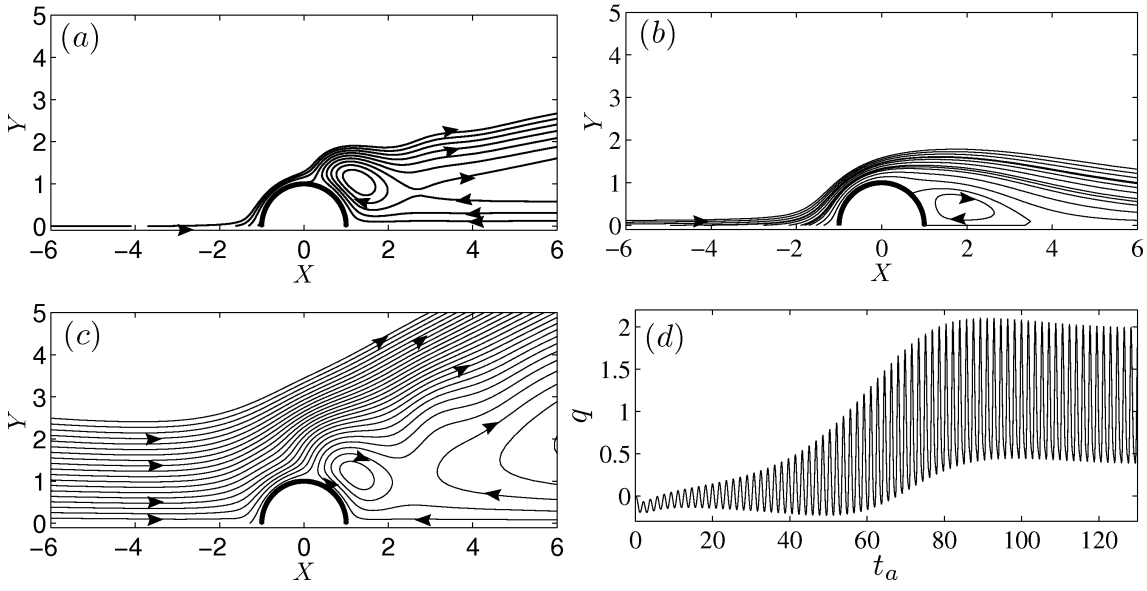

Figure 3.8: Flow streaming in the hydrodynamic zone, (*a*) streamlines averaged over one period of the limit cycle, (*b*) streamlines of the steady base flow, (*c*) streamlines of the velocity difference between (*a*) and (*b*), (*d*) evolution of the non-dimensional unsteady heat release rate (q), showing a significant mean shift: $K = 0.1785,\ x_f = 0.25,\ l_w = 10\ m,\ U_1(t=0) = 0.5,\ U_{m\neq 1}(t=0) = 0$ and $P_m(t=0) = 0$.

number (Re_s) are calculated as,

$$\begin{aligned} St &= f l_c/\bar{u} = \delta/2M = 1/2\varepsilon = 1 \\ Re_s &= (u_a|_{x_f})_{max} 2l_c/\nu \sim 80 \end{aligned} \tag{3.25}$$

where $f = c_0/2l_a$ is the fundamental frequency of the natural duct mode. The experiments performed in the above regimes of 'St' and 'Re_s' (Andres and Ingard, 1953) indicate that the steady streaming velocity is directed towards the cylinder in the direction of oscillation of the free stream flow field. The same is observed in the present simulation, as shown in Fig. 3.8(c). Streaming velocity field obtained from the present simulation cannot be compared with the experiments with externally excited acoustic field due to the presence of the global-acceleration term. The same term does not vanish even during limit cycles and therefore, only qualitative behaviour of the streamlines corresponding to the streaming velocity field can be compared with the experiments in acoustic streaming (Andres and Ingard, 1953).

A non-zero averaged mean flow, which appears above the steady base flow due to acoustic streaming results in non-zero averaged unsteady heat transfer from the heater. Fig. 3.8(d) shows the evolution of the unsteady, non-dimensional heat transfer rate ('q', see Section 3.3.6) from the heater. The unsteady heat transfer rate 'q' eventually reaches a limit cycle for linearly unstable systems (Section 3.5.1) where the oscillations during the limit cycle are about a non-zero mean. Acoustic streaming leads to a shift in the mean value of q.

3.6 Interim summary

An analysis of thermoacoustic instability in an electrically heated horizontal Rijke tube is performed. The analysis started with an examination of the conservation equations for fluid flow. In the limit of zero Mach number of the steady flow and compact size of the heat source compared to the acoustic length scale, the equations become stiff. Therefore, solving the governing system of equations by the CFD technique is a difficult task. Hence, an asymptotic analysis is performed, which gave further physical

insight into the problem. The flow variables are expanded in powers of Mach number. The equations thus obtained are identified as governing equations for the acoustic and hydrodynamic zones. An additional non-trivial term that has serious consequences on the stability of the system appeared in the momentum equation for the hydrodynamic zone, which cannot be obtained without performing the asymptotic analysis. The additional term is the global-acceleration term, which acts as a pressure gradient applied from the acoustic zone onto the hydrodynamic zone.

Numerical results show two stability regimes. In the first regime, the system is linearly stable. In the second regime, the system is linearly unstable and the perturbations eventually reach a limit cycle. Bifurcation diagram is then obtained with the heater power as the control parameter. The effect of global-acceleration term is investigated using bifurcation diagrams. The term acts as one of the coupling terms (the other one is from the boundary condition for the momentum equation in the hydrodynamic zone) from the acoustic to the hydrodynamic zone. Therefore, the absence of the same term weakens the coupling between the acoustic and hydrodynamic zones. Without the global-acceleration term, the transition from linearly stable to unstable behaviour occurs for a value of the non-dimensional heater power, which is one order of magnitude higher than the value of the heater power corresponding to the simulation with the above term. Thus the linear stability of the system is predicted incorrectly in the absence of the term. The same term appears due to the two length scale nature of the Rijke tube system, which is generic in thermoacoustic systems. The numerical computation of response functions in the past did not take into account the global-acceleration term. Hence the evaluation of the stability of thermoacoustic system using the response function has to be performed carefully in the future.

Finally the flow field during limit cycle oscillation is analysed. The limit cycle amplitude is observed to be comparable to the steady base flow. Flow reversal occurs in the hydrodynamic zone during part of a period of the limit cycle oscillation. This nonlinear behaviour of the unsteady flow is observed as acoustic streaming during the limit cycle. A mean shift in the unsteady heat release rate from the heater is observed due to acoustic streaming.

In brief, asymptotic analysis gives the correct system of equations for the dynamics

of the acoustic field and the heater. Also using any response functions for the dynamics of the heater without rigorous mathematical arguments can lead to incorrect governing equations, which will lead to erroneous results.

3.7 Outlook

Having obtained the right systems of governing equation

CHAPTER 4

Non-normal stability analysis of thermoacoustic instability in a Rijke tube system

In the previous chapter, asymptotic analysis technique is used to obtain the governing equations for the dynamics of the acoustic field and heat source. The asymptotic stability of the system is plotted using bifurcation diagram. As an extension of the same, the present chapter deals with the non-modal stability analysis of the obtained governing equations (Eqns. 4.5 and 4.6).

As explained in the introduction chapter (Chap. 1), non-normal nature of the thermoacoustic interaction leads to transient growth in the amplitude of the oscillations. The amount of transient growth depends on the choice of the initial condition. Hence it is important to find the initial condition ($t = 0$), which produces the maximum transient growth at a given time ($t = T_{opt}$). Conventional technique of obtaining the maximum transient growth and the corresponding initial condition is by performing singular value decomposition (SVD) on the linear operator governing the linearised sytem (Farrell and Ioannou, 1996*a*). The same technique is used in the analysis of thermoacoustic instability in SRM. (see Section 2.4 in Chapter 2). The above technique is suitable only for small systems (with fewer degrees of freedom). Hence the non-normal nature of small model problems (Baggett *et al.*, 1995; Balasubramanian and Sujith, 2008*b*) can be investigated easily using SVD technique.

In the present analysis, thermoacoustic instability in a Rijke tube is investigated by simultaneously solving the governing equations for the acoustic field and the unsteady heat transfer from the heat source. In this way, the dynamics associated with the heat source is also taken into account. Computational fluid dynamics technique (CFD) is used to solve the equations, governing the dynamics of the heat source. Hence the number of grid points for numerically solving the governing equations is of the order 10^4 (see table 4.1), where the use of SVD to obtain the optimum initial condition for maximum transient growth becomes computationally costly.

In this thesis, another technique known as 'adjoint optimisation technique' (Gunzburger, 2003) is used to obtain the maximum transient growth and the corresponding initial condition for the linearised governing equations of thermoacoustic instability in the Rijke tube. Adjoint optimisation technique has been employed successfully in fluid mechanics to obtain the optimum initial perturbation for maximum transient growth in space for the flow over a swept wing (Guegan *et al.*, 2008), investigate the transient growth of perturbations in flow over a cylinder (Abdessemed *et al.*, 2009) and stenotic flow (Mao *et al.*, 2009) etc. Though 'adjoint optimisation technique' is an optimisation algorithm, the adjoint equations obtained during the application of the algorithm yield physical insights into the problem.

Hill (1995) has explained that the eigenmodes of the adjoint system (adjoint modes) represents the sensitivity of the flow to perturbation based on the energy (norm) defined for obtaining the adjoint system. This physical interpretation is used in the control of fluid flows. The location of the actuator and sensor are determined from the shape of the eigenmodes of the adjoint and direct system respectively (Barbagallo *et al.*, 2009). The adjoint system is also used in the model reduction for control of fluid flows (Rowley, 2005; Barbagallo *et al.*, 2009). The mechanism of instability in some fluid flow problems are identified with the adjoint modes along with the eigenmodes of the direct system (Marquet *et al.*, 2009). An introduction to the non-modal stability theory applied to the stability of shear flows in fluid mechanics followed by the explanation of various tools (such as adjoint optimisation) to obtain the optimum initial condition is given in the review article by Schmid (2007).

The earlier investigation of the non-normal nature of the thermoacoustic systems in Rijke tube dealt with a simple model (Balasubramanian and Sujith, 2008*b*), where an algebraic model is used for the response of the heat source to the acoustic oscillations. Moreover, the results discussed in Section 2.7.3 of Chapter 2 have shown that including the dynamics of the heat source leads to a higher transient growth compared to that, using a response function for the heat source. Hence including the dynamics of the heat source leads to a more complete analysis of the non-normal nature of the system. In the previous chapter, thermoacoustic instability in the Rijke tube is modelled, taking into account the dynamics of the heat source. By simultaneously solving

the equations governing the chamber acoustic field and the unsteady heat transfer from the heat source, the dynamics associated with the heat source is taken into account. The additional global acceleration term is shown to have significant effects on the stability of the system. The frame work developed to study the thermoacoustic instability in a Rijke tube can be extended to other more complex systems. So it is worth to investigating the non-normal nature of thermoacoustic interaction starting from the governing equations obtained in (Mariappan and Sujith, 2010*a*).

The configuration of the Rijke tube investigated in the present paper is same as that given in Mariappan & SujithMariappan and Sujith (2010*a*). The following are the motivations for the present paper. 1) Investigate the non-normal nature of thermoacoustic interaction in the Rijke tube, taking into account the dynamics of the heat source. 2) The norm used to measure the transient growth plays a crucial role in analysing non-normal systems. The norm should ideally represent a physical energy in the disturbance. In the analysis of incompressible shear flows, plane Poiseuille flows in fluid mechanics, the total kinetic energy of the perturbations is defined as the norm (Schmid and Henningson, 2001) and the transient growth is measured in that norm. However, as one moves to more complex systems like in the present case, there is no general prescription to define a norm. In the present paper, a norm has been obtained systematically from the energy in the disturbance. 3) In analysing non-normal systems, one important element is to find the maximum transient growth and the corresponding initial condition termed as the 'optimum initial condition'. For small systems such as those studied by Balasubramanian & SujithBalasubramanian and Sujith (2008*a*,*b*), one can obtain the optimum initial condition by SVD, for which mathematical tools are readily available. The same technique becomes prohibitively expensive as one moves to more complex systems with large degrees of freedom as in the present case. In the present paper, 'adjoint optimisation technique', which is another standard technique, is performed to obtain the optimum initial condition. In the application of above optimisation technique, one obtains the adjoint equations, which gives the sensitivity of the system to the type of initial condition. Moreover in the present paper, the adjoint equations are obtained for a two length scale problem (single length scale problem was dealt in the past, for eg. to obtain the optimum initial conditions for the flow over a swept wing (Guegan *et al.*, 2008), flow over a cylinder (Abdessemed *et al.*, 2009) and in stenotic flows Mao

et al. (2009)) and a comparison of the direct and adjoint system gives interesting insight into the physics of the problem. 4) The fourth and the final motivation is to analyse the role played by non-normality in the subcritical transition regime of thermoacoustic instability.

4.1 Governing equations

The horizontal Rijke tube configuration considered here has a length $_a$ with the heater positioned at an axial location $\tilde{x}_f$ (figure 3.1). The electrical resistance heater, which acts as a heat source is made up of a thin wire of radius $_c$ strung around the heater frame. The effective length of the wire filament, which participates in the heat transfer to the fluid flow is $_w$. The typical length of the duct ($_a$) is around 1*m* and the dimension of the heater along the axial direction of the tube (thickness, $_c$) is around 1*mm*. The zone around the heat source is termed as the hydrodynamic zone and its length in the axial direction of the Rijke tube is also of the order of the thickness of the heater. The thickness of the heater is very small compared to the length scale of the acoustic zone. Hence the heater and the hydrodynamic zone can be assumed to be compact compared to the acoustic zone in the tube. The acoustic and hydrodynamic zones are schematically shown in figure 3.1. The heater heats the flow and hence there is a temperature rise across the heater. Since the heater is compact, piecewise constant steady flow properties can be assumed on either side of the heater (Kaufmann *et al.*, 2002). The flow is at very low Mach number $(M \sim 10^{-3})$, which leads to a negligible steady state pressure loss. Hence the steady state pressure is assumed to be constant in space. All upstream steady state variables are known and specifying any one downstream steady state variable, such as temperature is enough to compute the other steady state variables from the following ideal gas and steady state continuity equations:

$$\tilde{\rho}_0^d = \frac{\tilde{\rho}_0^u \tilde{T}_0^u}{\tilde{T}_0^d}, \; \tilde{u}_0^d = \frac{\tilde{\rho}_0^u \tilde{u}_0^u}{\tilde{\rho}_0^d} \tag{4.1}$$

where superscripts 'u' and 'd' represent upstream and downstream variables respectively, subscript '0' represents steady variables and '$\sim$' indicates dimensional variables.

The governing equations are

$$\frac{\partial \tilde{\rho}}{\partial \tilde{t}} + \tilde{\nabla} \bullet (\tilde{\rho}\tilde{u}) = 0 \tag{4.2a}$$

$$\tilde{\rho}\left(\frac{\partial}{\partial \tilde{t}} + \tilde{u} \bullet \tilde{\nabla}\right)\tilde{u} + \nabla \tilde{p} = \mu\left(\tilde{\nabla}^2 + \frac{1}{3}\tilde{\nabla}\left(\tilde{\nabla}\bullet\right)\right)\tilde{u} \tag{4.2b}$$

$$\tilde{\rho} C_p\left(\frac{\partial}{\partial \tilde{t}} + \tilde{u} \bullet \tilde{\nabla}\right)\tilde{T} = \left(\frac{\partial}{\partial \tilde{t}} + \tilde{u} \bullet \tilde{\nabla}\right)\tilde{p} + k\tilde{\nabla}^2\tilde{T} \tag{4.2c}$$

Non-dimensionalising the above equations using the following $\rho = \tilde{\rho}/\bar{\rho},\ p = \tilde{p}/\bar{p},\ u = \tilde{u}/\bar{u},\ T = \tilde{T}\Big/\bar{T},\ x = \tilde{x}/l_a,\ t_a = \tilde{t}/(l_a/a),\ t_c = \tilde{t}/(l_a/\bar{u})$, where $\bar{p} = \tilde{p}_0^u = \tilde{p}_0^d,\ \bar{\rho} = \left(\tilde{\rho}_0^u + \tilde{\rho}_0^d\right)/2,\ \bar{T} = \bar{p}/(\Re\bar{\rho}),\ \bar{u} = \left(\tilde{u}_0^u + \tilde{u}_0^d\right)/2,\ a = \sqrt{\gamma\Re\bar{T}},\ \Re$ is the specific gas constant and a is the local speed of sound, leads to

$$\frac{\partial \rho}{\partial t_a} + M\nabla_a \bullet (\rho u) = 0 \tag{4.3a}$$

$$\rho\left(\frac{\partial}{\partial t_a} + Mu \bullet \nabla_a\right)u + \frac{1}{\gamma M}\nabla_a p = \frac{M}{Re_a}\left(\nabla_a^2 + \frac{1}{3}\nabla_a\left(\nabla_a\bullet\right)\right)u \tag{4.3b}$$

$$\rho\left(\frac{\partial}{\partial t_a} + Mu \bullet \nabla_a\right)T = \frac{\gamma - 1}{\gamma}\left(\frac{\partial}{\partial t_a} + Mu \bullet \nabla_a\right)p + \frac{M}{Pe_a}\nabla_a^2 T \tag{4.3c}$$

where $Re_a = \bar{\rho}\bar{u}l_a/\mu,\ Pe_a = \bar{\rho}\bar{u}l_a C_p/k$, subscript '$a$' indicates non-dimensionalisation performed with the acoustic length scale $_a$.

Thermoacoustic instability analysis of the Rijke tube is the study of the dynamics of the coupled system comprising of the acoustic field in the tube and the unsteady heat transfer from the electrical wire filament. Therefore, it is important to track variations on the scale of the tube length (acoustic scale $_a \sim 1m$) and on the scale of the heater wire filament radius ($_c \sim 1mm$) in the hydrodynamic zone. Further, the acoustic time scale $t_{ac} = l_a/a$ and the wire heat transfer time scale $t_{cc} = l_c\big/\bar{U}$ are of the same order for typical values mentioned in the previous paragraphs. This leads to an effective coupling of the dynamics of the acoustic field and the unsteady heat release rate from the heater. The length and time scale ratios are defined as $\delta = l_c/l_a,\ \varepsilon = t_{ac}/t_{cc} = M/\delta \sim 1$. Now the present problem has two length scales separated by a large factor $(1/\delta \to \infty)$ and one time scale $(\varepsilon \sim 1)$. Asymptotic analysis has been performed on the governing equations and in the above limit $(\delta \to 0,\ M \to 0,\ \varepsilon \sim 1)$, as the governing equations

become stiff at low Mach numbers; in the present case $M \sim 10^{-3}$ (Mariappan and Sujith, 2010*a*). A separate system of equations are obtained in the two zones; acoustic and hydrodynamic zone (see figure 3.1). The following ansatz for the flow variables is used as the initial step in the asymptotic analysis:

$$\begin{aligned} &\rho = \rho_s + M\rho_a,\ u = u_s + u_a + u_c, \\ &p = 1 + Mp_a + M^2 p_c,\ T = T_s + T_c + MT_a \end{aligned} \tag{4.4}$$

where, subscript 's' stands for steady state variables, 'a' for fluctuations due to acoustic field, 'c' for fluctuations in the hydrodynamic zone. Here, acoustic fluctuations exist all along the length of the tube, while the fluctuations due to heater exists in a zone around the heater (hydrodynamic zone), which is small compared to the acoustic length scale. Hence the variables with subscript 'a' exist over the length of the tube (acoustic zone, see figure 3.1), while the variables with subscript 'c' exists over the region around the heater wire filament length scale l_c (hydrodynamic zone, see figure 3.1) and vanishes as one moves away from the heater. The explanation for choosing the particular form (power series in M) of the above ansatz (4.4), the detailed derivation of obtaining the separate equations for the two zones (acoustic and hydrodynamic zones) and the coupling between them are given in Mariappan & SujithMariappan and Sujith (2010*a*). Only the final system of governing equations are shown in the present paper. There are two separate system of equations; one in the acoustic zone and another in the hydrodynamic zone. A brief description of the system of equations is presented. The system of equations in the acoustic zone (one dimensionalised along the length of the Rijke tube) is as follows:

$$\rho_s \frac{\partial u_a}{\partial t_a} + \frac{1}{\gamma}\frac{\partial p_a}{\partial x_a} = 0 \tag{4.5a}$$

$$\frac{1}{\gamma}\frac{\partial p_a}{\partial t_a} + \frac{\partial u_a}{\partial x_a} + \zeta_n \omega_n p_a = q\widehat{\delta}\left(x - x_f\right) \tag{4.5b}$$

where $\zeta_n = \left(C_1\left(\omega_n/\omega_1\right) + C_2\sqrt{\omega_1/\omega_n}\right)/\left(2\pi\right)$, ζ_n represents damping in the acoustic zone due to viscosity and end losses, $C_1,\ C_2$ are the coefficients which determine the amount of damping (Matveev and Culick, 2003*a*) and $\omega_n/2\pi$ is the frequency associated with the Galerkin basis function (see § 4.1 of Mariappan & SujithMariappan and Sujith (2010*a*)) of the oscillation, $\widehat{\delta}(x)$ is the Dirac-delta function, which is used to

include the compactness of the hydrodynamic zone in the acoustic equations, subscript 'a', 'q' is obtained from (4.6) and $\partial/\partial x_a$ represents derivatives in the acoustic length scale l_a. The above system of equations (4.5) are solved by Galerkin technique as described in Mariappan & SujithMariappan and Sujith (2010a). Similarly the system of equations in the hydrodynamic zone is as follows:

$$\nabla_c \bullet (u_p) = 0 \tag{4.6a}$$

$$\left(\frac{\partial}{\partial t_c} + u_p \bullet \nabla_c\right) u_p + \frac{1}{\gamma}\nabla_c p_c = \frac{1}{Re_c}\nabla_c^2 u_p + \left.\frac{\partial u_a}{\partial t_c}\right|_{x_f} \tag{4.6b}$$

$$\frac{\partial T_p}{\partial t_c} + u_p \bullet \nabla_c T_p = \frac{1}{Pe_c}\nabla_c^2 T_p \tag{4.6c}$$

where, $q = \frac{l_w l_c}{Pe_c S_c}\left[\left(\int_0^{2\pi} \nabla_c \left(\left(\tilde{T}_w - \tilde{T}_0^u\right) T_p \Big/ \bar{T} - T_s\right)_{\hat{e}_r} d\theta\right)\right]$, $t_c = \varepsilon t_a,\ u_p = u_a|_{x_f} + u_s + u_c,\ u_a|_{x_f}$ represents acoustic velocity (u_a) at the non-dimensional heater location x_f, $\partial u_a/\partial t_c|_{x_f}$ represents $\partial u_a/\partial t_c$ at x_f, $Re_c = \bar{\rho}\bar{u}l_c/\mu,\ Pe_c = \bar{\rho}\bar{u}l_c C_p/k,\ S_c$ represents the cross section area of the Rijke tube and ∇_c represents gradient in the length scale of the hydrodynamic zone l_c. The hydrodynamic velocity fluctuations u_c is transformed into another variable u_p (transformation is given above), so as to make the convective terms in the momentum equation to be same as that of the convective terms in the conventional momentum equation for incompressible flows (Mariappan and Sujith, 2010a). In performing the above transformation, one moves from an inertial to an accelerated frame of reference ($u_a|_{x_f}$ varies with time). As a consequence, an additional global acceleration term $\partial u_a/\partial t_c|_{x_f}$ appear in 4.6b (last term). The global acceleration term appears due to the two length scale nature of the problem (Klein, 1995). This global acceleration term is shown to have profound effects on the stability and limit cycle characteristics of the Rijke tube system (Mariappan and Sujith, 2010a). The present study also shows that the same global acceleration term appears in the adjoint equations and the mapping between the direct and adjoint variables. In particular the global acceleration term forms one of the coupling between the adjoint equations in the acoustic and hydrodynamic zone. The above observations are explained in § 4.6.1. The non-normal nature of the thermoacoustic interaction is investigated. One of the aims of the present paper is to obtain the optimum initial condition for maximum growth of perturbations at any given time T_{opt}. Hence, a brief explanation about non-normal operator and its

connection to the present system of equations (4.5 & 4.6) are given in the following section.

4.2 Non-normality and transient growth

A linear dynamical system ($d\chi/dt = L\chi$) is said to be non-normal if the linear operator 'L' governing the evolution of the system does not commute with its adjoint $L^\dagger$ ($LL^\dagger \neq L^\dagger L,\ \dagger$ indicates adjoint operator) (Golub and Loan, 1989). In such systems, the eigenmodes (eigenvectors) are non-orthogonal. Any initial condition for the system can be written as a linear combination of the eigenmodes. For a linearised system, stable under classical linear stability (all the eigenvalues lie in the left half of the complex plane), all the eigenmodes are decaying monotonically in time. However, in the case of non-normal system, the vectorial sum of the eigenmodes which gives the state of the system at any time 't' can increase (for suitable initial condition) for a short time and eventually decay after a long time (Schmid and Henningson, 2001; Balasubramanian and Sujith, 2008*a*). Mathematically a transient growth occurs in the evolution of the L_2 norm of the system $\left(||\chi||^2 = \chi^\dagger\chi\right)$, which can be related to a physcial energy in the disturbance (Schmid and Henningson, 2001; Nagaraja *et al.*, 2009; Mariappan and Sujith, 2010*b*). The interplay between non-normality (transient growth) and nonlinearity plays an important role in the subcritical transition to instability (Balasubramanian and Sujith, 2008*a*; Mariappan and Sujith, 2010*b*).

In order to study the non-normal nature of the present Rijke tube system, the system of equations (4.5, 4.6) are linearised, to obtain the linear operator 'L'. The linear operator L thus obtained does not commute with its adjoint. The system of equations in the acoustic zone (4.5) is shown to be non-normal due to the inclusion of the unsteady heat release term 'q' by Balasubramanian & SujithBalasubramanian and Sujith (2008*b*). Also the equation (4.6b) is nothing but the Navier-Stokes equation for incompressible flows, with an additional global acceleration term $\partial u_a/\partial t_c|_{x_f}$. Navier-Stokes equation is shown to be non-normal (Waleffe, 1995). Hence the coupled system of equations (4.5 & 4.6) is non-normal. The amount of transient growth to be obtained in a non-normal system depends on the initial condition.

One of the important quantity to study non-normal system is the maximum possible transient growth at a given time T_{opt}. The corresponding initial condition, which gives the maximum transient growth is termed as the optimum initial condition. Using the above system of equations (4.5 & 4.6) as the starting point, the adjoint optimisation technique is performed to obtain the optimum initial condition, which gives the maximum transient growth. Usual techniques of finding the optimum initial condition, such as SVD (**?**) are computationally prohibitive due to large number of grids (see table 4.1) involved in solving (4.6) as described earlier in the end of § **??**. As the first step in the optimisation procedure, the governing equations (4.5 & 4.6) (also called as direct equations) with the corresponding boundary conditions are written in the appropriate domain as explained in the following section.

4.3 Direct equations

This section deals with the direct equations governing the thermoacoustic instability in a Rijke tube. Since the heater coil in its primitive form is a cylinder (figure 3.1), the system of equations (4.6) is solved for the configuration of flow over an heated cylinder. A two dimensional flow over cylinder is considered, as the spacing between the heating wire filament is very large compared to the wire diameter (wire diameter $\sim mm$, coil diameter $\sim cm$). Typical steady state Reynolds number ($2Re_c$) based on the diameter of the wire filament is around 20 and hence vortex shedding does not occur (see Appendix of Mariappan & SujithMariappan and Sujith (2010*a*)). Due to the absence of vortex shedding phenomenon, only one-half of the flow field is simulated and the symmetry boundary condition is enforced. Plane polar coordinate system is used so as to implement the no-slip boundary condition on the surface of the wire filament (circular cylinder). Moreover, fluid viscosity and thermal conductivity are assumed to be independent of temperature so that momentum and energy equations are decoupled. Hence, the continuity and momentum equations are solved simultaneously. The velocity field thus obtained, is used to compute the temperature field. For simplicity in notation, the subscripts '*p*' and '*c*' are dropped from (4.6). The flow domain is shown in figure (C.1). The system of equations (4.6) in plane polar co-ordinates are the following:

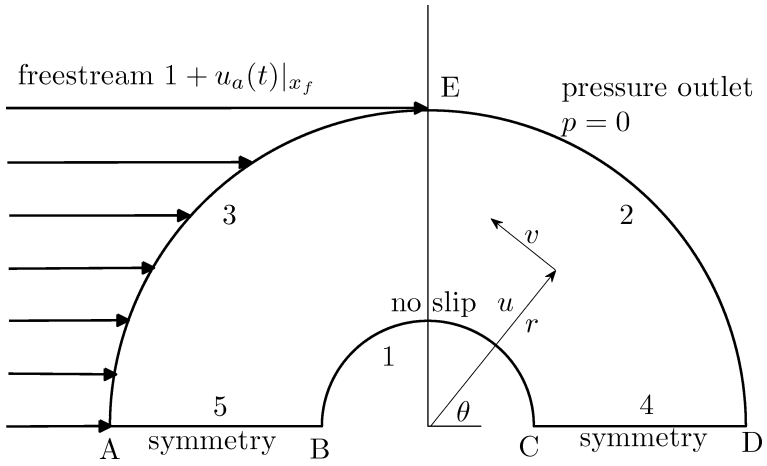

Figure 4.1: Flow domain and boundary conditions.

$$\text{Continuity}: \quad \frac{\partial u}{\partial r} + \frac{u}{r} + \frac{1}{r}\frac{\partial v}{\partial \theta} = 0 \tag{4.7a}$$

$$\text{`}r\text{' Momentum}: \quad \frac{\partial u}{\partial t} + \frac{\partial u^2}{\partial r} + \frac{1}{r}\frac{\partial uv}{\partial \theta} + \frac{u^2 - v^2}{r} = -\frac{\partial p}{\partial r} + \frac{1}{Re}\left(\nabla^2 u - \frac{u}{r^2} - \frac{2}{r^2}\frac{\partial v}{\partial \theta}\right) + \frac{\partial u_{ar}}{\partial t} \tag{4.7b}$$

$$\text{`}\theta\text{' Momentum}: \quad \frac{\partial v}{\partial t} + \frac{\partial uv}{\partial r} + \frac{1}{r}\frac{\partial v^2}{\partial \theta} + \frac{2uv}{r} = -\frac{1}{r}\frac{\partial p}{\partial \theta} + \frac{1}{\boldsymbol{Re}}\left(\nabla^2 v + \frac{2}{r^2}\frac{\partial u}{\partial \theta} - \frac{v}{r^2}\right) + \frac{\partial u_{a\theta}}{\partial t} \tag{4.7c}$$

$$\text{Energy}: \quad \frac{\partial T}{\partial t} + u\frac{\partial T}{\partial r} + \frac{v}{r}\frac{\partial T}{\partial \theta} = \frac{1}{\boldsymbol{Pe}}\nabla^2 T \tag{4.7d}$$

with the following boundary condition

$$\text{Cylinder surface } r = 1: \quad \left.\begin{aligned} &u(1,\theta) = v(1,\theta) = 0 \\ &\frac{\partial p(1,\theta)}{\partial r} = 0 \\ &T(1,\theta) = 1 \end{aligned}\right\} 0 \le \theta \le \pi$$

$$\text{Far field } r \to \infty: \quad \left.\begin{aligned} &u(r\to\infty,\theta) = 1 + u_a|_{x_f}\cos\theta \\ &v(r\to\infty,\theta) = 1 - u_a|_{x_f}\sin\theta \\ &\frac{\partial p(r\to\infty,\theta)}{\partial r} = 0 \\ &T(r\to\infty,\theta) = 0 \end{aligned}\right\} \frac{\pi}{2} \le \theta \le \pi, \quad \left.\begin{aligned} &\frac{\partial u(r\to\infty,\theta)}{\partial r} = 0 \\ &\frac{\partial v(r\to\infty,\theta)}{\partial r} = 0 \\ &p(r\to\infty,\theta) = 0 \\ &\frac{\partial T(r\to\infty,\theta)}{\partial r} = 0 \end{aligned}\right\} 0 \le \theta < \frac{\pi}{2}$$

$$\text{Symmetry } \theta = 0,\ \pi : \left.\begin{array}{l} \dfrac{\partial u(r,\theta)}{\partial \theta} = 0 \\ v(r,\theta) = 0 \\ \dfrac{\partial p(r,\theta)}{\partial \theta} = 0 \\ \dfrac{\partial T(r,\theta)}{\partial \theta} = 0 \end{array}\right\} 1 \leq r < \infty$$

where $\nabla^2 = \partial^2/\partial r^2 + \partial/(r\partial r) + 1/(r^2\partial\theta^2),\ u,\ v$ - velocity components in 'r' and 'θ' directions. Linear optimal is obtained in the present investigation; i.e. the optimum initial condition obtained from the linearised governing equations. The present paper applies the adjoint optimisation procedure to a problem which involves two length scale problems. Obtaining nonlinear optimal; i.e., the optimal initial condition obtained from the nonlinear governing equations is beyond the scope of the present paper. It is recommeded to first obtain the linear optimal and study the evolution of the linear optimal and understand the role of non-normality on the dynamics of the system. Obtaining the nonlinear optimal can the be performed as the next step. In obtaining the linear optimal, the governing equations (4.5, 4.7) are linearised. The system of equations (4.5) is already linear, whereas the system of equations (4.7) is nonlinear. The latter is linearised with the following decomposition $u = \bar{U} + u'$, $v = \bar{V} + v'$, $p = \bar{P} + p'$, $T = \bar{T} + T'$, where over bar $(\bar{})$ indicates the steady state variables and prime $(')$ indicates the fluctuations from the steady state. The decomposition of the variables is applied to (4.7) to

give the following linearised equations (primes $'$ are removed for convenience).

$$F_1 = \rho_s \frac{\partial u_a}{\partial t_a} + \frac{1}{\gamma}\frac{\partial p_a}{\partial x_a} = 0 \tag{4.9a}$$

$$F_2 = \frac{1}{\gamma}\frac{\partial p_a}{\partial t_a} + \frac{\partial u_a}{\partial x_a} + \zeta_n \omega_n p_a - \left(k \int_0^{\pi} \left.\frac{\partial T}{\partial r}\right|_{(1,\theta,t_a)} d\theta \right) \widehat{\delta}\ (x - x_f) = 0 \tag{4.9b}$$

$$F_3 = \frac{\partial u}{\partial r} + \frac{u}{r} + \frac{1}{r}\frac{\partial v}{\partial \theta} = 0 \tag{4.9c}$$

$$F_4 = \frac{\partial u}{\partial t_c} + 2\frac{\partial\left(\bar{U}u\right)}{\partial r} + \frac{1}{r}\frac{\partial\left(\bar{U}v + \bar{V}u\right)}{\partial \theta} + \frac{2}{r}\left(\bar{U}u - \bar{V}v\right) + \frac{\partial p}{\partial r} - \frac{1}{Re}\left(\nabla^2 u - \frac{u}{r^2} - \frac{2}{r^2}\frac{\partial v}{\partial \theta}\right) - \frac{\partial u_{af}}{\partial t}\cos\theta = 0 \tag{4.9d}$$

$$F_5 = \frac{\partial v}{\partial t_c} + \frac{\partial\left(\bar{U}v + \bar{V}u\right)}{\partial r} + \frac{2}{r}\frac{\partial\left(\bar{V}v\right)}{\partial \theta} + \frac{2}{r}\left(\bar{U}v + \bar{V}u\right) + \frac{1}{r}\frac{\partial p}{\partial \theta} - \frac{1}{\boldsymbol{Re}}\left(\nabla^2 v + \frac{2}{r^2}\frac{\partial u}{\partial \theta} - \frac{v}{r^2}\right) + \frac{\partial u_{af}}{\partial t}\sin\theta = 0 \tag{4.9e}$$

$$F_6 = \frac{\partial T}{\partial t_c} + \bar{U}\frac{\partial T}{\partial r} + u\frac{\partial \bar{T}}{\partial r} + \frac{\bar{V}}{r}\frac{\partial T}{\partial \theta} + \frac{v}{r}\frac{\partial \bar{T}}{\partial \theta} - \frac{1}{Pe}\nabla^2 T = 0 \tag{4.9f}$$

where, $k = 2l_w l_c\left(\tilde{T}_w - \tilde{T}_0^u\right)\Big/\left(Pe_c S_c \bar{T}\right)$, $\tilde{T}_w$ is the surface temperature of the heater wire, $\tilde{T}_0^u$ is the temperature upstream of the heater. The boundary conditions corresponding to (4.9) are the following:

Acoustic zone:

$$H_{a_1} = p_a\left(0, t\right) - p_{a0} = 0 \tag{4.10a}$$

$$H_{a_2} = p_a\left(1, t\right) - p_{a1} = 0 \tag{4.10b}$$

Hydrodynamic zone:

In the hydrodynamic zone, the numerical subscript indicates the location of the boundary condition as in figure (C.1), whereas the last subscript represents the variable to which the boundary condition is applied. For eg. H_{h1_u} has the numerical subscript '1', which corresponds to the surface of the cylinder as shown in figure C.1 and the last

subscript 'u' represents the variable u..

$$H_{h1_u} = u(1,\theta,t) - u_0 = 0, \qquad 0 \le \theta \le \pi \tag{4.11a}$$

$$H_{h2_u} = \partial u(\infty,\theta,t)/\partial r - u_{\infty d} = 0, \qquad 0 \le \theta \le \pi/2 \tag{4.11b}$$

$$H_{h3_u} = u(\infty,\theta,t) - u_{af}\cos\theta = 0, \qquad \pi/2 < \theta \le \pi \tag{4.11c}$$

$$H_{h4_u} = \partial u(r,0,t)/\partial\theta - u_{s1} = 0, \qquad 1 \le r < \infty \tag{4.11d}$$

$$H_{h5_u} = \partial u(r,\pi,t)/\partial\theta - u_{s2} = 0, \qquad 1 \le r < \infty \tag{4.11e}$$

$$H_{h1_v} = v(1,\theta,t) - v_0 = 0, \qquad 0 \le \theta \le \pi \tag{4.12a}$$

$$H_{h2_v} = \partial v(\infty,\theta,t)/\partial r - v_{\infty d} = 0, \qquad 0 \le \theta \le \pi/2 \tag{4.12b}$$

$$H_{h3_v} = v(\infty,\theta,t) + u_{af}\sin\theta = 0, \qquad \pi/2 < \theta \le \pi \tag{4.12c}$$

$$H_{h4_v} = v(r,0,t) - v_{s1} = 0, \qquad 1 \le r < \infty \tag{4.12d}$$

$$H_{h5_v} = v(r,\pi,t) - v_{s2} = 0, \qquad 1 \le r < \infty \tag{4.12e}$$

$$H_{h1_p} = \partial p(1,\theta,t)/\partial r - p_{0d} = 0, \qquad 0 \le \theta \le \pi \tag{4.13a}$$

$$H_{h2_p} = p(\infty,\theta,t) - p_\infty = 0, \qquad 0 \le \theta \le \pi/2 \tag{4.13b}$$

$$H_{h3_p} = \partial p(\infty,\theta,t)/\partial r - p_{\infty d} = 0, \qquad \pi/2 < \theta \le \pi \tag{4.13c}$$

$$H_{h4_p} = \partial p(r,0,t)/\partial\theta - p_{s1} = 0, \qquad 1 \le r < \infty \tag{4.13d}$$

$$H_{h5_p} = \partial p(r,\pi,t)/\partial\theta - p_{s2} = 0, \qquad 1 \le r < \infty \tag{4.13e}$$

$$H_{h1_T} = T(1,\theta,t) - T_0 = 0, \qquad 0 \le \theta \le \pi \tag{4.14a}$$

$$H_{h2_T} = \partial T(\infty,\theta,t)/\partial r - T_{\infty d} = 0, \qquad 0 \le \theta \le \pi/2 \tag{4.14b}$$

$$H_{h3_T} = T(\infty,\theta,t) - T_\infty = 0, \qquad \pi/2 < \theta \le \pi \tag{4.14c}$$

$$H_{h4_T} = \partial T(r,0,t)/\partial\theta - T_{s1} = 0, \qquad 1 \le r < \infty \tag{4.14d}$$

$$H_{h5_T} = \partial T(r,\pi,t)/\partial\theta - T_{s2} = 0, \qquad 1 \le r < \infty \tag{4.14e}$$

The initial conditions for (4.9) are given by

$$G_{u_a} = u_a(x,0) - u_a^0 = 0 \tag{4.15a}$$

$$G_{p_a} = p_a(x,0) - p_a^0 = 0 \tag{4.15b}$$

$$G_u = u(r,\theta,0) - u^0 = 0 \tag{4.15c}$$

$$G_v = v(r,\theta,0) - v^0 = 0 \tag{4.15d}$$

$$G_p = p(r,\theta,0) - p^0 = 0 \tag{4.15e}$$

$$G_T = T(r,\theta,0) - T^0 = 0 \tag{4.15f}$$

where $p_{a0} = p_{a1} = u_0 = u_{\infty d} = u_{s1} = u_{s2} = ... = T_{s1} = T_{s2} = 0$. Having obtained the linearised governing equations for the Rijke tube system, the next step is to define an energy, which measures the growth or decay of disturbances. The disturbance energy thus chosen is used to measure the non-normal nature of the system (see § 4.2). There has been a significant discussion in the past on choosing the correct energy in order to describe the non-normal nature of the system (Hanifi *et al.*, 1996; Sameen and Govindarajan, 2007; Guegan *et al.*, 2008). For incompressible flows the total kinetic energy of the perturbations over the domain is used as a measure (norm) in order to quantify the non-normal nature of the fluid flows (Schmid and Henningson, 2001). Also, when the total kinetic energy of the perturbations is used as a norm for incompressible flows, the contribution to the norm from nonlinear terms vanishes to zero. This is due to the fact that the nonlinear terms in the Navier-Stokes equation for incompressible flows are energy conserving in nature (provided the perturbations vanishes at the boundary, like in plane Poiseuille flow). Since the nonlinear terms are energy conserving, the transition to instability happens via linear mechanism - transient growth due to the non-normal nature of the system. Also it was shown that non-normal nature of the governing linearised operator is a necessary condition for the subcritical transition to instability in shear flows (Henningson *et al.*, 1993; Henningson and Reddy, 1994). The same conclusion can be extended to any system, where the nonlinear terms conserve energy (Krechetnikov and Marsden, 2009).

In the analysis of thermoacoustic instability in a model problem, Rijke tube, acoustic energy is chosen as the norm to study the non-normal nature of the thermoacoustic

interaction (Balasubramanian and Sujith, 2008*b*; Nagaraja *et al.*, 2009). In the above model problem of thermoacoustic interaction in a Rijke tube, an algebraic model (quasi-steady) for the unsteady heat release rate from the electrical heater due to acoustic velocity is used. Hence the degrees of freedom of the dynamical system (modeling the Rijke tube) is restricted to the acoustic variables. Instead of an algebraic model for the response of the heat source, solving the equations, which governs the dynamics of heat source gives a more representative solution for the physical problem. The inclusion of the dynamics of the heat source increases the number of degrees of the freedom of the thermoacoustic system, which now comprises of not only the acoustic variables but also the variables representing the dynamics of the heat source. The degrees of freedom in the unsteady heat release rate are shown to be important in the context of the non-normal nature of thermoacoustic instability in solid rocket motor (Mariappan and Sujith, 2010*b*). The energy defined in Mariappan & SujithMariappan and Sujith (2010*b*) not only included acoustic energy, but also the total contribution from the variables representing the dynamics of the heat source. The disturbance energy was obtained so that the L_2 norm of the state space variables represented the disturbance energy. This is due to the fact that L_2 norm of a dynamical system can be easily obtained using SVD (Golub and Loan, 1989) for which the tools are already well developed. Although, the disturbance energy was not obtained from rigorous mathematical arguments, the paper (Mariappan and Sujith, 2010*b*) explained the importance of the variables representing the dynamics of the heat source in the context of the non-normal nature of the system. Hence in the present paper, the dynamics of the heat source (4.9*c-f*) is included.

As an extension of acoustic energy, which gives the energy in isentropic disturbance (Rienstra and Hirschberg, 2008), Myers' energy (Myers, 1991) is used as the disturbance energy in the present paper. Myers' energy gives the energy in an arbitrary disturbance (not necessarily an isentropic disturbance) in non-reacting flows. An extension of Myers' energy for reacting flows is given by Nicoud & PoinsotNicoud and Poinsot (2005) , Giauque, Poinsot, Brear & NicoudGiauque *et al.* (2006). The nonlinear terms in the governing equations (4.2) do not conserve Myers' energy. This is in contrast to the nonlinear terms in the Navier-Stokes equation (governing incompressible flows), which conserves kinetic energy Henningson and Reddy (1994). Although the property of energy conservation by the nonlinear terms is not present in Myers' energy

(Myers, 1991), it is the most appropriate form of disturbance energy that is available at present to analyse the non-normal nature of the Rijke tube system. Myers' energy for isentropic and incompressible flows simplifies to acoustic and kinetic energy respectively (Chu, 1965; Myers, 1991). In the present problem, there are two length scales involved (see § 4.1). Hence the derivation of disturbance energy from Myers' energy has to be performed carefully and is performed in the following section.

4.4 Myers' energy

Disturbance energy is defined as the energy in any perturbations and can be used as a measure of growth or decay of the perturbations in a dynamical system. The starting point for the derivation of generalized disturbance energy is the expression from MyersMyers (1991), who obtained energy in any arbitrary perturbations with mean flow taken into account. The perturbations are not restricted to an acoustic disturbance. They can be any generalised perturbations in the flow field. In the present paper, the disturbance energy corresponding to the second order energy corallory from MyersMyers (1991) is used, as the asymptotic expansion (4.4) has terms upto second order in M. Moreover the leading order (in powers of M) representation of the disturbance energy (exact disturbance energy) corresponding to the exact energy corollary is precisely same as the disturbance energy (second order disturbance energy) corresponding to the second order energy corollary MyersMyers (1991). Thus it is sufficient to use the second order disturbance energy expression for the definition of disturbance energy in the present context. The disturbance energy per unit volume $\left(\tilde{E}_v\right)$, as defined by MyersMyers (1991) for (4.3) is

$$\tilde{E}_v = \frac{\bar{\rho}\bar{U}^2}{2}\left(\frac{\bar{P}}{\bar{\rho}\bar{U}^2}\left(\left(\frac{\rho'}{\rho_s}\right)^2 + \frac{1}{\gamma-1}\left(\frac{T'}{T_s}\right)^2\right) + \rho_s u'^2 + 2u_s\rho' u'\right) \tag{4.16}$$

where prime ($'$) represents the fluctuating quantities from the steady state. The fluctuating quantities in the above equation are identified from the ansatz (4.4) as following:

$$\begin{aligned} \rho' = M\rho_a,\ u' = u_a + u_c, \\ p' = Mp_a + M^2 p_c,\ T' = T_c + MT_a \end{aligned} \tag{4.17}$$

Substituting the above expressions in (4.16) gives

$$\tilde{E}_v = \frac{\bar{\rho}\bar{U}^2}{2} \left(\begin{array}{l} \dfrac{\bar{P}}{\bar{\rho}\bar{U}^2} \left(\left(\dfrac{M\rho_a}{\rho_s} \right)^2 + \dfrac{1}{\gamma - 1} \left(\dfrac{T_c + MT_a}{T_s} \right)^2 \right) \\ + \rho_s \left(u_a + u_c \right)^2 + 2u_s \left(M\rho_a \right) \left(u_a + u_c \right) \end{array} \right) \tag{4.18}$$

The total disturbance energy ($\tilde{E}_d$) is the integral of $\tilde{E}_v$ over the entire volume. The volume is divided into three regions. The first one is the acoustic zone upstream of the heater, second one is the hydrodynamic zone and the third one is again the acoustic zone downstream of the heater (figure 3.1). The disturbance energy in the three zones are then summed to get the total disturbance energy as follows:

$$\tilde{E}_d = S_c \int_0^{x_f - \varsigma} \tilde{E}_v d\tilde{x}_a + \iiint_{V_c} \tilde{E}_v d\tilde{V}_c + S_c \int_{x_f + \varsigma}^{l_a} \tilde{E}_v d\tilde{x}_a,\ \ \varsigma \to 0 \tag{4.19}$$

The above integrals are evaluated in the appropriate zones as explained in the following subsections. Disturbance energy in the acoustic zone is first evaluated as follows.

4.4.1 Acoustic zone

The first and last terms in (4.19) represent the energy stored in the acoustic field. The expression for acoustic energy is $\tilde{E}_{ac} = S_c \left(\int_0^{x_f - \varsigma} \tilde{E}_v d\tilde{x}_a + \int_{x_f + \varsigma}^{l_a} \tilde{E}_v d\tilde{x}_a \right),\ \varsigma \to 0.$ $\tilde{E}_{ac}$ is evaluated with the following additional equations, which simplifies the expression for $\tilde{E}_v$ in the acoustic zone.

$$\begin{aligned} u_c = 0,\ \delta \to 0,\ \frac{T_a}{T_s} = p_a - \frac{\rho_a}{\rho_s} \to \text{equation of state} \\ \frac{\rho_a}{\rho_s} = \frac{1}{\gamma} p_a \to \text{isentropic relation} \end{aligned} \tag{4.20}$$

Using the above equation, acoustic energy ($\tilde{E}_{ac}$) is obtained as:

$$\tilde{E}_{ac} = \left(\bar{\rho}\bar{U}^2 S_c l_a/2\right) \left(\begin{array}{l} \int\limits_0^{x_f-\varsigma} \left(\left(\frac{p_a}{\gamma}\right)^2 + \rho_s u_a^2 + 2M\rho_s u_s u_a \left(\frac{p_a}{\gamma}\right) \right) dx_a \\ + \int\limits_{x_f+\varsigma}^{1} \left(\left(\frac{p_a}{\gamma}\right)^2 + \rho_s u_a^2 + 2M\rho_s u_s u_a \left(\frac{p_a}{\gamma}\right) \right) dx_a \end{array} \right), \varsigma \to 0 \tag{4.21}$$

Now, as $M \to 0$, the last term in the integrals drops out. Further, non-dimensionalising $\tilde{E}_{ac}$ using $\bar{\rho}\bar{U}^2 S_c l_a/2$ gives the final form of non-dimensional acoustic energy (E_{ac}).

$$E_{ac} = \frac{\tilde{E}_{ac}}{\bar{\rho}\bar{U}^2 S_c l_a/2} = \int\limits_0^{x_f-\varsigma} \left(\left(\frac{p_a}{\gamma}\right)^2 + \rho_s u_a^2 \right) dx_a + \int\limits_{x_f+\varsigma}^{1} \left(\left(\frac{p_a}{\gamma}\right)^2 + \rho_s u_a^2 \right) dx_a, \; \varsigma \to 0 \tag{4.22}$$

It is important to note that the effect of mean flow does not appear in the acoustic energy, because the flow is at very low Mach number. The next step is the evaluation of the second integral in (4.19), which represents the disturbance energy in the hydrodynamic zone.

4.4.2 Hydrodynamic zone

Evaluation of disturbance energy in the hydrodynamic zone is performed as follows

$$\tilde{E}_c = \iiint\limits_{V_c} \tilde{E}_v d\tilde{V}_c = \frac{\bar{\rho}\bar{U}^2}{2} \iiint\limits_{V_c} \left(\begin{array}{l} \frac{1}{\gamma M^2} \left((M\rho_a)^2 + \frac{1}{\gamma - 1} \left(T_c + MT_a\right)^2 \right) \\ + \left(u_a + u_c\right)^2 + 2u_s \left(M\rho_a\right)\left(u_a + u_c\right) \end{array} \right) \tag{4.23}$$

where, V_c is the volume of hydrodynamic zone, $\rho_s = 1$ due to the constant density assumption (Buckmaster, 2002; Kurdyumov and Matalon, 2004) and non-dimensionalisation (§ 4.1) performed in the hydrodynamic zone. In obtaining $\tilde{E}_c$ in the hydrodynamic zone, the leading order contribution for $\tilde{E}_c$ from all the state space variables (u_c, T_c) in the hydrodynamic zone is taken into account. It is important to include the contribution (upto the leading order) from all the state space variables in $\tilde{E}_d$. Otherwise the mapping between the direct and adjoint variables (see 4.36 & 4.37) will be inconsistent. Non-dimensionalising $\tilde{E}_c$ using $\bar{\rho}\bar{U}^2 S_c l_a/2$ as before for $\tilde{E}_{ac}$ leads to the following ex-

pression for the non-dimensionalised disturbance energy in the hydrodynamic zone.

$$E_c = \frac{l_w l_c^2}{S_c l_a} \int_{r=1}^{\infty} \int_{\theta=0}^{2\pi} \left(u_c + u_a|_{x_f} \right)^2 r dr d\theta + \frac{l_w \epsilon^2}{S_c l_a \gamma \left(\gamma - 1 \right)} \int_{r=1}^{\infty} \int_{\theta=0}^{2\pi} \frac{T_c^2}{T_s} r dr d\theta \qquad (4.24)$$

According to our convention and linearisation of the variables as in § 4.3, E_c takes the following form

$$E_c = \frac{2 l_w l_c^2}{S_c l_a} \int_{r=1}^{\infty} \int_{\theta=0}^{\pi} \left(u^2 + v^2 \right) r dr d\theta + \frac{2 l_w l_c^2 \left(\tilde{T}_w - \tilde{T}_0^u \right)}{S_c l_a \gamma M \left(\gamma - 1 \right) \bar{T}} \int_{r=1}^{\infty} \int_{\theta=0}^{\pi} \frac{T^2}{T_s} r dr d\theta \qquad (4.25)$$

The symmetry boundary condition is enforced in the hydrodynamic zone (see appendix of Mariappan & SujithMariappan and Sujith (2010*a*)) and hence a factor '2' is included in the coefficients of (4.25). In the above equation, the limits of integration represent the boundary of the hydrodynamic zone in plane polar co-ordinates. The temperature fluctuations (T) in the hydrodynamic zone vanishes as one moves away from the hydrodynamic zone $(r \rightarrow \infty)$ due to its boundary conditions (4.14b & 4.14c). Thus the quantity T^2/T_s in the second integral of (4.25) vanishes as $(r \rightarrow \infty)$. It is also observed from the present numerical simulation that T^2/T_s decays to zero faster than $1/r^2$ for large values of 'r' $(r \sim 50)$. Hence the second integral in (4.25) converges. On the other hand, the freestream of the hydrodynamic zone is perturbed by the acoustic velocity $u_a|_{x_f}$ (see boundary conditions 4.11b, 4.11c, 4.12b & 4.12c). Hence the quantity $u^2 + v^2$ in the first integral of (4.25) does not vanish as $r \rightarrow \infty$, leaving a non-convergent integral. A convergence factor $\lambda(r) = e^{-((r-1)/L_{cu})^2}$ is used to make the integral convergent and E_c takes the form as shown in (4.26). In the expression for $\lambda(r)$, L_{cu} is the cut off radius, which limits the contribution of $u^2 + v^2$ to E_c beyond the cut off radius. It is also verified from the present simulation that optimum initial condition obtained does not vary significantly beyond some value of L_{cu} (see figure 4.3 & § 4.8.2). A similiar technique is followed by Guegan, Schmid & HuerreGuegan *et al.* (2008) in the problem of obtaining a spatial optimal disturbance in an infinite upstream

environment similiar to the present case. The final expression for E_c is given as follows:

$$E_c = \frac{2l_w l_c^2}{S_c l_a} \int_{r=1}^{\infty} \int_{\theta=0}^{\pi} \lambda(r) \left(u^2 + v^2\right) r dr d\theta + \frac{2l_w l_c^2 \left(\tilde{T}_w - \tilde{T}_0^u\right)}{S_c l_a \gamma M (\gamma - 1) \bar{\bar{T}}} \int_{r=1}^{\infty} \int_{\theta=0}^{\pi} \frac{T^2}{T_s} r dr d\theta \tag{4.26}$$

Now all the terms in (4.19) are evaluated. The sum of equations (4.22) and (4.26) give the total non-dimensionalised disturbance energy (E_d) and is given by:

$$\begin{aligned} E_d = E_{ac} + E_c = & \underbrace{\int_0^{x_f - \varsigma} \left(\left(\frac{p_a}{\gamma} \right)^2 + \rho_s u_a^2 \right) dx_a + \int_{x_f + \varsigma}^{1} \left(\left(\frac{p_a}{\gamma} \right)^2 + \rho_s u_a^2 \right) dx_a}_{\text{acoustic zone}} \\ & \underbrace{+ \frac{2l_w l_c^2}{S_c l_a} \int_{r=1}^{\infty} \int_{\theta=0}^{\pi} \lambda(r) \left(u^2 + v^2\right) r dr d\theta + \frac{2l_w l_c^2 \left(\tilde{T}_w - \tilde{T}_0^u\right)}{S_c l_a \gamma M (\gamma - 1) \bar{\bar{T}}} \int_{r=1}^{\infty} \int_{\theta=0}^{\pi} \frac{T^2}{T_s} r dr d\theta, \; \varsigma \to 0}_{\text{hydrodynamic zone}} \end{aligned} \tag{4.27}$$

The disturbance energy (E_d) obtained is also used as a measure for examining the growth or decay of oscillations in the system. The above expression for disturbance energy (4.27) is used as the norm to study the non-normal nature of the present Rijke tube system. This norm is used in the cost functional, which is to be maximised over all possible initial conditions and is taken up in the following section.

4.5 Definition of the cost functional

As already explained in § 4.2, thermoacoustic systems are non-normal. Due to the non-normal nature, the system shows a transient growth in energy during its evolution of an initial perturbation, even for a linearly stable system. But eventually the oscillations decay to zero. This transient growth must be measured with some scalar measure. The last part of § 4.3 dealt with the energy to be used to analyse the non-normal nature of the present thermoacoustic system. In the present paper, amplification of energy (from $t = 0$) in a small arbitrary perturbation (Myers' energy, § 4.4) is used as the measure for quantifying transient growth. The cost functional ($\Im$, equation 4.28) is defined as

the ratio of E_d^t at time $t = T$ and $t = 0$.

$$\Im = \frac{E_d^{T_{opt}}\left(p_a, u_a, u, v, p, T\right)}{E_d^0\left(p_a, u_a, u, v, p, T\right)} \tag{4.28}$$

where $E_d^t = \int_0^1 \left(p_a^2 + \rho_s u_a^2\right)|_{(x,t)}\, dx + \int_{r=1}^{\infty}\int_{\theta=0}^{\pi} \left(\beta T^2/T_s + \alpha\lambda\left(r\right)\left(u^2+v^2\right)\right)|_{(r,\theta,t)}\, r dr d\theta$, $\alpha = 2l_w l_c^2/S_c l_a,\ \beta = 2l_w l_c^2\left(\tilde{T}_w - \tilde{T}_0\right)\Big/\left(S_c l_a \gamma M\left(\gamma-1\right)\bar{T}\right)$ (see 4.27). Thus $\Im$ represents the amplification of the disturbance energy at $t = T_{opt}$. The above quantity ($\Im$) depends on the initial condition of the system. The aim of the present study is to identify that initial condition, which maximises $\Im$ at time $t = T_{opt}$. The above is an optimisation problem, with constraints as the governing equations (4.9), boundary (4.10, 4.11, 4.12, 4.13 & 4.14) and initial conditions (4.15). This constrained optimisation problem is converted into an unconstrained problem by introducing the Lagrange function (Γ), corresponding to the above cost functional (4.28), governing equations (4.9), boundary (4.10, 4.11, 4.12, 4.13 & 4.14) and initial conditions (4.15). The above technique is explained by GunzburgerGunzburger (2003). The expression for Γ is given by the following:

$$\begin{aligned}
\Gamma = \underbrace{\Im}_{\text{cost functional}} & \underbrace{- \left\langle F_1, \tilde{u}_a\right\rangle_a - \left\langle F_2, \tilde{p}_a\right\rangle_a - \left\langle F_3, \tilde{u}\right\rangle_h - \left\langle F_4, \tilde{v}\right\rangle_h - \left\langle F_5, \tilde{p}\right\rangle_h - \left\langle F_6, \tilde{T}\right\rangle_h}_{\text{governing equations}} \\
& \underbrace{\begin{aligned}
& - \sum_{m=0,1}\left\{H_{a_m}, \tilde{H}_{a_m}\right\}_a - \sum_{n=u,v,p,T}\left\{H_{h1_n}, \tilde{H}_{h1_n}\right\}_{h_{rs}} - \sum_{n=u,v,p,T}\left\{H_{h2_n}, \tilde{H}_{h2_n}\right\}_{h_{r1\infty}} \\
& - \sum_{n=u,v,p,T}\left\{H_{h3_n}, \tilde{H}_{h3_n}\right\}_{h_{r2\infty}} - \sum_{n=u,v,p,T}\left\{H_{h4_n}, \tilde{H}_{h4_n}\right\}_{h_\theta} - \sum_{n=u,v,p,T}\left\{H_{h5_n}, \tilde{H}_{h5_n}\right\}_{h_\theta}
\end{aligned}}_{\text{boundary conditions}} \\
& \underbrace{- \sum_{n=u_a,p_a}\left[G_n, \tilde{G}_n\right]_a - \sum_{n=u,v,p,T}\left[G_n, \tilde{G}_n\right]_h}_{\text{initial conditions}}
\end{aligned} \tag{4.29}$$

where

$$\langle q_1, q_2 \rangle_a = \int_{t=0}^{T_{opt}} \int_{x=0}^{1} q_1 q_2 dx dt, \;\; \langle q_1, q_2 \rangle_h = \int_{t=0}^{T_{opt}} \int_{\theta=0}^{\pi} \int_{r=1}^{\infty} q_1 q_2 r dr d\theta dt,$$

$$\{q_1, q_2\}_a = \int_{t=0}^{T_{opt}} q_1 q_2 dt, \;\; \{q_1, q_2\}_{h_{rs}} = \int_{t=0}^{T_{opt}} \int_{\theta=0}^{\pi} q_1 q_2 d\theta dt,$$

$$\{q_1, q_2\}_{h_{r1\infty}} = \int_{t=0}^{T_{opt}} \int_{\theta=0}^{\pi/2} q_1 q_2 r d\theta dt \Big|_{r\to\infty}, \;\; \{q_1, q_2\}_{h_{r2\infty}} = \int_{t=0}^{T_{opt}} \int_{\theta=\pi/2}^{\pi} q_1 q_2 r d\theta dt \Big|_{r\to\infty},$$

$$\{q_1, q_2\}_{h_\theta} = \int_{t=0}^{T_{opt}} \int_{r=1}^{\infty} q_1 q_2 dr dt, \;\; [q_1, q_2]_a = \int_{x=0}^{1} q_1 q_2 dx, \;\; [q_1, q_2]_h = \int_{\theta=0}^{\pi} \int_{r=1}^{\infty} q_1 q_2 r dr d\theta$$

Tilde ($\tilde{}$) represents the adjoint variables (in general called 'Lagrange multipliers'). Now the next step in the optimisation procedure is to derive the adjoint equations and the corresponding adjoint boundary conditions, which is performed in the next section.

4.6 Adjoint system

Maximisation of $\Im$ requires the first variation of Γ with respect to the direct and adjoint variables must be zero (Gunzburger, 2003). The zeros of the first variations of Γ $\left(\partial\Gamma/\partial\tilde{u}_a = \partial\Gamma \Big/ \partial\tilde{p}_a = ... = \partial\Gamma \Big/ \partial\tilde{G}_T = 0\right)$ with respect to the adjoint variables, give back the original governing equations (4.9) along with the initial (4.15) and boundary conditions (4.10, 4.11, 4.12, 4.13 & 4.14). The zeros of the first variations of Γ $(\partial\Gamma/\partial u_a = \partial\Gamma/\partial p_a = ... = \partial\Gamma/\partial G_T = 0)$ with respect to the direct variables, give rise to the adjoint equations with the adjoint initial and boundary conditions. A brief indication of the steps involved in deriving the adjoint equation and the corresponding boundary condition are given in Appendix D.

4.6.1 Adjoint equations

In the present paper, the derivation of the adjoint equations and the corresponding boundary and initial conditions is similar to that in Corbett & BottaroCorbett and Bot-

taro (2001) and Guegan, Schmid & HuerreGuegan *et al.* (2008). The adjoint equations obtained after performing the steps indicated in Appendix D are

$$\tilde{F}_1 = \rho_s \frac{\partial \tilde{u}_a}{\partial t_a} + \frac{1}{\gamma}\frac{\partial \tilde{p}_a}{\partial x_a} + \left(\int_{\theta=0}^{\pi} \int_{r=1}^{\infty} \left(\sin\theta \frac{\partial \tilde{v}}{\partial t_c} - \cos\theta \frac{\partial \tilde{u}}{\partial t_c} \right) r dr d\theta \right) \widehat{\delta}\,(x - x_f) = 0 \tag{4.30a}$$

$$\tilde{F}_2 = \frac{1}{\gamma}\frac{\partial \tilde{p}_a}{\partial t_a} + \frac{\partial \tilde{u}_a}{\partial x_a} - \zeta_n \omega_n \tilde{p}_a = 0 \tag{4.30b}$$

$$\tilde{F}_3 = \frac{\partial \tilde{u}}{\partial r} + \frac{\tilde{u}}{r} + \frac{1}{r}\frac{\partial \tilde{v}}{\partial \theta} = 0 \tag{4.30c}$$

$$\tilde{F}_4 = \frac{\partial \tilde{u}}{\partial t_c} + 2\bar{U}\frac{\partial \tilde{u}}{\partial r} + \frac{\bar{V}}{r}\frac{\partial \tilde{u}}{\partial \theta} + \bar{V}\frac{\partial \tilde{v}}{\partial r} - \frac{\bar{V}\tilde{v}}{r} + \frac{\partial \tilde{p}}{\partial r} - \frac{\partial \bar{T}}{\partial r}\tilde{T} + \frac{1}{Re}\left(\nabla^2 \tilde{u} - \frac{\tilde{u}}{r^2} - \frac{2}{r^2}\frac{\partial \tilde{v}}{\partial \theta} \right) = 0 \tag{4.30d}$$

$$\tilde{F}_5 = \frac{\partial \tilde{v}}{\partial t_c} + \bar{U}\frac{\partial \tilde{v}}{\partial r} - \frac{\bar{U}\tilde{v}}{r} + \frac{\bar{U}}{r}\frac{\partial \tilde{u}}{\partial \theta} - 2\bar{V}\frac{\partial \tilde{u}}{\partial r} + \frac{1}{r}\frac{\partial \tilde{p}}{\partial \theta} - \frac{1}{r}\frac{\partial \bar{T}}{\partial \theta}\tilde{T} + \frac{1}{Re}\left(\nabla^2 \tilde{v} + \frac{2}{r^2}\frac{\partial \tilde{u}}{\partial \theta} - \frac{\tilde{v}}{r^2} \right) = 0 \tag{4.30e}$$

$$\tilde{F}_6 = \frac{\partial \tilde{T}}{\partial t_c} + \bar{U}\frac{\partial \tilde{T}}{\partial r} + \frac{\bar{V}}{r}\frac{\partial \tilde{T}}{\partial \theta} + \frac{1}{Pe}\nabla^2 \tilde{T} = 0 \tag{4.30f}$$

There are two significant differences between the direct (4.9) and adjoint (4.30) equations and it is useful to discuss about them in the present context. The first difference is that the direct energy equation $F_6 = 0$ (4.9f) in the hydrodynamic zone is solved after obtaining the direct velocity fields from solving $F_3 = F_4 = F_5 = 0$ (4.9c, 4.9d & 4.9e). The temperature field T thus obtained is used as the source in the acoustic energy equation $F_2 = 0$ (4.9b). Thus the order in which the direct equations are solved is $F_3 = F_4 = F_5 = 0 \rightarrow F_6 = 0 \rightarrow F_1 = F_2 = 0$. On the other hand, in solving the adjoint equations (4.30) an exactly reverse order is employed. Note that the adjoint energy equations $\tilde{F}_6 = 0$ (4.30f) does not have any adjoint velocity fields but $\tilde{T}$ appears in the source terms of the adjoint momentum equations $\tilde{F}_4 = \tilde{F}_5 = 0$ (4.30d & 4.30e). Hence (4.30f) is solved first, followed by solving simultaneously (4.30c, 4.30d & 4.30e). The obtained adjoint velocity fields ($\tilde{u}$ & $\tilde{v}$) acts as a source for the adjoint acoustic momen-

tum equation $\tilde{F}_1 = 0$ (4.30a). Thus the order in which the adjoint equations are solved are as follows; $\tilde{F}_6 = 0 \rightarrow \tilde{F}_3 = \tilde{F}_4 = \tilde{F}_5 = 0 \rightarrow \tilde{F}_1 = \tilde{F}_2 = 0$. Hence the adjoint equations are solved exactly in the reverse order as that of the direct equations.

The second difference is the following. The Laplacian operator ∇^2 is self-adjoint (Appendix D.0.2). Other operators like gradient ∇ changes its sign (Appendix D.0.1). Hence there is a difference in the sign of the diffusion terms in the adjoint equations (4.30*d-f*, adjoint equations are multiplied by '-1' to make the term $\partial/\partial t$ positive) in-comparison to the diffusion terms (associated with the damping in the system) in the direct equations (4.9*d-f*). Also note that the damping term $\zeta_n \omega_n p_a$ in the direct acoustic energy equation (4.9b) changes its sign in the adjoint acoustic energy equation (4.30b). Thus the diffusion terms, which dampen the perturbations during the forward evolution of the direct equations (4.9), dampen the perturbations during the backward evolution of the adjoint equations (4.30). This observation is consistent with the solution procedure for solving the direct and adjoint equations, where the direct equations are marched forward in time, while the adjoint equations are marched backward in time. The above solution procedure for the direct and adjoint equations is discussed later in § 4.7.

As mentioned in § 4.1, the global acceleration term in the direct equations, last term in the momentum equations of the hydrodynamic zone, $(\partial u_{af}/\partial t)\cos\theta$ in (4.9d) & $-(\partial u_{af}/\partial t)\sin\theta$ in (4.9e) has profound implications in the adjoint equations (4.30) as follows. The term $-\int_{\theta=0}^{\pi}\int_{r=1}^{\infty}\left(\sin\theta\,(\partial\tilde{v}/\partial t_c) - \cos\theta\,(\partial\tilde{u}/\partial t_c)\right) r dr d\theta$ appearing in the adjoint acoustic momentum equation (4.30a) acts a source term from the hydrodynamic zone to the acoustic zone. The above term can be identified as an adjoint unsteady heat release rate term $\tilde{q}$ corresponding to the unsteady heat release rate term $q = k\int_0^{\pi}(\partial T/\partial r)|_{(1,\theta,t_a)}\,d\theta$ in the direct acoustic energy equation (4.9b). The origin of the adjoint heat release term $\tilde{q}$ is associated with the global acceleration term in the direct equations. During one of the steps in the extremisation of the Lagrangian Γ (§ 4.28), the global acceleration terms in (4.9d & 4.9e) are integrated by parts (as briefly explained in appendix D). The integrals obtained after the process (boundary terms also appear, which enter the mapping between the direct and adjoint variables and will be explained in § 4.6.3) appear as $\tilde{q}$. Thus the role of global acceleration term is identified as the coupling term from the adjoint equations in the hydrodynamic zone to the adjoint

equations in the acoustic zone.

4.6.2 Adjoint boundary conditions

The boundary conditions corresponding to (4.30) are the following:

Acoustic zone:

$$\tilde{p}_a\left(0,t\right)=\tilde{p}_a\left(1,t\right)=0 \tag{4.31}$$

Hydrodynamic zone:

$$\tilde{u}(1,\theta,t)=0, \qquad 0\leq\theta\leq\pi \tag{4.32a}$$

$$\tilde{u}(\infty,\theta,t)=0, \qquad 0\leq\theta\leq\pi \tag{4.32b}$$

$$\partial\tilde{u}(r,0,t)/\partial\theta=\partial\tilde{u}(r,\pi,t)/\partial\theta=0, \qquad 1\leq r<\infty \tag{4.32c}$$

$$\tilde{v}(1,\theta,t)=0, \qquad 0\leq\theta\leq\pi \tag{4.33a}$$

$$\tilde{v}(\infty,\theta,t)=0, \qquad 0\leq\theta\leq\pi \tag{4.33b}$$

$$\tilde{v}(r,0,t)=\tilde{v}(r,\pi,t)=0, \qquad 1\leq r<\infty \tag{4.33c}$$

$$\tilde{p}(1,\theta,t)=-\frac{1}{Re}\frac{\partial\tilde{u}(1,\theta,t)}{\partial r}, \qquad 0\leq\theta\leq\pi \tag{4.34a}$$

$$\tilde{p}(\infty,\theta,t)=-\frac{1}{Re}\frac{\partial\tilde{u}(\infty,\theta,t)}{\partial r}, \qquad 0\leq\theta\leq\pi \tag{4.34b}$$

$$\tilde{p}(r,0,t)=-\left(\bar{U}(r,0,t)\tilde{u}(r,0,t)+\frac{1}{Re}\frac{\partial\tilde{v}(r,0,t)}{\partial r}\right), \qquad 1\leq r<\infty \tag{4.34c}$$

$$\tilde{p}(r,\pi,t)=-\left(\bar{U}(r,\pi,t)\tilde{u}(r,\pi,t)+\frac{1}{Re}\frac{\partial\tilde{v}(r,\pi,t)}{\partial r}\right), \qquad 1\leq r<\infty \tag{4.34d}$$

$$\tilde{T}(1,\theta,t) = kPe\tilde{u}_a\left(x_f,t\right), \qquad 0 \le \theta \le \pi \tag{4.35a}$$

$$\tilde{T}(\infty,\theta,t) = 0, \qquad 0 \le \theta \le \pi \tag{4.35b}$$

$$\tilde{T}(r,0,t) = \tilde{T}(r,\pi,t) = 0, \qquad 1 \le r < \infty \tag{4.35c}$$

As described earlier (§ 4.30) about the difference between the direct and adjoint equations, the difference in the direct and adjoint equations are discussed as follows. One of the coupling from the acoustic zone to the hydrodynamic zone in the direct equations is through the freestream boundary condition for u & v (4.11c & 4.12c), which acts as the source for the direct momentum equations (4.9d & 4.9e). In contrast the coupling from the acoustic zone to the hydrodynamic zone in the adjoint equations is through the adjoint temperature $\tilde{T}$ at the surface of the heater (4.35a).

4.6.3 Mapping between direct and adjoint variables

The mapping ($D \rightarrow A$) from direct to adjoint variables at time $t = T_{opt}$ is given by

$$\begin{aligned}
\tilde{p}_a^{T_{opt}} &= \frac{2p_a^{T_{opt}}}{E^0},\ \tilde{u}^{T_{opt}} = \frac{2\alpha\lambda\varepsilon u^{T_{opt}}}{E^0},\ \tilde{v}^{T_{opt}} = \frac{2\alpha\lambda\varepsilon v^{T_{opt}}}{E^0},\ \tilde{T}^{T_{opt}} = \frac{2\beta\varepsilon T^{T_{opt}}}{E^0\bar{T}} \\
\tilde{u}_a^{T_{opt}} &= \frac{2u_a^{T_{opt}}}{E^0} + \left(\int_{\theta=0}^{\pi}\int_{r=1}^{\infty}\left(\frac{\tilde{u}^{T_{opt}}\cos\theta - \tilde{v}^{T_{opt}}\sin\theta}{\varepsilon\rho_s}\right)rdrd\theta\right)\widehat{\delta}\left(x - x_f\right)
\end{aligned} \tag{4.36}$$

The return mapping ($A \rightarrow D$) from adjoint to direct variables at time $t = 0$ is given by

$$\begin{aligned}
u_a^0 &= \frac{\left(E^0\right)^2}{2E^{T_{opt}}}\left(\tilde{u}_a^0 - \left(\int_{\theta=0}^{\pi}\int_{r=1}^{\infty}\left(\frac{\tilde{u}^0\cos\theta - \tilde{v}^0\sin\theta}{\varepsilon\rho_s}\right)rdrd\theta\right)\widehat{\delta}\left(x - x_f\right)\right) \\
p_a^0 &= \frac{\left(E^0\right)^2\tilde{p}_a^0}{2E^{T_{opt}}},\ u^0 = \frac{\left(E^0\right)^2\tilde{u}^0}{2\alpha\lambda\varepsilon E^{T_{opt}}},\ v^0 = \frac{\left(E^0\right)^2\tilde{v}^0}{2\alpha\lambda\varepsilon E^{T_{opt}}},\ T^0 = \frac{\left(E^0\right)^2\tilde{T}^0}{2\beta\varepsilon E^{T_{opt}}}
\end{aligned} \tag{4.37}$$

As mentioned in the last paragraph of § 4.6.1, the boundary terms obtained during the integration by parts applied to the global acceleration term appear inside the integrals in (4.36 & 4.37). If one neglects the peudo-acceleration term, the mapping simplifies to just rescaling the variables (Corbett and Bottaro, 2001). Another impor-

tant point to be noted here is that the homogeneous boundary condition for the adjoint velocity field $(u \ \& \ v)$ as $r \rightarrow \infty$ (4.32b & 4.33b) allows one to expect the integral over the hydrodynamic zone in (4.36 & 4.36) to converge. The convergence of the same has been checked from the present numerical simulation.

4.7 Solution procedure

The system of equations (4.9 & 4.30) are then solved with the corresponding boundary conditions (4.10-4.14 & 4.31-4.35) with the above mappings (4.36 & 4.37) between the direct and adjoint variables. In the present paper, power iteration procedureGuegan *et al.* (2008) is used to solve the direct and adjoint equations. The algorithm is as follows. An initial suitable guess value for the state space variables $(u_a^0,\ p_a^0,\ u^0,\ v^0,\ p^0 \ \& \ T^0)$ is used as the starting value for the algorithm. Then the direct equations (4.9) is marched forward in time upto $t = T_{opt}$. The direct variables at $t = T_{opt}$ is mapped to the adjoint variables at $t = T_{opt}$ using the mapping (4.36). Then the adjoint equations (4.30) is marched backward in time up to $t = 0$. Then the adjoint variables at $t = 0$ is mapped back to the direct variables at $t = 0$ using the mapping (4.37), which is again fed as the initial condition to the direct equations. The process is repeated until convergence in the initial condition in the direct variables are obtained. The final converged initial condition gives the optimum initial condition for maximum transient growth in the disturbance energy E_d^t. The power iteration algorithm fails if the initial guess value for the initial condition is orthogonal (corresponding to the inner product defined in § 4.5) to the optimum initial condition, which is a rare scenario. Both the direct (4.9a & 4.9b) and adjoint (4.30a & 4.30b) acoustic equations are solved by Galerkin technique, while the direct (4.9c - 4.9f) and adjoint (4.30c - 4.30f) equations in the hydrodynamic zone are solved by finite difference technique. The above procedure for solving the direct equations is given in detail in Mariappan & SujithMariappan and Sujith (2010*a*).

Table 4.1: Physical parameters in acoustic zone, hydrodynamic zone and convergence parameters in for solving the direct and adjoint equations

acoustic zone	hydrodynamic zone	convergence parameters		
$l_a = 1\ m,\ S_c = 0.01\ m^2$	$Re_d = 20$,	hydrodynamic zone grids $(r, \theta) = 100 \times 120$		
$\bar{P} = 1\ bar$	$l_c = 1\ mm$	residue	direct	adjoint
$\tilde{\rho}_0^u = 1.025\ kg\ m^{-3}$	$l_w = 16.4\ m$	continuity	10^{-5}	10^{-2}
$\tilde{T}_0^u = 295\ K$	$\tilde{T}_w = 1000\ K$	momentum	10^{-5}	10^{-5}
$\tilde{T}_0^d = 500\ K$	$M = 5 \times 10^{-4}$	energy	10^{-5}	10^{-5}

4.8 Results and discussion

Numerical simulations are performed with the parameters shown in table (4.1). Unless specified, the parameter values in table (4.1) are used for the simulations.

4.8.1 Disturbance energy evolution

One of the important part in the present paper is the derivation of the energy in the disturbances from Myers' energy (§ 4.4). The final form of the disturbance energy E_d for the Rijke tube system comprises of the disturbance energy in the acoustic zone (E_{ac}) and in the hydrodynamic zone (E_c) (see 4.27). So it will be interesting to analyse the contribution of E_d from both the zones. Figures 4.2(*a, b*) show the evolution of the energy stored in the acoustic zone (E_{ac}) and in the hydrodynamic zone (E_c) obtained from the nonlinear simulations. The two figures 4.2(*a, b*) correspond to the numerical simulations of a globally stable (stable for any large initial perturbation) and linearly unstable system respectively (nonlinearities included). It is observed that from the numerical simulations, E_c is more than E_{ac} by at least an order of magnitude. This is due to the value of the weight factors α & β in the expression for E_d (4.27). Hence the evolution of the disturbance energy $(E_d = E_{ac} + E_c)$ is approximately same as the evolution of E_c and hence E_d is not shown separately. Figure 4.2(*a*) corresponds to a globally stable system (note that the amplitude of u_a^0 is large in the caption of figure 4.2*a*), where the energies E_{ac} & E_c decay to zero in the asymptotic time limit.

In contrast, figure 4.2(*b*) corresponds to linearly unstable system. A small perturba-

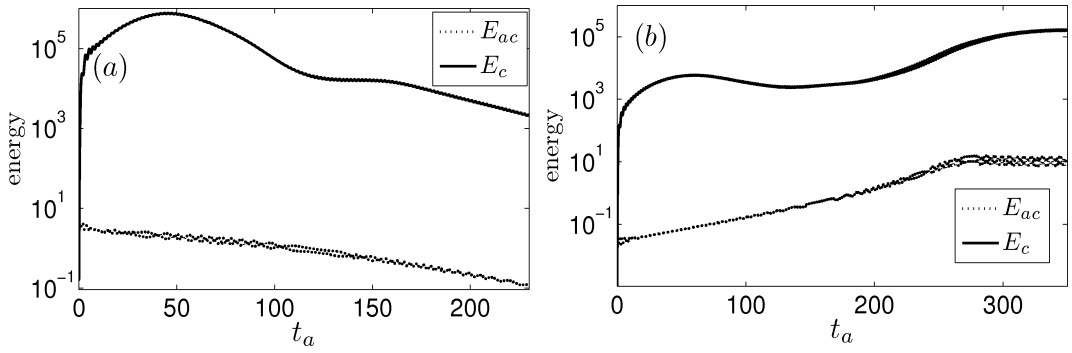

Figure 4.2: Evolution of the energy stored in the acoustic zone (E_{ac}) and in the hydrodynamic zone (E_c) obtained from the nonlinear simulations. *a*) Globally stable system, $C_1 = 0.3,\ C_2 = 0.1,\ x_f = 0.25,\ K = 0.66,\ \alpha = 3.3 \times 10^{-3},\ \beta = 4.17 \times 10^4,\ L_{cu} = 35,\ u_a^0(x_a) = 3cos(\pi x_a),\ p_a^0(x_a) = u^0 = v^0 = T^0 = 0$. *b*) Linearly unstable system, $C_1 = 0.3,\ C_2 = 0.1,\ x_f = 0.25,\ K = 0.81,\ \alpha = 3.3 \times 10^{-3},\ \beta = 4.18 \times 10^4,\ L_{cu} = 35,\ u_a^0(x_a) = 0.25cos(\pi x_a),\ p_a^0(x_a) = u^0 = v^0 = T^0 = 0$.

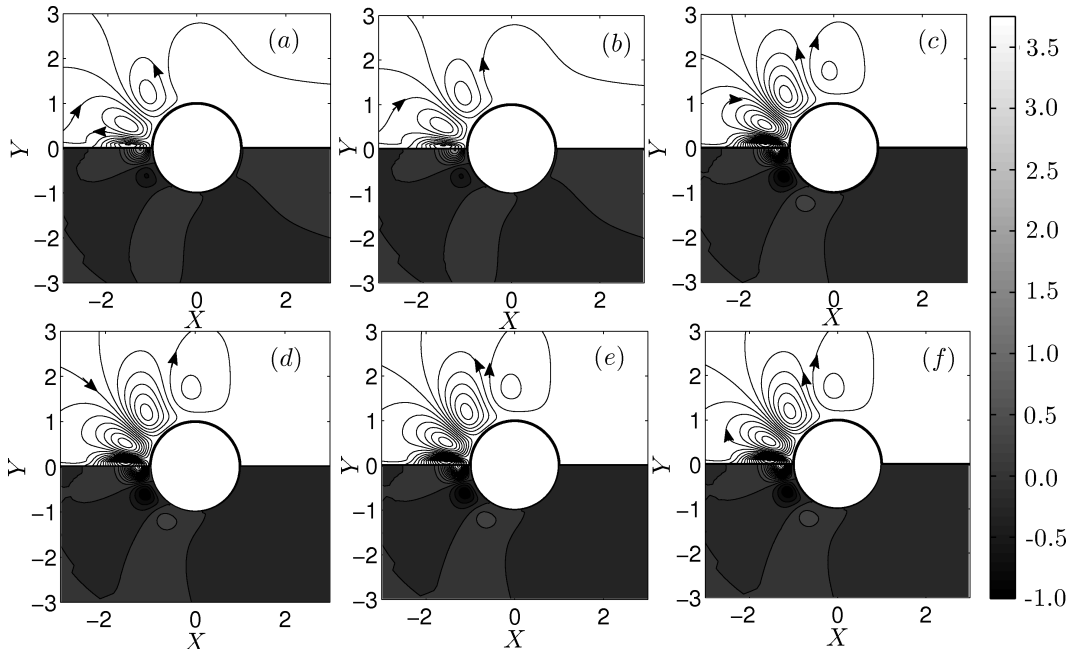

Figure 4.3: Streamlines of u & v (top half) and contour of temperature T (bottom half) corresponding to the optimum initial condition for maximum transient growth, $C_1 = 0.3,\ C_2 = 0.1,\ x_f = 0.25,\ K = 0.735,\ \alpha = 3.3 \times 10^{-3},\ \beta = 3.77 \times 10^4,\ T_{opt} = 0.5$ *a*) $L_{cu} = 15$, *b*) $L_{cu} = 20$, *c*) $L_{cu} = 25$, *d*) $L_{cu} = 30$, *e*) $L_{cu} = 35$, *f*) $L_{cu} = 40$

tion (note that the amplitude of u_a^0 is small, see the caption of figure 4.2*b*) leads to initial exponential growth of oscillations and the system eventually reaches a limit cycle. The energies E_{ac} & E_c reach a finite value corresponding to the energy in the limit cycle. Thus the disturbance energy E_d can be used as a measure to monitor the growth or decay of oscillations during the evolution of the system. Having analysed the contribution of disturbance energies from both the zones, the next step is to analyse the optimum initial condition for the maximum transient growth.

4.8.2 Optimum initial condition

In this subsection, the optimum initial condition for the maximum transient growth at $t = T_{opt}$ is analysed. A convergence factor $\lambda\,(r)$ is used during the derivation of E_d (§ 4.4). The convergence on the shape of the optimum initial condition with the cut off radius L_{cu} is investigated. Figure 4.3(*a-f*) shows the streamlines corresponding to velocity field u & v (top half) and contour of temperature distribution T (bottom half) near the cylinder for various values of L_{cu}. It can be observed that the shape of the optimum initial condition does not vary significantly beyond figure 4.3(*d*) $(L_{cu} = 30)$. Hence for the subsequent simulations the value of $L_{cu} = 35$ is chosen, which corresponds to figure 4.3(*e*). Moreover the patterns in the optimum initial condition confine to a non-dimensional radius $r \sim 5$ ensures the convergence of the optimum initial condition with the domain size (in the present case $r = 50$).

Figure (4.4) shows the distribution of the optimum initial condition in the state space variables. One can observe in the flow field corresponding to u & v, distinct patches of vortical structures are present (figure 4.4*a*). The temperature (T) contours (figure 4.4*b*) also shows a similar distinct patches as that of the flow field. The initial acoustic velocity (u_a^0) distribution shows a peak at the location of the heater. In the present paper, Galerkin technique is used to solve the acoustic equations (4.5). In order to capture the Dirac-delta function, which is used to represent the compactness of the heat source (4.9b), a total of 100 Galerkin modes are used and a corresponding modal convergence (less than 5 % change in the spatial variation of u_a & p_a) has been achieved for the optimum initial condition in the acoustic zone.

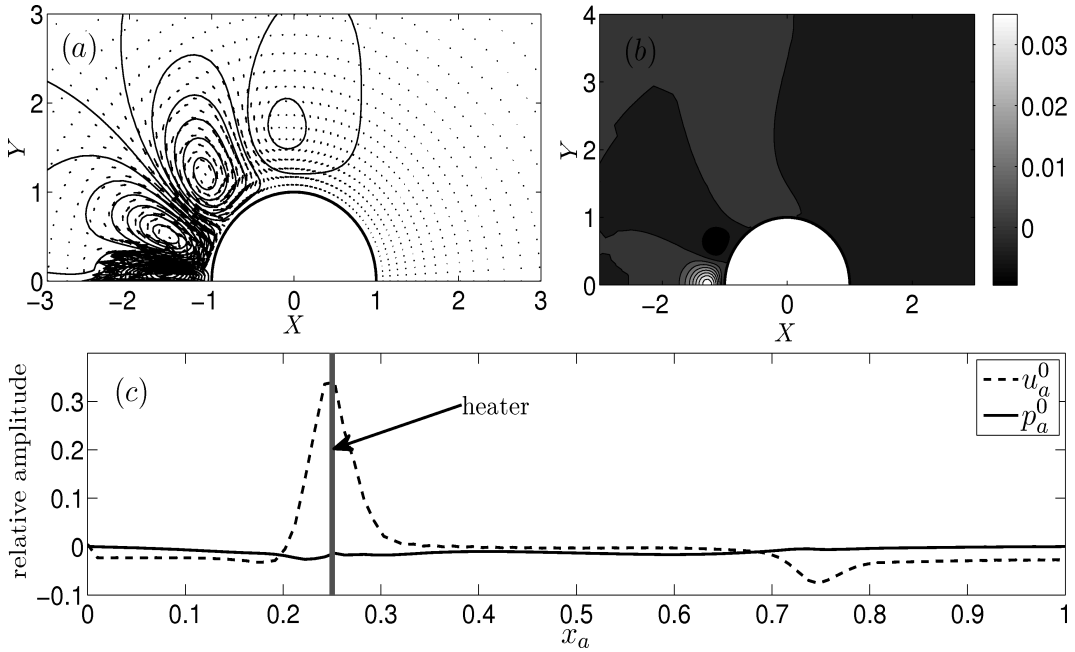

Figure 4.4: Distribution of optimum initial condition in the state space variables $C_1 = 0.3,\ C_2 = 0.1,\ x_f = 0.25,\ K = 0.735,\ \alpha = 3.3 \times 10^{-3},\ \beta = 3.77 \times 10^4,\ T_{opt} = 0.5,\ L_{cu} = 35$, (*a*) streamlines and velocity vectors corresponding to u & v, (*b*) temperature field T in the hydrodynamic zone, (c) acoustic field in the acoustic zone.

The optimum initial condition is not only distributed among the acoustic variables, but also among the variables in the hydrodynamic zone. The distribution of the optimum initial condition in the state space variables shows that for obtaining the maximum transient growth a non-acoustic disturbance (disturbance in the hydrodynamic zone) is also required (shape of it is shown in figure 4.4*a*, *b*). Hence in the Rijke tube system, it is important to include the dynamics of the heat source apart from the dynamics of the chamber acoustic field in order to understand the non-normal nature of the system. The same idea has been emphasized in the recent paper on thermoacoustic instability in solid rocket motors Mariappan and Sujith (2010*a*). In order to understand the effect of the obtained optimum initial condition, the evolution of the system is tracked with the optimum initial condition using the linearised (4.9) and the nonlinear (4.5 & 4.6) solver of the direct equations. The results of the same are taken up in the next section.

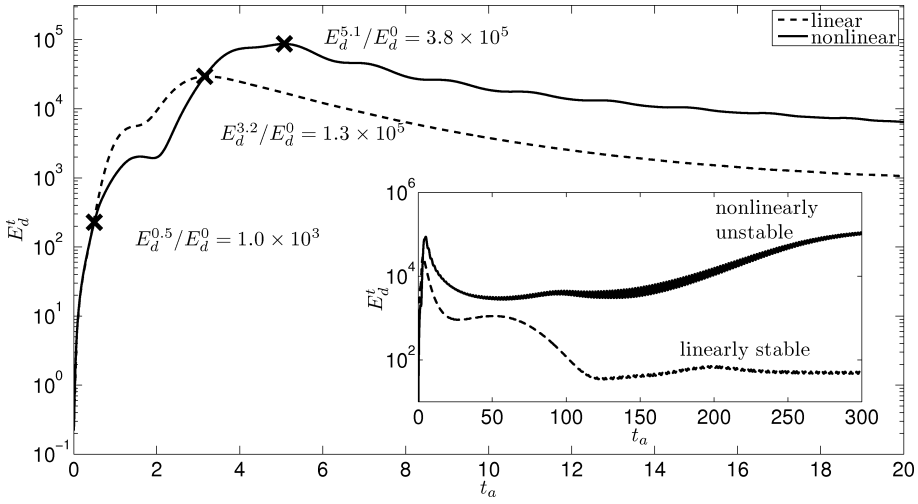

Figure 4.5: Evolution of the disturbance energy E_d^t for the optimum initial condition. $C_1 = 0.3$, $C_2 = 0.05$, $K = 0.738$, $T_{opt} = 0.5$. The optimum initial condition obtained for the linearised equations (4.9) from the adjoint optimisation procedure is always normalised so that $E_d^0 = 1$. For the nonlinear simulation the initial condition given is the optimum initial condition scaled by a factor '-0.48'. The above initial condition corresponds to an initial disturbance energy $E_d^0 = 0.23$. Cross marks indicate the points, where the amplification of disturbance energy (E_d^t/E_d^0) at various time t_a is indicated. The perturbation flow field at these points are shown in figures (4.6 & 4.7).

4.8.3 Linear and nonlinear evolution of the optimum initial condition

Before going into the details of the evolution of the optimum initial condition, it is worth observing some of the important things in the evolution of E_d^t. Figure (4.5) compares the evolution of the disturbance energy (E_d^t) for the optimum initial condition with linear and nonlinear simulations.

Initially the evolution of E_d^t is same for the linear and nonlinear simulations. As the amplitude of the oscillation increases, the deviation between the two curves becomes significant. The nonlinear simulation shows a lesser decay rate of disturbance energy compared to the linear simulation. Another important observation is that, although the optimisation procedure is performed for $T_{opt} = 0.5$, the energy growth happens beyond that time (in the case of figure 4.5, the maximum transient growth happens at $t_a = 3.2$ and $t_a = 5.1$ for the linear and nonlinear simulations repectively with the optimum initial condition for $T_{opt} = 0.5$). Similiar behaviour is observed by Guegan, Schmid

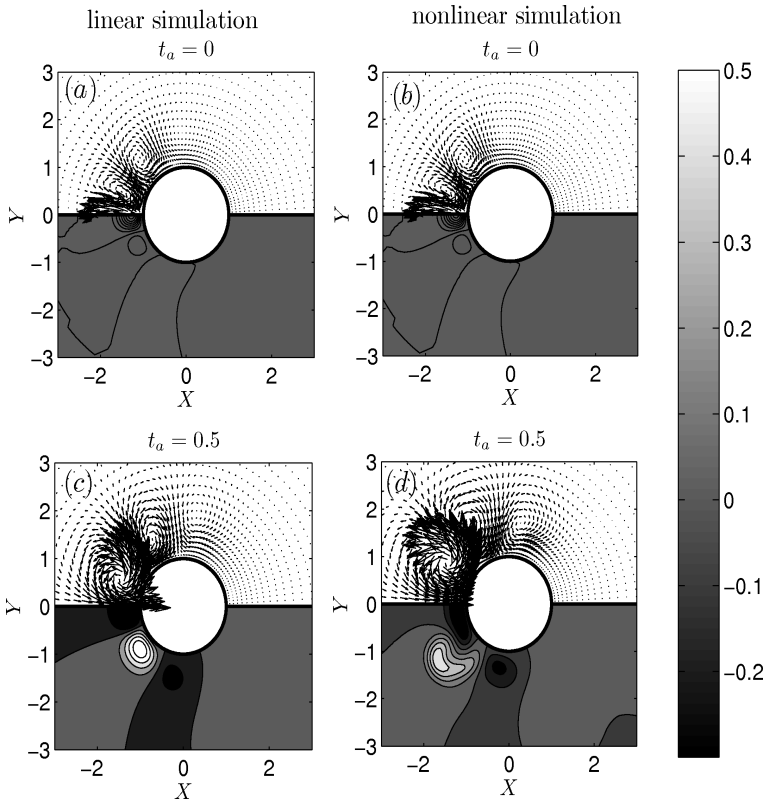

Figure 4.6: for caption, see figure 4.7

.

& HuerreGuegan *et al.* (2008), where they obtain the optimum initial condition for the flow over the leading edge of a swept wing by adjoint optimisation technique. Finally one can observe that the energy amplification is orders of magnitude during the initial short time and eventually decaying to zero in the asymptotic time limit for the linear simulation.

In figure 4.5, the simulation is performed for the non-dimensional heater power $K = 0.738$, which lies in the subcritical transition regime of the system (see figure 6 in Mariappan & SujithMariappan and Sujith (2010*a*)). In the subcritical transition regime, the system is linearly stable (stable for infinitesimally small amplitude perturbations), but nonlinearly unstable (unstable for large amplitude perturbations). The inset of figure 4.5 shows the long time behaviour of the system. The linear simulation leads to a fixed point (steady state) in the asymptotic time limit, whereas the nonlinear simulation for the same optimum initial condition leads to a limit cycle in the asymptotic time limit. A comparison of the fluctuating flow and temperature field in the hydrodynamic zone from the linear and nonlinear simulations are shown in figures 4.6 & 4.7. Figures 4.6 &

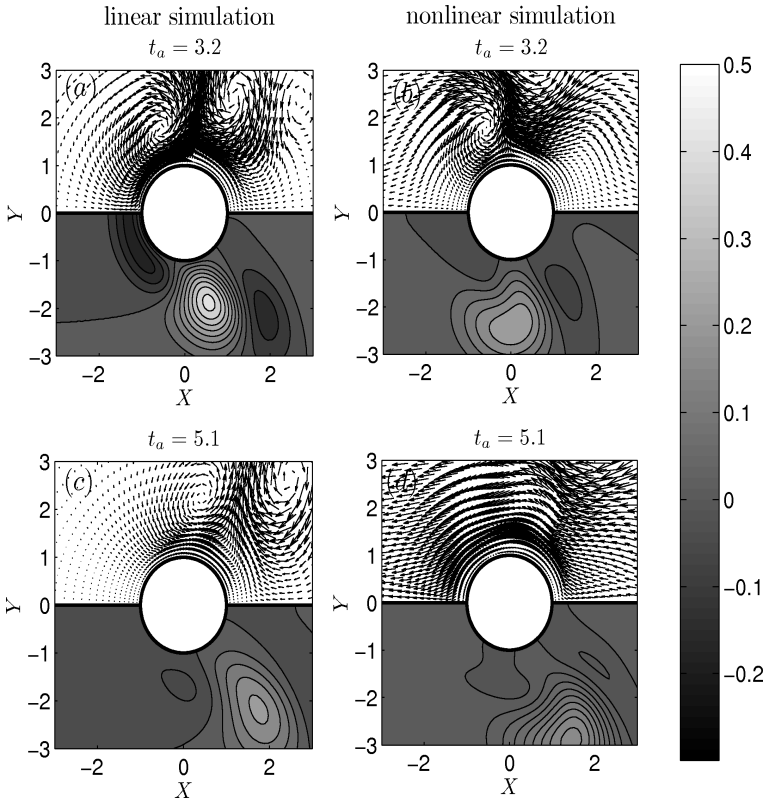

Figure 4.7: Evolution of the perturbation flow field, top: velocity vector '$u,\ v$' and bottom: temperature field 'T' for the optimum initial condition and the sytem's parameter given in figure 4.5. In figures 4.6 & 4.7, linear simulations (4.9) are shown in the left and the corresponding nonlinear simulations (4.5 & 4.6) are in the right, with the time t_a indicated on the top of each subfigure.

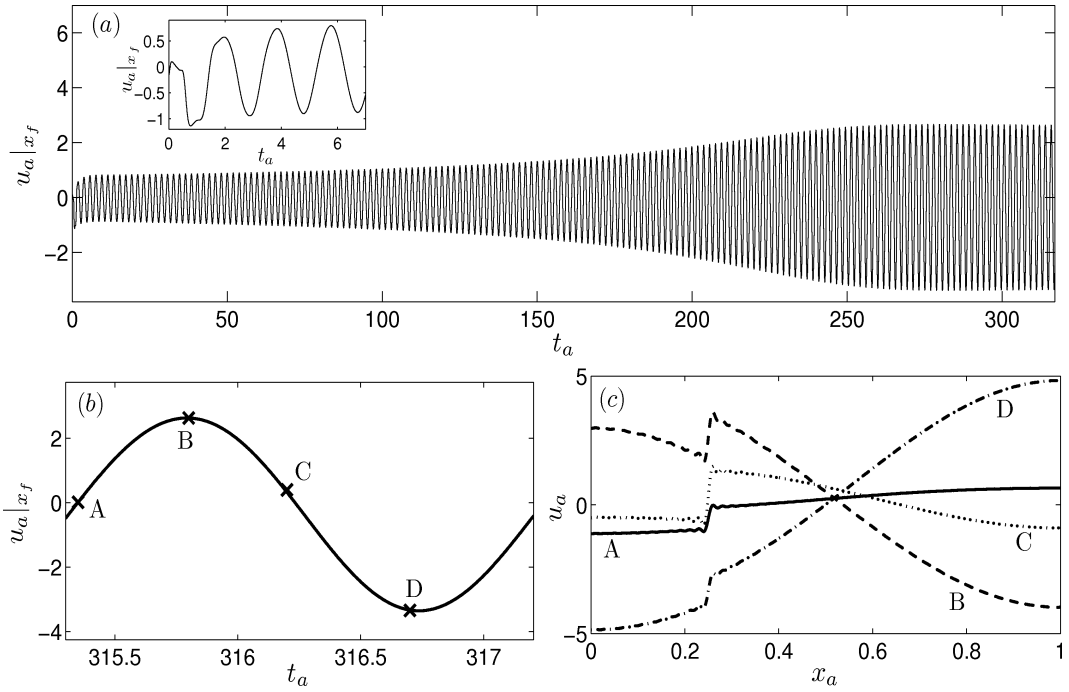

Figure 4.8: (a) Nonlinear evolution of $u_a|_{x_f}$, reaching eventually a limit cycle. The inset a initial small acoustic velocity $u_a|_{x_f} = -0.1705$ (compared to the limit cycle) corresponding to the optimum initial condition. (b) One period of a limit cycle. (c) Spatial distribution of the acoustic velocity u_a at various instants of a limit cycle. The parameters are same as in figure 4.7

4.7 corresponds to the time instants indicated by a cross-mark in figure 4.5. At $t_a = 0$, the optimum initial condition is evolved using the linear and nonlinear solvers. First the linear evolution is discussed, followed by the comparison with the nonlinear simulation.

When the optimum initial condition is evolved (by the linear solver), one can observe a transient growth in the variables of the hydrodynamic zone. In figure 4.6(c) ($t_a = 0.5$), the length of the fluctuating velocity vectors increases compared to the initial condition at $t_a = 0$ (figure 4.6a). Similarly there is also an increase in the fluctuating temperature T in the hydrodynamic zone. Note that the bright spot appears in the temperature field in figure 4.6(c), which is not present in figure 4.6(a). The above transient increase in the flow variables is captured by the transient increase in E_d^t in figure 4.5 for the linear simulation. As time evolves, there is a further increase in E_d^t beyond $T_{opt} = 0.5$ and increases to a maximum for $t_a = 3.2$. The same is reflected in figure 4.7(a), as more and more bright spots in T field appears. Since the system is linearly stable, the transient growth obtained is followed by an exponential decay in the asymptotic time limit and the same is shown in figure 4.5 (E_d^t decays to zero as

$T_a \rightarrow 0$).

The nonlinear simulation for the same optimum initial condition (as that in the above linear simulation) shows initially the same trend (figure 4.6b, d) as that from the linear simulation, but soon deviates and reaches a different dynamical behaviour (limit cycle) in the asymptotic time limit. Similar to the linear simulation, the growth in E_d^t happens beyond $T_{opt} = 0.5$ in the nonlinear simulation and reaches a maximum at $t_a = 5.1$. The corresponding fluctuating flow and temperature fields are shown in figure 4.7(d). Unlike in the linear simulation, where the system approached a fixed point in the asymptotic time limit, in the nonlinear simulation, the system reaches the limit cycle. The initial amplitude (for the optimum initial condition) of the disturbance $E_d^0 = 0.23$ is enough for the system to reach a limit cycle. Figure 4.8(a) shows the nonlinear evolution of the acoustic velocity ($u_a|_{x_f}$) at the location (x_f of the heat source reaching a limit cycle. Also figure 4.8(c) shows the spatial distribution of the acoustic velocity at various instants during one period (figure 4.8b) of the limit cycle. One can observe an acoustic velocity jump at the location of the heat source (in the present case $x_f = 0.25$) due to the Dirac-delta function in (4.5b).

4.8.4 Role of non-normality in subcritical transition to instability

The present subsection discusses on the non-normal effects on the evolution of the system. The evolution of the system to various kinds of initial conditions are analysed. In this section, two kinds of initial conditions are investigated. The first one is the optimum initial condition (see figure 4.4) for maximum transient growth in $\Im$ and the second kind is the acoustic initial condition, where fundamental natural duct mode of the system is excited initially. Figure 4.9 shows the comparison of the evolution of E_d^t with the optimum and acoustic initial condition. The strength of the initial conditions are chosen such that the initial disturbance energy ($E_d^0 = 5.64 \times 10^{-2}$) is same for both the initial conditions (see the inset of figure 4.9). The dynamical evolution of the system and the asymptotic state of the system are completely different. The optimum condition asymptotically evolves to a limit cycle and the acoustic initial condition of the same E_d^t reaches a steady state. Therefore, the initial energy required for the system to reach

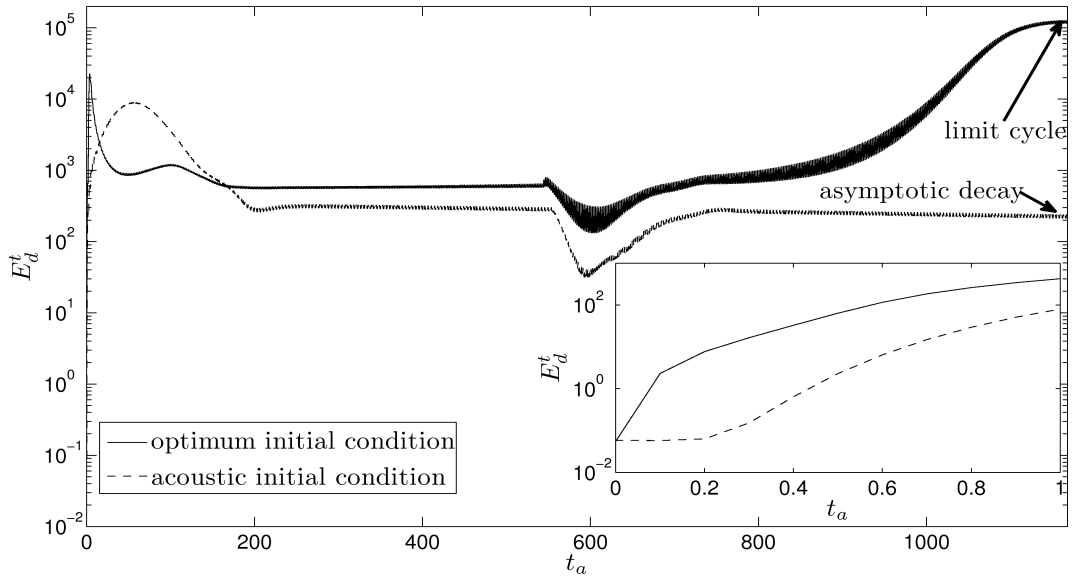

Figure 4.9: Comparison of the evolution of the disturbance energy E_d^t with the initial condition, a) optimum initial condition ($T_{opt} = 0.5$, fig. 4.4) and b) acoustic initial condition ($u_a^0(x_a) = Acos(\pi x_a)$, $p_a^0(x_a) = u^0 = v^0 = T^0 = 0$, '$A$' determines the initial energy of the disturbance) having different initial energy (the inset shows evolution of E_d^t zoomed near the initial evolution). $C_1 = 0.3,\ C_2 = 0.05,\ K = 0.738$.

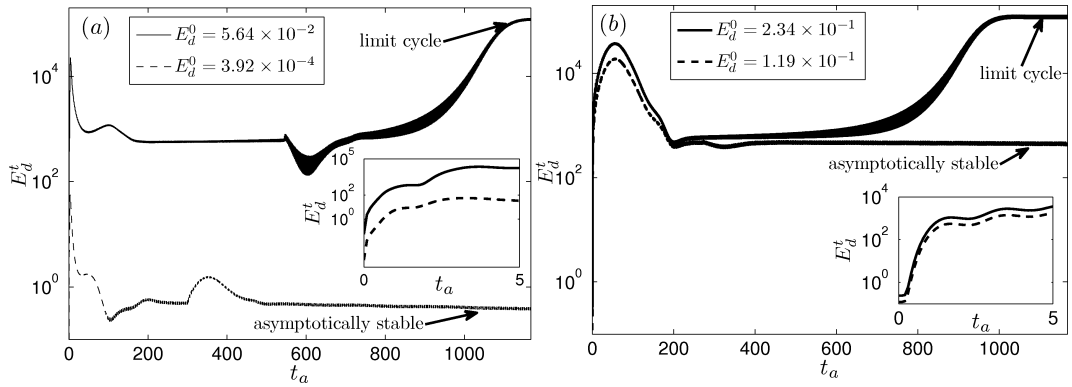

Figure 4.10: Comparison of the evolution of the disturbance energy E_d^t with the initial condition, a) optimum initial condition ($T_{opt} = 0.5$) and b) acoustic initial condition, having different initial energy $E_d^0 = 5.64 \times 10^{-2}$ (the inset shows evolution of E_d^t zoomed near the initial evolution. $C_1 = 0.3,\ C_2 = 0.05,\ K = 0.738$.

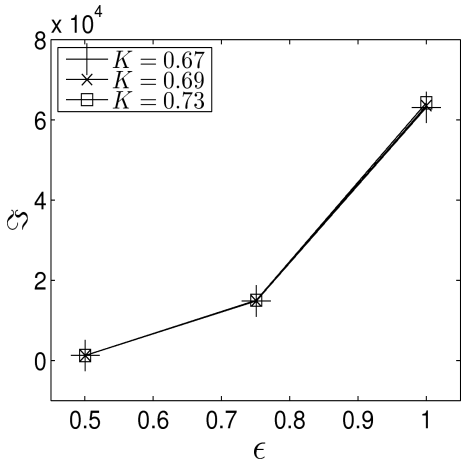

Figure 4.11: Variation of the cost functional $\Im_{max}$ corresponding to the optimum initial condition for $T_{opt} = 0.5$ with the time scale ratio ϵ for various values of the heater power K. $C_1 = 0.3,\ C_2 = 0.05$.

the limit cycle is less for the optimum initial conditon compared to the purely acoustic initial condition.

In the next figure 4.10, the evolution of E_d^t for various strengths of the optimum and acoustic condition are shown. Figure 4.10*a*, shows the system with $E_d^0 = 5.64 \times 10^{-2}$ reaches a limit cycle with the optimum initial condition. The system is stable for energies lesser than $E_d^0 = 5.64 \times 10^{-2}$ in the optimum initial condition (obtained from the numerical simulations from a time marching code). On the other hand, figure 4.10*b* indicates that the system reaches a limit cycle for $E_d^0 = 2.34 \times 10^{-1}$ for an acoustic initial condition. The initial energy for the acoustic initial condition ($E_d^0 = 2.34 \times 10^{-1}$) is an order of magnitude more than the initial energy for the optimum initial condition ($E_d^0 = 5.64 \times 10^{-2}$) for the system to be nonlinearly unstable and reach a limit cycle. For the present simulation, the linear stability theory predicts that the system is stable. The prediction fails, when the initial condition is above some threshold energy. This threshold energy varies for the two kinds of initial conditions discussed. The threshold energy is less (by an order of magnitude) for the optimum initial condition compared to the acoustic initial condition. Hence the non-normal nature of the system is reflected in the reduction in the range of linearisation (threshold energy) of the system. The present analysis is performed only for the two types of initial conditions and verifying the same for all possible initial conditions is not feasible.

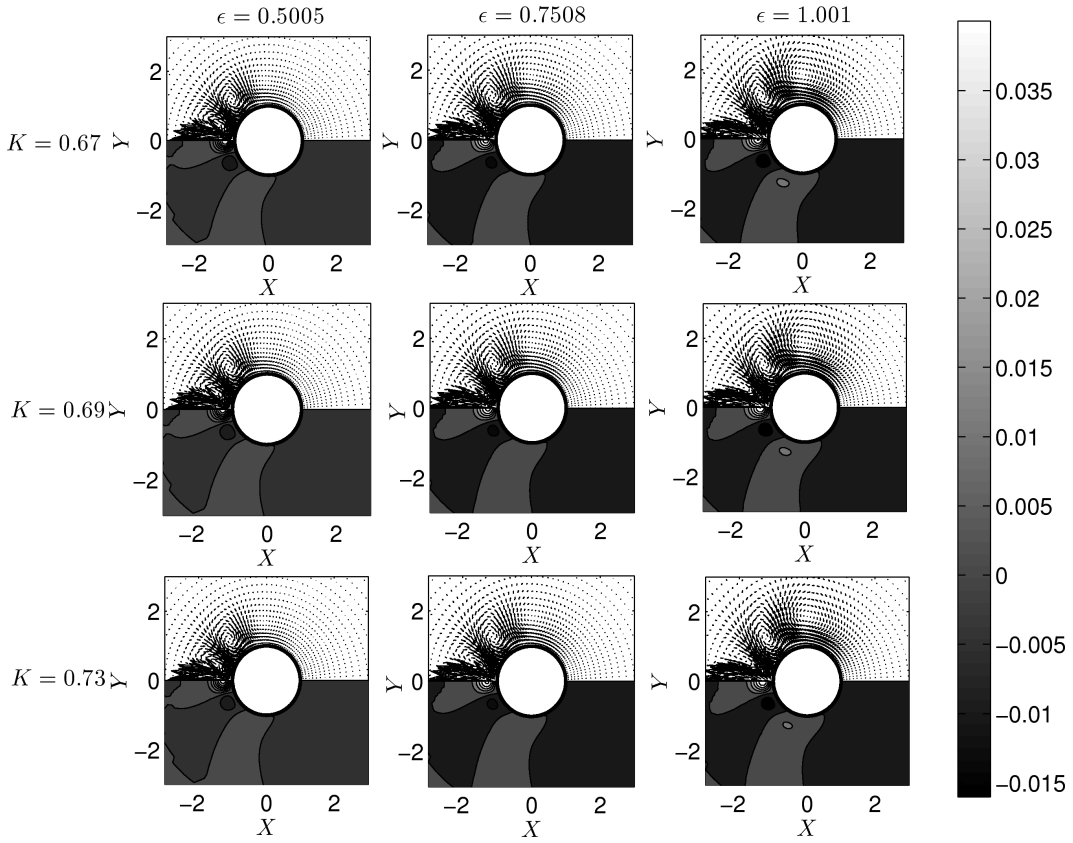

Figure 4.12: The optimum initial condition (top: velocity vector corresponding to 'u & v', bottom: temperature 'T' contour) corresponding to maximum cost functional $\Im_{max}$ as shown in figure 4.11. The variation of the optimum initial condition with K and ϵ are shown along the rows and columns of the figure respectively.

4.8.5 Parametric study

A parametric study is performed to analyse the non-normal nature of the system with the variation of the important parameters in the system. In the present case, two such parameters are chosen. The first one is the non-dimensional heater power ($k = 2l_w l_c \left(\tilde{T}_w - \tilde{T}_0^u\right) \Big/ \left(Pe_c S_c \bar{T}\right)$, see § 4.3) and the second one is the ratio of the time scales ($\epsilon = t_{ac}/t_{cc}$, see § 4.1) associated with the acoustic (t_{ac}) and hydrodynamic (t_{cc}) zones. Figure 4.11 shows the variation of the cost function $\Im_{max}$ corresponding to the optimum initial condition with K & ϵ. One can observe that $\Im_{max}$ varies by an order of magnitude for the variation in ϵ, whereas with K, $\Im_{max}$ varies by a small amount. The optimum initial conditions corresponding to $\Im_{max}$ (figure 4.11) is shown in figure 4.12. The optimum initial condition in the hydrodynamic zone does not vary much with K & ϵ and hence can be a generic initial condition, which promotes transient growth in this Rijke tube system.

4.9 Conclusion

Non-normal nature of the thermoacoustic interaction in an electrically heated horizontal Rijke tube is investigated. The dynamics of the heat source is taken into account and the coupled problem (dynamics of the acoustic field and the heat source) is solved simultaneously (two length scale problem). The analysis started from the equations governing the dynamics of the chamber acoustic field (acoustic zone) and the heat source (hydrodynamic zone). In order to study the non-normal nature of the system, a norm is defined to measure the transient growth observed in the non-normal systems. Since the dynamics of the heat source is taken into account, the degrees of freedom of the system not only comprised of the acoustic variables, but also the variables determining the dynamics of the heat source. Hence the norm defined has to be a physical energy, which should take into consideration the energy in the disturbance present both in the acoustic and hydrodynamic zone. A norm is defined based on the disturbance energy proposed by Myers, which gives the energy in an arbitrary disturbance with a non-zero steady base flow and no chemical reaction. Myers' energy simplifies to acoustic and kinetic energy for isentropic and incompressible perturbations respectively. The norm defined by this manner can, in principle be extended to more complex thermoacoustic problems and the non-normal nature of the system can be investigated.

In order to study the non-normal nature of the present problem, the optimum initial condition, which produces the maximum transient growth (measured in the norm defined in the above paragraph) is obtained. In the present case, 'adjoint optimisation technique' is applied to obtain the optimum initial condition as the number of degrees of freedom of the system is large ($\sim 10^4$). As the first step in understanding the non-normal nature of the system, linear optimal (optimum initial condition for maximum transient growth for the linearised coupled problem) is obtained. In the process of the application of the adjoint optimisation technique, adjoint equations are obtained. The coupling between the two length scales (acoustic and hydrodynamic zone) in the adjoint equations occurs in an elegant way. The adjoint temperature in the hydrodynamic zone acts as a source for the adjoint velocity in the adjoint momentum equations, which is in the opposite way as in the direct equations in the hydrodynamic zone. The global acceleration term in the direct equations in the hydrodynamic zone is responsible for

forming the coupling from the adjoint hydrodynamic to the adjoint acoustic zone. The above term in the adjoint acoustic energy equation is equivalent to the unsteady heat release rate term in the direct acoustic energy equation. Thus the global acceleration term present in the direct momentum equations in the hydrodynamic zone produces terms in the adjoint acoustic energy equation, which can be regarded as the adjoint unsteady heat release rate term. The global acceleration term also appears in the mapping between the direct and the adjoint variables. Power iteration algorithm is used to solve both the direct and the adjoint equations to obtain the optimum initial condition.

The optimum initial condition obtained has components both in the acoustic and the hydrodynamic zone. In the acoustic zone, the optimum initial condition requires the acoustic velocity peak at the location of the heat source. In the hydrodynamic zone, optimum initial condition projects as distinct patches of high voriticy and corresponding patches in the temperature field. This optimum initial condition is evolved using the linear solver and a transient growth in the state space variables of the system is observed as expected. Simulatios are performed for the parameter values, where the system is in the regime of subcritical transition to instability. Hence the linear simulation decayed to a fixed point in the asymptotic time. The same optimum initial condition (as in the above linearised case) is evolved using the nonlinear solver. Again a transient growth is observed. However, this time, the system eventually reached a limit cycle. Both in the linear and nonlinear evolution of the optimum initial condition, the growth in the disturbance energy happens beyond the time for which the initial condition is optimised. Also the threshold energy for the system to reach a limit cycle is shown to be less for the optimum initial condition than for the acoustic initial condition.

In summary, the non-normal nature of the thermoacoutic system can be measured using a physically relevant norm, which can in principle be obtained for a generic thermoacoustic system using the above prescription. Then adjoint optimisation procedure can be applied to obtain the optimum initial condition. The non-normal nature of the system is reflected in the reduction in the range of linearisation (threshold energy) of the system.

CHAPTER 5

Experimental investigation

5.1 Schematic of the experimental configuration

A schematic diagram of the experimental setup is shown in figure 5.1. The airflow was established by a 1 HP blower by Continental Airflow Systems (type CLP-2-1-650). The blower was run in suction mode to provide smooth laminar flow inside the tube. The desired mass flowrate through the tube is maintained by the blower. Two decouplers are used in the upstream and downstream of the Rijke tube, so as to reduce the effect of noise from the blower and ambient atmosphere. In the present case, Rijke tube (made of aluminium sheet with 7 mm thick) is 1 m long with 9.3 $\times$ 9.3 mm cross section area. In the present experiment, a mesh type electrical heater is used inorder to have a uniform heating across the cross section area (figure 5.3). Thick copper rods are used to supply electrical power to the mesh. The electrical resistance of the mesh is of the order of milli Ohms and hence, the DC power supply is required to supply high currents for power levels $\sim$ 800 W . In the present case the output range of the DC power supply is 0-8 V & 0-400 A. The heater is housed in a ceramic stand inorder to ensure both electrical and thermal insulation with the Rijke tube.

5.2 Introduction

Thermoacoustic instability is a plaguing problem in solid and liquid rockets, ramjets, aircraft and industrial gas turbines, etc. Thermoacoustic instability occurs, when the amplitude of acoustic pressure oscillations in the combustion chamber are amplified by the positive feedback of the unsteady heat release rate from the heat source in the chamber. A fundamental understanding of thermoacoustic interaction can be obtained by analysing thermoacoustic instability in a model problem; the Rijke tube. It is a simple

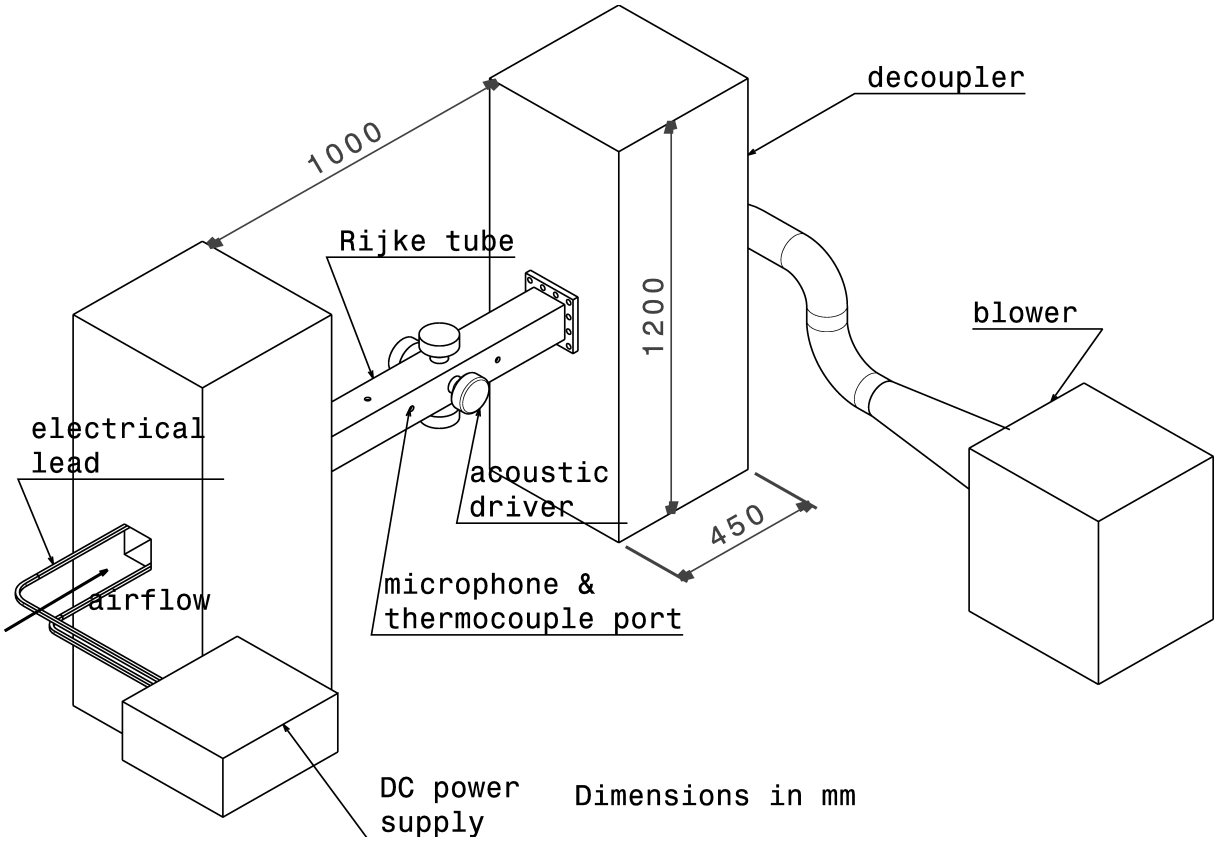

Figure 5.1: Schematic of the Rijke tube experimental setup.

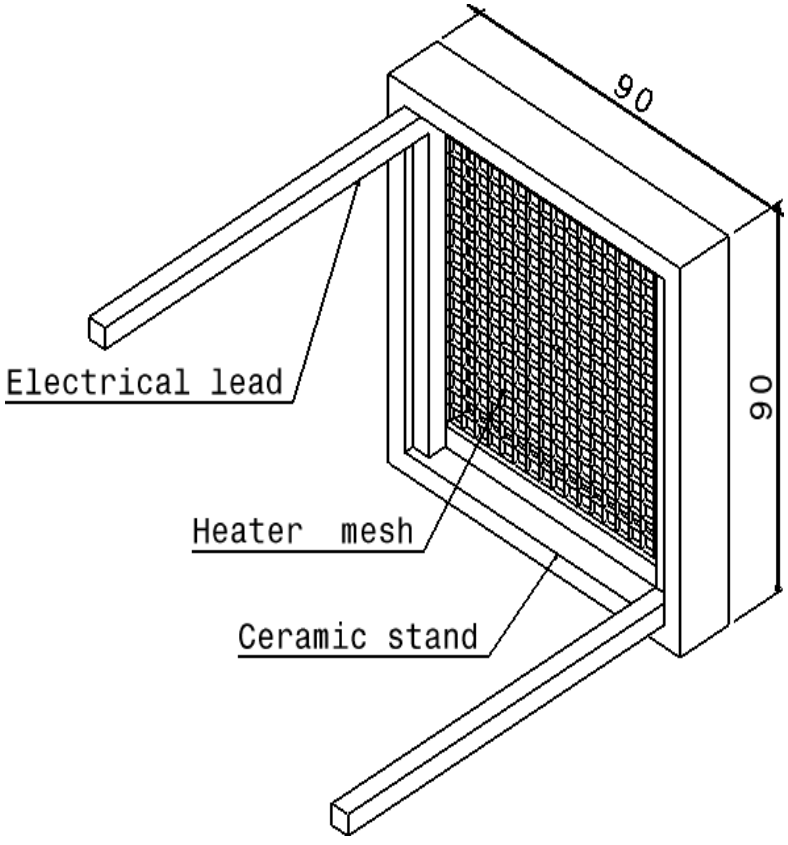

Figure 5.2: Electrical heater along with the ceramic holder.

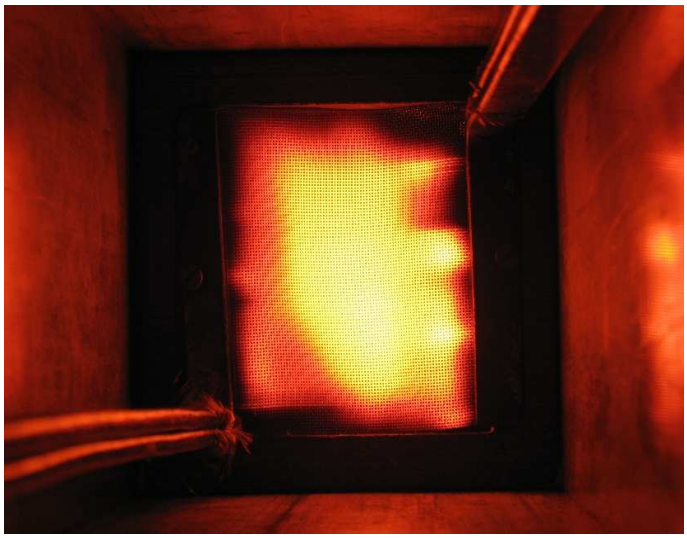

Figure 5.3: Mesh type electrical heater, operating at $\sim 1\ kW$.

thermoacoustic device, but has much of the essential physics of thermoacoustic interaction. Thermoacoustic instability of the Rijke tube has been investigated for a long time. Acoustic oscillations in Rijke tube were first observed by Rijke (Rijke, 1859) in a vertical tube with coiled electrical heating filament as the heat source. A number of numerical simulations (Kwon and Lee, 1985; Hantschk and Vortmeyer, 1999; Mariappan and Sujith, 2010*a*; Subramanian *et al.*, 2010*b*) and experiments (Matveev, 2003; Song *et al.*, 2006) were performed to understand the basic mechanism of the coupling between the chamber acoustic field and the unsteady heat release rate.

Recently, thermoacoustic systems are shown to be non-normal, which leads to the non-orthogonality of the eigenmodes (Balasubramanian and Sujith, 2008*b*). This non-orthogonality of eigenmodes leads to transient growth of oscillations for appropriate set of initial conditions, even when the system is linearly stable. Hence it is important to investigate the short term dynamics of the system (Schmid and Henningson, 2001; Mariappan and Sujith, 2010*b*). The effects due to non-orthogonal eigenmodes in thermoacoustic systems were discussed numerically in the context of thermoacoustic instability in Rijke tube (Balasubramanian and Sujith, 2008*b*), ducted diffusion flame (Balasubramanian and Sujith, 2008*a*) and solid rocket motor (Mariappan and Sujith, 2010*b*).

The concept of transient growth was first investigated in the analysis of the stability of shear flows (Schmid, 2007). A number of numerical analysis, leading to the identifi-

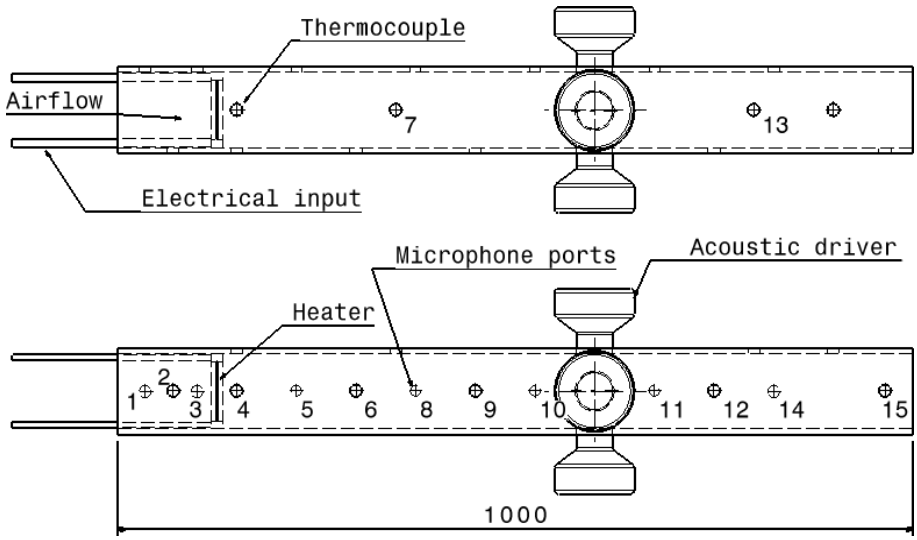

Figure 5.4: Configuration of the Rijke tube showing the heater, microphone ports and acoustic drivers. The location of the microphone ports are numbered and their distance from the upstream end is given in table 5.1

cation of the role of transient growth in the stability of fluid flows have been performed (Henningson and Reddy, 1994; Hanifi *et al.*, 1996). There has also been a significant number of experimental investigations performed to identify transient growth in fluid dynamics instability. The earliest experimental results were reported by Mayer and Reshotko (1997), who have observed transient growth of the disturbance amplitude in a pipe flow experiment. The formation of streaky structures (regions of high and low velocity field), which appear due to non-normal nature of the system was observed in experiments in boundary layer (Matsubara and Alfredsson, 2001). In the same experiment, stable laminar streaks were generated experimentally and a transient growth in the amplitude of disturbance was observed in the stream wise direction (Fransson *et al.*, 2004). Further, a passive control of transition to turbulence in boundary layer was performed by exploiting the non-normal nature of the system (Fransson *et al.*, 2006).

A number of experimental investigations mentioned in the previous paragraph aid to understand the role of transient growth in practical applications. In a similar way, experiments related to the investigation of non-normal nature of thermoacoustic system help to improve our understanding of the same. In the present paper an attempt is made to identify the non-normal nature of the thermoacoustic interaction in a Rijke tube and its consequence; transient growth.

The present paper focusses on two main issues. The first one is obtaining the eigenmodes of the system experimentally. This is performed by a technique called Dynamic Mode Decomposition (DMD) and is described in Schmid (2010). This is followed by the determination of non-orthogonality between the extracted eigenmodes. The second issue deals with the identification of transient growth in the oscillations by generating an appropriate initial condition; acoustic pressure from the acoustic driver. The rest of the paper is structured as follows. The experimental configuration of the Rijke tube system is discussed in § 5.3, which is followed by a section on the experimental procedure (§ 5.4). Finally, the results of the main focus of the paper are discussed in § 5.5.3 & 5.5.4.

5.3 Experimental configuration of the Rijke tube

The present experimental configuration consists of $1\ m$ long Rijke tube made of Aluminium. The cross section dimension of the tube is $92 \times 92\ mm^2$. A mean flow is setup by a blower. The volume flow rate is measured by a compact orifice mass flow meter (Rosemount 3051 SFC), whose range is 0-5 g/s with an uncertainty of $\pm 2.1\%$ of the mass flow rate. Two decouplers ($120 \times 45 \times 45\ cm^3$), one upstream and the other one downstream of the tube are placed so as to provide acoustically open-open boundary conditions. A mesh (size 30) type electrical heater is placed at desired axial locations (figure 5.4). A programmable DC power supply (GEN8-400, $0 - 8\ V,\ 0 - 400\ A$) is used to power the electrical heater. The horizontal Rijke tube configuration described in the present paper is similar to the one described in Matveev (2003); Song *et al.* (2006). There are two thermocouples, one at the inlet of the tube and the other downstream of the heater. They are used to monitor the steady state temperature in the duct. Four acoustic driver units (Ahuja AU 60) are placed in the tube to give a precise acoustic initial condition to the system. A total of 15 microphones are placed along the duct in order to record the evolution of acoustic pressure. The microphones are distributed in a way so as to obtain efficiently the first two eigenmodes of the system. The location of the heater, thermocouples, acoustic drivers and microphones are schematically represented in figure 5.4 and tabulated in table (5.1). Data are acquired simultaneously by

Table 5.1: The locations of the microphones, heater, thermoacouple and loudspeakers measured from the upstream end of the Rijke tube.

Microphone no.	Location (mm)	Microphone no.	Location (mm)
1	35	10	675
2	70	11	750
3	100	12	800
4	150	13	825
5	225	14	900
6	300	15	965
7	375	Heater	125
8	450	Thermocouple	150
9	525	Acoustic driver unit	600

programmable National Instruments PCI 6221 & 6251 data acquisition cards at 8 kHz.

5.4 Experimental procedure

Non-normal nature of the thermoacoustic system leads to non-orthogonal eigenmodes, which in turn leads to transient growth of the oscillations. Transient growth is a linear phenomenon. For low amplitudes of perturbations (precise definition is given in § 5.4.2), system behaves linearly. In the present experimental setup, an attempt is made to estimate the non-orthogonality between the first two eigenmodes of the system and observe transient growth associated with the non-normal nature of the system. The modes from DMD technique, termed as 'dynamic modes' are obtained from experimental data. Further, dynamic modes coincide with the eigenmodes of the system, only when the experiment is performed in the linear regime (Schmid, 2010). The experiments dealing with the investigation of non-normal nature of the system have to be performed in the linear regime. Hence, the first step in the present investigation is to identify the linear regime of the system and is obtained as described in the following subsections.

5.4.1 Bifurcation diagram

Bifurcation diagram is obtained initially, in order to obtain the stability limits of the system. Bifurcation diagram is plot between any control parameter of the system and

the asymptotic state of the system, indicated by a chosen representative variable. It is observed from the present investigation (to be discussed in § 5.5.1) that transition to instability happens via subcritical Hopf bifurcation as the power supplied to the heater is increased. Further investigations are performed in the above regime as transient growth plays an important role in the subcritical transition to instability regime. The triggering amplitude required for the system to reach a limit cycle is then identified. This is obtained by initially perturbing the system using the acoustic drivers. The amplitude of the initial perturbation is increased till the amplitude, where the system becomes nonlinearly unstable and eventually reaches a limit cycle. The above threshold amplitude is noted as the triggering amplitude and gives an estimate of the amplitude of acoustic pressure oscillations at which nonlinearity plays an important role in the qualitative behaviour (limit cycle or fixed point) of the system. This is followed by estimating the limit of linearity, which is taken up in the next subsection.

5.4.2 Linearity

A linear system is one in which, when the amplitude of the input is scaled, the amplitude of the output is also scaled by the same amount. In the present case, the input is the voltage supplied to the acoustic drivers and the output is the acoustic pressure measured at some location of the tube. At a given heater power, the above input is varied and the output is recorded to obtain the response curve of the system. In the present case, the limit of linearity is determined when the deviation of the response of the system from the linearised response function (explained in § 5.5.2) is more than 5% of the corresponding triggering amplitude. The results of the same are discussed in § 5.5.2. The experiments related to the investigation of non-normal nature of the system are performed with the amplitude levels lower than the limit of linearity.

5.4.3 Dynamic Mode Decomposition

In fulfilling the first aim of the present investigation, eigenmodes of the system are extracted using DMD technique. An alternative for DMD technique in the extraction of the eigenmodes is by using network models for each acoustic elements (Bellucci *et al.*,

2004). The individual acoustic elements are described by transfer matrices, which are obtained either experimentally (Bellucci *et al.*, 2004) or numerically (Schuermans *et al.*, 2005). The eigenfrequencies and the corresponding eigenmodes of the system are then calculated from the assembled network matrix. The transfer matrices associated with the flame elements are obtained by forcing the flame continuously and the response of the same is measured experimentally. The above experiment has be to be performed at low amplitudes of forcing, where the system behaves linearly. Identifying and obtaining the transfer matrices in the above regime may be difficult (Hosseini and Lawn, 2005). The acoustic field upstream and downstream of the heat source have to be modeled as separate acoustic elements. Separate experiments for each acoustic element will be required to complete the above process, which is time consuming. The error made in the calculation of any one of the transfer matrices will reflect on the final results. Moreover, the above technique is developed for frequency domain analysis and extending to time domain is not straight forward. To bypass the above issues, DMD technique is performed. The eigenmodes of the system can be obtained in one shot from acoustic pressure measured simultaneously at various locations of the Rijke tube. In this technique the eigenmodes of the system are measured rather than calculated as it is performed in the above network models approach. Hence, DMD technique is preferred to obtain the eigenmodes of the system.

Dynamic mode decomposition technique is based on using the snapshots of the flow field to obtain the dominant dynamic features. The dominant flow structures obtained during the above analysis are termed as 'dynamic modes'. Both data from numerical simulations and experiments can be used for this analysis. When the underlying flow process is linear, the method is equivalent to a global stability analysis. The dynamic modes thus obtained are the eigenmodes of the system. In nonlinear flows, the above analysis produces flow structures, which are associated with the linear tangent approximation of the original flow. This technique was first applied to analyse flow in a lid driven cylindrical cavity (Schmid *et al.*, 2009). Time-resolved particle-image velocimetry (PIV) data captured from a cross-sectional plane of the flow field is fed to DMD technique and bifurcation points are obtained for the variation of the Reynolds number. Schmid *et al.* (2010) applied this technique to the data obtained from the Schlieren snapshots of a helium jet, along with the time-resolved PIV measurements to

obtain the spatial wave numbers and temporal frequencies of the modal structures of the shear layer. Recently, the dominant frequency and the associated flow structures were detected using the data from the numerical simulation for a jet flame and experiments for a water jet by Schmid (2011).

In the present investigation, experiments are performed to extract first two eigenmodes of the system. The Rijke tube system is initially perturbed using acoustic driver units, so that the first two eigenmodes of the system are excited. The evolution of acoustic pressure is recorded from microphones and then DMD technique is applied to the obtained experimental data. After the above postprocessing step, the first two eigenmodes of the system corresponding to the acoustic pressure are obtained. The whole procedure is performed in the linear regime, as identified by the procedure explained in § 5.4.2. After obtaining the eigenmodes of the system, the amount of non-orthogonality between the obtained eigenmodes are determined by defining the inner product $\langle p_i, p_j \rangle = \int_0^L p_i^* p_j dx$, where p_i represents the i^{th} eigenmode of the system with the normalisation $\langle p_i, p_i \rangle = 1$, L is the length of the tube, * represents the complex conjugate. The definition of inner product to obtain the angle between the eigenmodes is same as followed in the literature to analyse thermoacoustic instability (Culick, 2006; Nicoud *et al.*, 2007). The above inner product is calculated for various values of heater power levels and the results of the same are discussed in § 5.5.3.

5.4.4 Theoretical investigation of the eigenmodes

In order to understand the effect of heater on the non-orthogonality of the eigenmodes of the system, it is important to first theoretically investigate the same. To facilitate the above, thermoacoustic interaction of the Rijke tube system is represented by the following linearised acoustic momentum and energy equations in non-dimensional form (Balasubramanian and Sujith, 2008*b*).

$$\frac{\partial u}{\partial t} + \frac{\partial p}{\partial x} = 0 \tag{5.1a}$$

$$\frac{\partial p}{\partial t} + \frac{\partial u}{\partial x} = Q\delta\left(x - x_f\right) \tag{5.1b}$$

where, u & p are the acoustic velocity and pressure respectively, Q is the unsteady heat release rate and x_f is the location of the heat source. The heat source is assumed to be compact compared to the length of the tube and is represented by a Dirac-delta function ($\delta(x)$). The jump conditions (Poinsot and Veynante, 2005) across the heater are as follows

$$p^+(x_f, t) = p^-(x_f, t) \tag{5.2a}$$

$$u^+(x_f, t) - u^-(x_f, t) = Q(t) \tag{5.2b}$$

where, - & + indicates the value of the variables upstream and downstream of the heat source. The unsteady heat release rate from the heat source is modeled using '$n - \tau$' model and is of the form:

$$Q = nu^-(t - \tau) \tag{5.3}$$

where, n is the interaction index, which indicates the power supplied to the heater and τ is the time lag associated with the acoustic velocity fluctuations upstream of the heat source. Acoustically 'open-open' boundary conditions are assumed. The eigenmodes of the system are obtained from the above equations (5.1-5.3). The eigenmodes ($\hat{p}$) corresponding to acoustic pressure of the system, defined in the form $p(x,t) = \hat{p}(x)e^{\omega t}$ are given as follows:

$$\hat{p}(x) = \begin{cases} \sinh(\omega x), & 0 \leq x \leq x_f \\ \sinh(\omega(x-1)) \dfrac{\sinh(\omega x_f)}{\sinh(\omega(x_f - 1))}, & x_f < x \leq 1 \end{cases} \tag{5.4}$$

The eigenvalues ω, are obtained by solving the following dispersion relation.

$$\sinh(\omega) - \frac{n}{2} e^{-\omega\tau} \sinh(\omega(2x_f - 1)) = 0 \tag{5.5}$$

The theoretical eigenmodes associated with acoustic pressure (p) of the system are shown on the left hand side in figure 5.5. The heater is placed at $x = 0.125$, where the first two eigenmodes of the system becomes less stable (Matveev, 2003). The eigenmodes are numbered as $p_1,\ p_2, ...$ in the ascending order of imaginary part of the eigenfrequencies $\omega_1,\ \omega_2, ...$ The first two eigenmodes of the system are shown with their real and imaginary parts. When the heater is switched off ($n = 0$), eigenmodes coincide

with the natural duct mode. As the value of n is increased, the eigenmodes drifts away from the natural duct modes. A discontinuity in the slope of the eigenmodes is present at the location of the heat source. This is because of the $\delta(x)$ function used in (5.1b). The above discontinuity in slope increases with increase in the value of n. Further, the discontinuity in slope is more pronounced in the imaginary part, compared to the real part of the eigenmode. The eigenmodes with the value of the non-dimensional heater power 'n' and the absolute value of the inner product $|\langle p_1, p_2 \rangle|$ are indicated in the title of each subfigures. The above inner product $\langle p_1, p_2 \rangle$ is used to measure the degree of non-orthogonality of the system as described in § 5.4.3.

In cold flow ($n = 0$), the eigenmodes of the system are shown in figure 5.5(*a*). The real part of the eigenmodes are sine functions and the imaginary part is zero. The inner product $\langle p_1, p_2 \rangle$, which determines the non-orthogonality of the system is very small. Hence, the eigenmodes are orthogonal. As the value of n is increased, the imaginary part of the eigenmodes become non-zero, which increases the non-orthogonality of the eigenmodes. The above argument can be seen from figures 5.5(*a*, *c*, *e* & *g*). Thus, the non-orthogonality between the eigenmodes appears due to discontinuity in the slope of the eigenmodes at the location of the heater and the value of discontinuity is proportional to the heater power n. The microphones, which are used for the acoustic pressure measurements have to be arranged, so that the above slope discontinuity can be captured well. Hence, three microphones are placed upstream of the heater and the remaining twelve microphones are distributed (see table 5.1) in an optimal manner, so as the capture the first two eigenmodes of the system efficiently.

5.4.5 Extraction of dynamic modes

In the present investigation, the eigenmodes are obtained by applying DMD to the experimental data. Hence, it is important to first understand the shape of the eigenmodes that will be recovered from DMD analysis. To facilitate the above, data synthesised from theoretical analysis (5.1) are used as the input for DMD. The theoretical acoustic pressure data are acquired at the same locations as in experiments (table 5.1). A total of 700 snapshots are used with 0.025 non-dimensional time as the time interval between

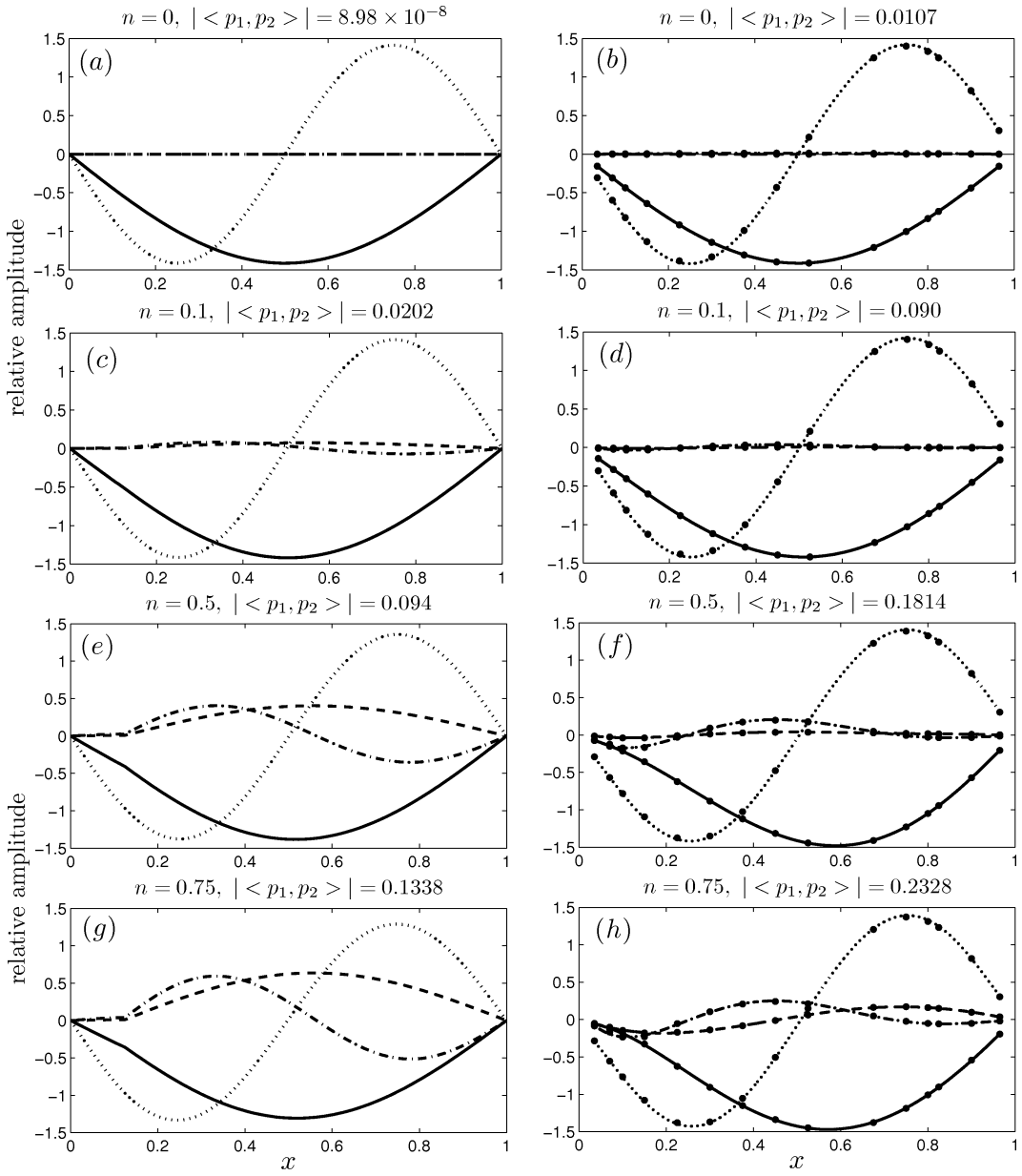

Figure 5.5: Comparison of the first two eigenmodes obtained analytically from $n - \tau$ model with the eigenmodes obtained by performing DMD on the data obtained from the same model. The eigenmodes along with the value of the non-dimensional heater power 'n' and the absolute value of the inner product $\langle p_1, p_2 \rangle$ are indicated in the title of each subfigures. Legend: '——' real part of first eigenmmode, '$\cdots\cdots$' real part of second eigenmode, '$- - -$' imaginary part of first eigenmode, '$\cdot - \cdot - \cdot$' imaginary of second eigenmode. The parameters are $x_f = 0.125,\ \tau = 0.2$ (Lighthill, 1954).

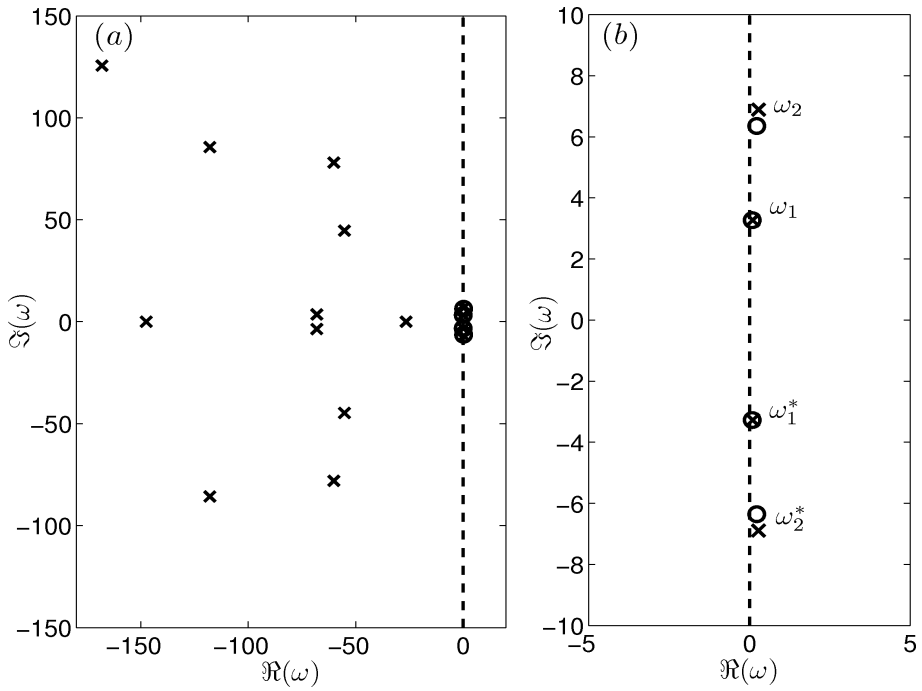

Figure 5.6: Comparison of the eigenvalues (ω_i) obtained from DMD (cross mark) with the actual one (hollow circles) obtained from (5.4) for $n = 0.5$, $\tau = 0.2$ & $x_f = 0.125$. *a*) Spectrum with all the eigenvalues from DMD. The four cross mark near the imaginary axis represents the actual eigenvalues. Other eigenvalues are spurious. *b*) The spectrum 'zoomed in' near the imaginary axis. Four eigenvalues correspond to the first two eigenmodes, along with their complex conjugate of the system.

them. The obtained DMD modes, which are same as the eigenmodes (because linear equations 5.1 are used) are shown on the right hand side of figure 5.5. The black dots indicate the locations of the microphones, from which the data is used to perform DMD. The discontinuity in slope of the theoretical imaginary part of the theoretical pressure eigenmodes is captured as wiggles around the location of the heater in the dynamic modes (compare figures 5.5*c* & *f*). The amplitude of the wiggles also increases with increase in the heater power n (see figures 5.5*b*, *d*, *f* & *h*). Also, one can observe that the wiggles are pronounced in the imaginary part of the eigenmodes. The real part of the eigenmodes did not distort much from the sine function in all the subfigures in figure 5.5.

In order to ensure that wiggles discussed above represent the discontinuity in the slope of the actual eigenmodes, the following verifications are performed. The eigenvalues obtained from DMD are compared with the actual eigenvalues and is shown in figure 5.6(*a*). The eigenvalues, which are close to the imaginary axis match with the actual eigenvalues. It is also observed that there are spurious eigenvalues with high frequency and decay rate. Figure 5.6(*b*) shows 'zoomed in' view of the spectrum near the imaginary axis with the relevant eigenvalues, which represents the first two eigenmodes of the system. The eigenvalues appear in complex conjugate pairs. Since there is no damping included in (5.1), the eigenvalues are unstable. The eigenvalue of the first mode matches well with the actual eigenvalue, whereas there is only a fair match for the second one.

For a linear system, the solution of the state space variables can be represented by eigenmode expansion (Strogatz, 2000). Figure 5.7(*a*) represents a typical synthetic acoustic pressure data, which is fed to DMD. The system is excited initially in first two eigenmodes. The dynamics of the system can be now represented only by the same two eigenmodes. DMD is performed on this synthetic data to obtain the dynamic modes. The evolution of the system can be represented in terms of dynamic modes as follows (Schmid, 2010).

$$p\left(x_j, t\right) = \sum_{j=1}^{N} A_j\left(t\right) p_j^d\left(x_j\right) \tag{5.6}$$

where, $p(x_j, t)$ is the synthetic acoustic pressure data generated at the location of the

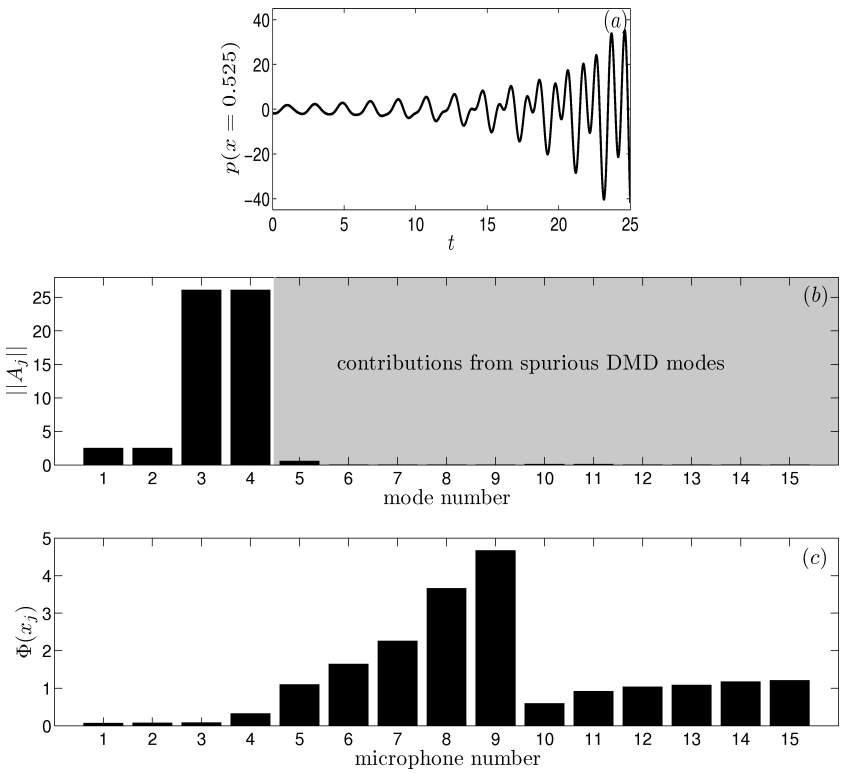

Figure 5.7: *a*) The input waveform synthesised by solving (5.1) to perform DMD. The initial condition is $p(x,0) = 0.6p_1(x) - 0.6p_1^*(x) + 0.3p_2(x) - 0.3p_2^*(x)$. *b*) Relative contribution (root mean square value) of the dynamic modes during the evolution of the system. The first four dynamic modes correspond to the first two eigenmodes, along with their complex conjugates. *c*) The percentage difference ($\Phi(x_j) = (||p(x_j,t) - p_r(x_j,t)||)\,/||p(x_j,t)|| \times 100$) between the input data and the reconstructed data using the first four dynamic modes of the system at all the locations of microphones. The parameters are same as in figure 5.6.

microphones x_j, p_j^d is the j^{th} dynamic mode, A_j is the projection coefficient and N is the total number of dynamic modes, which is 15 in the present case. Obtaining the rms value of A_j during the evolution of the system gives the relative contribution of p_j^d to the dynamics of the system. The same has been shown in figure 5.7(*b*), where it is observed that the first four dynamic modes, which represents the first two eigenmodes of the system (along with their complex conjugates) has dominant contributions in the evolution of the system. The above four dynamic modes are used to reconstruct acoustic pressure field ($p_r(x_j, t)$). The normalised difference between $p(x_j, t)$ and $p_r(x_j, t)$, calculated as $\Phi\left(x_j\right) = \left(\left(\|p\left(x_j, t\right) - p_r\left(x_j, t\right)\|\right)/\|p\left(x_j, t\right)\|\right) \times 100$, gives the percentage deviation of the reconstructed pressure field from the actual one. Figure 5.7(c) shows that the above deviation is less than 5% at all x_j and the first four dynamic modes represents the evolution of the system accurately. Hence the first four p_j^d are the first two eigenmodes of the system p_1 & p_2. Thus, the wiggles in the obtained eigenmodes are the manifestation of the discontinuity in the slope of the actual eigenmodes. Hence from the present experiments, it is expected that one should observe higher amplitude wiggles in the imaginary part of the dynamic modes, when the heater power is increased. Before applying DMD to the experimental data, the robustness of the above technique with the noise in the measurement of the data and the evaluation of uncertainty in the results are performed. The same has been explained in Appendix (I).

5.4.6 Transient growth experiment

The amount of transient growth depends on the direction of the initial condition. To observe transient growth, the initial condition given to the system should have projections on at least two eigenmodes (Schmid, 2007). In the present case, this is achieved by exciting the system initially for few cycles in time by a signal composing of two eigenfrequencies, which are obtained by DMD technique. Moreover, the relative amplitude of the two frequencies are varied to achieve various initial conditions, which shows variable degree of transient growth. The experiments are performed in the above sequence and the results are presented in the same order.

5.5 Results and discussions

Experiments are performed at an ambient temperature of 295-297 K, with a relative humidity of 72-74% so that the acoustic damping remains within required limits (Kinsler *et al.*, 2000). The exponential decay rate of the system in cold flow is measured as -10.5 $/s$ at 156 Hz, which corresponds to the eigenfrequency of the first natural mode. Decay rates are measured at the start of the experiments. The experiments are further continued only when the decay rates are within 5% of the value specified earlier. The above procedure is to ensure that acoustic damping does not vary significantly during the course of the experiments. The heater is located at $x_f = 0.125\ m$. Since the length of the Rijke tube is $1\ m$, the non-dimensional axial location x, which is used in the figures is numerically same as dimensional axial location.

5.5.1 Bifurcation diagram

Bifurcation diagram is first obtained, in order to identify the behaviour of the system with the variation of the control parameter. In the present case, electrical power (K) supplied to the heater is the control parameter and the 'root mean square (rms)' value of the acoustic pressure fluctuations ($P_{rms}|_{x=0.525}$) at $x = 0.525$ is the representative variable. Figure 5.8 shows the bifurcation diagram for various mass flow rates ($\dot{m}$). Initially, the power supplied to heater is low (see point A in figure 5.8*a*) so that the system is linearly and nonlinearly (globally) stable. The system is allowed to reach steady state and is confirmed by monitoring the temperature at the inlet and downstream ($x = 0.15$) of the heater. This process will take around 30 minutes. At this value of K, $P_{rms}|_{x=0.525}$ is noted. Now the voltage supplied to the heater is increased by $0.05\ V$, which amounts to an increase in power of less than $20\ W$. By leaving the system at a given power level for 4 minutes, the system is allowed to reach a steady state (Matveev, 2003). In this manner, the power supplied to the heater is increased in a quasi-steady manner. Increasing the heater power rapidly than the above specified values leads to premature transition to instability (Matveev, 2003).

The asymptotic state of the system is recorded for increase in the value of K and

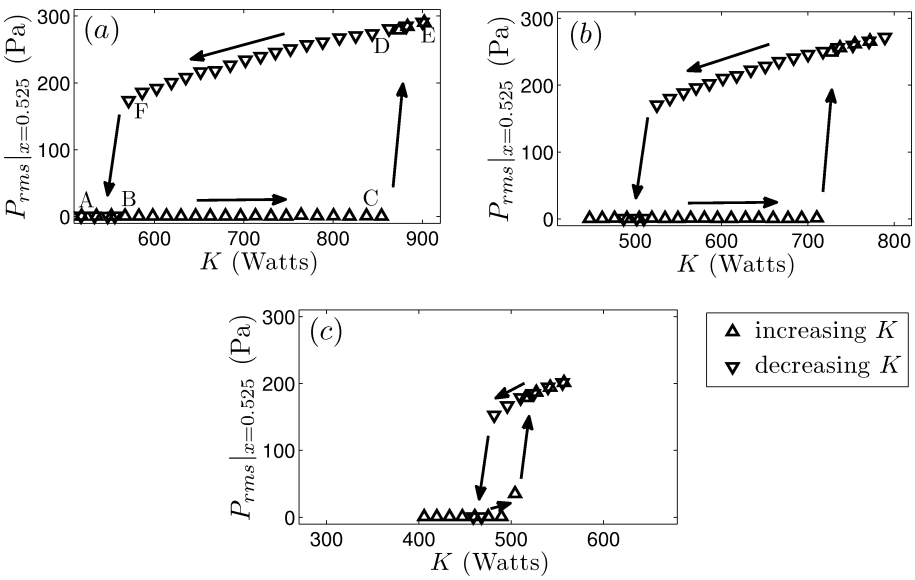

Figure 5.8: Bifurcation diagram. (a) $\dot{m}$ = 2.34 g/s, (b) $\dot{m}$ = 2.19 g/s, (c) $\dot{m}$ = 2.03 g/s.

is termed as 'forward path'. The term 'return path' is associated with the decrease in the value of K. The behaviour of the system with the variation in K is shown in figure 5.8(a). For low values of K (line AB), the system is globally stable. As the value of K is increased beyond point C (854 W), the system becomes linearly unstable and reaches limit cycle (point D). Further increase in K results in increase in the amplitude of the limit cycle (line DE). Now, as the value of K is decreased from point E, the system retraces the path till point D and then continues to stay in the limit cycle up to point F (571 W). Beyond F, the system reaches back to the steady state. The return path (ECFBA) is not same as the forward path (ABCDE). The system shows hysteresis behaviour with the power supplied to the heater. From dynamical systems' point of view, the above scenario of transition from globally stable to globally unstable behaviour is termed as 'subcritical Hopf bifurcation' (Strogatz, 2000). In the hysteresis zone (BCDF), the system is linearly stable, but nonlinearly unstable. This means that there is a threshold initial perturbation amplitude (also called triggering amplitude), above which the system becomes unstable and eventually reaches to a limit cycle. Our next step is to identify this triggering amplitude. It is also important to note that the hysteresis zone becomes smaller (figure 5.8 *b* & *c*) as one decreases $\dot{m}$, which is also observed by Matveev (2003). Since our main goal in the present paper is to analyse the non-normal nature of the system, which is important in the hysteresis (subcritical

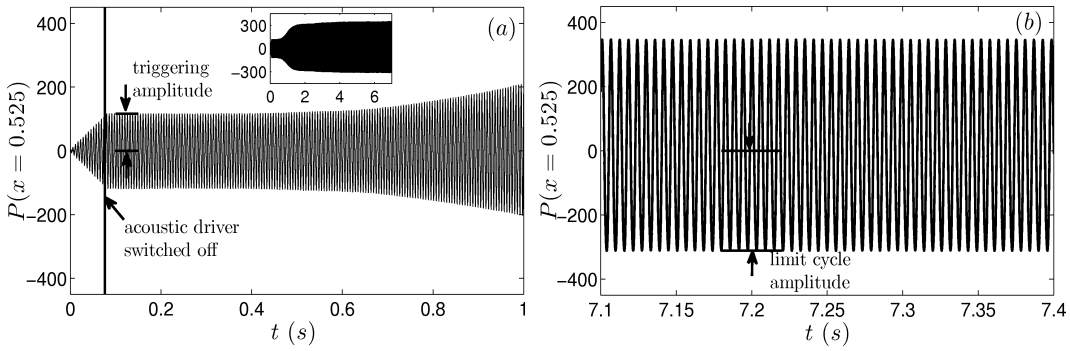

Figure 5.9: Determination of triggering and the corresponding limit cycle amplitudes. $K = 782\ W$, $\dot{m}$ = 2.34 g/s.

transition) zone, the configuration with $\dot{m} = 2.34$ g/s is chosen for further analysis, as it has a larger hysteresis zone.

The triggering amplitude of the system is obtained as follows. The system is first allowed to attain a steady state in the hysteresis region. Now, using the acoustic driver units, an initial acoustic pulse train is fed to the system. The pulse train consists of 14 cycles of sinusoidal wave with frequency equal to the first eigenfrequency of the system. The amplitude of the input wave is increased till the system is triggered from a linearly stable state to nonlinearly unstable state. When the excitation is in the frequency of the second eigenmode, higher triggering amplitude is required to make the system nonlinearly unstable. Hence the triggering amplitude is estimated by exciting the first eigenmode alone. Also, the triggering amplitudes are different for acoustic and non-acoustic type of initial conditions (Mariappan *et al.*, 2010). However, in the present experiments, only acoustic initial conditions are analysed. Hence, triggering amplitude associated with the acoustic initial conditions are investigated. Figure 5.9(*a*) shows the evolution of the system, when the initial pulse triggers the system to nonlinearly unstable state. The inset shows the evolution of the system eventually to a limit cycle. The initial $P_{rms}|_{x=0.525}$ (after the acoustic drivers are switched 'off') is noted as the triggering amplitude. The corresponding limit cycle obtained is shown in figure 5.9(*b*) and the value of $P_{rms}|_{x=0.525}$ is recorded for the same.

The above exercise of obtaining the triggering and limit cycle amplitudes are repeated for various values of K and the consolidated results are shown in figure 5.10.

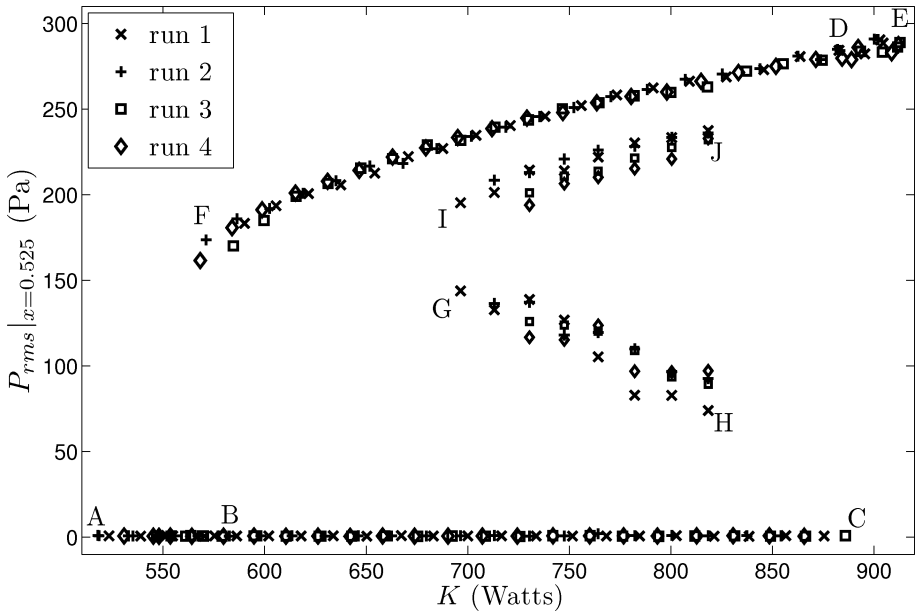

Figure 5.10: Bifurcation diagram showing the hysteresis behaviour along with triggering (GH) and limit cycle (IJ) amplitudes. In order to confirm repeatability, four experiments are performed. $\dot{m}$ = 2.34 g/s.

Bifurcation diagram is represented by ABCDEF as earlier. The triggering and the corresponding limit cycle amplitudes are represented by 'GH' and 'IJ' respectively. In order to confirm repeatability, four experiments are performed. The limit cycle amplitudes in the bifurcation diagram are highly repeatable. The uncertainty in Hope (C) and fold (F) points are observed to be within a band of 40 W, which are less than 4.5 % of the power levels at the respective points. Further, the spread in the triggering and the corresponding limit cycle amplitudes are less than 12 % of the respective mean values. Thus repeatability of the experimental results is ensured. Determination of triggering amplitudes beyond H, prescribed by the above spread is difficult, as one is close to the Hopf point (C) and hence are not obtained. The acoustic drivers used in the present case cannot trigger the system to nonlinearly unstable state beyond point G. Hence triggering experiments are not performed beyond point G. The amplitude of the limit cycle (IJ) obtained by triggering the system is smaller than that obtained from the bifurcation diagram (FD). This can be attributed to the difference in the mean temperature in the duct during the phase of increasing and decreasing (path ABCDE and EDFBA in figure 5.8) heater power as shown in figure 5.11. The increase in the mean temperature is due to non-zero mean heat transfer effects happening during intense thermoacoustic

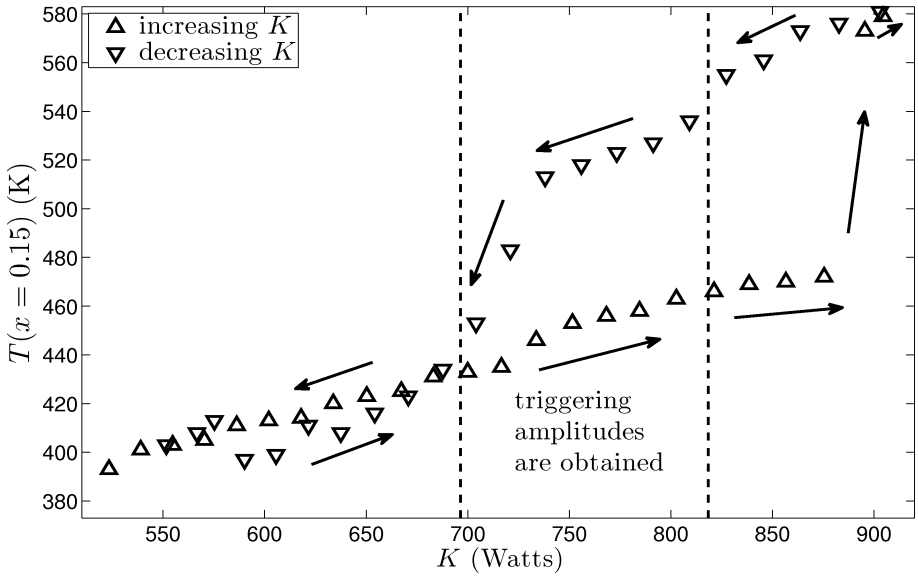

Figure 5.11: Steady state temperature recorded downstream of the heater during experimental run 1. The steady state temperature during increasing and decreasing values of 'K' are shown. Vertical lines indicate the power level associated with the region IJ shown in figure 5.10.

oscillations. The above phenomenon is also observed by Matveev (2003). The region GHJI is the subcritical transition region, which can be accessed with the present experimental setup. The next step is to obtain the regime of linearity, so that investigations of non-normal nature of the system can be performed.

5.5.2 Identification of linear regime

In this section, the range of linearity is determined as already described in § 5.4.2. In order to identify the linear regime, it is important to characterise the acoustic drivers for its linearity. The equations governing the classical acoustic field in a duct is linear. The above fact is used to analyse the linearity of the acoustic drivers. The Rijke tube system is excited continuously using acoustic drivers with the heater and blower switched off at a given frequency. The response of the system is recorded from the microphones. The voltage supplied to the acoustic driver is also noted and varied. A response curve for the acoustic driver unit is obtained and is shown for three forcing frequencies in figure H.1. In the x-axis, the rms value of the voltage supplied to the acoustic driver units is shown and in the y-axis, the rms value of the acoustic pressure fluctuations ($P_{rms}|_{x=0.525}$) is

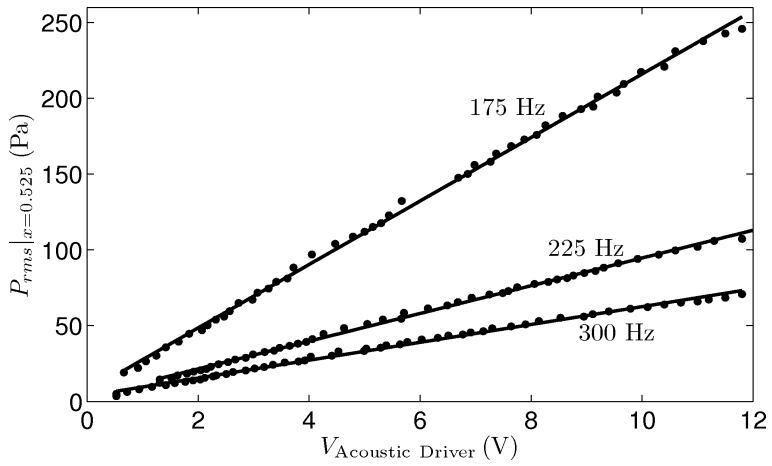

Figure 5.12: Characteristics of the acoustic driver unit, obtained for three different frequencies. The rms value of the voltage supplied to the acoustic driver unit is indicated in 'x' axis. The dots indicate the actual data, while the continuous line is the corresponding linear fit.

shown. The dots indicate the actual data and the line indicates the linear fit. From the response curve, one can conclude that the linear fit represents the actual data with less than 0.5% spread. Hence for the voltage range indicated in figure H.1, the relationship between the voltage supplied to acoustic driver and the acoustic pressure generated is linear.

The heater and blower are now switched on. Due to reasons explained in the last paragraph of § 5.5.1, linear regime is identified only in zone GH. Figure H.2 represents the response of the system to continuous excitation with the acoustic driver and the output as the rms value of acoustic pressure fluctuations. As earlier, dots indicate the actual data. It can be observed that the dots does not form a straight line and it grows sub linearly for larger amplitudes of the voltage supplied to the acoustic driver. Dashed line indicates a quadratic fit to the actual data with a spread of 0.3%. A linear fit, shown as a continuous line is performed with the actual data at low amplitudes of $V_{\text{Acoustic driver}}$, which in the present case is less than 3 V. The triggering amplitude is marked as a chained horizontal line. In the present case, the limit of linearity is determined when the deviation of the actual data from the linear fit is more than 5% of the corresponding triggering amplitude. The amplitude at which nonlinear nature of the system is significant is indicated by the triggering amplitude and hence is chosen as the

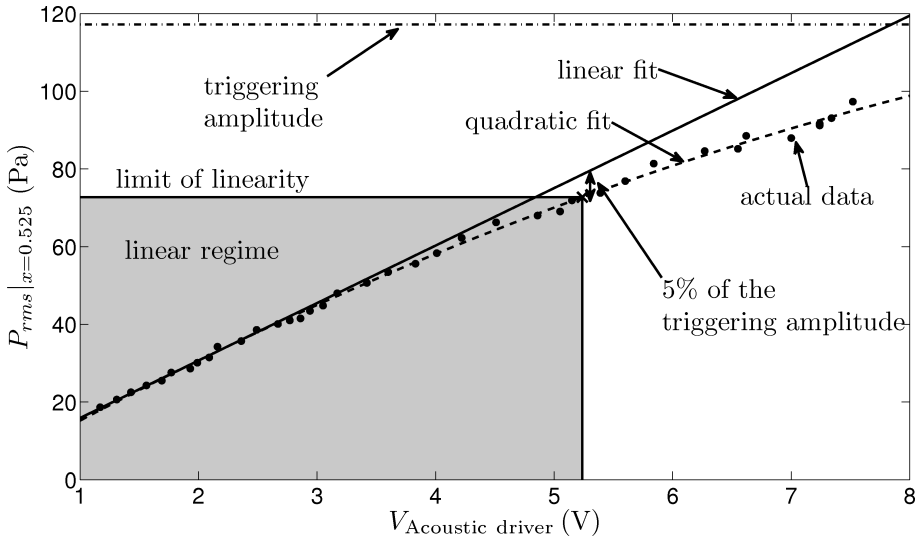

Figure 5.13: Identification of linear regime. Acoustic forcing is performed at 300 Hz with $K = 764$ W & $\dot{m}$ = 2.34 g/s. Shaded grey area indicates the linear regime.

reference. The above defined linear regime is shaded in grey as shown in figure H.2. For a given power supplied to the heater, the acoustic pressure amplitude corresponding to the limit of linearity is the upper limit of acoustic pressure level in the duct, where the system behaves as a linear system. The contribution from the nonlinearity of the system can be neglected in the above regime.

The power supplied to the heater is now varied and the same procedure is repeated. The limit of linearity is obtained and is shown in figure 5.14 along with the triggering amplitude. In the consolidated bifurcation plot, 'LN' represents the limit of linearity. Line segments GH and IJ represent the mean value of the triggering and the corresponding limit cycle amplitudes over different experiments shown previously in figure 5.10. Experiments, which are focussed on the investigation of transient growth are performed in the regime indicated in grey colour. It is observed from figure 5.14, that the linear regime is fairly large in the bifurcation diagram, so that the measurements can be obtained with low noise level. As the first step in the investigation of the non-normal nature of the thermoacoustic interaction, the non-orthogonality of the eigenmodes of the system are investigated experimentally. The results of the same are discussed in the following subsection.

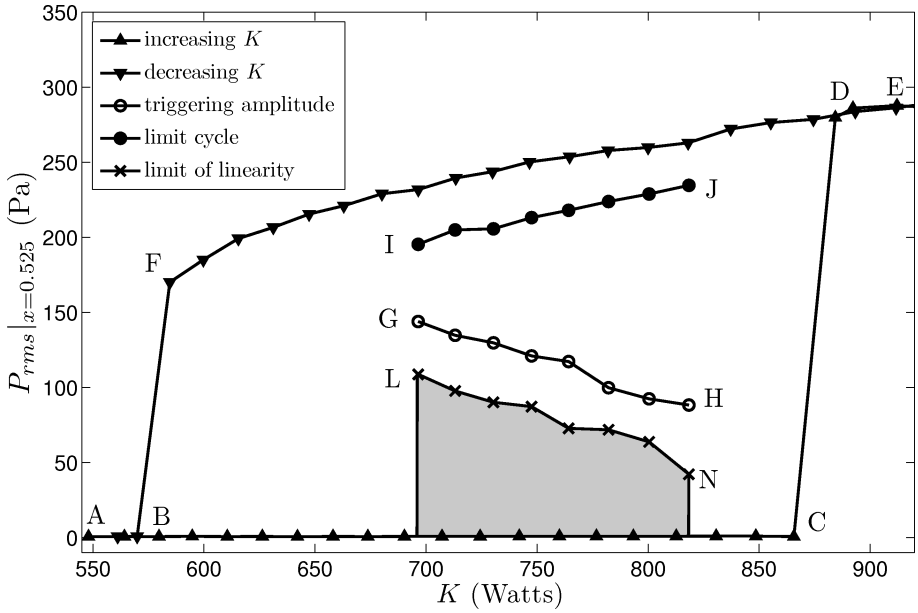

Figure 5.14: Consolidated bifurcation diagram, showing triggering amplitude, limit cycle and the extent of linear regime. The experiments associated with the investigation of non-normal nature of the system are performed in the linear regime, shaded in 'grey'.

5.5.3 Non-orthogonality of the eigenmodes

Acoustic pressure data recorded by the microphones are used for DMD analysis. A total of 742 snapshots are used with 0.125 ms as the time interval between them is used in DMD. The amplitudes of the recorded acoustic pressure data are below the linearity limit defined in § 5.5.2. A typical data used for DMD analysis are shown in figures I.1(*b* & *d*) and the effect of noise in the measurements are discussed in Appendix (I). As described earlier in § 5.4.3, the non-orthogonality of the eigenmodes is determined by the numerical value of $|\langle p_1, p_2 \rangle|$. The eigenmodes and the corresponding value of $|\langle p_1, p_2 \rangle|$ obtained from experimental data are shown in figure 5.15. As the power supplied to the heater is increased, the amplitude of the wiggles are observed to increase in the imaginary part of the eigenmodes. The corresponding value of $|\langle p_1, p_2 \rangle|$ also increases with increase in the value of K. The uncertainty in the value of $|\langle p_1, p_2 \rangle|$ is 10% for the noise level encountered in the present experiments (see Appendix I). The variation of $|\langle p_1, p_2 \rangle|$ with the value of K is shown in figure 5.15(*g*) along with the associated error bars. From the above figure, it can be concluded that the non-orthogonality of the

eigenmodes of the system increases with increase in the power supplied to the heater.

As before in § 5.4.5, verifications are performed in order to ensure that the wiggles represent the discontinuity in the slope of the eigenmodes. Figure 5.16(*a*) shows the spectrum obtained by applying DMD on the data associated with figure 5.15(*f*). The eigenvalues are numbered and again, the first four represent the eigenvalues of the system. The other eigenvalues are spurious. For example, eigenvalues like 5 - 9 are real numbers and just represent the decay of the perturbations without any oscillations. On the other hand, eigenvalues 10 & 11 corresponds to high frequency and fast decaying oscillations. The above eigenvalues do not have any physical significance associated with the dynamics of the system. The contribution of all the dynamic modes in the evolution of the system is shown in figure 5.16(*b*). The contribution from the first four dynamic modes are significant and since the experiment is performed in the linear, the above four represent the first two eigenmodes of the system. The acoustic pressure data are reconstructed using the first two eigenmodes and are compared with the original evolution data of the system as before in figure 5.16(*c*). The maximum error observed is 20%, which is reasonable for a reconstruction of an experimental data (Podvin *et al.*, 2006).

5.5.4 Evidence of transient growth

The eigenmodes of the system are non-orthogonal and hence transient growth of the initial perturbations is present. The amount of transient growth is characterised by a scalar measure. In the present system, total acoustic energy defined as $\tilde{E}(t) = \frac{S_c}{2}\left(\int_0^L \left(\bar{\rho}u^2 + p^2/\left(\gamma\bar{p}\right)\right) dx\right)$ is used as the measure. The same measure is used by Balasubramanian and Sujith (2008*b*) in the theoretical analysis of the same Rijke tube system. S_c is the cross section area of the tube and overbar ($\bar{}$) represents the steady state quantities. Acoustic pressure (p) is measured already at 15 locations and the acoustic velocity (u) is obtained by two microphone technique (Bellows, 2006). The largest spacing between any two microphones in the present experiment is 75 mm and the cross section dimension is 92 mm, which facilitate to measure acoustic velocity fluctuations in the frequency range 100 Hz - 1.76 kHz (Abom and Boden, 1988). In the

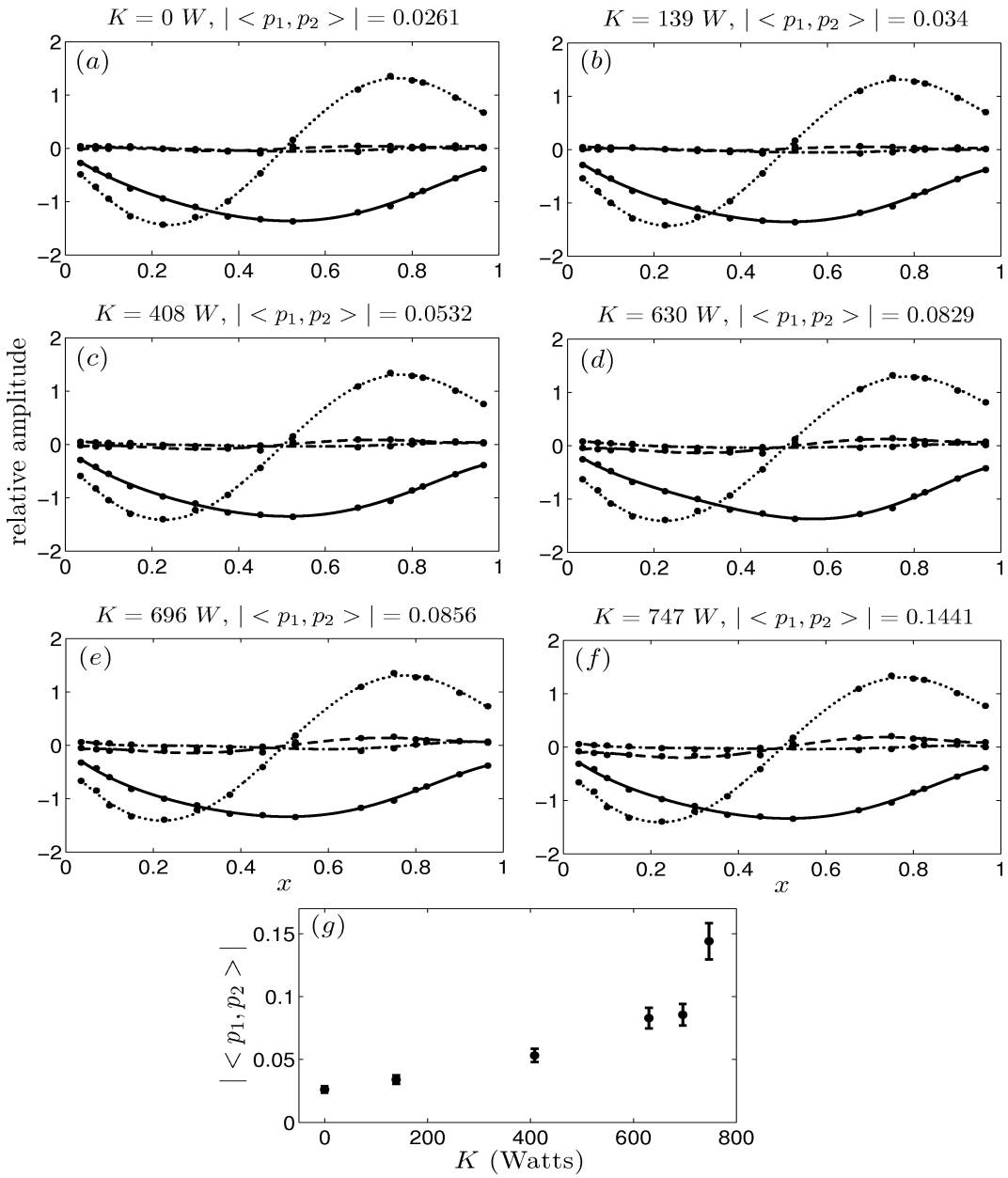

Figure 5.15: *a-f*) First two eigenmodes obtained by performing DMD on the data obtained from experiments. The eigenmodes with the value of the heater power 'K' and the absolute value of the inner product $\langle p_1, p_2 \rangle$ are indicated in the title of each subfigures. Legends are same as in figure 5.5. *g*) Variation of $|\langle p_1, p_2 \rangle|$ with the power supplied to the heater, along with the associated error bars.

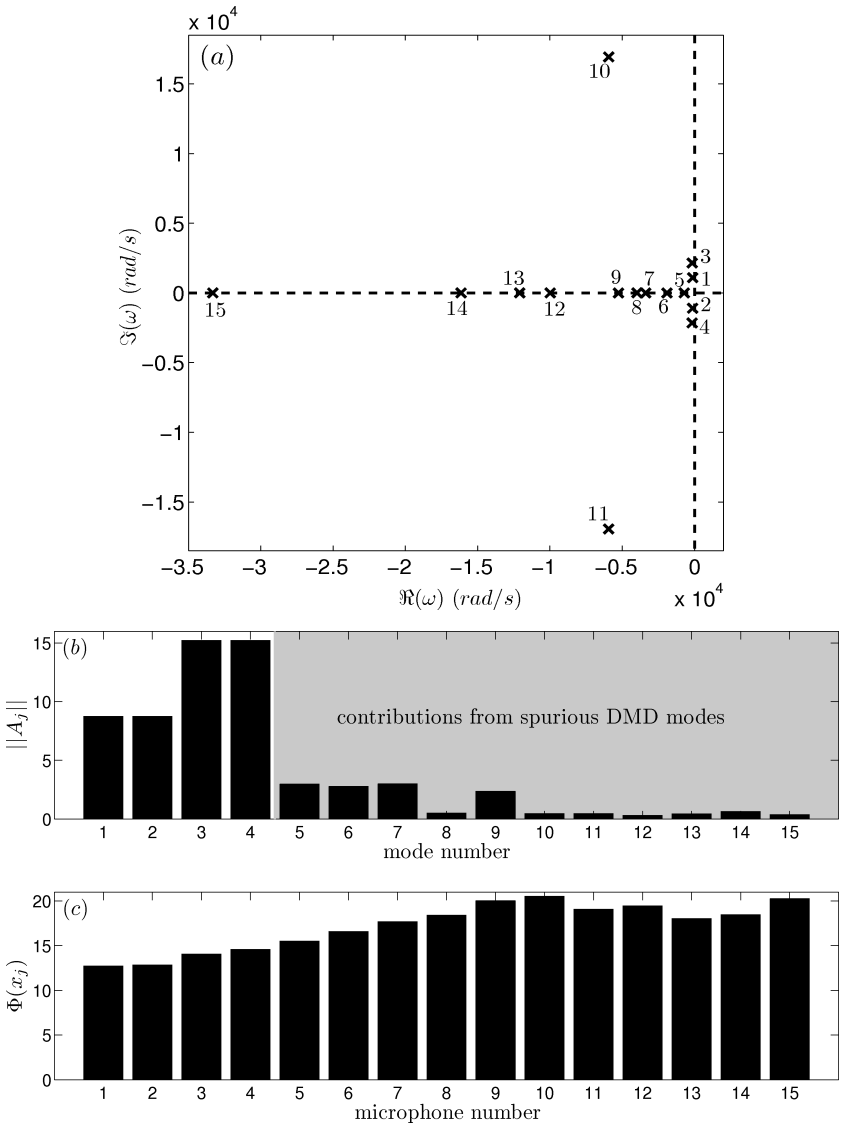

Figure 5.16: *a*) Spectrum obtained by applying DMD on the data associated with figure 5.15(*f*). The eigenvalues are numbered and corresponds to the dynamic mode number in the next subfigure. The dotted horizontal and vertical lines represent the real and imaginary axis respectively. The first four eigenvalues represent the first two eigenmodes of the system. *b*) Relative contribution (root mean square value) of the dynamic modes during the evolution of the system. The first four dynamic modes correspond to the first two eigenmodes, along with their complex conjugates. *c*) The percentage difference ($\Phi(x_j) = (||p(x_j,t) - p_r(x_j,t)||) / ||p(x_j,t)|| \times 100$) between the input data and the reconstructed data using the first four dynamic modes of the system at all the locations of microphones.

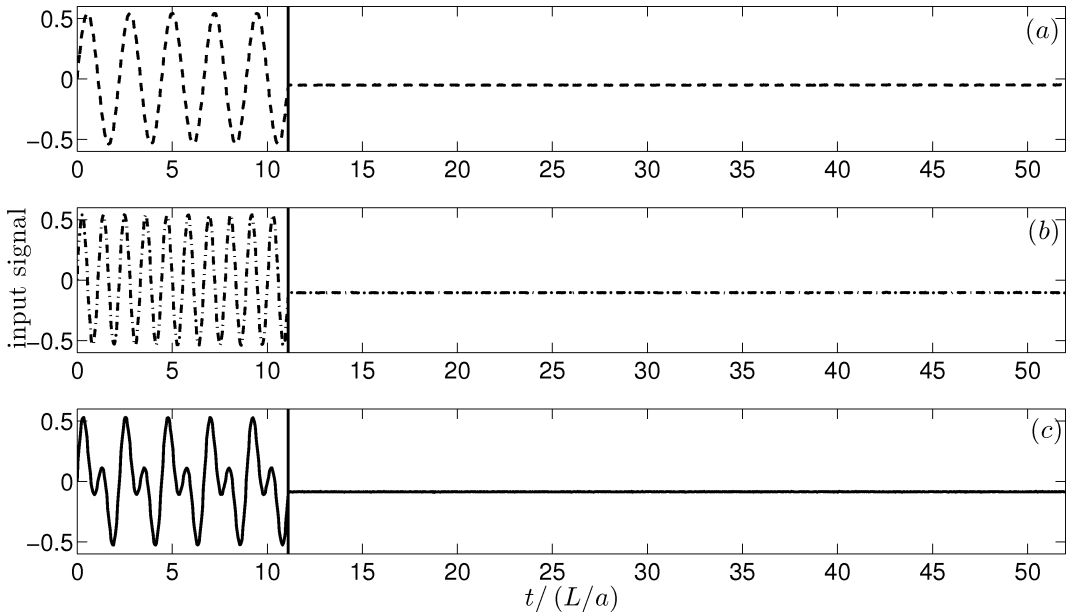

Figure 5.17: Three kinds of initial perturbations given to the system through acoustic driver. Sinusoidal input of the form *a*) $0.54sin(2\pi f_1 t)$, *b*) $0.54sin(2\pi f_2 t)$, *c*) $0.3sin(2\pi f_1 t) + 0.3sin(2\pi f_2 t)$, where f_1 & f_2 are the frequencies of the first and second eigenmodes of the system. The vertical black line indicates the time location, where the acoustic driver is switched off and implies the same in figure 5.18

present case, first ($\approx 175\ Hz$) and second ($\approx 350\ Hz$) eigenmodes of the system are of interest. Hence, the above spacing is suitable for the present experimental investigation. Since the amount of transient growth depends on the type of initial condition, three kinds of initial perturbations are considered as shown in figure 5.17. The first two kinds of initial conditions correspond to excitation with a pure sinusoidal frequency of the first two eigenmodes respectively. The waveform of the last kind of initial perturbation is a linear combination of first two eigenfrequency of the system. The vertical black line indicates the time location, where the acoustic driver is switched off and implies the same in figure 5.18. The evolution of the system to the above three initial conditions is analysed. Two cases, heater switched 'off' and 'on' are investigated. When the heater is switched off, the non-dimensional acoustic energy ($E = \tilde{E}/\left(S_c \rho_u u_u^2/2\right)$, subscript '$u$' represents upstream steady state quantities) decays monotonically in time after the excitation from the acoustic driver ceases. This is shown in figure 5.18(*a*). The grey area indicates the region, where the forcing from the acoustic driver is present. The amplification of acoustic energy ($E(t)/E(0)$) measured from the instant when the

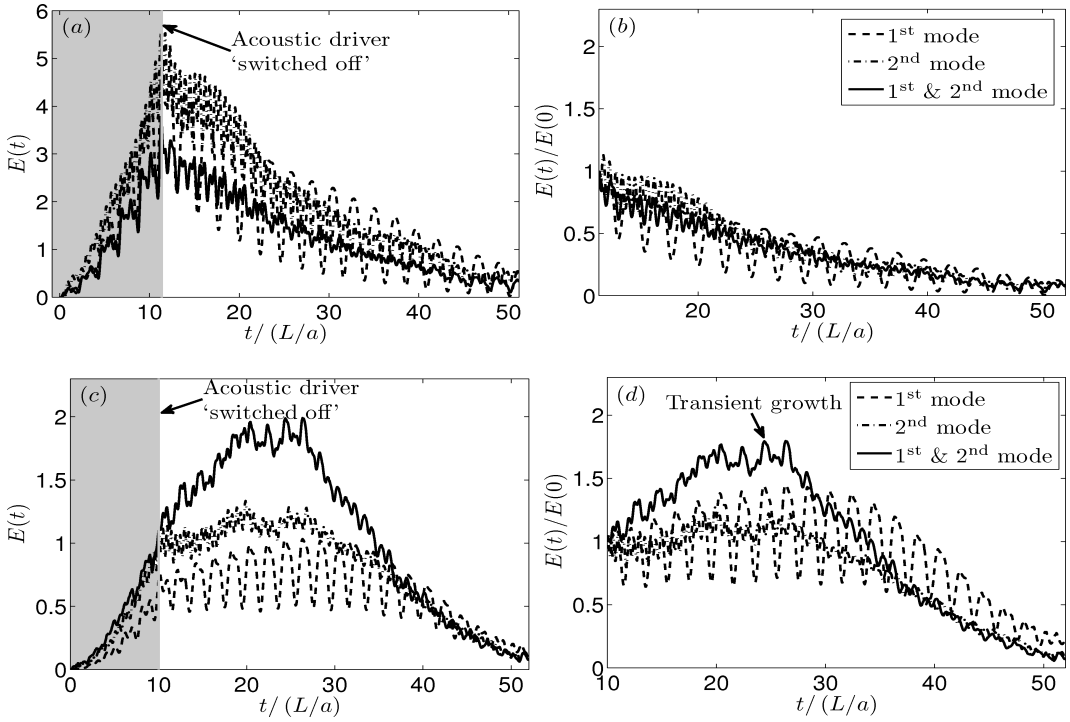

Figure 5.18: Evolution of non-dimensional acoustic energy defined as $E(t) = \left(\int_0^L \left(\rho u^2 + p^2/\left(\gamma p_u\right)\right) dx\right) / \left(\rho_u u_u^2\right)$. *a*) heater switched off, & *c*) heater switched on ($K = 747\ W$). Evolution of the amplification of acoustic energy $E(t)/E(0)$ with *b*) heater switched off, & *d*) heater switched on. The colours indicate evolutions corresponding to three kinds of initial conditions shown in figure 5.17. Grey area indicates the region, where the acoustic driver is switched on.

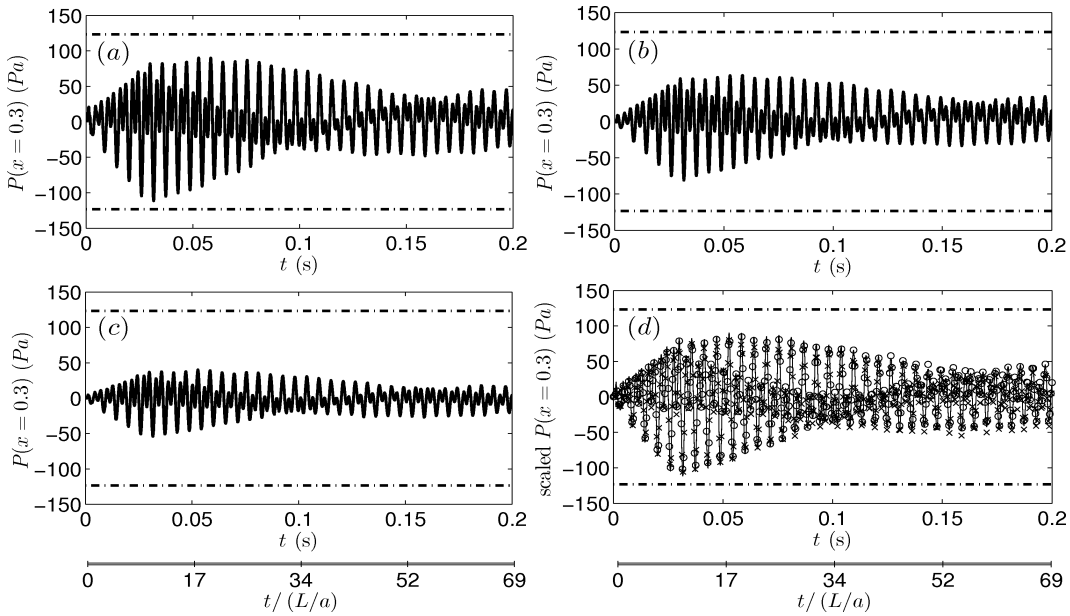

Figure 5.19: Evolution of acoustic pressure at $x = 0.3$ in the linear regime. Chained lines in all the subfigures represent the amplitude of the limit of linearity. The amplitude of the initial perturbation is scaled and the subsequent evolution of the system is recorded. *a*) $0.1sin(2\pi f_1 t) + 0.1sin(2\pi f_2 t)$, *b*) $0.075sin(2\pi f_1 t) + 0.075sin(2\pi f_2 t)$, *c*) $0.05sin(2\pi f_1 t) + 0.05sin(2\pi f_2 t)$, *d*) Rescaled evolution of acoustic pressure from subfigures (*a*-*c*). Hollow circles and cross mark are associated with the data from subfigures (*b* & *c*) respectively. The duration of the evolution of the system shown is $0.2\ s$, which corresponds to a non-dimensional time $(t/\ (L/a))$ of 69. $K = 747\ W$

acoustic speaker is switched off, is plotted in figure 5.18(*b*). Note the shift in the time axis, as it starts from 11.13. The numerical value of $E(t)/E(0)$ measures directly the amount of transient growth present in the system. There is no transient growth observed in cold flow for all kinds of initial conditions, indicating that the dynamics of the pure acoustic field is normal. The same exercise is repeated with the heater switched 'on' at 747 W. Figure 5.18(*c*) represents the evolution of acoustic energy. When the system is excited using first and second kind of initial condition, there is no significant transient growth. After the above initial condition, mostly only one eigenmode is excited and due to the linearly stable nature of the system, $E(t)$ decreases monotonically. However, when the initial condition has projections on two eigenmodes (figures 5.17*c*), transient growth (green curve) is observed. The amount of transient growth can be seen from figure 5.18(*d*). The amplification of acoustic energy is 1.8 for the third kind of initial condition to the system. The growth in energy is of the same order as reported numerically by Balasubramanian and Sujith (2008*b*). The amplitude of the acoustic pressure in the above experiment is below the limit of linearity (section 5.5.2). In order to further ensure that the growth observed is due to non-normal nature of the system, following check was performed. Figure 5.19(*a*) shows the evolution of acoustic pressure, which portrayed transient growth in figure 5.18(*c*) and it corresponds to the third kind of initial condition. Two horizontal lines indicate the limit of linearity. To check linearity, the initial perturbation amplitudes are scaled by 0.75 & 0.5 and the subsequent evolution of the system is shown in figure 5.19(*b* & *c*) respectively. The shape of the acoustic pressure trace is same in all the cases (figure 5.19*a* - *c*). The pressure evolutions in figure 5.19(*b* & *c*) are rescaled and are compared with the original evolution. The results are plotted in figure 5.19(*d*). The dotted lines indicate and the rescaled evolution of pressure and the continuous line correspond to the original pressure trace. The rescaled pressure traces match well (within 3%) with the original one. Moreover, the above match is confirmed for a duration of 69 non-dimensional time, which contains the time duration shown in figure 5.18. The above exercise indicates that the evolution of the system is linear and the transient growth observed in figure 5.18(*c*) is indeed due to the non-normal nature of the thermoacoustic interaction.

5.6 Conclusion

In the present paper, experiments are performed to identify the non-normal nature of thermoacoustic interaction in an electrically heated horizontal Rijke tube. A total of 15 microphones are placed along the tube to measure acoustic pressure and 2 thermocouples, one at the inlet of the tube and the other just downstream of the heater, to monitor the steady state temperature in the duct. The system is perturbed using four acoustic driver units located on the tube. Since non-normality is a linear phenomenon, the experiments have to be performed in a regime, where the system is linear. To identify the linear regime, the following procedure is performed. First, the bifurcation diagram is obtained with the power supplied to the heater as the control parameter. The transition from linearly stable to unstable to behaviour happens via subcritical Hopf bifurcation and is manifested as an hysteresis behaviour. Then, in the hysteresis region, triggering amplitude for the system to become nonlinearly unstable is obtained. As the last step, the linear regime is identified by forcing the system continuously at a particular frequency and measuring the response of the same. The limit of linearity is determined as the amplitude of the acoustic pressure level in the tube, at which the response of the system deviates from the linearised response by 5% of the triggering amplitude. Experiments associated with the investigation of the non-normal nature of the system are performed below this limit of linearity.

Two sets of experiments are performed, in order to observe the non-normal nature of the system. The first one deals with the extraction of the eigenmodes of the system from the experimental data. Dynamic mode decomposition (DMD) technique is applied to the obtained acoustic pressure data to extract the eigenmodes. From the theoretical investigation, a discontinuity in the slope of the pressure eigenmodes at the location of the heater is observed. The above discontinuity increases with the increase in the heater power and it increases the non-orthogonality of the eigenmodes of the system. The synthetic data from the above theoretical analysis is fed to DMD and the discontinuity in the slope of the eigenmodes is captured as wiggles near the location of the heat source. The non-orthogonality between the eigenmodes obtained from DMD also increases with heater power. From the experimental data, first two eigenmodes are extracted and again the wiggles are observed in the same. The uncertainty in the non-orthogonality between

the eigenmodes are evaluated from the consideration of the background noise present in the system. It is observed that the non-orthogonality of the experimentally obtained eigenmodes increases (with the associated error bars) with increase in the heater power, thus identifying the non-normal nature of thermoacoustic interaction.

The second set of experiments are performed in order to capture transient growth experimentally. The amount of transient growth is measured in terms of acoustic energy in the system. Acoustic pressure is measured directly and acoustic velocity is calculated by applying two microphone technique onto the obtained pressure data. Three kinds of initial conditions are given to the system. The first two kinds of initial conditions correspond to excitation with a pure sinusoidal frequency of the first two eigenmodes respectively for a brief period of time. Afterwards, the system is allowed to evolve on its own. The waveform of the last kind of initial perturbation is a linear combination of first two eigenfrequency of the system. With the heater switched on, when the system is excited using first and second kind of initial condition, there is no significant transient growth. On the other hand, transient growth of approximately two fold increase in acoustic energy is observed during the the excitation of the system with the third kind of initial condition. Moreover, when the above experiment is performed with the heater switched off, no significant transient growth is observed for all the three kinds of initial perturbations. The above experiment confirms that transient growth is indeed present and is due to the non-normal nature of thermoacoustic interactions.

APPENDIX A

Coupling terms in Eqns. (2.9) and (2.10)

The linear and nonlinear coupling terms used in Eqns. (2.9) and (2.10) are given below:

$$
\begin{aligned}
I^1_{n,m} &= \int_0^1 \left[M\bar{U}\omega_m \cos(\omega_m x) + M\frac{d\bar{U}}{dx}\sin(\omega_m x) - k_m \sin(\omega_m x) \right] \sin(\omega_n x) dx \\
I^2_{n,m} &= \int_0^1 \left(\frac{M^2\bar{U}}{\gamma}\frac{d\bar{U}}{dx}\cos(\omega_m x) - \omega_m \sin(\omega_m x) \right) \sin(\omega_n x) dx \\
I^3_{n,m} &= -\int_0^1 k_m \bar{U} \cos(\omega_m x)\sin(\omega_n x) dx \\
I^4_{n,m} &= -\int_0^1 k_m \bar{U} \sin(\omega_m x)\sin(\omega_n x) dx \\
I^5_{n,m} &= \int_0^1 \gamma M \omega_m \cos(\omega_m x)\sin(\omega_n x) dx \\
I^6_{n,m} &= \int_0^1 \left[(\lambda M)^2 \frac{d\bar{U}}{dx}\bar{U}\cos(\omega_m x) - \gamma M^2 \bar{U}\omega_m \sin(\omega_m x) \right] \cos(\omega_n x) dx \\
I^7_{n,m} &= -\int_0^1 k_e \cos(\omega_m x)\cos(\omega_n x) dx \\
N^1_n &= \int_0^1 \left[\sum_{m=1}^{N} \left(R^c_m \cos(\omega_m x) + R^s_m \sin(\omega_m x) \right) \sum_{k=1}^{N} U_k \sin(\omega_k x) \right] \sin(\omega_n x) dx \\
N^2_n &= \int_0^1 \left[\sum_{m=1}^{N} U_m \sin(\omega_m x) \sum_{k=1}^{N} U_k \omega_k \cos(\omega_k x) \right] \sin(\omega_n x) dx \\
N^3_n &= \int_0^1 \left[\sum_{m=1}^{N} P_m \cos(\omega_m x) \sum_{k=1}^{N} P_k \omega_k \sin(\omega_k x) \right] \sin(\omega_n x) dx \\
N^4_n &= \int_0^1 \left[\sum_{m=1}^{N} U_m \sin(\omega_m x) \sum_{k=1}^{N} P_k \omega_k \sin(\omega_k x) \right] \cos(\omega_n x) dx \\
N^5_n &= \int_0^1 \left[\sum_{m=1}^{N} P_m \cos(\omega_m x) \sum_{k=1}^{N} U_k \omega_k \cos(\omega_k x) \right] \sin(\omega_n x) dx
\end{aligned}
\tag{A.1}
$$

APPENDIX B

Linearised equations

The linearised evolution equation, corresponding to Eqns. (2.25, 2.26, 2.29 & 2.30) for the coupled acoustic – burn rate equation is

$$\frac{d\chi}{dt} = L\chi$$

$$L = \begin{pmatrix} A_{2N\times 2N} & B_{2N\times(2N(M_g-1))} \\ C_{(2N(M_g-1))\times 2N} & D_{2N(M_g-1)\times 2N(M_g-1)} \end{pmatrix}_{(2NM_g)\times(2NM_g)}$$

$$A = -2\begin{pmatrix} I^1_{1,1} & I^2_{1,1} & I^1_{1,2} & I^2_{1,2} & . & . \\ I^5_{1,1}/\gamma M & I^6_{1,1}/\gamma M - (\alpha_{NO}+\xi_1)/2 & I^5_{1,2}/\gamma M & I^6_{1,2}/\gamma M & . & . \\ I^1_{2,1} & I^2_{2,1} & I^1_{2,1} & I^2_{2,2} & . & . \\ I^5_{2,1}/\gamma M & I^6_{2,1}/\gamma M & I^5_{2,1}/\gamma M & I^6_{2,2}/\gamma M - (\alpha_{NO}+\xi_2)/2 & . & . \\ . & & & & . & . \\ . & & & & . & . \\ . & & & & & \\ . & . & . & . & . & . \end{pmatrix}_{2N\times 2N}$$

$$B = -\frac{2m}{\beta_1}\begin{pmatrix} E^c_{1,1} & E^c_{1,2} & . & . & E^c_{1,N} & E^s_{1,1} & E^s_{1,2} & . & . & E^s_{1,N} \\ E^c_{2,1} & E^c_{2,N} & . & . & E^c_{2,N} & E^s_{2,1} & E^s_{2,1} & . & . & E^s_{2,1} \\ . & . & . & & & & & & & \\ & & & & & & & & & . \\ . & . & . & . & . & . & . & . & . & . \end{pmatrix}_{2N\times(2N(M_g-1))}$$

$E^c_{j,n}(1,1) = I^3_{j,n}$, $E^c_{j,n}(2,1) = I^7_{j,n}$, $E^s_{j,n}(1,1) = I^4_{j,n}$.

All other entries are zero. Note that $E^c_{j,n}$ and $E^s_{j,n}$ are $2 \times (M_g - 1)$ matrices.

$$C = \begin{pmatrix} S_1 \\ S_2 \\ S_3 \\ . \\ . \\ S_N \\ 0 \\ 0 \\ 0 \\ . \\ . \end{pmatrix}_{(2N(M_g-1)\times 2N)} \qquad S_q(2,2) = \gamma M F \beta_1 \left(B(1-k) + \frac{2Bk}{\Delta\eta} \right)$$

S_q is $(M_g\text{-}1)\times 2N$ matrix. All other entries are zero.

$$D = \begin{pmatrix} D^c & 0 \\ 0 & D^s \end{pmatrix}, \quad D^s = D^c = \begin{pmatrix} G_1 & 0 & 0 & . & . \\ 0 & G_2 & 0 & . & . \\ & & & & . \\ & & & . & . \\ 0 & 0 & . & . & G_N \end{pmatrix}_{(M_g-1)N\times(M_g-1)N}$$

$$G_N = F \begin{pmatrix} B^c_1 & 0 & B^c_2 & 0 & 0 & 0 & . & . \\ H^1_2 + H^4_2 & H^2_2 & H^3_2 & 0 & 0 & 0 & . & . \\ H^4_3 & H^1_3 & H^2_3 & H^2_3 & 0 & 0 & . & . \\ . & & & & & & & \\ . & & & & & & . & . \\ . & & & & & . & . & . \\ . & & & & & . & . & 0 \\ H^4_{M_g-1} & . & . & 0 & 0 & H^1_{M_g-1} & H^2_{M_g-1} & H^3_{M_g-1} \end{pmatrix}_{(M_g-1)\times(M_g-1)}$$

$$B_1^c = A(k-1) - \left(\frac{k}{\Delta\eta}\right)^2 \left(1 + \frac{2\Delta\eta A}{k}\right) - mB_2^c = \frac{\beta_1}{\beta_3}\left(\frac{k}{\Delta\eta}\right)^2$$

$$H_q^1 = \frac{\beta_i}{\beta_{i-1}}\left(\frac{k\eta_q - k^2\eta_q}{2\Delta\eta} + \left(\frac{k\eta_q}{\Delta\eta}\right)^2\right) H_q^2 = -2\left(\frac{k\eta_q}{\Delta\eta}\right)^2$$

$$H_q^3 = \frac{\beta_i}{\beta_{i+1}}\left(\left(\frac{k\eta_q}{\Delta\eta}\right)^2 - \frac{k\eta_q - k^2\eta_q}{2\Delta\eta}\right) H_q^4 = -\frac{\beta_i}{\beta_1} m_p \eta_q^{1/k}$$

where η_q is the co-ordinate at q^{th} discretised point. Note that $\Delta\eta$ is the same between all successive grid points.

APPENDIX C

Governing equations and boundary conditions involved in the hydrodynamic zone:

An unsteady heat transfer problem is solved with the system of equations (4.6). The heater in its primitive form is a thin wire filament wound around the heater frame. The heater wire filament is arranged in the form of a rack (a schematic diagram of the same is shown in Fig. C.1a). The typical spacing between the racks of the wire filament is 50 times larger than the wire radius ($\sim mm$). Hence, a two-dimensional flow over a single cylinder is considered, as shown in Fig. (C.1b). The heat transfer from the single cylinder is multiplied by the effective length of the wire filament l_w to obtain the total heat transfer from the hydrodynamic zone.

Typical Reynolds number Re_d ($= 2Re_c$) of the base flow, based on the diameter of the wire filament is around 20. Also, it is observed from Fig. 3.3(a) that the maximum non-dimensional acoustic velocity at the heater location 'u_f' is approximately four. The fluctuating flow over the heater wire experiences a freestream flow with a maximum flow velocity of five times the base flow during one cycle. Hence, the maximum Reynolds number (Re_m) to be obtained is 100 during one cycle. Sarpkaya (1986) experimentally obtained the condition for the above oscillatory flow to become unstable and shed vortices based on the non-dimensional number; Keulegan-Carpenter number K_c ($K_c = U_m T/D$) for a given viscous scale parameter β ($\beta = Re_m/K_c$), where U_m is the maximum velocity of the free stream encountered during a cycle and T is the time period of oscillation. For the present problem (parameter values from table 4.1), the values of the above non-dimensional numbers are $K_c = 1.25$ and $\beta = 80$. For $\beta = 80$, the critical value of K_c above which the oscillatory flow over the cylinder becomes unstable to shed vortices is 2.11 (Sarpkaya, 1986), which is larger than that investigated in the present case. Hence vortex shedding does not occur. Owing to this, only one half of the flow domain is considered for the present simulation and the symmetry boundary condition is enforced.

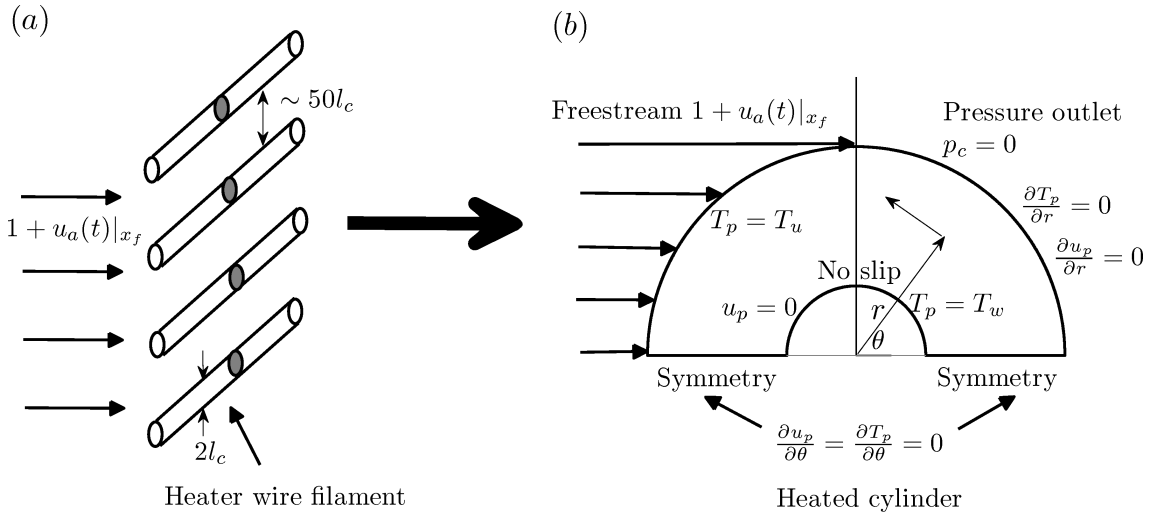

Figure C.1: Schematic representation of the heat source, (a) rack of the heater wire filament (b) boundary conditions for the two dimensional flow over a heated circular cylinder.

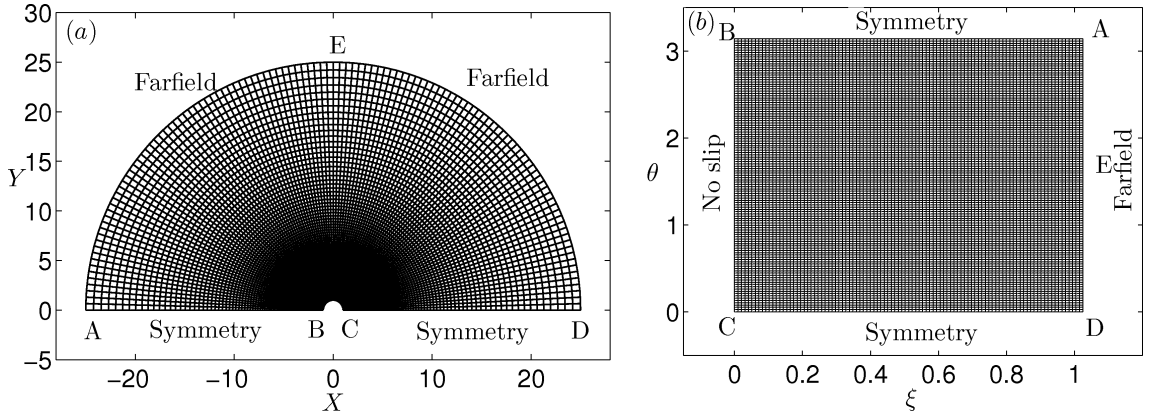

Figure C.2: Grid generated (121×101) for flow in the hydrodynamic zone (a) Physical domain with grid clustering near the cylinder surface with $k = \pi$. Flow domain is shown only up to $r = 25$ so that the presence of the cylinder can easily be visible in the figure. Numerical simulations are performed for the domain size $r = 50$. Convergence tests are performed and it is found that there is less than 5% change in the results with the domain size for $r = 50$, (b) Computation domain with uniform grids.

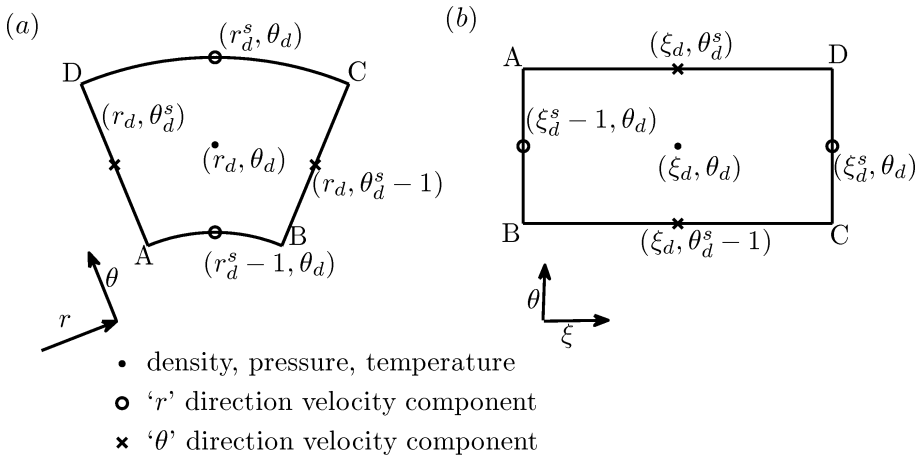

Figure C.3: Staggered grid arrangement, indicating density, pressure, temperature and velocity nodes. (*a*) Physical domain, (*b*) Computational domain.

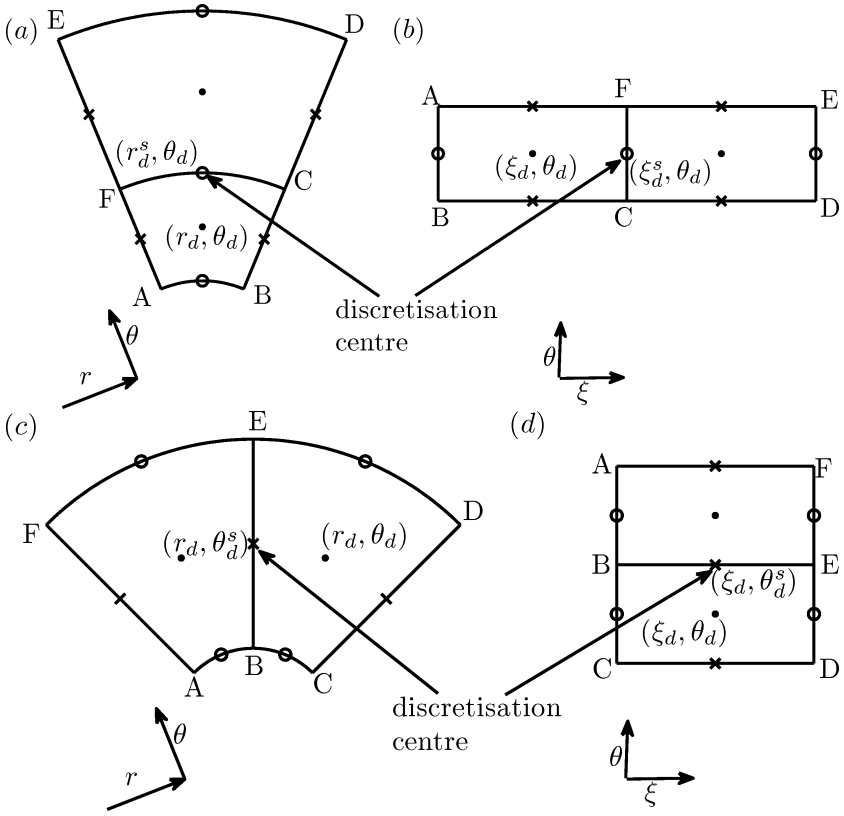

Figure C.4: (*a-b*) 'r' direction velocity component discretisation stencil. (*c-d*) 'θ' direction velocity component discretisation stencil. (*a* & *c*) Physical domain, (*b* & *d*) Computation domain.

A plane polar coordinate system is used to implement the no-slip boundary condition on the surface of the wire filament (circular cylinder). Moreover, fluid viscosity and thermal conductivity are assumed to be independent of temperature. The flow domain and the boundary conditions are shown in Fig. (C.1). The switch from Dirichlet to Neumann boundary condition at $\theta = \pi/2$ (from upstream to downstream in Fig. C.1) for $u_p,\ T_p$ is to have the numerical solvability of the hydrodynamic equations. The above switch is performed in Abu-Hijleh (2003) for a similar problem. The Dirichlet boundary condition (specified by the upstream acoustic zone) is applied in the farfield upstream boundary and the Newmann boundary condition is applied in the farfield downstream boundary for $\rho_p,\ u_p$ and T_p. The average of the above flow variables in the downstream boundary of the hydrodynamic zone is used in the one dimensional acoustic zone downstream of the heat source.

Near the cylinder surface, the gradient is large and it is important to cluster more number of grids near the cylinder surface. Therefore, grid clustering is incorporated by the following transformation $r = e^{k\xi}$, where k is the grid clustering parameter, which determines the rate at which the grid grows as one moves away from the cylinder surface. A uniform grid in '$\xi,\ \theta$' plane (computational plane) will give a stretched grid in '$r,\ \theta$' plane (physical plane) with more grids clustered around the cylinder surface. Fig. C.2(*a*) shows the generated grid for the present problem, where the grid size near the cylinder surface is very small compared to the far field and the grid size increases exponentially as '*r*' increases. The corresponding grid in the computational domain is uniform and is shown in Fig. C.2(*b*). The system of equations (4.6) with the above transformation is solved by using semi-implicit method for pressure linked equation (SIMPLE) algorithm (Patankar, 1980) with fast Poisson solver (Press *et al.*, 2007) for solving the pressure correction equation in the SIMPLE algorithm.

Staggered grid arrangement is implemented in the present computation as recommended by Patankar (1980) and is shown in Fig. C.3. The location indexed as (r_d, θ_d) represents a grid point. The grid point is shifted by half grid length to obtain the staggered grid point, which is indexed as (r_d^s, θ_d^s). The values of the variables associated with density, pressure and temperature are stored in the node, which is in the middle of the primitive cell (ABCD) as shown in Fig. C.3. On the other hand, the velocity com-

Property	$Re_d = 20$	$Re_d = 30$
Recirculation zone length (in terms of $2l_c$)	1.24 (1.15)	1.54 (1.54)
Separation angle from trailing edge (in radians)	0.79 (0.78)	0.87 (0.87)
Nusselt number	2.50 (2.40)	2.98 (2.83)

Table C.1: Comparison of various steady state flow properties between the present simulation and experiments. Numerical values in parentheses indicate values obtained from experiments. Experimental results for the recirculation zone length and the separation angle are obtained from Coutanceau and Bouard (1977), whereas the Nusselt number, defined as $Nu_d = \frac{2\tilde{T}_0^u}{2\pi(\tilde{T}_w - \tilde{T}_0^u)} \left[\left(\int_0^{2\pi} \left(-\frac{\partial T_p}{\partial r} \right)_{r=1} d\theta \right) \right]$ is obtained from Collis and Williams (1959).

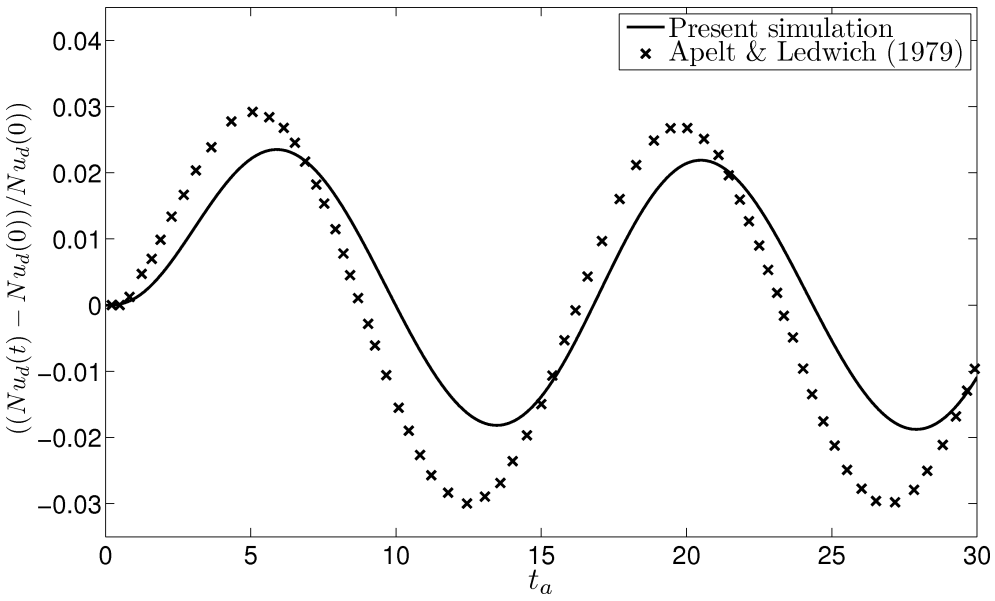

Figure C.5: Response of the unsteady heat transfer from the heated cylinder for the forcing of the freestream velocity, $u_p(r \to \infty, \pi/2 < \theta < \pi) = 1 + 0.1\sin(t_a/2.43)$. The parameters are, $Re_d = 10$, $\tilde{T}_u = 295\ K$, $\tilde{T}_w = 700\ K$.

ponents are stored in the edges of the cell. The continuity (3.24a) and energy (3.24c) equations , are discretised with its centre as the grid point (r_d, θ_d). Whereas, the momentum equation (4.6b) in the 'r' and 'θ' direction are discretised around (r_d^s, θ_d) and (r_d, θ_d^s) nodes. The same is shown in Fig. C.4 for both physical and computational domain. First order up winding scheme is used for the continuity equation, while second order central difference scheme is used for the rest.

The results in the present numerical simulation (without the global-acceleration term) of the hydrodynamic zone are compared with the existing results for validation. The steady state properties are compared in table (C.1) with experimental results from Coutanceau and Bouard (1977) and Collis and Williams (1959). A good agreement (with less than a 10% difference) is observed for the steady state properties. The response of the unsteady heat transfer from the heated cylinder to sinusoidal forcing is compared with the numerical simulation performed by Apelt and Ledwich (1979) and is shown in Fig. C.5. A reasonable agreement in the response of the system is observed. The constant density formulation used by Apelt and Ledwich (1979) might be the reason for the difference in the above two responses of the unsteady heat release rate.

APPENDIX D

Brief indication of the steps involved in obtaining the adjoint equation:

A brief explanation of the steps involved in derving the adjoint equations (4.30), the corresponding boundary conditions (4.31-4.35) and the mapping (4.36 & 4.37) between the direct and adjoint equations are given as follows. The adjoint equations and the corresponding boundary conditions are obtained when the first variation of the Lagrangian (Γ) with respect to the direct variables are set to zero (see § 4.28). There are various terms in Γ and the structure of these terms are fewer in number. One representative member is chosen for each structure and the first variation of the same member with the direct variables is performed. The first variation thus obtained for the above member is set to zero (which gives the adjoint system) and the contributions of the same member to the adjoint equations and the boundary conditions are analysed. Let ϕ represent any one of the direct variables ($u_a,\ p_a,\ u,\ v$....) and $\tilde{\phi}$ represents the adjoint variable corresponding to the direct variable ϕ.

D.0.1 Acoustic zone

Algebraic term

The following generic algebraic term is considered from the expression for Lagrangian Γ (4.29) in the acoustic zone.

$$\left\langle \phi, \tilde{\phi} \right\rangle_a = \int_{t=0}^{T_{opt}} \int_{x=0}^{1} \phi \tilde{\phi} dx dt \tag{D.1}$$

Taking first variation of the above expression with respect to ϕ gives the following

$$\left\langle \frac{\partial \phi}{\partial \phi} \delta\phi, \tilde{\phi} \right\rangle_a = \int_{t=0}^{T_{opt}} \int_{x=0}^{1} \tilde{\phi} \delta\phi dx dt \tag{D.2}$$

The δ used in the above expression indicates the variation of the variable ϕ. Since $\delta\phi$ in the right hand side of the above expression is arbitrary, the first variation of the above expression vanishes when the integrand itself vanishes. Similar terms from Γ which have the same form as that of the above expression (D.2) are gathered and the final integrand obtained is equated to zero. Thus the right hand side of the above expression is one of the term, which contributes to the adjoint equation (4.30). Other terms in Γ, which has gradient and laplacian forms are discussed below. The first variation of these terms generate terms, which contribute to the boundary conditions (4.31-4.35) for the adjoint equation and the mapping between the direct and adjoint variables (4.36 & 4.37).

Gradient term

A generic gradient term has the following form in Γ.

$$\left\langle \frac{\partial \phi}{\partial t}, \tilde{\phi} \right\rangle_a = \int_{t=0}^{T_{opt}} \int_{x=0}^{1} \frac{\partial \phi}{\partial t} \tilde{\phi} dx dt \tag{D.3}$$

Taking first variation with respect to ϕ as before in § D.0.1, one obtains the following:

$$\left\langle \frac{\partial}{\partial \phi} \left(\frac{\partial \phi}{\partial t} \right) \delta\phi, \tilde{\phi} \right\rangle_a = \int_{t=0}^{T_{opt}} \int_{x=0}^{1} \frac{\partial \delta\phi}{\partial t} \tilde{\phi} dx dt \tag{D.4}$$

Now integration by parts is performed for the variable $\partial\delta\phi/\partial t$ so as to move the operator $\partial/\partial t$ from $\delta\phi$ to $\tilde{\phi}$. The expression thus obtained is as follows.

$$\left\langle \frac{\partial}{\partial \phi} \left(\frac{\partial \phi}{\partial t} \right) \delta\phi, \tilde{\phi} \right\rangle_a = \int_{x=0}^{1} \tilde{\phi} \delta\phi \Big|_{t=0}^{T_{opt}} dx - \int_{t=0}^{T_{opt}} \int_{x=0}^{1} \frac{\partial \tilde{\phi}}{\partial t} \delta\phi dx dt \tag{D.5}$$

The first integral in the right hand side of the above expression contributes to the mapping between the direct and adjoint variables (4.36 & 4.37) and the second integral contributes to the adjoint equations (4.30). In the above case, gradient in t is considered. Similarly the first variation of the terms with gradient in x can be performed with one difference. The difference is that the surface terms obtained after performing in-

tegration by parts (like tht first integral in D.5) contribute to the boundary conditions (4.31-4.35) for the adjoint equations. It is important to note that the second integral in (D.5) has the same form as the integral in (D.4) with a sign difference. This implies the fact that the gradient term is non-self adjoint. The same conclusion about the non-self adjoint nature of the gradient operator is applicable to the gradient terms in the governing equations (4.7) of the hydrodynamic zone. In the present paper, the gradient terms in the equations (4.7) governing the hydrodynamic zone contribute to the non-normal nature of the system. The higher order derivatives in space (e.g. Laplacian) generate more surface terms, which again contribute to the boundary conditions.

D.0.2 Hydrodynamic zone

Laplacian term

In this section, the first variation of a term in Γ involving Laplacian operator in the hydrodynamic zone is performed and is given by the following.

$$\left\langle \frac{\partial}{\partial\phi}\left(\nabla^2\phi\right)\delta\phi, \tilde{\phi}\right\rangle_h = \int_{t=0}^{T_{opt}}\int_{\theta=0}^{\pi}\int_{r=1}^{\infty}\left(\frac{\partial^2\delta\phi}{\partial r^2}+\frac{1}{r}\frac{\partial\delta\phi}{\partial r}+\frac{1}{r^2}\frac{\partial^2\delta\phi}{\partial\theta^2}\right)\tilde{\phi}r dr d\theta dt \quad \text{(D.6)}$$

As before in § D.0.1, integration by parts is performed on the above expression leaving the expression in the following form:

$$\begin{aligned}\left\langle \frac{\partial}{\partial\phi}\left(\nabla^2\phi\right)\delta\phi, \tilde{\phi}\right\rangle_h = &\int_{t=0}^{T_{opt}}\int_{\theta=0}^{\pi}\left(\tilde{\phi}r\frac{\partial\delta\phi}{\partial r}-\frac{\partial r\tilde{\phi}}{\partial r}\delta\phi+\tilde{\phi}\delta\phi\right)\Bigg|_{r=1}^{\infty} d\theta dt \\ &+\int_{t=0}^{T_{opt}}\int_{r=1}^{\infty}\left(\frac{\tilde{\phi}}{r}\frac{\partial\delta\phi}{\partial\theta}-\frac{1}{r}\frac{\partial\tilde{\phi}}{\partial\theta}\delta\phi\right)\Bigg|_{\theta=0}^{\pi} r dr dt+\int_{t=0}^{T_{opt}}\int_{\theta=0}^{\pi}\int_{r=1}^{\infty}\left(\nabla^2\tilde{\phi}\right)\delta\phi r dr d\theta dt\end{aligned} \quad \text{(D.7)}$$

The first two integrals in the right hand side of the above expression contributes to the adjoint boundary conditions and the last integral contributes to the adjoint equation. Note that the last integral in (D.7) has the same form as the integral in (D.6). This is due to the fact that Laplacian ∇^2 is a self-adjoint operator. In this way (D.0.1, D.0.1 &

D.0.2) the first variation of all the terms in the expression for the first variation of Γ with respect to the state space variables of the system are evaluated and the adjoint system is obtained.

APPENDIX E

Detailed drawing of the Rijke tube experimental setup

A detailed drawing for the configuration of the Rijke tube setup shown in Fig. 5.1 is presented in this section. The material used for making the major elements in the setup are tabulated in Table E.1.

Description	Material
Rijke tube	Aluminium
Decoupler	Mild steel
Heater stand	Cynthanium
Heater mesh	Stainless steel
Electrical leads	Copper
Insulation	Glass fibre

Table E.1: Materials used to make the major components of the Rijke tube setup.

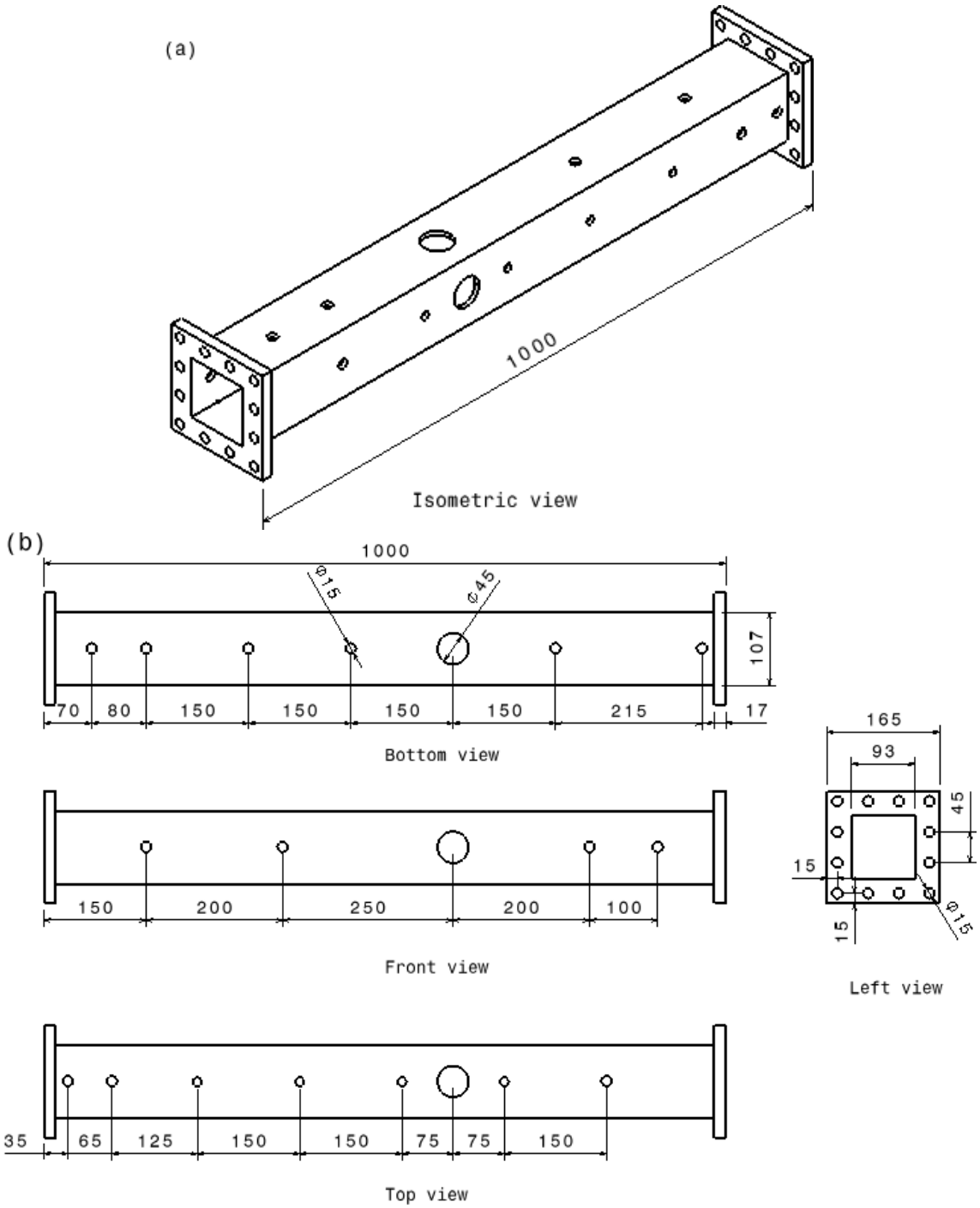

Figure E.1: Detailed drawing for the Rijke tube along with provisions for instrumentations; *a*) isometric, *b*) Orthographic view. Microphones and thermocouples are mounted in the small holes, while acoustic drivers are mounted in the large holes. All dimensions are in mm.

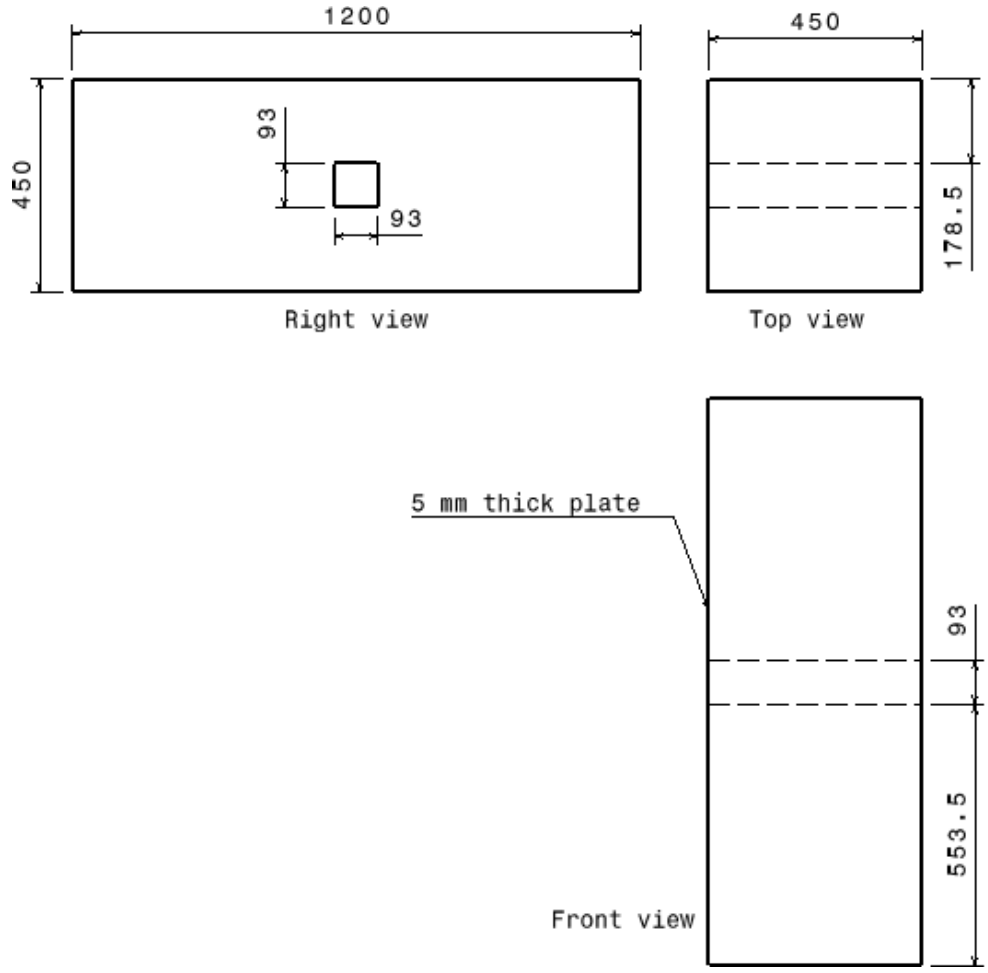

Figure E.2: Detailed drawing for the decoupler (orthographic projections). All dimensions are in mm.

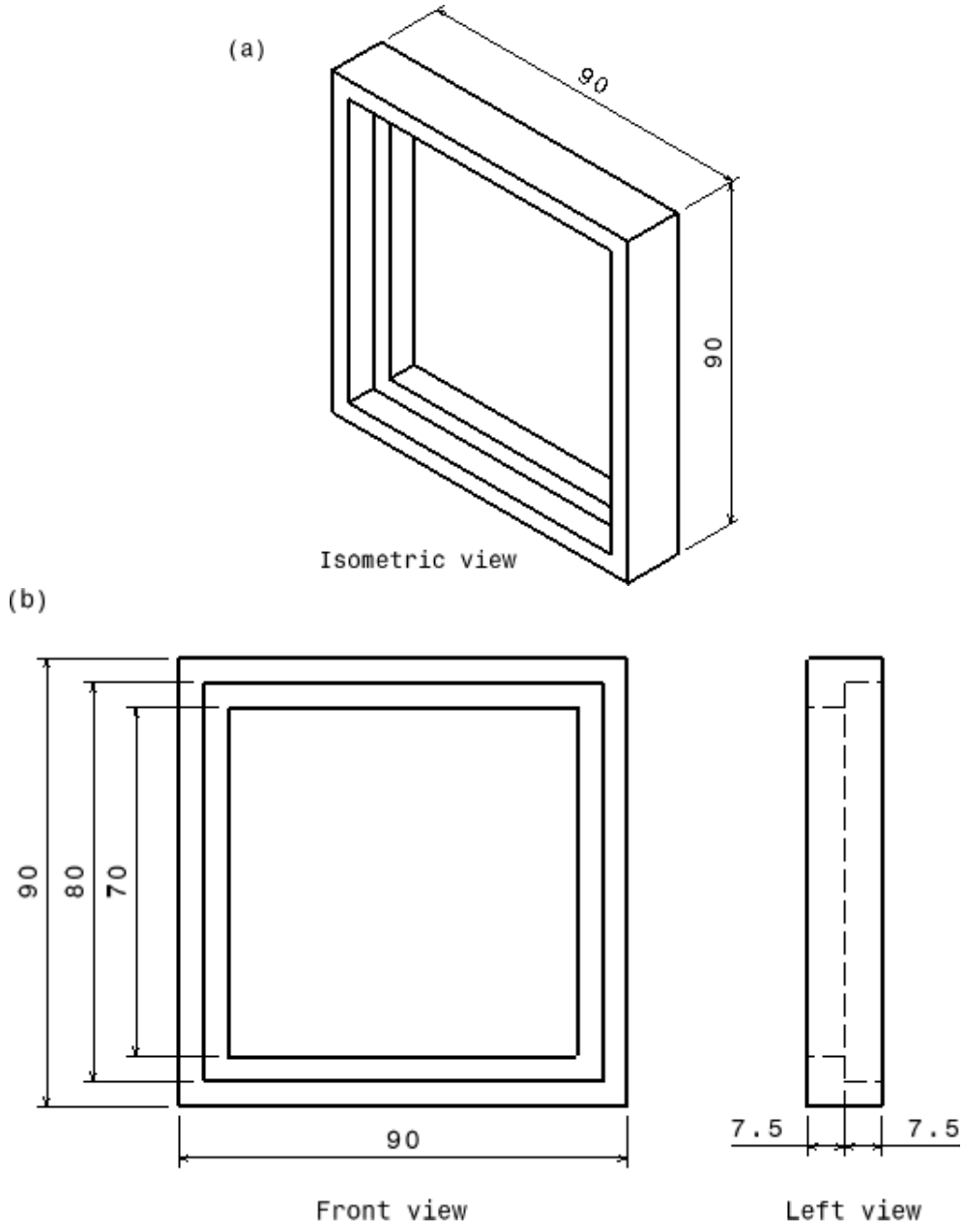

Figure E.3: Detailed drawing for the heater stand; *a*) isometric, *b*) Orthographic view. All dimensions are in mm.

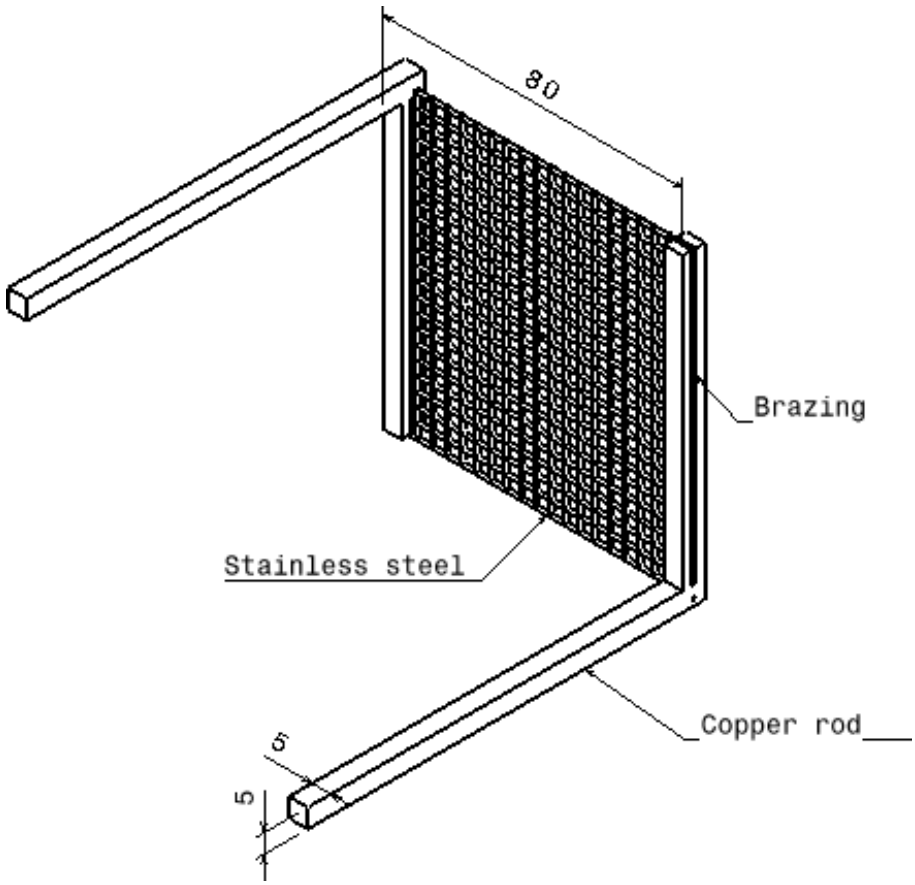

Figure E.4: Detailed drawing for the heater mesh brazed with the copper rod. All dimensions are in mm.

APPENDIX F

Calibration of microphones

A total of 15 microphones are used to track the evolution of acoustic pressure along the length of the duct. It is important to calibrate them for their relative sensitivity and phase in the frequency of interest. Towards this purpose, one microphone, model - PCB 103B02 SN 5236 is chosen as the reference, which has a sensitivity of $223.65\ mV/kPa$. A schematic of the calibration setup is shown in figure F.2(*a*). A calibration tube of length $0.9\ m$ and internal diameter (d_{cal}) of $0.11\ m$ is used as an acoustic resonator. The above tube is used to reduce the effect of ambient noise in the measurement. In the present case, the cutoff frequency (f_{cut}) for the propagation of a non-planar mode (radial mode) is $1.8\ kHz$ ($f_{cut} = 1.84a/(2\pi d_{cal}/2)$ taken from Kinsler *et al.* 2000). The frequency of interest in the present investigation is in the range $100-500\ Hz$, which is much below f_{cut} and hence only longitudinal modes propagate in the duct. Four microphones are placed on the end plate of the calibration tube and the arrangement is shown in figure F.2(*b*). A reference microphone is placed at one of the ports and the rest of the three ports are used to calibrate other microphones. An 18" extended low frequency Ahuja acoustic driver (L18-SW650) is used for exciting the system.

The calibration is performed as follows. At a given frequency, the system is excited continuously and the acoustic pressure is recorded by the microphones. The amplitude of pressure oscillations from the microphones are obtained and compared with the reference. Further, the phase difference between a microphone measurement and the reference is also noted. The experiment is repeated for various frequencies in the range 100 - 500 Hz, which is of interest in the present investigation (see § 5.5.4). A typical calibration data is shown in figure F.2 for the microphone 103B02 SN 5235. The amplitude ratio is defined as $A_{calib} = A_m/A_{ref}$, where A_m & A_{ref} represent the amplitudes measure from the above microphone and the reference. The mean value is used to obtain the relative sensitivity of the microphone. It is observed from figure F.2(*a*), that the variation of $A_{calib} = A_m/A_{ref}$ in the frequency of interest is less than 4% of the mean

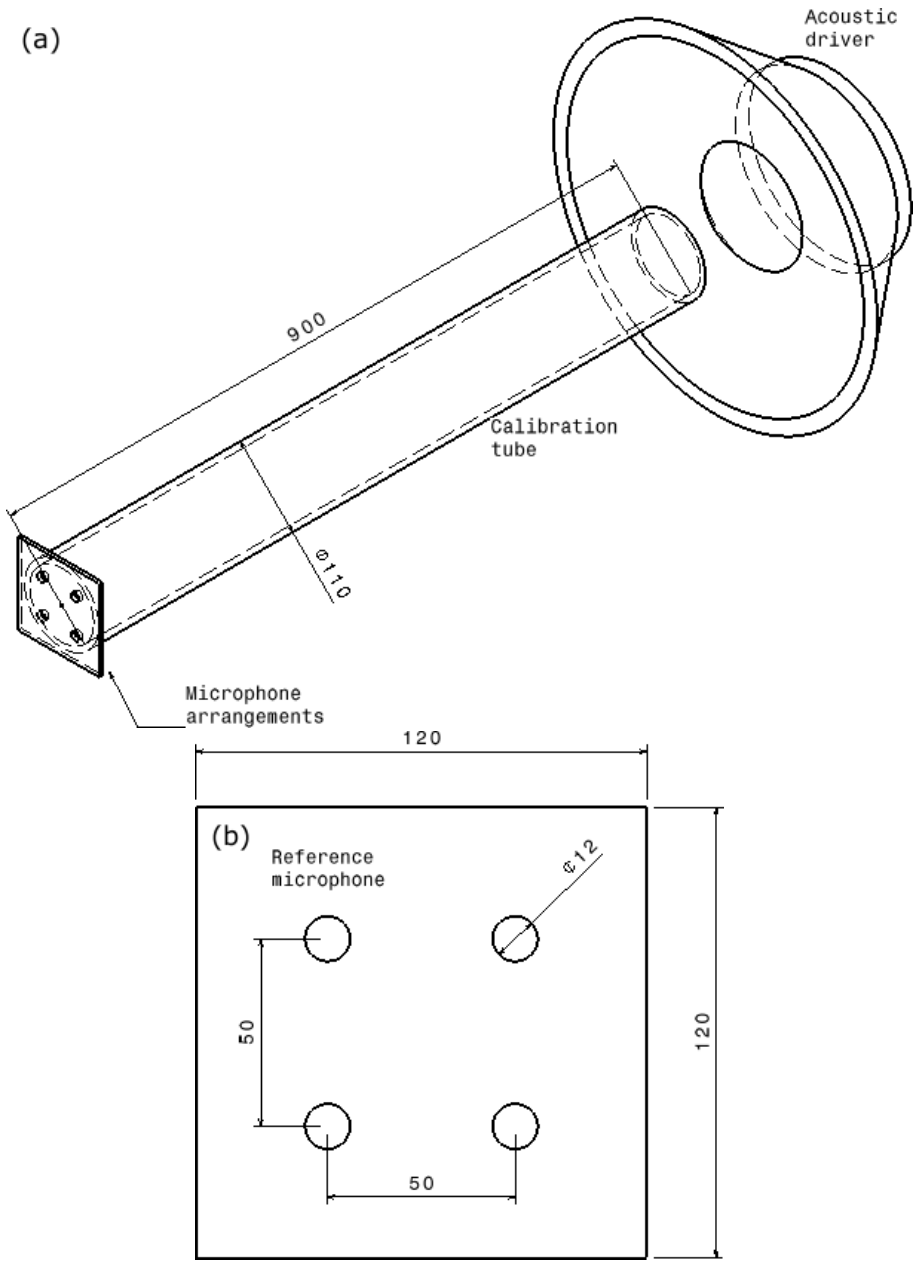

Figure F.1: (*a*) Schematic representation of the microphone calibration setup. (*b*) Microphone arrangements for calibration. All dimensions shown are in mm.

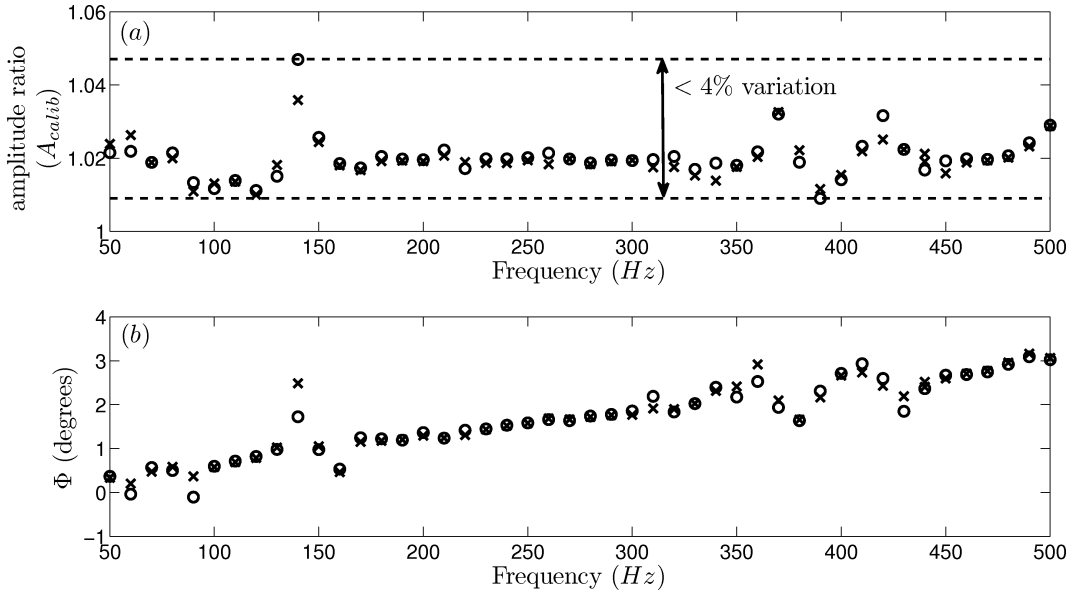

Figure F.2: Calibration data for a microphone, 103B02 SN 5235 in the frequency range $50 - 500\ Hz$. Calibration is performed twice to ensure repeatability and are shown as cross and hollow circular symbols. (a) Amplitude ratio $A_{calib} = A_m/A_{ref}$, A_m & A_{ref} represent the amplitudes measure from the above microphone and the reference. (b) Phase difference between the microphone and the reference.

value. Moreover, the phase difference between the above microphone and the reference is also less than $4\ degrees$. The above exercise is repeated for other microphones and the obtained values of $A_{calib} = A_m/A_{ref}$ are tabulated in table F.1. Since the phase difference is small, the same is neglected. The calibration data of the microphones are used further in the analysis to obtain the acoustic pressure values.

S. No	Model number	location (mm)	$A_{calib} = A_m/A_{ref}$
1	41064	0.035	4.79
2	41061	0.070	4.02
3	111212	0.010	3.65
4	5246	0.150	1.03
5	5234	0.225	1.00
6	4753	0.300	0.91
7	5245	0.375	0.94
8	111206	0.450	3.72
9	111213	0.525	3.56
10	5238	0.675	0.99
11	4752	0.750	0.95
12	5236 (reference)	0.800	1.00
13	111207	0.825	3.62
14	5235	0.900	1.02
15	377B11	0.965	23.81

Table F.1: Calibration data, $A_{calib} = A_m/A_{ref}$ for all the microphones used in the present investigation. All the microphones used belongs to PCB SN series. The model number along with the location in the Rijke tube are also shown. The sensitivity of the reference microphone, SN 5236 is $223.65\ mV/kPa$.

APPENDIX G

Measurement of acoustic damping

In order to ensure repeatability of the experimental results, the acoustic damping in the system should be estimated and monitored in the subsequent realisations. The experiments are performed at a prescribed ambient condition (see § 5.5). The exponential decay rate of the system is determined for a given frequency as follows.

In the cold flow, the system is excited for a brief period of time at the frequency of the first eigenmode. In the present case, the above value is $156\ Hz$. After the acoustic driver is switched 'off', the system decays according to the decay rate corresponding to the first eigenfrequency. A typical acoustic pressure data at $x = 0.525$ is shown in figure G.1(a). Data used for the determination of acoustic damping is shown in light grey region. The instantaneous amplitude of the signal is obtained by the absolute value of the Hilbert transform of the signal (King, 2009). The evolution of the logarithmic decay of the instantaneous amplitude, defined as $log\left(|\mathrm{H}(P(t))|/|\mathrm{H}(P(t_{st}))|\right)$ is plotted in figure G.1(b). t_{st} is the time at the start of the light grey region. The straight line part of the curve indicates the exponential decay of the instantaneous amplitude. The slope of the same gives the decay rate (α) of the system. In the present case, the value of α is $-11.5\ /s$. Decay rates are measured at the start of the experiments. The experiments are further continued only when the decay rates are within 5% of the value specified earlier. The above procedure is to ensure that acoustic damping does not vary significantly during the course of the experiments.

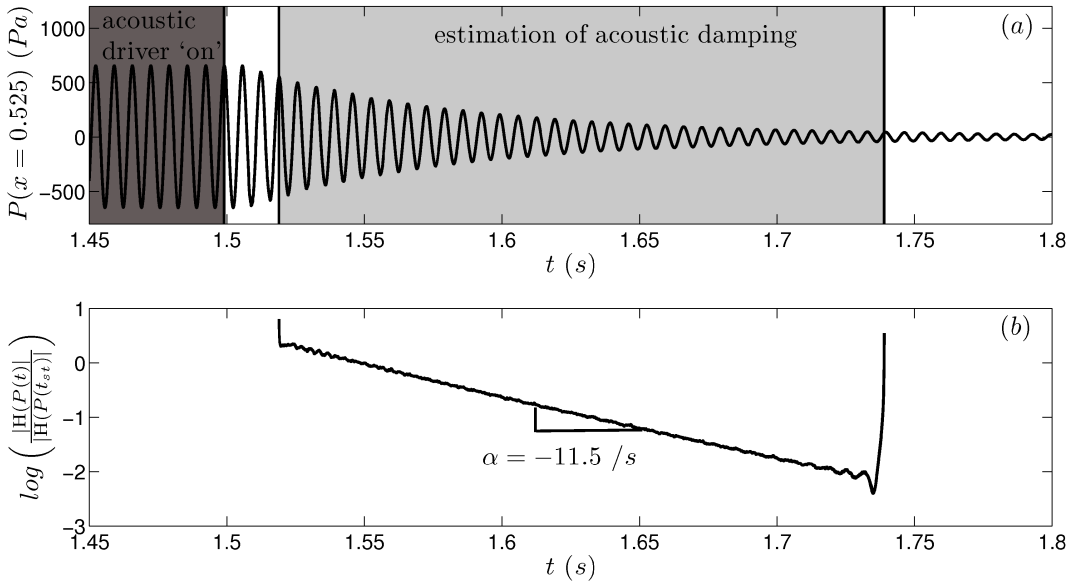

Figure G.1: Estimation of acoustic damping in the system. (a) Acoustic pressure measured at $x = 0.525$, which is used for damping measurement. Dark grey region indicates the period during which the acoustic driver is switched 'on' at a frequency of $156\ Hz$. Data used for the determination of acoustic damping is shown in light grey region. (b) Determination of the decay rate of the system by plotting the evolution of the logarithm of the instantaneous amplitude ratio $(log\,(|\mathrm{H}(P(t))|/|\mathrm{H}(P(t_{st}))|))$. The exponential decay rate (α) is obtained by the slope of the above curve.

APPENDIX H

Experimental determination of the amplitude of the linear regime

In this section, the range of linearity is determined as already described in § 5.4.2. In order to identify the linear regime, it is important to first characterise the acoustic drivers for its linearity. The equations governing the classical acoustic field in a duct is linear (Rienstra and Hirschberg, 2008). The above fact is used to analyse the linearity of the acoustic drivers. The Rijke tube system is excited continuously using acoustic drivers with the heater and blower switched off at a given frequency. The response of the system is recorded from the microphones. The voltage supplied to the acoustic driver is also noted and varied. A response curve for the acoustic driver unit is obtained and is shown for three forcing frequencies in figure H.1. In the x-axis, the rms value of the voltage supplied to the acoustic driver units is shown and in the y-axis, the rms value of the acoustic pressure fluctuations ($P_{rms}|_{x=0.525}$) is shown. The dots indicate the actual data and the line indicates the linear fit. From the response curve, one can conclude that the linear fit represents the actual data with less than $\pm 0.25\%$ spread. Hence for the voltage range indicated in figure H.1, the relationship between the voltage supplied to acoustic driver and the acoustic pressure generated is linear.

The heater and blower are now switched on. Due to reasons explained in the last paragraph of § 5.5.1, linear regime is identified only in zone GH. Figure H.2 represents the response of the system to continuous excitation with the acoustic driver and the output as the rms value of acoustic pressure fluctuations. As earlier, dots indicate the actual data. It can be observed that the dots does not form a straight line and it grows sub linearly for larger amplitudes of the voltage supplied to the acoustic driver. Dashed line indicates a power law fit to the actual data with a spread of $\pm 0.15\%$. A linear fit, shown as a continuous line is performed with the actual data at low amplitudes of $V_{\text{Acoustic driver}}$, which in the present case is less than 3 V. The triggering amplitude is marked as a chained horizontal line. In the present case, the limit of linearity is

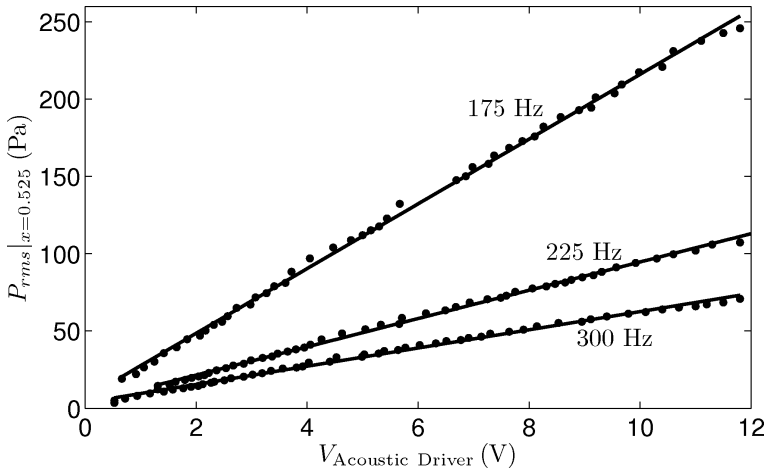

Figure H.1: Characteristics of the acoustic driver unit, obtained for three different frequencies. The rms value of the voltage supplied to the acoustic driver unit is indicated in 'x' axis. The dots indicate the actual data, while the continuous line is the corresponding linear fit.

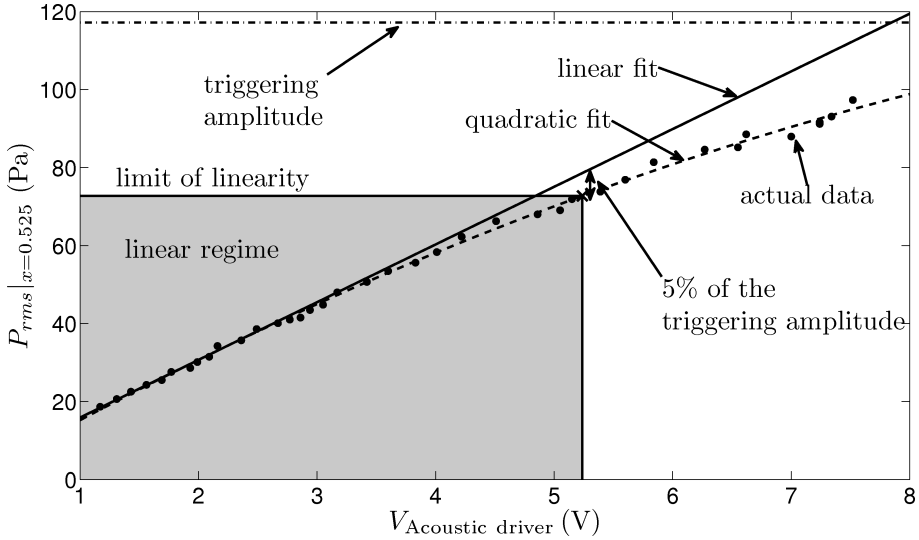

Figure H.2: Identification of linear regime. Acoustic forcing is performed at 300 Hz with $K = 764\ W$ & $\dot{m}$ = 2.34 g/s. A power law is used to fit the response of the system. The equation of the fit is $28.36V_p^{0.67} - 14.24$. Shaded grey area indicates the linear regime.

determined when the deviation of the actual data from the linear fit is more than 5% of the corresponding triggering amplitude. The amplitude at which nonlinear nature of the system is significant is indicated by the triggering amplitude and hence is chosen as the reference. The above defined linear regime is shaded in grey as shown in figure H.2. For a given power supplied to the heater, the acoustic pressure amplitude corresponding to the limit of linearity is the upper limit of acoustic pressure level in the duct, where the system behaves as a linear system. The contribution from the nonlinearity of the system can be neglected in the above regime.

APPENDIX I

Application of DMD in the presence of noise

The application of the DMD technique to determine the eigenmodes of the system from the synthetic data by solving (5.1) is illustrated in § 5.4.3. A good agreement between the eigenmodes extracted by the DMD technique and the actual eigenmodes is observed. The extension of applying the DMD technique to experimental data requires the estimation of robustness of the DMD algorithm in the presence of noise and the corresponding uncertainty in the relevant output quantities.

As the first step, the noise in the system has to be characterised. Figure I.1 illustrates the estimation of noise level in the system. The noise levels measured at locations $x = 0.1 \ \& \ 0.8$ are shown in figures I.1(*a* & *c*). The input waveforms at the same locations, in order to perform DMD are shown in figures I.1(*b* & *d*). The above waveform has contributions mostly from the second eigenmode of the system. The horizontal line indicates the rms level of the corresponding signal, which is used measure the signal strength. The noise level is estimated as the ratio of the rms level of the noise to the rms level of the signal at the locations of the microphones. The above noise level data, along the duct is shown in figure I.1(*e*). The maximum noise level is 4.2% at $x = 0.525$. Since the second eigenmode of the system is excited, the above location is close to the acoustic pressure node and hence has the highest noise level. Similarly, the noise level is determined for the waveforms, which are used to determine the first eigenmode and are indicated in figure I.1(f). Moreover, the power supplied to the heater in the present case is $K = 747 \ W$, which is in the subcritical transition zone (see figure 5.14) and the rms amplitude of the signals in figures I.1(*b* & *d*) are smaller than the rms amplitude (87 Pa) of the linearity limit. As the experiment is performed for lower values of K, acoustic pressure data with higher signal to noise ratio can be used as the amplitude of the linearity limit is higher. In the present experiments for the determination of eigenmodes, the maximum value of K used is 747 W (figure 5.15). Hence the maximum noise level encountered in the determination of eigenmodes of the system is 4.2%.

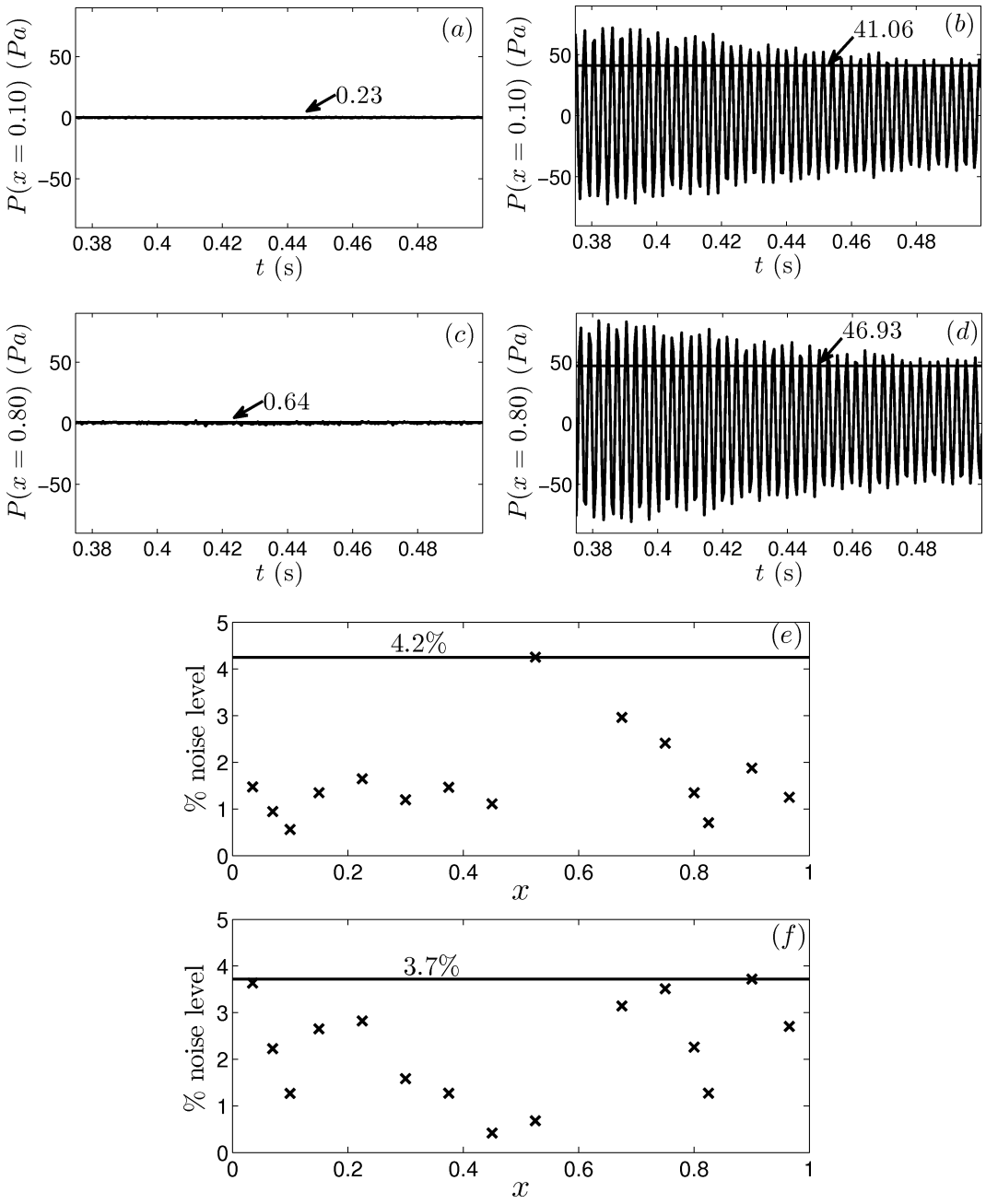

Figure I.1: Estimation of noise level encountered in the experiments. *a*) & *c*) noise level measured at locations $x = 0.10$ & 0.80. *b*) & *d*) the input waveform measured at the same locations to perform DMD. The horizontal line indicates the rms level of the corresponding signal. The noise level is estimated as the ratio of the rms level of the noise to the rms level of the signal at the locations of the microphones. The same is shown for the investigation of determining the, *e*) second and *f*) first eigenmode of the system. The parameters are $\dot{m} = 2.34\ g/s$ & $K = 747\ W$.

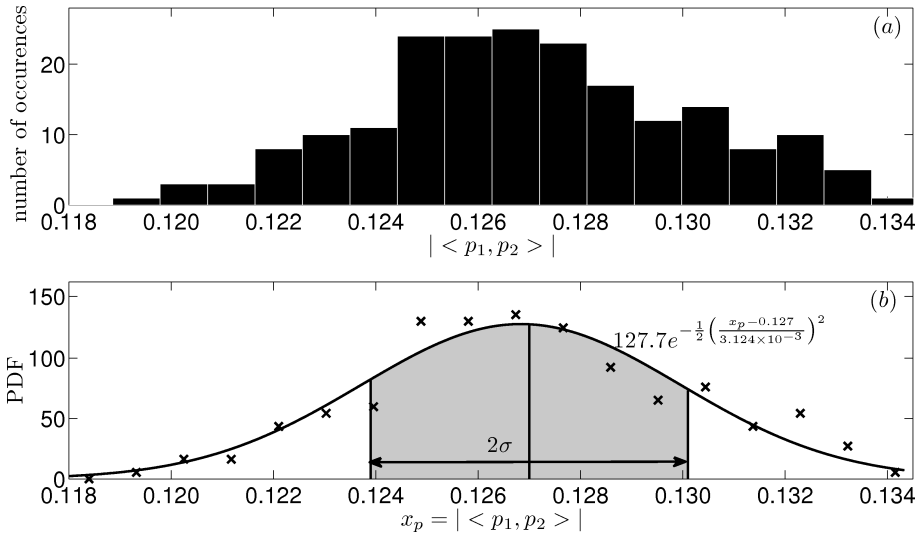

Figure I.2: Illustrates the robustness of the DMD algorithm in the presence of noise. *a*) Histogram plot having 20 bins for the value of the inner product $|< p_i, p_j >|$ from 200 realisations with a random noise added to the experimental data. The added noise level is same as shown in figure I.1(*e,f*). *b*) Probability density function (PDF) for the above histogram. The cross symbols indicate the histogram data and the continuous line indicates a Gaussian distribution fit. The equation of the same is also indicated. The mean value (x_m) of $|< p_i, p_j >|$ is 0.127 and the standard deviation (σ) is 3.124×10^{-3}. The percentage error associated with $|< p_i, p_j >|$ is evaluated as $\sigma/x_m \times 100 = 2.46$. This is used as the amplitude of the error bar (**?**) indicated in figure 5.15(*d*). The parameters are same as in figure I.1.

The uncertainty in the value of the inner product $| < p_i, p_j > |$, which determines the non-orthogonality among the eigenmodes is performed as follows. In order to have a conservative estimate, noise of level shown in figures I.1(*e* & *f*) is added numerically to the data set obtained from experiments and then DMD is performed. Further, this procedure of estimating the uncertainty is followed, as several experimental realisations are not possible. Several numerical realisations (in the present case 200) are performed and the value of $| < p_i, p_j > |$ is noted. The data used for DMD are first projected onto the proper orthogonal decomposition (POD) modes in order to reduce the effect of noise (Negrete *et al.*, 2008) in the determination of the eigenmodes. In the present case, a lower cut-off is defined on the number of POD modes to be used for projection based on their energy content (Schmid, 2010). The above cut-off is set as 10 for the application of DMD in the downstream side of the heater, while no such cut-off is set for the upstream side.

The obtained values of $| < p_i, p_j > |$ are distributed in 20 bins of size 2×10^{-3} for the data range $0.114 - 0.134$. Figure I.2(*a*) shows the histogram for the above realisations. The histogram is normalised with the total number of realisations to obtain the probability density function (PDF) for the value of $| < p_i, p_j > |$ as indicated in figure I.2(*b*). A normal distribution is fitted for the above PDF and is of the form $127.7e^{-\left((x_p-0.127)/3.124\times10^{-3}\right)^2/2}$, where x_p represents the random variable $| < p_i, p_j > |$. From the above distribution, the mean (x_m) and standard deviation (σ) are found to be 0.127 and 3.124×10^{-3} respectively. The percentage normalised standard deviation is determined as $\sigma/x_m \times 100 = 2.5$ and is used as the percentage amplitude of the error bar (**?**) indicated in figure 5.15(*d*). The above region of spread in the value of $| < p_i, p_j > |$ is indicated as shaded region in figure I.2(*b*).

REFERENCES

1. **Abdessemed, N.**, **A. S. Sharma**, **S. J. Sherwin**, and **V. Theofilis** (2009). Transient growth analysis of the flow past a circular cylinder. *Physics of Fluids*, **21**(4), 044103. URL `http://link.aip.org/link/?PHF/21/044103/1`.

2. **Abom, M.** and **H. Boden** (1988). Error analysis of two-microphone measurements in ducts with flow. *The Journal of the Acoustical Society of America*, **83**(6), 2429–2438.

3. **Abu-Hijleh, B. A.** (2003). Numerical simulation of forced convection heat transfer from a cylinder with high conductivity radial fins in cross-flow. *International Journal of Thermal Sciences*, **42**(8), 741 – 748. ISSN 1290-0729.

4. **Anathakrishnan, N.**, **S. Deo**, and **F. E. C. Culick** (2005). Reduced-order modeling and dynamics of nonlinear acoustic waves in a combustion chamber. *Combustion Science & Technology*, **177**, 221–247.

5. **Anderson, J. D.**, *Computational fluid dynamics: the basics with applications*. McGraw-Hill, New York, 2001, 8 edition.

6. **Andres, J. M.** and **U. Ingard** (1953). Acoustic streaming at low reynolds numbers. *J. Acoustical Soc. of America*, **25**, 932–938.

7. **Annaswamy, A. M.**, **M. Fleifil**, **J. P. Hathout**, and **A. F. Ghoneim** (1997). Impact of linear coupling on the design of active controllers for the thermoacoustic instability. *Combustion Science & Technology*, **128**, 131–180.

8. **Anthoine, J.**, **J. M. Buchlin**, and **A. Hirschberg** (2002). Effect of nozzle cavity on resonance in large srm: Theoretical modelling. *J. Propul. Power*, **18**, 304–311.

9. **Apelt, C. J.** and **M. A. Ledwich** (1979). Heat transfer in transient and unsteady flows past a heated circular cylinder in the range $1 \leq \mathrm{Re} \leq 40$. *J. Fluid Mech.*, **95**(04), 761–777.

10. **Baggett, J. S.**, **T. A. Driscoll**, and **L. N. Trefethen** (1995). A mostly linear model of transition to turbulence. *Phys. Fluids*, **7**(4), 833–838.

11. **Balasubramanian, K.** and **R. I. Sujith** (2008*a*). Non-normality and nonlinearity in combustion acoustic interaction in diffusion flames. *J. Fluid Mech.*, **594**, 29–57.

12. **Balasubramanian, K.** and **R. I. Sujith** (2008*b*). Thermoacoustic instability in a Rijke tube: Non-normality and nonlinearity. *Phys. Fluids*, **20**, 044103.

13. **Barbagallo, A.**, **D. Sipp**, and **P. J. Schmid** (2009). Closed-loop control of an open cavity flow using reduced-order models. *J. Fluid Mech.*, **641**, 1–50.

14. **Barkley, D.** and **L. S. Tuckerman** (1999). Stability analysis of perturbed plane Couette flow. *Phys. Fluids*, **11**, 1187–1195.

15. **Baum, J. D.** and **J. N. Levine** (1986). Modelling of nonlinear longitudinal instability in solid rocket motors. *AIAA. J.*, **13**, 339–348.

16. **Bellows, B. D.** (2006). *Characterization of Nonlinear Heat Release-Acoustic Interactions In Gas Turbine Combustors*. Ph.D. thesis, Georgia Institute of Technology, Atlanda.

17. **Bellucci, V.**, **B. Schuermans**, **D. Nowak**, **P. Flohr**, and **C. O. Paschereit** (2004). Thermoacoustic modeling of a gas turbine combustor equipped with acoustic dampers. *Proceedings of ASME Turbo Expo, Power for Land, Sea, and Air*, GT2004–53977.

18. **Bittanti, S.**, **A. Marco**, **G. Poncia**, and **W. Prandoni** (2002). Identification of a model for thermoacoustic instabilities in a Rijke tube. *IEEE Transactions on control systems technology*, **10**, 490–502.

19. **Blomshield, F. S.**, **H. B. Mathes**, **J. E. Crump**, **C. A. Beiter**, and **M. W. Beckstead** (1997*a*). Nonlinear stability testing of full-scale tactical motors. *Journal of Propulsion and Power*, **13**, 356–366.

20. **Blomshield, F. S.**, **H. B. Mathes**, **J. E. Crump**, **C. A. Beiter**, and **M. W. Beckstead** (1997*b*). Stability testing of full-scale tactical motors. *Journal of Propulsion and Power*, **13**, 349–355.

21. **Brewster, Q.** and **S. F. Son** (1995). Quasi-steady combustion modeling of homogeneous solid propellants. *Combust. Flame*, **103**(1-2), 11 – 26.

22. **Buckmaster, J.** (2002). Edge-flames. *Progress in Energy and Combustion Science*, **28**(5), 435 – 475.

23. **Butler, K. M.** and **B. F. Farrell** (1992). Three-dimensional optimal perturbations in viscous shear flow. *Phys. Fluids A*, **4**(8), 1637–1650.

24. **Candel, S.** (2002). Combustion dynamics and control: Progress and challenges. *Proceedings of the Combustion Institute*, **29**(1), 1 – 28. ISSN 1540-7489.

25. **Carvalho, J. A.**, **M. A. Ferreira**, **C. Bressan**, and **L. G. Ferreira** (1989). Definition of heater location to drive maximum amplitude acoustic oscillations in a Rijke tube. *Comb. Flame*, **76**, 17–27.

26. **Chu, B. T.** (1965). On the energy transfer to small disturbances in fluid flow (part I). *Acta Mech.*, **3**, 215–234.

27. **Cohen, N. S.** and **L. D. Strand** (1985). Combustion response to compositional fluctuations. *AIAA J.*, **23**, 760–767.

28. **Collis, D. C.** and **M. J. Williams** (1959). Two-dimensional convection from heated wires at low Reynolds numbers. *J. Fluid Mech.*, **6**(03), 357–384.

29. **Corbett, P.** and **A. Bottaro** (2001). Optimal linear growth in swept boundary layers. *J. Fluid Mech.*, **435**, 1–23.

30. **Coutanceau, M.** and **R. Bouard** (1977). Experimental determination of the main features of the viscous flow in the wake of a circular cylinder in uniform translation. part 1. steady flow. *J. Fluid Mech.*, **79**(02), 231–256.

31. **Cozzi, F.**, **L. T. Deluca**, and **B. V. Novozhilov** (1999). Linear stability and pressure-driven response function of solid propellants with phase transitions. *Journal of Propulsion and Power*, **15**, 806–815.

32. **Criminale, W. O.** and **P. G. Drazin** (1999). The initial-value problem for a modeled boundary layer. *Phys. Fluids*, **12**, 366–374.

33. **Crocco, L.** (1956). Theory of combustion instability in liquid propellant rocket motors. Technical Report Rep 0429886, RTO AGARDorgraph.

34. **Culick, F. E. C.** (1963). Stability of high-frequency pressure oscillations in rocket combustion chambers. *AIAA. J.*, **1**, 1097–1104.

35. **Culick, F. E. C.** (1968). A review of calculations for unsteady burning of a solid propellant. *AIAA. J.*, **6**, 2241–2255.

36. **Culick, F. E. C.** (1976*a*). Nonlinear behavior of acoustic waves in combustion chambers. Part I. *Acta Astronaut.*, **3**(9-10), 715 – 734.

37. **Culick, F. E. C.** (1976*b*). Nonlinear behavior of acoustic waves in combustion chambers. Part II. *Acta Astronaut.*, **3**(9-10), 735 – 757.

38. **Culick, F. E. C.** (1994). Some recent results for nonlinear acoustics in combustion chambers. *AIAA J.*, **32**, 146–169.

39. **Culick, F. E. C.** (1997). A note on ordering perturbations and the insignificance of linear coupling in combustion instabilities. *Combust. Sci. Tech.*, **126**, 359–379.

40. **Culick, F. E. C.** (2006). Unsteady motions in combustion chambers for propulsion systems. Technical Report AG-AVT-039, RTO AGARDorgraph.

41. **Culick, F. E. C.**, **V. Burnley**, and **G. Swenson** (1995). Pulsed instabilities in solid-propellant rockets. *J. Propul. Power*, **11**, 657–665.

42. **Culick, G., F. E. C. & Isella**, Modelling the combustion response function with surface and gas phase dynamics. *In In Thirty-Eighth Aerospace Sciences Meeting and Exhibit*. AIAA, Reno, NV, 2000.

43. **Deluca, L.**, **R. Disilvestro**, and **F. Cozzi** (1995). Intrinsic combustion instability of solid energetic materials. *Journal of Propulsion and Power*, **11**, 804–815.

44. **Farrell, B. F.** and **P. J. Ioannou** (1996*a*). Generalized stability theory. Part I. Autonomous operators. *Journal of the Atmospheric Sciences*, **53**(14), 2025–2040.

45. **Farrell, B. F.** and **P. J. Ioannou** (1996*b*). Generalized stability theory. Part II. Nonautonomous operators. *Journal of the Atmospheric Sciences*, **53**(14), 2041–2053.

46. **Flandro, G. A.** (1995*a*). Effects of vorticity on rocket combustion stability. *J. Propul. Power*, **11**, 607–625.

47. **Flandro, G. A.**, On flow turning. *In In Thirty-First ASME, SAE, and ASEE, Joint Propulsion Conference and Exhibit*. 95-2730, San Diego, CA, 1995*b*.

48. **Flandro, G. A.**, Nonlinear combustion instability data reduction. *In In Thirty-Second ExhibitAIAA/ASME/SAE/ASEE Joint Propulsion Conference and Exhibit*. 96-3251, Lake Buena Vista, Florida, 1996.

49. **Flandro, G. A.**, **S. R. Fischbach**, and **J. Majdalani** (2007). Nonlinear rocket motor stability prediction: Limit amplitude, triggering and mean pressure shift. *Phy. Fluids*, **19**, 094101.

50. **Flandro, G. A.** and **J. Majdalani** (1996). Aeroacoustic instability in rockets. *AIAA*, **41**, 485–497.

51. **Fransson, J. H. M.**, **L. Brandt**, **A. Talamelli**, and **C. Cossu** (2004). Experimental and theoretical investigation of the nonmodal growth of steady streaks in a flat plate boundary layer. *Phy. Fluids*, **16**, 3627–3638.

52. **Fransson, J. H. M.**, **A. Talamelli**, **L. Brandt**, and **C. Cossu** (2006). Delaying transition to turbulence by a passive mechanism. *Phys. Rev. Lett.*, **96**(6), 064501.

53. **Friedly, J. C.** and **E. E. Petersen** (1966). Influence of combustion parameters on instability in solid propellant motors. (p)art I. development of model and linear analysis. *AIAA J*, **4**, 1604–1610.

54. **Fu, W. S.** and **B. H. Tong** (2002). Numerical investigation of heat transfer from a heated oscillating cylinder in a cross flow. *International Journal of Heat and Mass Transfer*, **45**(14), 3033 – 3043.

55. **Gebhardt, T.** and **S. Grossmann** (1994). Chaos transition despite linear stability. *Phys. Rev. E*, **50**(5), 3705–3711.

56. **Giauque, A.**, **T. Poinsot**, **M. J. Brear**, and **F. Nicoud** (2006). Budget of disturbance energy in gaseous reacting flows. *In Proc. Summer Program 2006, Center for Turbulence Research, Stanford University*.

57. **Golub, G. H.** and **C. E. V. Loan**, *Matrix Computations*. The Johns Hopkins University Press, UK, 1989.

58. **Guegan, A.**, **P. J. Schmid**, and **P. Huerre** (2008). Spatial optimal disturbances in swept attachment-line boundary layers. *J. Fluid Mech.*, **603**, 179–188.

59. **Gunzburger, M. D.**, *Perspectives in flow control and optimization*. SIAM, 2003.

60. **Gusachenko, L.** and **V. Zarko** (2008). Analysis of unsteady solid-propellant combustion models (review). *Combust. Explo. Shock Waves*, **44**, 31–42. ISSN 0010-5082.

61. **Gustavsson, L. H.** (1991). Energy growth of three-dimensional disturbances in plane Poiseuille flow. *J. Fluid Mech.*, **224**, 241–260.

62. **Hanifi, A.**, **P. J. Schmid**, and **D. S. Henningson** (1996). Transient growth in compressible boundary layer flow. *Physics of Fluids*, **8**(3), 826–837. URL `http://link.aip.org/link/?PHF/8/826/1`.

63. **Hantschk, C. C.** and **D. Vortmeyer** (1999). Numerical simulation of self-excited thermoacoustic instabilities in a Rijke tube. *Journal of Sound and Vibration*, **227**, 511–522.

64. **Harris, P. G.** and **A. D. Champlain** (1998). Experimental database describing pulse-triggered nonlinear instability in solid rocket motors. *Journal of Propulsion and Power*, **14**, 429– 439.

65. **Heckl, M. A.** (1990). Nonlinear acoustic effects in the Rijke tube. *Acustica*, **72**, 63–71.

66. **Heckl, M. A.** and **M. S. Howe** (2007). Stability analysis of the Rijke tube with a Green's function approach. *Journal of Sound and Vibration*, **305**, 672–688.

67. **Henningson, D. S.**, **A. Lundbladh**, and **A. V. Johansson** (1993). A mechanism for bypass transition from localized disturbances in wall-bounded shear flows. *J. Fluid Mech.*, **250**, 169–207.

68. **Henningson, D. S.** and **S. Reddy** (1994). On the role of linear mechanisms in transition to turbulence. *Phy. Fluids*, **6**, 1396–1398.

69. **Hill, D. C.** (1995). Adjoint systems and their role in the receptivity problem for boundary layers. *J. Fluid Mech.*, **292**, 183–204. URL `http://journals.cambridge.org/action/displayAbstract?fromPage=online&aid=354563&fulltextType=RA&fileId=S0022112095001480`.

70. **Hosseini, S. M. R.** and **C. J. Lawn** (2005). Non-linearities in the thermo-acoustic response of a premixed swirl burner. *Twelfth International Congress on Sound and Vibration*, 11–14 July, Lisbon.

71. **Juniper, M. P.** (2011). Triggering in the horizontal Rijke tube: Non-normality, transient growth and bypass transition. *Journal of Fluid Mechanics*, **667**, 272–308.

72. **Junye, W.** (2000). Non-linear analysis of solid propellant burning rate behavior. *Intl. J. Numer. Methods Fluids*, **33**(5), 627–640.

73. **Kaufmann, A.**, **F. Nicoud**, and **T. Poinsot** (2002). Flow forcing techniques for numerical simulation of combustion instabilities. *Combustion and Flame*, **131**(4), 371 – 385.

74. **Kedia, K. S.**, **S. B. Nagaraja**, and **R. I. Sujith** (2008). Impact of linear coupling on thermoacoustic instabilities. *Combust. Sci. Tech.*, **180**, 1588 – 1612.

75. **King, F. W.** Cambridge University Press, 2009. URL `http://dx.doi.org/10.1017/CBO9780511735271`.

76. **Kinsler, L. E.**, **A. R. Frey**, **A. B. Coppens**, and **J. V. Sanders**, *Fundamentals of Acoustics*. John Wiley & Sons, Inc., USA, 2000, 4 edition.

77. **Klebanoff, P. S.**, **K. D. Tidstrom**, and **L. M. Sargent** (1962). The three-dimensional nature of boundary-layer instability. *J. Fluid Mech.*, **12**(01), 1–34.

78. **Klein, R.** (1995). Semi-implicit extension of a Godunov-type scheme based on low mach number asymptotics i: one-dimensional flow. *Journal of Computational Physics*, **121**, 213–237.

79. **Klein, R.**, **N. Botta**, **T. Schneider**, **C. D. Munz**, **S. Roller**, **A. Meister**, **L. Hoffmann**, and **T. Sonar** (2001). Asymptotic adaptive methods for multi-scale problems in fluid mechanics. *Journal of Engineering Mathematics*, **39**, 261–343.

80. **Kopitz, J.** and **W. Polifke** (2008). Cfd based application of the Nyquist criterion to thermoacoustic instabilities. *Journal of Computational Physics*, **227**, 6754–6778.

81. **Kourta, A.** (1997). Shear layer instability and acoustic interaction in solid propellant rocket motors. *Intl. J. Numer. Methods Fluids*, **25**(8), 973–981.

82. **Krasnov, D. S.**, **E. Zienicke**, **O. Zikanov**, **T. Boeck**, and **A. Thess** (2004). Numerical study of the instability of the hartmann layer. *J. Fluid Mech.*, **504**, 183–211.

83. **Krechetnikov, R.** and **J. E. Marsden** (2009). On the origin and nature of finite-amplitude instabilities in physical systems. *Journal of Physics A: Mathematical and Theoretical*, **42**(41), 412004 (18pp). URL `http://stacks.iop.org/1751-8121/42/412004`.

84. **Krier, H.**, **S. J. T'ien**, **W. A. Sirignana**, and **M. Summerfield** (1968). Nonsteady burning phenomena of solid propellants: Theory and experiments. *AIAA J.*, **6**, 278–285.

85. **Kulkarni, R.**, **K. Balasubramanian**, and **R. I. Sujith** (2011). Non-normality and its consequences in active control of thermoacoustic instabilities. *J. Fluid Mech.*, **670**, 130–149.

86. **Kumar, K. R.** and **K. N. Lakshmisha** (2000). Nonlinear intrinsic instability of solid propellant combustion including gas-phase thermal inertia. *Combust. Sci. Tech*, **158**, 135–166.

87. **Kuo, K. K.** and **M. Summerfield** (1984). Nonsteady burning phenomena of solid propoellants: Theory and experiments. *Prog. Astronaut. Aeronaut.*, **90**, 760–767.

88. **Kurdyumov, V. N.** and **M. Matalon** (2004). Dynamics of an edge flame in a mixing layer. *Combustion and Flame*, **139**(4), 329 – 339.

89. **Kwon, Y. P.** and **B. H. Lee** (1985). Stability of the Rijke thermoacoustic oscillation. *J. Acoust. Soc. Am.*, **78**, 1414–1420.

90. **Lee, J. G.** and **D. A. Santavicca** (2005). Experimental diagnostics of combustion instabilities. *Prog. Astronaut. Aeronaut.*, **210**, 481–529.

91. **Levine, J. N.** and **J. D. Baum** (1983). A numerical study of nonlinear instability phenomena in solid rocket motors. *AIAA. J.*, **21**, 557–564.

92. **Lighthill, M. J.** (1954). The response of laminar skin friction and heat transfer to fluctuations in the stream velocity. *Proceedings of the Royal Society of London. Series A, Mathematical and Physical Sciences*, **224**(1156), 1–23. ISSN 00804630. URL `http://www.jstor.org/stable/99502`.

93. **Lin, A. C.** and **S. Y. Wang**, Investigation of aluminized solid propellant combustion instability by means of a T-burner. *In In Thirty-Third Aerospace sciences meeting and exhibit*. 95-0606, Reno, US, 1995.

94. **Mao, X.**, **S. J. Sherwin**, and **H. M. Blackburn** (2009). Transient growth & bypass transition in stenotic flow with physiological waveform. *Theoretical & Computational Fluid Dynamics*.

95. **Margolis, S. B.** and **R. C. Armstrong** (1986*a*). Diffusional/thermal coupling and intrinsic instability of solid propellant combustion. *ombust. Sci. Tech*, **59**, 27–84.

96. **Margolis, S. B.** and **R. C. Armstrong** (1986*b*). Two asymptotic models for solid propellant combustion. *ombust. Sci. Tech*, **47**, 1–38.

97. **Mariappan, S.**, **P. J. Schmid**, and **R. I. Sujith** (2010). Role of transient growth in subcritical transition to thermoacoustic instability in a horizontal rijke tube. *16th AIAA/CEAS Aeroacoustics Conference, 7 - 9 June 2010, Stockholm, Sweden, AIAA 2010-3857*.

98. **Mariappan, S.** and **R. I. Sujith** (2010*a*). Modeling nonlinear thermoacoustic instability in an electrically heated Rijke tube. *48th AIAA Aerospace Sciences Meeting Including the New Horizons Forum and Aerospace Exposition, 4 - 7 January 2010, Orlando, Florida, AIAA 2010-25*.

99. **Mariappan, S.** and **R. I. Sujith** (2010*b*). Thermoacoustic instability in solid rocket motor - non-normality and nonlinear instabilities. *J. Fluid Mech.*, **653**, 1–33.

100. **Marquet, O.**, **M. Lombardi**, **J. M. Chomaz**, **D. Sipp**, and **L. Jacquin** (2009). Direct and adjoint global modes of a recirculation bubble: lift-up and convective non-normalities. *J. Fluid Mech.*, **622**, 1–21.

101. **Matsubara, M.** and **P. H. Alfredsson** (2001). Disturbance growth in boundary layers subjected to free-stream turbulence. *J. Fluid Mech.*, **430**, 149–168.

102. **Matveev, K. I.** (2003). *Thermo-acoustic instabilities in the Rijke tube: Experiments and modeling*. Ph.D. thesis, California Institute of Technology, Pasadena.

103. **Matveev, K. I.** and **F. E. C. Culick** (2003*a*). A model for combustion instability involving vortex shedding. *Combustion Science and Technology*, **175**(6), 1059 – 1083.

104. **Matveev, K. I.** and **F. E. C. Culick** (2003*b*). A study of the transition to instability in a rijke tube with axial temperature gradient. *Journal of Sound and Vibration*, **264**(3), 689 – 706.

105. **Mayer, E. W.** and **E. Reshotko** (1997). Evidence for transient disturbance growth in a 1961 pipe flow experiment. *Phy. Fluids*, **9**, 242–244.

106. **Mcmanus, K.**, **T. Poinsot**, and **S. Candel** (1993). A review of active control of combustion instabilities. *Progress in Energy and Combustion Science*, **19**, 1 – 29.

107. **Moeck, J.**, **M. Oevermann**, **R. Klein**, **C. Paschereit**, and **H. Schmidt** (2009). A two-way coupling for modeling thermoacoustic instabilities in a flat flame rijke tube. *Proceedings of the Combustion Institute*, **32**(1), 1199 – 1207. ISSN 1540-7489. URL `http://www.sciencedirect.com/science/article/B7GWS-4TN5MPT-7/2/4c47f380da9fe8ee4599feec6c2a807b`.

108. **Moeck, J. P.**, **H. Schmidt**, **M. Oevermann**, **C. O. Paschereit**, and **R. Klein**, An asymptotically motivated hydrodynamic-acoustic two-way coupling for modeling thermoacoustic instabilities in a Rijke tube. *In ICSV14*. Technical University Berlin, Cairns, Australia, 2007.

109. **Mukhopadhyay, B.**, **N. Afshordi**, and **R. Narayan** (2006). Growth of hydrodynamic perturbations in accretion disks: Possible route to non-magnetic turbulence. *Adv. Space Res.*, **38**(12), 2877–2879.

110. **Myers, M. K.** (1991). Transport of energy by disturbances in arbitrary steady flows. *J. Fluid Mech.*, **226**, 383–400.

111. **Nagaraja, S.**, **K. Kedia**, and **R. Sujith** (2009). Characterizing energy growth during combustion instabilities: Singularvalues or eigenvalues? *In Proceedings of the Comb. Institute*, **32**(2), 2933 – 2940. ISSN 1540-7489.

112. **Negrete, D. C.**, **D. A. Spong**, and **S. P. Hirshman** (2008). Proper orthogonal decomposition methods for noise reduction in particle-based transport calculations. *Phy. Plasmas*, **15**, 092308.

113. **Nicoud, F.**, **L. Benoit**, **C. Sensiau**, and **T. Poinsot** (2007). Acoustic modes in combustors with complex impedances and multidimensional active flames. *AIAA J.*, **45**, 426–441.

114. **Nicoud, F.** and **T. Poinsot** (2005). Thermoacoustic instabilities: Should the Rayleigh criterion be extended to include entropy changes? *Combustion and Flame*, **142**, 153ï£¡159.

115. **Orr, W. M.** (1907). The stability or instability of the steady motions of a perfect liquid and of a viscous liquid. part i: A perfect liquid. *Proceedings of the Royal Irish Academy. Section A: Mathematical and Physical Sciences*, **27**, pp. 9–68.

116. **Padmanabhan, M. S.** (1975). *The effect of nozzle nonlinearities on the nonlinear stability of liquid rocket motors*. Ph.D. thesis, Georgia Institute of Technology, Atlanta, USA.

117. **Patankar, S. V.**, *Numerical heat transfer and fluid flow*. Hemisphere Publishing Corporation, Washington, 1980.

118. **Podvin, B.**, **Y. Fraigneau**, **F. Lusseyran**, and **P. Gougat** (2006). A reconstruction method for the flow past an open cavity. *Journal of Fluids Engineering*, **128**, 531–540.

119. **Poinsot, T.** and **D. Veynante**, *Theoretical and numerical combustion*. R.T. Edwards, Inc., Philadelphia, 2005, second edition.

120. **Preetham**, **H. Santosh**, and **T. Liewen** (2008). Dynamics of laminar premixed flames forced by harmonic velocity disturbances. *Journal of Propulsion and Power*, **24**(6), 1390 – 1402.

121. **Press, W. H.**, **S. A. Teukolsky**, and **B. P. Flannery**, *Numerical recipes: the art of scientific computing*. Cambridge University Press, UK, 2007, third edition.

122. **Price, E. W.** (1984). Fundamentals of solid-propellant combustion. *Prog. Astronaut. Aeronaut.*, **90**, 479–513.

123. **Rayleigh, L.** (1878). The explanation of certain acoustical phenomenon. *Nature*, **18**, 319–321.

124. **Reddy, S. C.** and **L. N. Trefethen** (1994). Pseudospectra of the convection-diffusion operator. *SIAM Journal on Applied Mathematics*, **54**(6), pp. 1634–1649.

125. **Rienstra, S. W.** and **A. Hirschberg**, *An introduction to acoustics*. Technische Universiteit Eindhoven, Netherlands, 2004, IWDE 92-06 edition.

126. **Rienstra, S. W.** and **A. Hirschberg** (2008). An introduction to acoustics. *Intl. journal of spray and combustion dynamics*, IWDE 92–06.

127. **Rijke, P. L.** (1859). The vibration of the air in a tube open at both ends. *Philosophical Magazine*, **17**, 419–422.

128. **Riley, K. F.**, **M. P. Hobson**, and **S. J. Bence**, *Mathematical Methods for Physics and Engineering*. Cambridge University Press, UK, 2006, third edition.

129. **Romanov, O. Y.** (1999). Unsteady burning of solid propellants. *Journal of Propulsion and Power*, **15**, 823–836.

130. **Rowley, C. W.** (2005). Model reduction for fluids, using balanced proper orthogonal decomposition. *International journal of bifurcation and chaos*, **15**, 997–1013.

131. **Sameen, A.** and **R. Govindarajan** (2007). The effect of wall heating on instability of channel flow. *J. Fluid Mech.*, **577**, 417–442.

132. **Sarpkaya, T.** (1986). Force on a circular cylinder in viscous oscillatory flow at low keulegan-carpenter numbers. *J. Fluid Mech.*, **165**, 61–71.

133. **Schmid, P.** (2011). Application of the dynamic mode decomposition to experimental data. *Experiments in Fluids*, 1–8. ISSN 0723-4864.

134. **Schmid, P. J.** (2007). Nonmodal stability theory. *Annu. Rev. Fluid Mech.*, **39**(1), 129–162.

135. **Schmid, P. J.** (2010). Dynamic mode decomposition of numerical and experimental data. *J. Fluid Mech.*, **656**, 5–28.

136. **Schmid, P. J.** and **D. S. Henningson** (1992). A new mechanism for rapid transition involving a pair of oblique waves. *Phy. Fluids*, **4**, 1986–1989.

137. **Schmid, P. J.** and **D. S. Henningson**, *Stability and Transition in Shear Flows*. Springer-Verlag, New York, 2001.

138. **Schmid, P. J.** and **D. S. Henningson** (2002). On the stability of a falling liquid curtain. *J. Fluid Mech.*, **463**, 163–171.

139. **Schmid, P. J.**, **L. Li**, **M. P. Juniper**, and **O. Pust** (2010). Applications of the dynamic mode decomposition. *Theor. Comput. Fluid Dyn.*, **641**.

140. **Schmid, P. J.**, **K. E. Meyer**, and **O. Pust**, Dynamic mode decomposition and proper orthogonal decomposition of flow in a lid-driven cylindrical cavity. *In 8th International Symposium on Particle Image Velocimetry*. Melbourne, Australia, 2009.

141. **Schuermans, B.**, **H. Luebcke**, **D. Bajusz**, and **P. Flohr** (2005). Thermoacoustic analysis of gas turbine combustion systems using unsteady cfd. *Proceedings of ASME Turbo Expo, Power for Land, Sea, and Air*, GT2005–68393.

142. **Schuller, T.**, **D. Durox**, and **S. Candel** (2003). Self-induced combustion oscillations of laminar premixed flames stabilized on annular burners. *Combustion and Flame*, **135**(4), 525 – 537. ISSN 0010-2180.

143. **Selimefendigil, F.**, **S. Föller**, and **W. Polifke**, Nonlinear identification of the unsteady heat transfer of a cylinder in pulsating crossflow. *In Int. Conf. on Jets, Wakes and Separated Flows*. Technical University Berlin, Berlin, Germany, 2008.

144. **Selimefendigil, F.**, **R. Sujith**, and **W. Polifke** (2011). Identification of heat transfer dynamics for non-modal analysis of thermoacoustic stability. *Applied Mathematics and Computation*, **217**(11), 5134 – 5150. Special issue on Fluid Flow and Heat Transfer.

145. **Shimada, T.**, **M. Hanzawa**, **T. Kata**, **T. Yoshikawa**, and **Y. Wada**, Stability analysis of solid rocket motor combustion by computational fluid dynamics. *In In Thirteenth AIAA/CEAS Aeroacoustics Conference*. 2007-3427, 2007.

146. **Song, W. S.**, **S. Lee**, **D. S. Shin**, and **Y. Na** (2006). Thermo-acoustic instability in the horizontal Rijke tube. *Journal of Mechanical Science and Technology*, **20**, 905–913.

147. **Strogatz, S. H.**, *Nonlinear Dynamics and Chaos: with applications to Physics, Biology, Chemistry, and Engineering*. Westview Press, Colorado, 2000, first edition.

148. **Subramanian, P.**, **S. Mariappan**, **P. Wahi**, and **R. I. Sujith** (2010*a*). Bifurcation analysis of thermoacoustic instability in a rijke tube. *International journal of spray and combustion dynamics*, **2**, 325–356.

149. **Subramanian, P.**, **S. Mariappan**, **P. Wahi**, and **R. I. Sujith** (2010*b*). Bifurcation analysis of thermoacoustic instability in a rijke tube. *n3l - IntŠl Summer School and Workshop on Non-Normal and Nonlinear Effects in Aero- and Thermoacoustics, May 17-21, 2010, Munich*.

150. **Subramanian, P.** and **R. I. Sujith** (2011). Non-normality and internal flame dynamics in premixed flame-acoustic interaction. *J. Fluid Mech.*, **accepted for publication**.

151. **Sutton, G. P.** and **O. Biblarz**, *Rocket Propulsion Elements*. Wiley-IEEE, New York, 2001, 7 edition.

152. **Telionis, D. P.**, *Unsteady viscous flows*. Springer-Verlag, New York, 1981.

153. **Ting, L.**, **R. Klein**, and **O. M. Knio**, *Vortex Dominated Flows: Analysis and Computation for Multiple Scales*. Springer Verlag, New York, 2007, Series in Applied Mathematical Sciences edition.

154. **Trefethen, L. N.** and **M. Embree**, *Spectra and Pseudospectra, The Behaviour of Non-normal Matrices and Operators*. Princeton University Press, New Jersey, 2005, first edition.

155. **Tulsyan, B.**, **K. Balasubramanian**, and **R. I. Sujith** (2009). Revisiting a model for combustion instability involving vortex shedding. *Combust. Sci. Tech.*, **181**, 457 – 482.

156. **Vuillot, J.** (1995). Vortex shedding phenomena in solid rocket motors. *J. Propul. Power*, **11**, 626–639.

157. **Waleffe, F.** (1995). Transition in shear flows: non-linear normality versus non-normal linearity. *Phy. Fluids*, **7**, 3060–3066.

158. **Ward, M. J.**, **S. F. Son**, and **M. Q. Brewster** (1998). Steady deflagration of hmx with simple kinetics: a gas phase chain reaction model. *Combust. Flame*, **114**(3-4), 556 – 568. ISSN 0010-2180.

159. **Wicker, J. M.**, **W. D. Greene**, **S.-I. Kim**, and **V. Yang** (1996). Triggering of longitudinal combustion instabilities in rocket motors: nonlinear combustion response. *Journal of Propulsion and Power*, **12**, 1148–1158.

160. **Wieczorek, K.**, **C. Sensiau**, **W. Polifke**, and **F. Nicoud** (2010). Assessing non-normal effects in thermoacoustic systems with non zero baseline flow. *n3l - Int'l Summer School and Workshop on Non-Normal and Nonlinear Effects in Aero- and Thermoacoustics, May 17-21, 2010, Munich*.

161. **Williams, F. A.** (1962). Response of a burning solid to small-amplitude pressure oscillations. *J. Appl. Phys.*, **33**, 3153–3166.

162. **Williams, F. A.**, *Combustion Theory*. Addison-Wesley, New York, 1985, second edition.

163. **Wu, X.** and **P. Moin** (2010). Large-activation-energy theory for premixed combustion under the influence of enthalpy fluctuations. *J. Fluid Mech.*, **655**, 3–37.

164. **Wu, X.**, **M. Wang**, **P. Moin**, and **N. Peters** (2003). Combustion instability due to the nonlinear interaction between sound and flame. *J. Fluid Mech.*, **497**, 23–53.

165. **Yang, V.**, **S. I. Kim**, and **F. E. C. Culick** (1990). Triggering of longitudinal pressure oscillations in combustion chambers. Part I. Nonlinear gasdynamics. *Combust. Sci. Tech.*, **72**, 183–214.

166. **Yoon, H. G.**, **I. Peddieson**, and **K. R. Purdy** (2001). Non-linear response of a generalized Rijke tube. *Intl. J. Engng. Sci.*, **39**, 1707–1723.

167. **Zeytounian, K. H.**, *Asymptotic modelling of fluid flow phenomena*. Kluwer academic publisher, Netherlands, 2002.

168. **Zinn, B. T.** (1972). Longitudinal mode acoustic losses in short nozzles. Technical Report AD0744623, Research Rep. Naval Weapons Center China Lake.

169. **Zinn, B. T.** and **T. C. Lieuwen**, *Combustion instabilities: Basic concepts - Combustion Instabilities in Gas Turbine Engines: Operational Experience, Fundamental Mechanisms, and Modeling*. AIAA, USA, 2006.

170. **Zinn, B. T.** and **M. E. Lores** (1971). Application of the Galerkin method in the solution of non-linear axial combustion instability problems in liquid rockets. *Combust. Sci. Tech.*, **4**, 269–278.

LIST OF PAPERS BASED ON THESIS

Referred Journals:

1. **Sathesh Mariappan and R. I. Sujith Thermoacoustic instability in a solid rocket motor: non-normality and nonlinear instabilities.** ***Journal of Fluid Mechanics*** **, 653, 1-33, (2010).**

2. **Sathesh Mariappan and R. I. Sujith Modeling nonlinear thermoacoustic instability in an electrically heated Rijke tube.** ***under accepted for publication in Journal of Fluid Mechanics*** **, , , (2011).**

International Conferences:

1. **Sathesh Mariappan and R. I. Sujith Thermoacoustic instability in a solid rocket motor: non-normality and nonlinear instabilities.** ***48^{th} AIAA Aerospace Sciences Meeting Including the New Horizons Forum and Aerospace Exposition*****, 4 - 7 January, Orlando, Florida, AIAA 2010 - 1517, (2010).**

2. **Sathesh Mariappan and R. I. Sujith Modeling nonlinear thermoacoustic instability in an electrically heated Rijke tube.** ***48^{th} AIAA Aerospace Sciences Meeting Including the New Horizons Forum and Aerospace Exposition*****, 4 - 7 January, Orlando, Florida, AIAA 2010 - 25, (2010).**

3. **Sathesh Mariappan, R. I. Sujith and P. J. Schmid Non-normal and nonlinear dynamics of thermoacoustic instability in a horizontal Rijke tube.** ***n^3l - Int'l Summer School and Workshop on Non-Normal and Nonlinear Effects in Aero and Thermoacoustics*****, 17 - 21 May, Munich, Germany, (2010).**

4. **Sathesh Mariappan, P. J. Schmid and R. I. Sujith Role of transient growth in subcritical transition to thermoacoustic instability in a horizontal Rijke tube.** ***16^{th} AIAA/CEAS Aeroacoustics Conference*****, 7 - 9 June, Stockholm, Sweden, AIAA 2010 - 3857, (2010).**

5. **Sathesh Mariappan, R. I. Sujith and P. J. Schmid Subcritical transition to thermoacoustic instability in a horizontal Rijke tube: Non-normal and nonlinear effects.** ***13^{th} Asian Congress of Fluid Mechanics*****, 17 - 21 December, Dhaka, Bangladesh, (2010).**